Mesoscopic few-electron voltage pulse source

Thibaut Jullien

To cite this version:

Thibaut Jullien. Mesoscopic few-electron voltage pulse source. Condensed Matter [cond-mat]. Université Paris Sud - Paris XI, 2014. English. NNT : 2014PA112071 . tel-01158785

UNIVERSITÉ PARIS-SUD

ECOLE DOCTORALE PHYSIQUE DE LA RÉGION PARISIENNE
SERVICE DE PHYSIQUE DE L'ETAT CONDENSÉ DE L'IRAMIS-CEA

DISCIPLINE : PHYSIQUE MÉSOSCOPIQUE

THÈSE DE DOCTORAT

Version : 20 février 2014

Thibaut Jullien

Source mésoscopique à quelques électrons par pulses de tension

Directeur de thèse : M. Christian Glattli CEA-Saclay

Composition du jury :

Président du jury :	....	..... (......)
Rapporteurs :	Dr. Christian Flindt	University of Geneva
	Dr. Charles Marcus	University of Copenhagen
Examinateurs :	M. Marc Sanquer	CEA-Grenoble
	M. Pascal Simon	Université Paris-Sud
	M. Xavier Waintal	CEA-Grenoble
Invité :	M. Preden Roulleau	CEA-Saclay

4GHz33

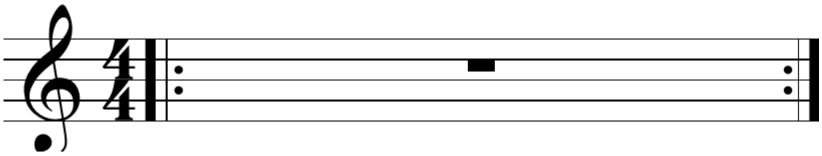

Summary

Mesoscopic few-electron voltage pulse source

The on-demand generation of well-controlled quantum excitations leads to the operation of increasingly complex quantum systems. However, the collective response of the Fermi sea to a perturbation typically includes holes and electrons and the control of a few degrees of liberty is difficult to achieve. A means of generating a time-resolved elementary excitation through short-time voltage pulses $V_p(t)$ applied on the contacts of a one-dimensional coherent conductor has been predicted[90]. For most voltage pulses, a finite number of neutral electron-hole pairs are injected. The only possibility to suppress hole-generation, which means that the Fermi sea appears unmodified, is through Lorentzian-shaped voltage pulses with quantized flux $e/h \int_{-\infty}^{+\infty} V_p(t)dt = n$. The transferred quantum states, termed levitons, have strikingly simple statistical properties : they minimize the shot noise when impinging a static potential barrier.

In this thesis, we study the generation of this states and show that Lorentzian pulses implement an on-demand electron source. GHz pulses are applied on a partially-transmitting quantum point contact (QPC) below 50 mK and realized from a two-dimensional electron gas in a GaAs/AlGaAs heterostructure. The resulting Photo-Assisted Shot Noise (PASN) is proportional to the number of electron and holes, thus testing the source properties. Additional characterization performed with the PASN includes the energy-distribution of the excitations and the time-extension.

Keywords : on-demand source, elementary excitation, photo-assisted shot noise

Résumé

Source mésoscopique à quelques électrons par pulse de tension

La génération à la demande d'excitations quantiques dans un état contrôlé permet la construction de systèmes quantiques de plus en plus complexe. Cependant, la réponse collective de la mer de Fermi à une perturbation comprend généralement à la fois des électrons et des trous, ce qui rend la manipulation d'un nombre limité de degrés de liberté plus difficile. Une méthode permettant de générer une excitation élémentaire résolue en temps dans un conducteur cohérent unidimensionnel a été proposée[90] : l'application de pulses de tension de forme lorentzienne. Un pulse $V_p(t)$ de forme quelconque injecte un nombre fini de paires électron-trou. La seule possibilité de supprimer les trous et de laisser la mer de Fermi intacte est d'appliquer des pulses lorentziens dont le flux est quantifié $e/h \int_{-\infty}^{+\infty} V_p(t)dt = n$. Les paquets d'onde transferrés sont des quasi-particules appelés Levitons. Ils ont des propriétés statistiques remarquables : ils minimisent le bruit de grenaille.

Dans cette thèse, on étudie la génération de ces objets et on démontre que des pulses Lorentzians constituent une source d'électrons à la demande. Des pulses GHz sont appliqués sur un contact ponctuel quantique (QPC) semi-réfléchissant et refroidi au-dessous de 50 mK. Le bruit de grenaille photo-assisté (PASN) généré est proportionnel au nombre total d'électrons et de trous, ce qui permet de tester la source. Le PASN permet également de déterminer la distribution en énergie et le profil temporel des paquets d'onde.

Mots-clés : source à la demande, excitation élémentaire, bruit de grenaille photo-assisté

Contents

List of Figures

List of Tables

Chapitre 0

Motivation, context and outline

This manuscript addresses the experimental study of coherent ballistic transport in one-dimensional mesoscopic systems undergoing sub-nanosecond voltage pulses and their application to few-electron on-demand sources. The main motivation is to demonstrate the fast and precise injection of a controlled number of electrons provided by voltage pulses, down to one particle at a time in a well-defined quantum state[90][65][71][38]. This approach offers new possibilities to investigate the Full Counting Statistics (FCS) of mesoscopic circuits, to implement interference experiments inspired by quantum optics with photons, or to realize flying qubits in conductors. We characterize the states excited by the pulses with low-frequency shot-noise measurements. The shot noise is indeed known to be proportional to the number of elementary carriers reflected or transmitted by a scatterer[14][152][95]. It contrasts with a current measurement which indicates the number of transmitted charges, and provides information on the presence or absence of neutral electron-hole pairs in the excited system.

This work is a contribution to mesoscopic physics, which studies the properties of samples whose size is smaller than the electronic coherence length. In this regime, wave-packets keep a well-defined phase, and quantum properties persist all along the transport through these systems. This scale is observed experimentally in cooled-down nano-lithographied structures. A convenient system to study quantum transport is a Quantum Point Contact (QPC) made from a GaAs/AsGaAs hetero-structure[141] : it realizes a ballistic one-dimensional conductor with a tunable potential barrier. Transport experiments in the DC regime have successfully verified that the properties of such a conductor are well-described by the Landauer-Büttiker formalism[26]. In this approach, transport is understood as the scattering of electron waves entering the conductor. They are either transmitted or reflected, two possible outputs with respective probabilities D and $1 - D$. A full transmission results in a quantized conductance[151][145]. The Pauli principle is responsible for the shot noise reduction below the Poisson level, as observed when recording the current fluctuations over time[12][121][78]. Over the two last decades, the physics of quantum wires submitted to an AC field has also been explored, both theoretically and experimentally. The FCS[89] has been developed to predict all transport statistics and the Photo-Assisted Scattering theory[114][86] shows the role of photo-absorption and photo-emission in the AC transport. These two mechanisms have been confirmed thanks to the measurable partition noise of photo-assisted electron-hole pairs[128][120], even in the absence of a net current. The FCS determination is still limited to the few first statistical moments[119][155][47].

The subject of this thesis, the application of voltage pulses to QPCs, constitutes a special case of AC transport which is remarkably relevant to the realization of new experiments analogous to quantum optics ones with few photons. The field of electronic quantum optics has rapidly progressed thanks to the availability of electronic beam-splitters, with QPCs, and electronic waveguides implemented by the chiral edge channels in the Integer Quantum Hall regime (IQH)[73][22]. Up to now, most experiments have been conducted using the stationary stream of electrons induced by a DC bias[91][110][66][105][124], but the attention is now moving toward synchronized single-charge emitters. Over the years, varied strategies have been developed to trigger time-controlled electron transfer[32][61][99][15][42]. Some of these devices have been primarily designed to meet the metrologic requirement[115] of a fast and accurate current. Realized with a different perspective, the recent Single-Electron-Source based on a mesoscopic capacitor[41] has led to a series of experimental[17][16] advances in electronic optics, and triggered theoretical contributions[102][72][69][56]. The working principle is as follows : a quantum dot whose highest occupied energy level is suddenly risen above the Fermi energy of the leads and injects an electron in an IQH channel. The source is coherent and energy-resolved, exactly as frequency-resolved single-photon sources, and the energy is tunable. The recent demonstration of the indistinguishability between two electrons from two separate sources[16] has confirmed[1] the potential for addressing quantum information problems[106].

The time-resolved electron source described in this manuscript follows the proposal from Levitov et al. in [90][65] where charge is injected using voltage pulses $V_p(t)$ applied at a quantum wire contact. Remarkably, a pulse with the correct shape and amplitude

---

[1] For a recent review : [18].

(lorentzian with a quantized action $e/h\int_{-\infty}^{+\infty}V_p(t)dt = 1$) is expected to excite a single electron just above the Fermi level and add no other excitation. This minimal-excitation state has been called a leviton to emphasize its quasi-particle behavior. The physics behind the voltage pulse source involves non-trivial Fermi statistics properties which have not been observed yet. This new method is attractive for several reasons. No nano-lithographied structure is required besides the quantum wire in which the charge is injected. The mechanism is universal while the physics of devices based on quantum dots and QPCs depends on their geometry. The number of electrons injected at the same time is arbitrary, as is the time-delay between charge pulses.

The manuscript is organized as follows. In chapter 1, we review the effect of a time-dependent voltage pulse on a coherent and ballistic one-dimensional conductor. The prediction of Levitov et al. is presented. The photo-assisted description is emphasized since most experiments presented afterwards have a simple interpretation in terms of photo-absorption (electronic excitation) and photo-emission processes (hole-like excitation). The low-noise cross-correlation set-up necessary to characterize the electron source is presented in chapter 2. Past results about QPC conductance, thermal noise and shot noise are found again and then used to understand the system. It is completed by radio-frequency calibration in chapter 3. The core of the work is presented in chapter 4. Voltages pulses with various shape and amplitude are applied and the photo-assisted shot noise serves as a probe to verify the nature of the excited state, in terms of injected particle(s), energy-distribution and time-extension. The two last chapters propose additional verification of the theory, with a scheme aimed at a full determination of the Floquet Scattering Matrix (chapter 5) which could also lead to a full Quantum State Tomography of a single-electron excitation, and complementary results about the effect of temperature on the voltage-pulse injection (chapter 6).

Chapitre 1

Leviton : time-resolved minimal excitation [1]

In this chapter, we address the physics of the on-demand injection of a small finite number of electrons N_e in a coherent conductor using voltage pulses $V_p(t)$ applied on a contact. The device is the simplest possible one : a tunnel junction between two coherent leads. This problem was analysed by Levitov and Lesovik[90][65] as the special case of AC Transport in one-dimensional system realised when $\int\limits_{-\infty}^{\infty} V_p(t)dt$ is finite and induces a time-localised charge pulse. They showed that a lorentzian pulse carrying an integer charge implements an ideal clean on-demand source of electrons. By clean we mean that the number of transported charges Q_e is exactly the number of electrons N_e involved : no neutral electron-pair accompanies the charge pulse. This property can be verified by shot noise measurements.

In section 1.1, we quickly review the DC transport and the fundamental mechanism leading to shot noise. From section 1.2 to 1.3 we follow Dubois et al. in [38] and analyze the purity of the source by calculating the low-frequency shot noise resulting from periodically repeated particle scattering on a tunnel barrier. This presentation is particularly relevant as it corresponds to an experimental scheme which realizes particle counting. The difference between zero temperature and a realistic experiment at finite temperature is emphasized.

Section 1.5 and 1.6 develop additional noise measurements leading to a complete characterization of the pulsed injection in energy and time-domain. In section 1.7 we consider in details the interpretation of the lorentzian charge pulse as a single particle moving freely

---

[1] This chapter is adapted from[38] : Integer and fractional charge lorentzian voltage pulses analyzed in the framework of photon-assisted shot noise.

on top of the unmodified Fermi sea and injected on-demand : the leviton.

1.1 DC electron flow

DC transport in coherent and ballistic one-dimensional conductors is strongly governed by two principles : the Fermi exclusion and the Heisenberg principle. In this section, we review the consequences of these principles on the low-frequency current fluctuations.

1.1.1 Single channel and quantized conductance

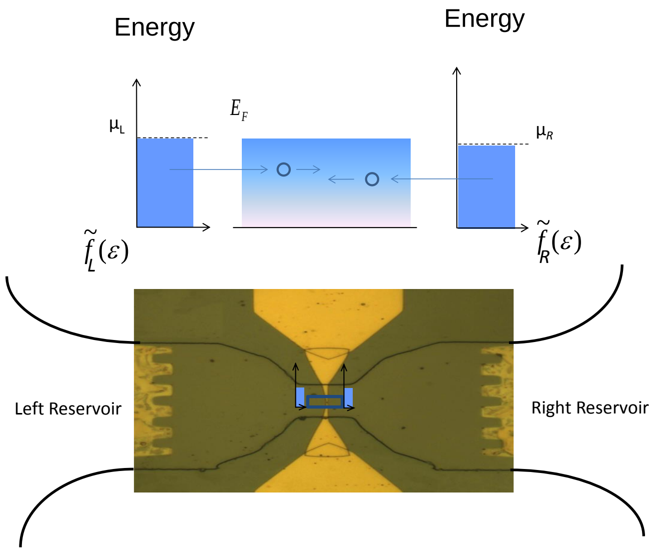

FIGURE 1.1 – A one-dimension ballistic coherent conductor and its model[26]. Bottom Figure : Optical photography[3] of a QPC with contacts, top gates and mesa (Sample “A”, see Appendix B). This system implements the one-dimension ballistic quantum conductor. Size L_s of the region combining one-dimensional, ballistic and coherent transport is typically defined at 35 mK and using high mobility 2DEG by the gate pattern. Its length is shorter than the coherence length even for the highest energy involved, about 100 µV. Top Figure : Schematic description of the QPC. Two reservoirs emit electrons in the coherent wire.

Fig. 1.1 represents a QPC fabricated on a high mobility 2DEG. At low-temperature, this system behaves as a one-dimension ballistic coherent conductor[4]. Such a quantum wire

---

[3] Not real proportions.

[4] Transport characteristics from the 2DEG properties are reviewed in Appendix B.

between two incoherent reservoirs is conveniently represented by the superposition of two independent fermionic systems moving in opposite directions. These systems are labeled L or R according to the reservoir —Left or Right— the particles originate from. We note V_{ds} the DC bias applied on the left contact. The electrochemical potential $\mu_R = E_F + eV_{ds}$ and $\mu_L = E_F$ and temperature T_e of these reservoirs impose $f_L(\varepsilon)$ and $f_R(\varepsilon)$, respectively the left and right Fermi distribution. They are given as :

$$f_{L,R}(\varepsilon) = \frac{1}{1 + e^{\frac{\varepsilon - \mu_{L,R}}{k_B T_e}}} \tag{1.1}$$

An electron wave leaving the quantum wire and re-absorbed in a lead may end up coming back into the conductor after multiple scattering, but it will have lost memory of both its previous phase and its previous energy. It will thus not generate quantum interference. The separation between the quantum wire and the incoherent "reservoir" embodies this idea, and the details of the transition can be overlooked. Once the density of state and energy-dependent velocity are taken into account, each energy level from each Fermi sea contributes to a fraction of current as :

$$\pm \frac{e}{h} f_{L,R}(\varepsilon) \tag{1.2}$$

The sign $+(-)$ corresponds to the right-moving (left-moving) wave. $f_L(\varepsilon)$ and $f_R(\varepsilon)$ represent the probabilities for a level to be occupied according to Fermi statistics. The factor e/h, i.e. carrier charge over Planck constant, is universal. It results from the strict spacing in time $\Delta\tau$ for the fermions occupying a band of size $\Delta\varepsilon$ imposed by the combination of the Fermi exclusion and the Heinsenberg uncertainty principle : $\Delta\tau = h/\Delta\varepsilon$.

A localized potential barrier separates each incoming wave-packet in a reflected wave and a transmitted wave. Using a QPC provides a tunable transmission. We assume that the transmission is energy-independent.

In quantum optics language, the scatterer implements an electron beam-splitter. The transmitted part has a probability amplitude reduced by a factor $S_{L,R}(\varepsilon)$ (Fig. 1.2). This is easily integrated in Eq. 1.2. The average transmitted current is reduced by $|S_{L,R}(\varepsilon)|^2 = D$ ($D < 1$) for each incoming contribution and the total current is :

$$< I > = \frac{e}{h} \int_{-\infty}^{\infty} (D f_L(\varepsilon) - D f_R(\varepsilon)) d\varepsilon = D \frac{e^2}{h} V_{ds} \tag{1.3}$$

Eq. 1.3 is the well-known Landauer formula for one dimensional transport.

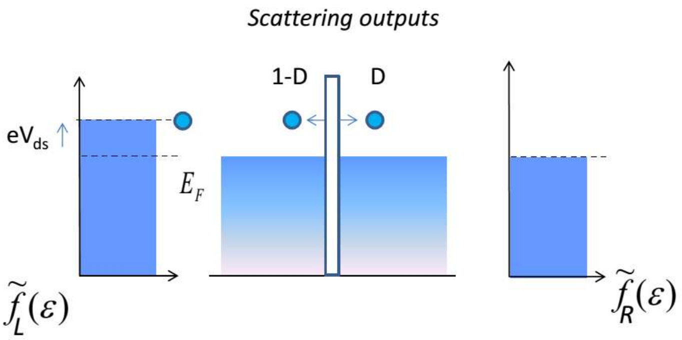

FIGURE 1.2 – Scattering of incoming particles on a localized and energy-independent barrier, with the two possible outputs. D is the transmission probability for a particle, or the amplitude of the transmitted fraction of the wave.

1.1.2 DC Shot Noise

We have emphasized two kinds of stochastic processes to be associated when deriving the current amplitude : transmission probability D and occupation probability $f_{L,R}(\varepsilon)$ (variable (ε) can be omitted for the sake of simplicity). Both statistics are binomial and generate fluctuations in the current, or noise. The picture is complete when we include the effect of the Fermi exclusion, or fermionic antibunching. It correlates scattering events between the two sides since two indistinguishable fermions (i.e. in our case two electrons at the same energy) cannot end in the same reservoir. Thus, noise occurs only when an electron incoming from the left finds no incoming electron from the right or if a hole incoming from the left finds no incoming hole from the right.

$$\begin{aligned} S_I^{DCSN}(T_e, V_{ds}) &= \frac{1}{\Delta\nu}(< I(\nu=0)I(\nu=0) > - < I(\nu=0) >^2) \\ &= 2\frac{e^2}{h}\int (D[f_L(1-f_R) + f_R(1-f_L)] \\ &- D^2\left[f_L - f_R\right]^2)dE \end{aligned} \tag{1.4}$$

DCSN stands for DC Shot Noise, the noise observed at finite temperature T_e and finite DC bias V_{ds}. We can decompose this equation into several terms. First line in Eq. 1.4 is the definition of the noise Power Spectral Density (PSD) at zero frequency. The second line contains the probability of the two events giving rise to a single charge change

$(\pm\Delta Q_e)^2$=1. The third line is simply the square of the average charge increase $<\Delta Q_e>^2$ in a single scattering event at energy ε, as it was written in Eq. 1.3. The difference between the two last expressions defines a variance. The integration has the same meaning than in the current derivation (Eq. 1.3) : each energy level contributes separately to the noise. The origin of the dimensional factor e^2/h is not covered in details here [5], but can easily be checked to provide the ratio $e^2\Delta\varepsilon/\Delta\nu$ expected from the integration over all energies and a current spectral density. From a physical point of view, it contains the average rate of the individual scattering events.

The integrated form is more compact.

$$S_I^{DCSN}(T_e, V_{ds}) = 4k_BT_e\frac{e^2}{h}\left(D^2 + D(1-D)\frac{eV_{ds}}{2k_BT_e}coth(\frac{eV_{ds}}{2k_BT_e})\right) \tag{1.5}$$

At zero temperature and for zero AC voltage, the noise is zero. The zero-bias limit at finite temperature obeys the Johnson-Nyquist formula[81][67][107] for equilibrium noise :

$$S_I^{DCSN}(T_e, 0) = 4k_BT_eD\frac{e^2}{h} \tag{1.6}$$

The other limit, zero-temperature and finite bias is :

$$S_I^{DCSN}(0, V_{ds}) = 2eV_{ds}\frac{e^2}{h}D(1-D) \tag{1.7}$$

When $D \ll 1$, Eq. 1.7 reduces to $2e<I>$, the Skottky formula first derived for rare and uncorrelated electron transfer in a vacuum tube[131]. The other limit shows a different behavior. The noise vanishes when the scatterer becomes transparent $D = 1$. This signature of the quantum temporal correlation was experimentally verified by Reznikov et al.[121] and Kumar et al.[78]. The general situation when several channels coexist, like the two defined by the spins, is simply the algebraic sum for both the current and the noise.

---

[5] It could be recovered without quantum calculations using the definition of the average current $lim_{t\to-\infty} < Q_e(t)/t >$ and the mathematical definition of the noise PSD at zero frequency as given by the Wiener-Khintchine theorem. This operation provides for instance the factor 2. See [13]. The central role of the charge binomial statistics is emphasized in [89]. Full calculation of the shot noise starting from the decomposition of electrons into individual wave-packets was developed in the work of Martin and coworkers[96][80].

1.1.3 Stochastic processes and quantum scattering theory

In the previous section 1.1.2, we have extensively used our knowledge of the possible outputs of a simple "charge" measurement and avoided full quantum calculations. Such calculations start with the correct definition of the measured quantum operator.

$$2\pi\Delta\nu S_I^{DCSN}(T_e, V_{ds}) =< \hat{\mathbf{I}}_L(w=0)\hat{\mathbf{I}}_L(w=0) > - < \hat{\mathbf{I}}_L(w=0) >^2 \tag{1.8}$$

Where $\hat{\mathbf{I}}(w = 2\pi\nu)$ is the Fourier Transform of the current operator :

$$\hat{\mathbf{I}}(t) = \frac{e}{h}\int_{-\infty}^{+\infty} dEdE'[\hat{a}_L^\dagger(E)\hat{a}_L(E') - \hat{b}_L^\dagger(E)\hat{b}_L(E')]exp(i(E-E')\frac{t}{\hbar}) \tag{1.9}$$

Operator $\hat{a}_L(\varepsilon)$ and $\hat{b}_L(\varepsilon)$ are respectively annihilation operators for the incoming wave and the outcoming waves in the Left lead. The corresponding operators in the Right lead are $\hat{a}_R(\varepsilon)$ and $\hat{b}_R(\varepsilon)$. $\hat{a}_{L,R}(\varepsilon)$ evolves over time as a free electron wave of energy ε and accumulates a phase amplitude $\sim exp(-i\varepsilon t/\hbar)exp(\pm ik(\varepsilon)x)$. $\hat{b}_{L,R}(\varepsilon)$ are defined from the two incoming operators :

$$\begin{pmatrix}\hat{b}_L(\varepsilon)\\ \hat{b}_R(\varepsilon)\end{pmatrix} = \begin{pmatrix}S_{L,L} & S_{L,R}\\ S_{R,L} & S_{R,R}\end{pmatrix}\begin{pmatrix}\hat{a}_L(\varepsilon)\\ \hat{a}_R(\varepsilon)\end{pmatrix} \tag{1.10}$$

The matrix $\{S_{\alpha,\beta}\}$ must be unitary to respect current conservation. The scattering matrix theory, developed in [24], leads also to Eq. 1.5. This equation is similarly derived with the generating function developed for the FCS in [89][104].

The stochastic decomposition emphasizes the structure of the DC shot noise : a perfectly coherent and regular beam of electrons is scattered with binomial statistics. But it must be mentioned that it would impair the understanding of the measurement in some situations. For instance, even an ultra-low temperature and perfectly transmitting quantum wire is known to display a logarithmically diverging charge noise $<Q_e^2>-<Q_e>^2 \sim log(t_f E_F/h)$ when the measurement time t_f is finite[87]. These quantum fluctuations are associated with the starting and ending of the measurement for delocalized electron over time[88].

1.2 Floquet scattering theory of photo-assisted shot noise

We want to analyze the difference between DC transport and on-demand charge-injection, a particular case of AC transport. A periodic train of voltage pulses $V_p = V_{ds} + V_{ac}(t)$ is applied to a quantum conductor. A single voltage pulse is defined when $\int\limits_{-\infty}^{\infty} V_p(t)dt$ is finite. We show that the effect of the AC part $V_{ac}(t)$ can be interpreted in terms of photo-excited quasi-particles.

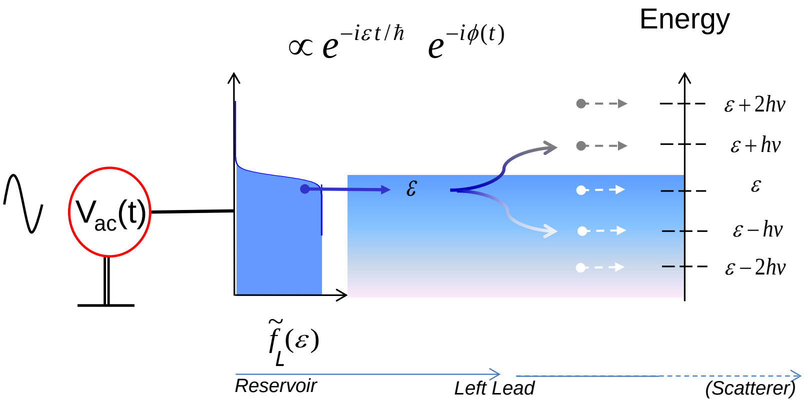

FIGURE 1.3 – Phase accumulation and photo-assisted interpretation in a quantum conductor.

1.2.1 Photo-assisted interpretation of AC transport

The Left contact is now periodically driven by a purely AC voltage $V_{ac}(t)$ of frequency $\nu = 1/T$ (Fig. 1.3). We have $< V_{ac}(t) >= 0$. The geometry of the field can be kept simple. The voltage drop is localized at the scatterer [6]. The external field vary slowly compared to the scattering time $t_{sc} \sim \hbar|\partial S_{L,R}(\varepsilon)\partial\varepsilon|$. This regime defines instantaneous scattering. The detailed response function[6] of the system is negligible. The scatterer is unaffected and

---

[6] The field is considered screened anywhere else. The effective field is exactly the applied field, an assumption which avoid a more complex formalism to be developed in order to maintain self-consistency[27]. Physical effects of screening for the photo-assisted theory are discussed in [114]

energy-independent.

Solving the wave equation in presence of this classical field is performed using a gauge transformation, whose states are easy to visualize. Free electron waves $\sim exp(i\varepsilon t/\hbar)$ accumulate an additional amplitude $exp(-i\phi(t))$. If we consider the travel from the left reservoir to the scatterer, the time-dependent phase is given as :

$$\phi(t) = 2\pi \int_{-\infty}^{t} V_{ac}(t')dt' \tag{1.11}$$

The Fourier transform of the amplitude :

$$e^{-i\phi(t)} = \sum_{l=-\infty}^{+\infty} p_l \, e^{-i2\pi l\nu t} \tag{1.12}$$

has a simple interpretation. It gives the probability amplitude p_l for an electron to absorb ($l > 0$) or emit ($l < 0$) photons[7]. When we consider the movement of the entire Fermi sea, the emission of a photon appears as a hole creation.[8] An individual electron wave thus reaches the scatterer in a superposition of states at different energies entirely predicted from the $\{p_l\}$. For a sine wave of amplitude V_{ac}, we have $p_l = \mathrm{J}_l(\alpha)$, where $\mathrm{J}_l(\alpha)$ is the l^{th}-order Bessel function and the dimensionless ratio α is $eV_{ac}/h\nu$. The dimensionless parameter α illustrates the general scalability of the formalism.

1.2.2 Floquet Formalism

The properties of the p_l are remarkably useful when expressed in the framework of the Floquet scattering theory[101]. The continuous energy range $[-\infty, +\infty]$ is sliced into energy windows of size $h\nu$, i.e. we replace the quantum number ε by a set of two quantum numbers $\varepsilon \to \varepsilon' + lh\nu$, with ε' now restricted to $[-h\nu, 0]$. Photo-assisted processes can be viewed as the coherent scattering of the electrons between these energy windows. The scattering matrix $\hat{\mathbf{P}}(\varepsilon)$ corresponding to this evolution relates the set of annihilation operators "far inside the left lead" $\hat{\mathbf{a}}_L^F(\varepsilon)=\{\hat{a}_L^F(\varepsilon, l)\}_{l\in\mathbb{Z}}$ (right part of Fig. 1.3) to the already mentioned stationary annihilation operators "at the input of the left lead" $\hat{\mathbf{a}}_L(\varepsilon'')=\{\hat{a}_L(\varepsilon'', m)\}$ (right

---

[7] The classical nature of the field and the absence of environment does not lead to restriction in photons except the quantification $h\nu$, and their presence as intermediary particles is mostly transparent.

[8] Charge conservation is ensured at a larger level. In practice, the two reservoirs are connected in a close circuit. In the model where an infinite wire and an infinitely deep Fermi sea are used, there is a hole going in the opposite direction.

part of Fig. 1.3, see section 1.1.3). We have for individual electron wave :

$$\hat{a}_L^F(\varepsilon', l) = \sum_{m=-\infty}^{+\infty} p_{l-m} \delta(\varepsilon' - \varepsilon'') \hat{a}_L(\varepsilon'', m) \tag{1.13}$$

Written as a scattering matrix :

$$\hat{\mathbf{a}}_L^F(\varepsilon) = \hat{\mathbf{P}}(\varepsilon) \hat{\mathbf{a}}_L(\varepsilon) \tag{1.14}$$

In all above equations, bold characters ($\hat{\mathbf{a}}$) refer to a set of operators ($\hat{a}$) written in vector form. By definition, we find $\hat{\mathbf{P}}(\varepsilon)_{l,m} = \{p_{l-m}\}$. To satisfy unitarity $\hat{\mathbf{P}}^\dagger \hat{\mathbf{P}} = 1$, the amplitude have to be orthogonal :

$$\sum_{l=-\infty}^{+\infty} p_l^* p_{l+k} = \delta_{k,0} \tag{1.15}$$

In particular, the sum of the probabilities $P_l = |p_l|^2$ to absorb or emit photons or to do nothing is equal to 1. As shown in section 1.5, the probabilities P_l can be inferred from shot-noise spectroscopy, when in addition to the AC voltage a tunable DC voltage is applied between the contacts of a partially transmitting conductor. However, the set of P_l does not contain all the information on the system. Products $p_l^* p_{l+k} \neq 0$ (entering in the non-diagonal part of the photo-excited density matrix), enters in the calculation of the coherence function[55][54]. Chapter 5 covers partially this subject.

The periodic repetition might seem arbitrary. The original proposal from Levitov et al. is about a single pulse of lorentzian time-profile with integer flux. From the experimental point of view, the need for voltage periodicity is associated with the need for repeated experiments in a statistical measurement. However, it does not affect the physics or the validity of the theoretical description.

The partial tunneling through the local barrier can be inserted. Under matrix form, the Floquet states are scattered according to :

$$\begin{pmatrix} \hat{\mathbf{b}}_L^F(\varepsilon) \\ \hat{\mathbf{b}}_R^F(\varepsilon) \end{pmatrix} = \begin{pmatrix} S_{L,L} & S_{L,R} \\ S_{R,L} & S_{R,R} \end{pmatrix} \begin{pmatrix} \hat{\mathbf{a}}_L^F(\varepsilon) \\ \hat{\mathbf{a}}_R^F(\varepsilon) \end{pmatrix} \tag{1.16}$$

The total effect of the time-varying potential and the static barrier can now be expressed in the basis of the reservoir states :

$$\begin{pmatrix} \hat{\mathbf{b}}_L(\varepsilon) \\ \hat{\mathbf{b}}_R(\varepsilon) \end{pmatrix} = \begin{pmatrix} \hat{\mathbf{P}}^\dagger(\varepsilon) & 0 \\ 0 & 1 \end{pmatrix} \begin{pmatrix} S_{L,L} & S_{L,R} \\ S_{R,L} & S_{R,R} \end{pmatrix} \begin{pmatrix} \hat{\mathbf{P}}(\varepsilon) & 0 \\ 0 & 1 \end{pmatrix} \begin{pmatrix} \hat{\mathbf{a}}_L(\varepsilon) \\ \hat{\mathbf{a}}_R(\varepsilon) \end{pmatrix} \tag{1.17}$$

The possibility to treat separately the fluctuating voltage and then use the same boundary conditions as in the static problem is a direct consequence of the assumed geometry. Similarly, the effect of an arbitrary voltage pulse $V_p(t)$, the total voltage with both an AC part equal to $V_{ac}(t)$ and a DC part V_{ds}=<$V_p(t)$> is easily found by adding the DC part as a shift in the electro-chemical potential μ_L. This formal separation allows a clear physical interpretation of all the underlying processes. In a complementary description, AC transport was also shown to be made of elementary processes leading either to a charge transfer or to a neutral electron-hole pair excitation (respectively called “unidirectional” and “bidirectional” events) by Vanevic et al. [148]. This is particularly useful when the current fluctuations are considered since they have different experimental signatures. We analyze these signatures in the next section.

1.3 Photo-Assisted Shot Noise (PASN)

A periodic train of voltage pulses $V_p(t)$=V_{ds}+$V_{ac}(t)$ applied to a quantum conductor transfer on average an arbitrary charge $q = (eV_{ds})/h\nu$, strictly determined by the DC part V_{ds} of the voltage while the noise is the consequence of all particles involved, independently from their charge sign. As a consequence, the PASN noise amplitude associated with $V_p(t)$ can be arbitrarily high compared to the DCSN associated with V_{ds}.

1.3.1 Noise fluctuations

The final form Eq. 1.17 for the transport under a purely AC voltage $V_{ac}(t)$ allows to use the equation for the current and the noise in the case of a system with multiple channels and contacts from[25].

Current fluctuations in this situation are referred to as Photon-Assisted Shot Noise (PASN). The general theory [86][114][125][148] was verified experimentally in [120] for the case with a QPC and with a coherent but diffusive conductor in [128]. The low-frequency PASN is :

$$S_I^{PASN}(T_e, V_{ac}(t)) = S_I^0 \int_{-\infty}^{+\infty} \frac{d\varepsilon}{h\nu} \sum_{l=-\infty}^{+\infty} \mathrm{P}_l \left[f_L(\varepsilon - lh\nu)(1 - f_R(\varepsilon)) + (1 - f_L(\varepsilon - lh\nu))f_R(\varepsilon)\right] \\ + 4k_B T_e D^2 \frac{e^2}{h} \tag{1.18}$$

where $S_I^0 = 2\frac{e^2}{h}D(1-D)h\nu$. The last term can be understood as the thermal noise of the reservoirs. It only involves the variance of the independent binomial statistics from the two Fermi distributions and not the one from the partitioning or the more complex photo-assisted distribution.

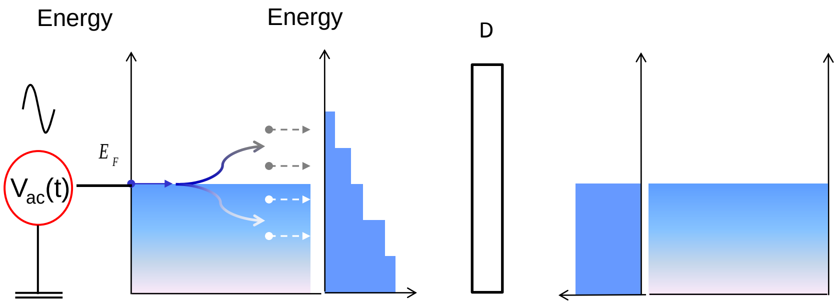

FIGURE 1.4 – Scattering of photo-excited particles and noise production. All electrons from the left Fermi sea migth have absorbed ($l > 0$) or emited ($l < 0$) l photons with probability $|P_l|$, generating partial upward or downward shift of the Fermi sea. Energy population for the out-of-equilibrium conductor are depicted by the distribution $\tilde{f}_L = \sum_{l=-\infty}^{+\infty} P_l f_L(\varepsilon - lh\nu)$. Note that unlike the unaffected Fermi sea, the energy distribution$\tilde{f}_L$ misses the information about the coherence between energy levels. The production of electron and hole is actually correlated[125].

In the absence of $V_p(t)$, the thermal noise vanishing at zero temperature of Eq. 1.6 is found again. Both photo-excited electrons or holes impinging (Fig.1.4) the barrier generate current and possibly noise according to the same rules as in the case of a DC current. For a hole (electron), noise arises when there is no hole (electron) incoming from the other side. This is straightforward in the zero temperature limit.

$$S_I^{PASN}(0, V_{ac}(t)) = S_I^0 \sum_{l=-\infty}^{+\infty} |l| P_l \tag{1.19}$$

Note that S_I^0 and therefore the noise vanishes also when $D = 0$. The sum in the right-hand side is directly proportional to the number of photo-excited particles per period. This is summarized by using the period-average output of the number operator for right-moving excited particles in the left lead. It gives the average number of excited electron per pulse when we consider positive energy :

$$N_e = \int_{-hv}^{0} \frac{d\varepsilon}{h\nu} \sum_{l=1}^{+\infty} \left\langle \hat{a}_L^{F\dagger}(\varepsilon, l)\hat{a}_L^{F}(\varepsilon, l) - \hat{a}_L^{\dagger}(\varepsilon, l)\hat{a}_L(\varepsilon, l) \right\rangle = \sum_{l=1}^{+\infty} l\, P_l \tag{1.20}$$

It gives the average number of holes per pulse when we consider negative energy :

$$N_h = \int_{-hv}^{0} \frac{d\varepsilon}{h\nu} \sum_{l=-\infty}^{0} \left\langle \hat{a}_L^{\dagger}(\varepsilon, l)\hat{a}_L(\varepsilon, l) - \hat{a}_L^{F\dagger}(\varepsilon, l)\hat{a}_L^{F}(\varepsilon, l) \right\rangle = \sum_{l=-\infty}^{-1} (-l) P_l \tag{1.21}$$

Using the Fourier transform property linking lp_l to the Fourier Transform of $\partial_t exp(-i\phi(t))$, we can check that N_h=N_e.

$$\begin{aligned} N_e - N_h &= \sum_{l=-\infty}^{+\infty} l p_l \overline{p_l} \\ &= \sum_{l=-\infty}^{+\infty} \frac{1}{-i2\pi\nu T^2} \int_0^T \int_0^T dt dt' \frac{-i\partial\phi(t)}{\partial t} e^{-i\phi(t)} e^{i\phi(t')} e^{i2\pi l\nu(t-t')} \\ &= \frac{e < V_{ac}(t) >^t}{h\nu} \\ &= 0 \end{aligned} \tag{1.22}$$

Current conservation leads to the same number of hole and electron. We see that equation 1.19 is :

$$S_I^{PASN}(0, V_{ac}(t)) = S_I^0 (N_e + N_h) \tag{1.23}$$

As emphasized for the general case in the next section, the noise at finite temperature does not remain equal to expression 1.23. A similar equation arises in the case of periodic injection of energy-resolved single electron and single hole from a quantum dot, injected with an exact separation of half a period. In this context, the presence of excited particles N_e=1 and N_h=1 originates from a different mechanism[41]. It was recently verified experimentally in[17].

1.3.2 Excess noise

In the context of on-demand particle injection, we want to transfer exactly n particles using a given pulse. Reducing the repetition frequency $\nu \to 0$ in the formalism shows the direct equivalence between the problem per period and the on-demand situation. We can analyze this situation in the Floquet formalism without loss of generality. A net transferred charge of value q per pulse is not possible without a DC component in $V_p(t)$. Injecting in Eq. 1.18 the shifted Fermi distribution for the left lead, we find a slightly modified version of Eq. 1.19 for the PASN at zero temperature :

$$S_I^{PASN}(0, V_p(t)) = S_I^0 \sum_{l=-\infty}^{+\infty} |l+q| \mathrm{P}_l \tag{1.24}$$

Where $q = eV_{ds}/h\nu$. In Eq. 1.24, the $\{p_l\}$ distribution is computed from $exp(-i\phi(t))$ using only the part $V_{ac}(t)$. That way all P_l are identical when we consider the impact of changing the quantity "q".

Expression 1.24 is again proportional to the total number of electrons and holes N_{eh} $=N_h(V_p)+N_e(V_p)$ in the left lead, as could be checked by calculating again the two expressions 1.20 and 1.21 with the DC shifted Fermi sea. Note that we have considered an excitation to be a hole compared to the right reservoir Fermi level. The average current is :

$$< I(V_p) >= \frac{e}{h} \int_{-\infty}^{+\infty} d\varepsilon \sum_{l=-\infty}^{+\infty} |P_l| D(f_L(\varepsilon - lh\nu) - f_R(\varepsilon)) = e\nu D(N_e(V_p) - N_h(V_p)) = e\nu Dq \tag{1.25}$$

The noiseless situation in Eq. 1.19 and 1.24 when the scatterer is fully transparent and S_I^0=0 ensures us that the transferred charge q is a precise quantity given by the pulse average amplitude. We can express the current directly using the controlled field $V_p(t)$. We find conveniently the Ohm law :

$$< I(V_p) > = e\nu D \int_0^T \frac{eV_p(t')}{h\nu} dt'$$

The noise induced when the same pulse[9] is applied to a conductor with 0≤ D ≤1 has

---

[9] When the conductor is partially transmitting the electronic, the current is reduced, but the framework

a different behavior : it can be arbitrarily high. This situation contrasts with the DCSN where the noise and the current were strictly related. By subtracting the PASN of Eq. 1.24 and its limit when $V_{ac}(t) \rightarrow 0$ we define the excess shot noise. This limit is simply the noise arising when transferring q charges per period with a constant current.

$$\Delta S_I = S_I^0 \left[\sum_{l=-\infty}^{+\infty} (|l+q| - |q|) P_l \right] \tag{1.26}$$

The most important result is the fact that this quantity cannot be negative [10] and is zero in the limit of a DC current. In other words, for a given transferred charge and a certain transmission D, it is impossible to reduce the noise below the DC level whatever way the the time-profile $V_{ac}(t)$ is modified. To stress the link between this quantity and the presence of neutral electron-hole pairs, it is interesting to define the quantity :

$$\begin{aligned} \Delta N_{eh} &= \sum_{l=-\infty}^{+\infty} (|l+q| - |q|) P_l \\ &= N_e(V_p) + N_h(V_p) - |q| \end{aligned} \tag{1.27}$$

ΔN_{eh} is the total number of electrons and holes in excess compared to the total transferred charge per pulse.

The derivative of Eq. 1.27 has a "stairs" structure and shows singularities each time q is an integer. This singularities in the slope are a direct proof of the existence of quantized photo-assisted process in the coherent AC transport. The situation $q \in \mathbb{Z}$ corresponds also to a quantized current of an integer number of charges per period. It was observed in a diffusive metallic wire[128] and with a ballistic conductor (a QPC)[120]. The condition for the presence of a singularity offers also a measurement of the carrier charge. The second derivative of Eq. 1.27 has consequently a "comb" structure and shows how the PASN measurement while varying q (or V_{ds}) provides direct information on the full P_l distribution.

$$\frac{\partial \Delta N_{eh}^2}{\partial q^2} = (2P_0 - 2)\delta(q-0) + 2\sum_{l \neq 0} P_l \delta(q+l) \tag{1.28}$$

Inferring the distribution of photo-excited particles from the PASN has been discussed in [77] and is developped in the next section. In a realistic experimental situation, we have

---

shows that the photo-assisted mechanisms are unchanged.

[10] If we suppose $q \geq 0$, developing the absolute value shows that we have two comparisons to make $\sum_{l=-\infty}^{l\leq -q}(-l-q)\mathrm{P}_l \geq 0$, and $\sum_{l=0}^{l+\infty} l\mathrm{P}_l = \sum_{l=-\infty}^{0}(-l)P_l \geq \sum_{l=-\infty}^{l\leq -q}(-l)P_l \geq \sum_{l=-\infty}^{l\leq -q} qP_l$.

to use the finite temperature excess noise version of Eq. 1.26, again obtained from the integration of Eq. 1.18 when the left reservoir is shifted by eV_{ds}. In that case, when we define $\Delta N_{eh} = \Delta S_I / S_I^0$ we no longer obtain an expression for the number of photo-assisted particles or holes in the left lead, but only a reduced unit for the noise.

$$\Delta S_I(V_{ac}(t), q, T_e) = S_I^0 \Delta N_{eh}(\alpha, q, \theta_e) = S_I^0 \sum_{l=-\infty}^{+\infty} ((l+q) coth(\frac{l+q}{2\theta_e}) - (q) coth(\frac{q}{2\theta_e})) P_l(\alpha) \tag{1.29}$$

The reduced unit $\theta_e = k_B T_e / h\nu$ for the temperature is used. As $x \times coth(x)$ tends to x when $x \rightarrow \pm\infty$, and tends to 1 when $x \rightarrow 0$ the main change concerns photon-assisted processes for which the energy $lh\nu$ is lower or comparable to the typical thermal energy available $k_B T_e$. The history (from $t{=}-\infty$ in a reservoir to $t{=}\infty$ again in a reservoir) of an electron is randomized by exchanges of thermal energy in the reservoir prior to the entrance in the ballistic conductor, for which there is no quantification. The possibility to minimize the finite-temperature PASN noise 1.29 has been investigated for a few selected pulse shapes by Gabelli et al. in [44]. The next part 1.4 is dedicated to the minimization of the zero-temperature noise for a fixed DC level q. This optimization problem is more fitted to the field of on-demand injection, as in this case only the noise is a direct tool to understand the photo-excited content in the wave-packet traveling in the perfectly transmitting wave-guide. As long as there is no thermal processes, discussing the PASN or discussing the presence of holes and electrons is equivalent. A discussion of the thermal effects on the photo-assisted processes as well as the experimental meaning of the finite temperature PASN measurement is considered next. We show that at low-enough temperature, PASN measurements are still a suitable tool.

1.4 Integer and arbitrary charge injection

Pulses of arbitrary shape and arbitrary charge are shown to give a marked minimum in the excess PASN at low-temperature when the flux is an integer multiple of e/h. The case of the lorentzian-shape voltage is shown to produce the same level of noise than a DC current and leads to zero excess PASN. This corresponds to the ideal situation in which a minimal excitation travels in the coherent conductor and can be send on-demand.

1.4.1 Injection with a lorentzian voltage pulse

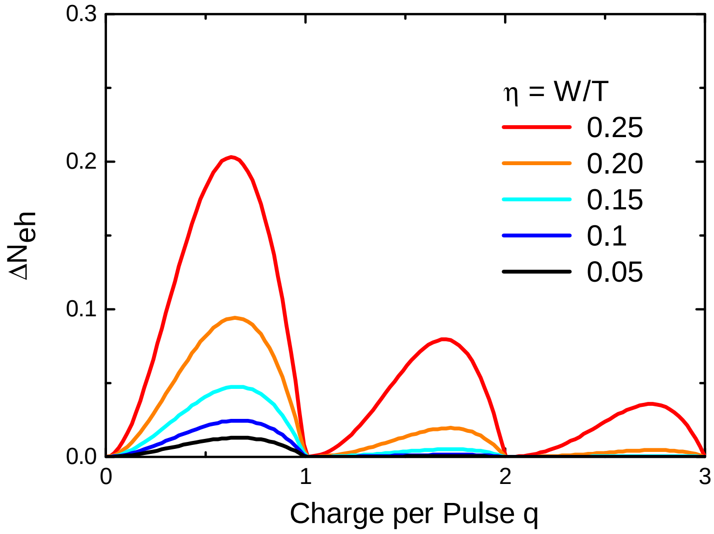

FIGURE 1.5 – Excess noise at zero temperature induced by lorentzian pulses with various typical width W compared to the period T and amplitude $V_p(t = 0)$. As defined in the main text, the charge per pulse is also the charge per period q, and amplitudes are labeled using $q = \alpha$.

In the previous section we have developed the arguments which show the equivalence between the PASN amplitude and the numbers of excited particles in the quantum wire $N_e(V_p) + N_h(V_p)$. The minimization corresponds to a remarkably simple condition :

$$\begin{aligned} N_e(V_p) + N_h(V_p) - |q| &= 0 \\ N_e(V_p) + N_h(V_p) - |N_e(V_p) - N_h(V_p)| &= 0 \\ &\Leftrightarrow N_e(V_p) = 0 \\ &or N_h(V_p) = 0 \end{aligned} \tag{1.30}$$

Equivalently, the Fermi sea (or the equivalent for a hole-like excitation) appears unmodified. These equations were first derived and analyzed by Levitov et al. in a set of two papers [90] and [65]. They expressed what it implied for the analytical expression of the voltage pulse [11]. In the context of a periodic train of identical pulses it must be given by :

---

[11] We have written the pulse as a sum of a DC component and an AC component. The p_l were

$$V_p(t) = \frac{\pm nh}{We\pi} \sum_{k=-\infty}^{+\infty} \frac{1}{1+(t-kT)^2/W^2} \tag{1.31}$$

When applied to a $D = 1$ quantum conductor, $V_p(t)$ with a plus (minus) sign sends exactly an integer positive (negative) charge $q = \pm n$ per period. The Full Width at Half Maximum for each individual pulse (FWHM) $2W$ can take any value. Interestingly, no voltage pulse can verify the conditions expressed in Eq. 1.30 if q is not an integer charge. The excess PASN cannot be zero in such a case, for which the phase term $\phi(t) = 2\pi n$ or equivalently the action $\int eV_p(t){=}nh$ are not quantized. Note that the limit of a lorentzian train of pulses with $W \rightarrow +\infty$ is a DC bias. The AC part from which we have to calculate the photo-assisted distribution $\{p_l\}$ is :

$$V_{ac}(t) = \frac{nh\nu}{e} \frac{cos(2\pi\nu t) - e^{-2\pi\eta}}{cosh(2\pi\eta) - cos(2\pi\nu t)} \tag{1.32}$$

Where $\eta = W\nu$ and $\nu = 1/T$. It is interesting to generalize the above definition to an arbitrary charge injection and label the amplitude of any lorentzian AC profile $V_{ac}(t)$ using the quantity α which can take any real value and is equal to n for integer charge injection.

$$V_{ac}(t) = \frac{\alpha h\nu}{e} \frac{cos(2\pi\nu t) - e^{-2\pi\eta}}{cosh(2\pi\eta) - cos(2\pi\nu t)} \tag{1.33}$$

There is only one possibility to combine the AC part with amplitude α and a DC part $q = eV_{ds}/h\nu$ and maintain a true pulse injection. It is when $\alpha = q$. In any other situation, the voltage does not go back to zero between each voltage peak. Varying α and q independently to obtain detailed information about the quantum mechanism at work is done in the next section 1.5, while we focus here on the experimental situation in which on-demand charge injection is tried.

The distribution $\{P_l(\alpha{=}1)\}$ has a simple structure : $P_l = 0$ for $l < -1$, $P_{-1}{=}exp(-4\pi\eta)$,

---

defined using only the AC part. If we remove this restriction, use the limit $T \rightarrow +\infty$ when lhv converges to continuous variable ε, and consider the absence of photo-assisted electron first, we can sketch the reasoning in a few lines. The condition $P(\varepsilon) = P(\varepsilon)\Theta(\varepsilon)$ transposed in the time domain has a form often considered when calculating path integrals. The equality is true as soon as the Cauchy path integral in the upper complex plane circling out the time t and the Cauchy principal value at t both exist and are equals for the phase amplitude $exp(-i\phi_{ac+ds}(t))$. The key and obvious condition is the absence of poles in the upper plane. The strong requirement $|exp(-i\phi_{ac+ds}(t))| = 1$ leads to products of the form $exp(-i\phi_{ac+ds}(t)) = \prod_m (\tau_m - i(t-t_m))/(\tau_m + i(t-t_m))$, with any t_m and τ_m. The case in which holes are absent leads to a similar question in the lower complex plane. See [90][65] for a rigorous analysis of these arguments.

and $P_l = exp(-4\pi\eta(l))[1 - exp(-4\pi\eta)]^2$ for $l > -1$ (see also [148]). The expression for each $\{P_l(\alpha{=}n)\}$ involves the same exponential factor and a Laguerre Polynomial. If we consider the number of excess particles per pulse $\Delta N_{eh}(\alpha{=}n)$, we find always zero. The complete expression for any value of $\alpha = q$ is described in [38] and ΔN_{eh} is represented in Fig. 1.5. ΔN_{eh} oscillates with q and is locally minimal at $q = n$.

Two conclusions are reached. The lorentzian voltage pulses with quantized action realizes a charge injection and leaves the Fermi sea unmodified. The second is that the granularity of the charge has a strong signature. When trying to inject an arbitrary charge from a given set of carriers, a complex combination must be used. Authors in[84] analyzed this point and considered the sharp inversion point near $q = n$ to reflect a dynamical analog of the Anderson Orthogonality Catastrophe[4]. The presence of minima does not depend on the frequency or the pulse width. But as can be seen on Fig. 1.5, the maxima are strongly influenced by the characteristic ratio $\eta = W/T$.

1.4.2 Comparison with various pulse shapes

In this section, we address the comparison between several types of integer charge pulses : the square, the sine, the rectangular, and the lorentzian. Using the PASN results of section 1.3, we calculate the number of electron-hole pairs in excess compared to the transported charge.

A periodic square pulse is defined as :

$$V_p(t) = 2\frac{\alpha h\nu}{e} \qquad if \quad 0 \leq t \leq 0.5T \tag{1.34}$$

$$= 0 \qquad if \quad 0.5T < t < T \tag{1.35}$$

A sine function can be used as a voltage window and defines a train of pulses :

$$V_p(t) = \frac{\alpha h\nu}{e}(sin(2\pi\nu t) + 1) \tag{1.36}$$

These functions are defined so that the number of charges injected per period q when the voltage amplitude associated is α verifies $\alpha = q$. This is again the only situation which corresponds to a repeated charge injection processes. The $V_{ac}(t)$ part is then deduced by subtracting the average amplitude and used to define the $\{p_l(\alpha)\}$. Fig.1.6 represents the number of excess particles found for each pulse. These curves were proposed in [148] and

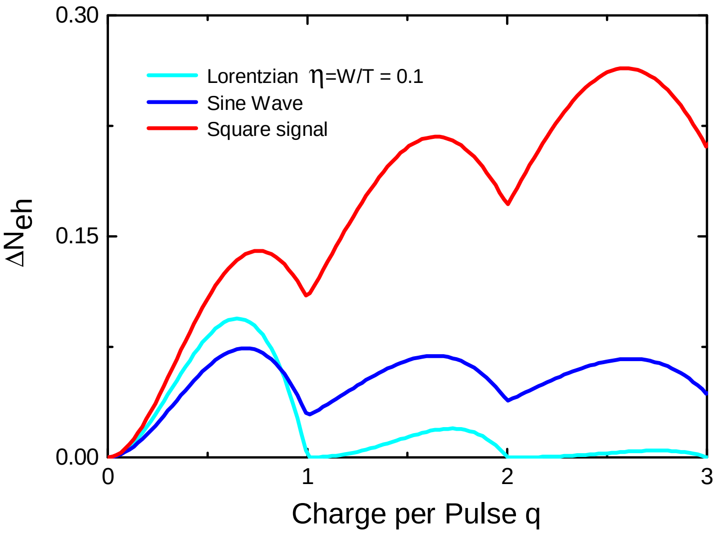

FIGURE 1.6 – Excess noise and excess particles generation at zero temperature as induced for the on-demand charge injection "q" using various pulse shapes : square wave, sine wave and lorentzian pulse (reproduced for comparison). As defined in the main text, the voltage amplitude of each pulse is linked to the charge injection using $q = \alpha$.

[147]. Again, local minimization occurs with a marked singularity each time $\alpha = q$. But the number of excess particles is not zero : a cloud of neutral electrons-pairs has been excited from the Fermi sea. The $\{P_l(\alpha)\}$ for integer value of α can be calculated for all three proposed pulses in Fig. 1.6. The presence of a $log(n)$ asymptotic divergence in the noise for the square wave can be verified.

When analyzing the lorentzian pulse, an additional parameter was available : the FWHM, which is missing for the two basic situations of the square wave and the sine wave. A periodic rectangular pulse of FWHM W is defined as :

$$V_p(t) = \frac{T\alpha h\nu}{We} \qquad if \quad 0 \leq t < W \tag{1.37}$$

$$= 0 \qquad if \quad W \leq t < T \tag{1.38}$$

The ratio $\eta = W/T$ is used to label the curves in Fig. 1.7. Again the sharpness increase the resolution of minima and maxima. To extend this partial analysis of the role of the shape, we consider a periodic train of gaussian pulses. A train of gaussian pulses is defined

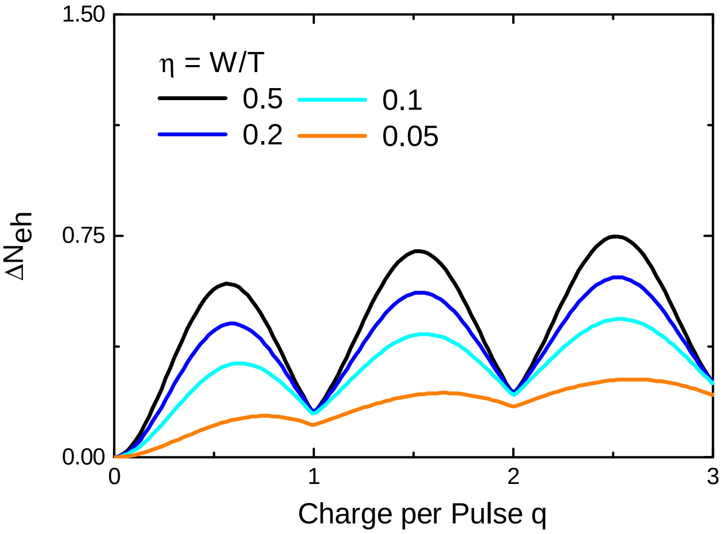

FIGURE 1.7 – Excess noise and excess particles generation at zero temperature as induced for the on-demand charge injection "q" using rectangular window of voltage bias with various width W compared to the repetition time T. As defined in the main text, the voltage amplitude of each pulse is linked to the charge injection using $q = \alpha$ for all points.

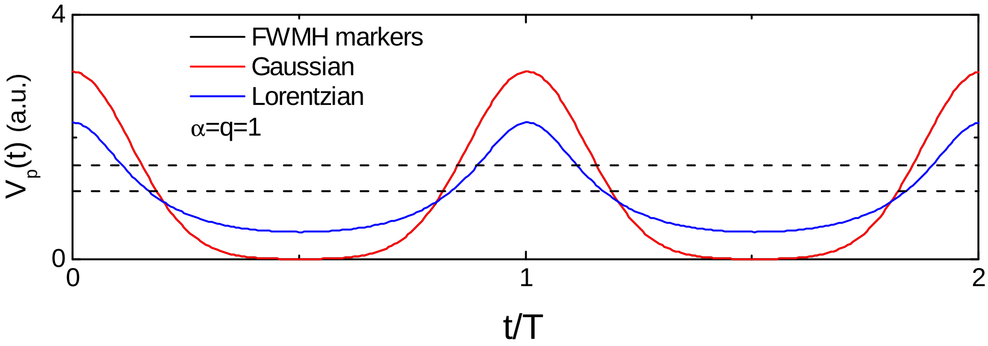

FIGURE 1.8 – Definition of a periodic train of gaussian voltage pulses. The FWHM is equivalent between a lorentzian and a gaussian pulse when $\sqrt{2ln(2)}\sigma = W$.

as :

$$V_p(t) = \frac{\alpha h\nu}{e} \sum_{k=-\infty}^{+\infty} \frac{1}{\sqrt{2\pi\sigma^2}} exp(-\frac{(x-kT)^2}{2\sigma^2}) \tag{1.39}$$

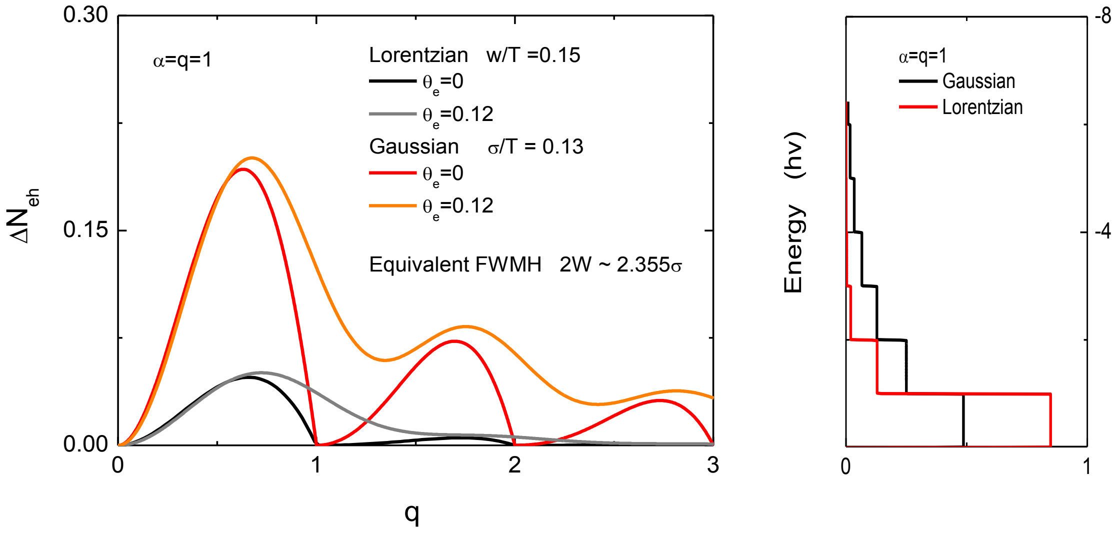

FIGURE 1.9 – Excess noise and excess particles generation at zero temperature as induced for the on-demand charge injection "q" using gaussian or lorentzian voltages pulses on the contact with equal FWHM compared to the repetition time T. As defined in the main text, the voltage amplitude of each pulse is linked to the charge injection using $q = \alpha$ for all points.

A gaussian pulse and a lorentzian pulse such as $\sqrt{2ln(2)}\sigma = W$ have the same FWHM (Fig. 1.8). For a given integer charge injection, the noise is strikingly close to zero for a gaussian pulse, even if it can be checked to be finite with precise enough numerical simulations. The higher contrast between minima and maxima in Fig.1.9 in the excess particles number is qualitatively related to the higher energy dispersion of the excited state. It can be verified by comparing the out-of-equilibrium energy distributions $\tilde{f}_L(\varepsilon) = \sum_{l=-\infty}^{+\infty} P_l f_L(\varepsilon - lh\nu - qh\nu)$ with the original equilibrium Fermi sea $f_L(\varepsilon)$. See the right part of Fig.1.9. The higher characteristic energy of the gaussian-generated excitation would conserve its phase-coherence on a shorter travel path than the lorentzian. The idea of an "engineered state", for which the optimization in terms of excess particles, characteristic energy, time-profile, depends on the problem it should be used for is not explored in this work.

1.4.3 Finite temperature PASN

Effects of temperature increase on a PASN measurement

In a realistic experiment, the temperature is finite. The typical range of frequency that can be used is 0–30 GHz, and a temperature below 50 mK is reasonable with commercially available traditional dilution fridges and cryogen-free dilution fridges. In reduced units, the typical temperature scale is $\theta_e = k_B T_e / hv$. As can be seen in Fig.1.10 and Fig.1.11 the noise to be measured quickly loses its quantum signatures with "q" when θ_e is increased. The contrast between minima and maxima is lost until only a curve with a single maximum appears. Along the temperature variation, local minima are not only smoothed and loose their singular behavior (cusps) but also drift from the exact quantization $q = n$. Additionally, we observe that the drift is typically larger for the lorentzian injection than for the sine-window.

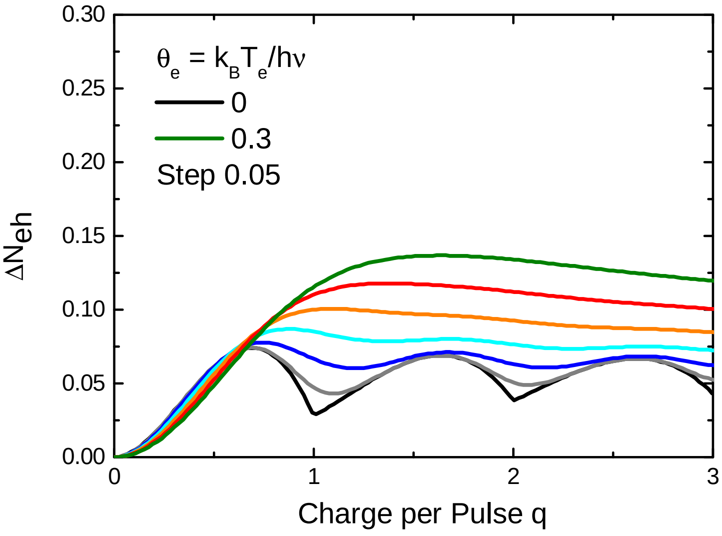

FIGURE 1.10 – Excess noise at finite temperature T_e as induced for the on-demand charge injection "q". As defined in the main text, the voltage amplitude of each pulse is linked to the charge injection using $q = \alpha$.

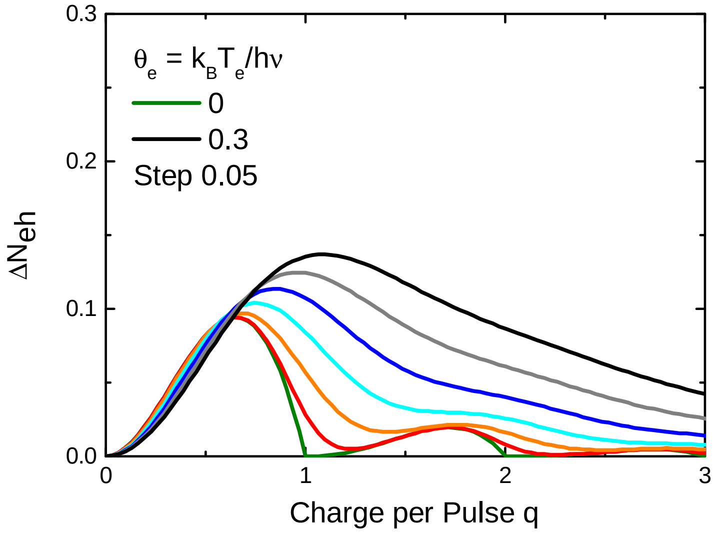

FIGURE 1.11 – Excess noise generation at finite temperature T_e as induced for the on-demand charge injection “q” using a pulse with a sine window. As defined in the main text, the voltage amplitude of each pulse is linked to the charge injection using $q = \alpha$.

Role of the two reservoirs

To understand these effects, we must consider that several statistics are combined. First, the states in the left lead impinging the scatterer are the result of independent photo-assisted processes and random thermal energy exchanges in the left reservoir. They are scattered in correlation to the right-coming states, which have also experienced random thermal energy exchanges in the reservoir before being injected in the coherent conductor. There is no trivial way to separate these effects.

Some thought experiments might be questioned to see this. The temperature of the left lead is first set to θ_e, while the right reservoir is maintained arbitrarily at zero temperature. The noise measurement in reduced units provides :

$$\begin{aligned}\Delta N_{eh} &= \frac{1}{h\nu}\sum_{l=-\infty}^{+\infty}(|f_L(\varepsilon - lh\nu - qh\nu) - f_R(\varepsilon)| - |f_L(\varepsilon - qh\nu) - f_R(\varepsilon)|)P_l \\ &= \sum_{l=-\infty}^{+\infty}(2ln(\frac{1+e^{l\theta_e+q\theta_e}}{1+e^{q\theta_e}})\theta_e - l)P_l \qquad (1.40)\end{aligned}$$

The term previously labeled as the "thermal noise of the reservoirs" (see Eq. 1.18) is still identical between the pure DC and $V_p(t)=V_{ac}(t)+V_{ds}$ situations (but divided by 2). The complementary thought experiment is the noise in reduced units when the temperature of the right lead is set to θ_e, while the left reservoir is maintained arbitrarily at zero temperature. It would provide the same expression as Eq. 1.40. The qualitative behavior of Eq. 1.40 is very similar to the realistic experiment, but with a slower smoothing dependence with θ_e (e.g. about 2/3 for a lorentzian $\eta = 0.1$). Two conclusions are reached :

- The picture of the quantum state traveling in the wire as deduced from the PASN is partially impoverished by the comparison at the semi-transmitting barrier with the hot second Fermi sea.
- There is no direct interpretation of the absolute level of noise at finite temperature.

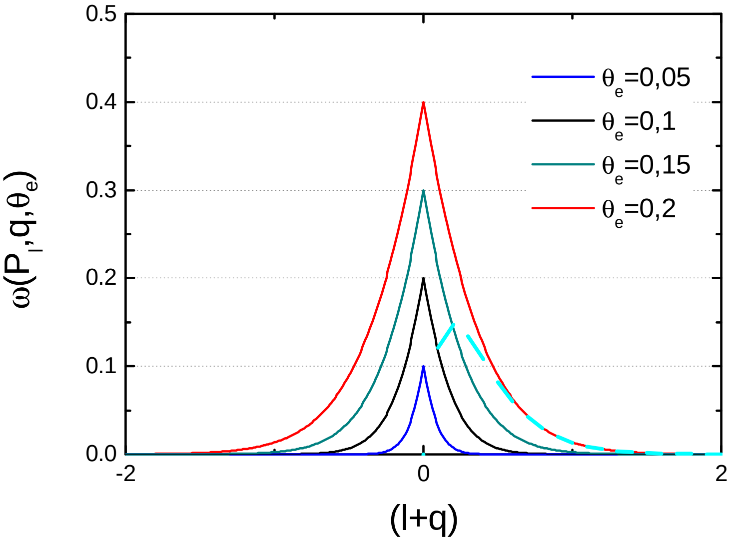

FIGURE 1.12 – Smearing function $\omega(l,q,\theta_e)$ impacting thermal PASN increase. $\omega(l,q,\theta_e)$ depends only on $|l+q|$ when $q/\theta_e \gg 1$ and shows a sharp peak around "$-q$" of amplitude $2\theta_e$(solid lines). When $q=n$, the asymptotic behavior (dash blue line) $\sim 2(|l+q|exp(-|l+q|/\theta_e)$ strongly limits the weight of all other probability amplitudes $P_{l\neq -q}$.

Separation of energy windows

From a quantitative analysis of the noise level, the main properties of the photo-assisted distribution can still be observed. The noise increase between the excess PASN at finite but small θ_e and zero temperature is virtually determined by at most 2 photo-assisted processes. To see this, we define the weight $\omega(l,q,\theta_e)$ such that :

$$\Delta N_{eh}(\alpha,q,\theta_e) - \Delta N_{eh}(\alpha,q,0) = \sum_{l=-\infty}^{+\infty} ((l+q)coth(\frac{l+q}{2\theta_e}) - (q)coth(\frac{q}{2\theta_e}) - |l+q| + |q|)P_l$$
$$= \sum_{l=-\infty}^{+\infty} \omega(l,q,\theta_e)P_l \qquad (1.41)$$

$\omega(l,q,\theta_e)$ gives the additional noise associated with the particles absorbing/emitting l photons.

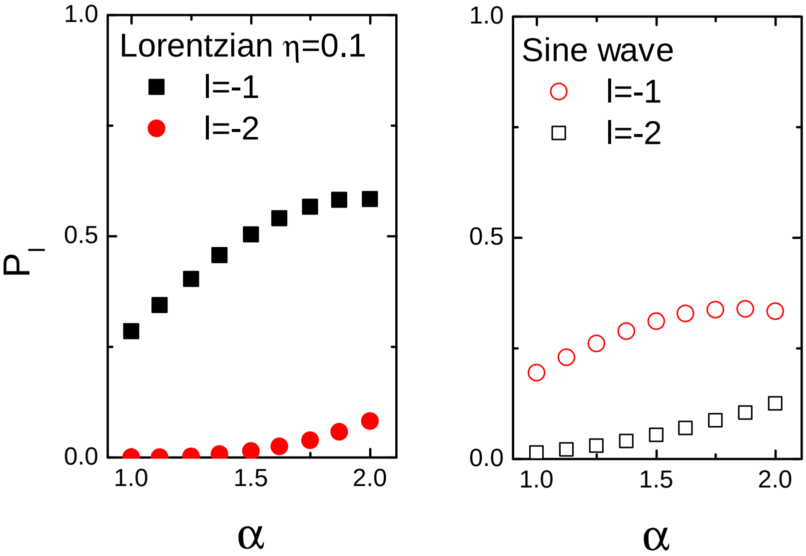

FIGURE 1.13 – Difference between the probability amplitude $P_{-1}(\alpha = q)$ and $P_{-2}(\alpha = q)$ when the AC time-profile is lorentzian or based on a sine window.

Each term $(x)coth(x/2\theta_e) - |x|$ forms a sharp peak around 0, of amplitude $2\theta_e$. As long as $q/\theta_e \gg 1$, $\omega(l,q,\theta_e)$ depends only on $(l+q)$ (see Fig.1.12). The additional PASN found with $\theta_e \ll 1$ compared to zero temperature and when $q = n$ is therefore $2\theta_e P_{-q}(\alpha = q)$. In brief, if the temperature is not large enough to mix energy windows $[lh\nu, (l+1)h\nu]$, photo-assisted transitions are still observed independently.

This additional noise has an interesting physical interpretation. One can derive this quantity by considering the anti-bunching of electrons for which nothing has happened in the left reservoir (probability $P_{-q}(\alpha = q)$) and all others in the right reservoir.

The behavior around $q = 0$ is different. [12]. We find a drop of amplitude $2\theta_e(P_0(\alpha) - 1)$. When we consider charge injection, it has no consequence since all $P_l(\alpha = q)$ are 0 when $q = 0$. But the effect is expected for an arbitrary pulse.

The introduction of the smearing function $\omega(l, q, \theta_e)$ also offers an explanation for the drift of the local minima. When q evolves from n to $n + 1$, the noise increase involves $P(\alpha = q)_{-n-1}$ and $P(\alpha = q)_{-n}$ with exchanging weights. If $P_{-n-1}(\alpha = q) \gg P_{-n}(\alpha = q)$, the minimum is displaced towards $n+1$. The typical situation for $q = n = 1$ is represented for the two pulse shape previously discussed in Fig.1.10 and 1.11, where we see the strong asymmetry $\mathrm{P}_{-1} > \mathrm{P}_{-2}$. Additionally, the difference is even stronger for a lorentzian pulse.

1.5 Energy spectroscopy

A direct consequence of Eq. 1.28 is the possibility to extract the entire set of $\mathrm{P}_l(\alpha)$ from a PASN measurement. Such an experiment implements an energy spectroscopy of the excited Fermi sea. We compare the results of such an experiment for various voltage profiles. The calculations and graphs are done and displayed at zero and finite temperatures.

1.5.1 Zero-temperature

Fig. 1.14 represents the excess number of particles per pulse for a voltage excitation $V_p(t)$=V_{ds}+$V_{ac}(t)$ with a varying DC average "q" and two fixed-amplitude periodic repetitions of lorentzian pulses α=1 and 2. The absence of excess particles is observed when the particle injection is recovered at $q = \alpha$. There is a singularity at each integer value $q = n$. The number of excess particles observed for different values of "q" gives either the number of holes or the number of electrons above or below this energy level for the AC part alone. To see this we can use Eq. 1.27.

$$\begin{aligned} q > 0 \Rightarrow \Delta N_{eh} &= N_e(V_p) + N_h(V_p) - |N_e(V_p) - N_h(V_p)| = 2N_h(V_p) \\ q < 0 \Rightarrow \Delta N_{eh} &= N_e(V_p) + N_h(V_p) - |N_e(V_p) - N_h(V_p)| = 2N_e(V_p) \end{aligned} \tag{1.42}$$

After a DC shift $+|q|h\nu$, only photo-excited holes below the energy $-qh\nu$ are still hole-like excitations and counted in $N_h(V_p)$. Symmetrically, after a DC shift $-|q|h\nu$, only photo-excited electrons above the energy $-qh\nu$ are still electron-like excitations and counted

---

[12] See also Fig. 1.17, 1.18 and 1.19. At small θ_e, the noise decreases at $q = 0$ with the temperature while it increases for the other values of q.

in $N_e(V_p)$. The decrease of excess noise in the left part is associated with the inverse exponential law in energy for excited electrons after a lorentzian pulse.

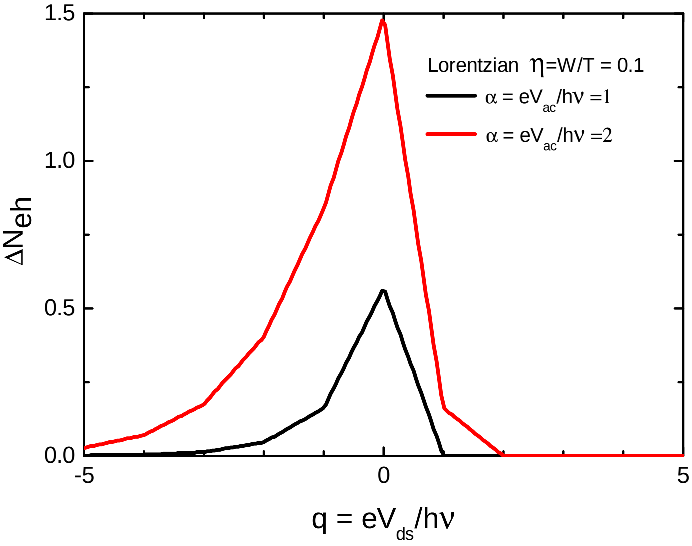

FIGURE 1.14 – Zero-temperature excess noise in the energy spectroscopy for voltage pulses with sine window and amplitude $\alpha = n = 1$ and $\alpha = n = 2$. As defined in the main text, the injection procedure under study is recovered when the DC bias q is equal to the amplitude α. The symmetry is a necessary consequence of flux parity $\phi(t)$ when $V_p(t)$= $V_{ac}(t)$ and V_{ds}=0.

Fig. 1.15 represents the excess number of particles per pulse for a voltage excitation $V_p(t)$=V_{ds}+$V_{ac}(t)$ with an arbitrarily varying DC average "q" and two fixed-amplitude sine waves α=1 and 2. The spectrum is symmetrical around q=0, a consequence of the odd symmetry $V_{ac}(t)$=-$V_{ac}(-t)$.

1.5.2 Finite-temperature

The second derivative of the experimental curves associated to Fig. 1.14 and 1.15 with respect to q provide directly the $P_l(\alpha)$ when $q = -l$.

$$\frac{\partial \Delta N_{eh}^2}{\partial q^2} = (2P_0 - 2)\delta(q-0) + 2\sum_{l\neq 0} P_l \delta(q+l) \tag{1.43}$$

At finite temperature this is no longer true. The singularities are rapidly smoothed

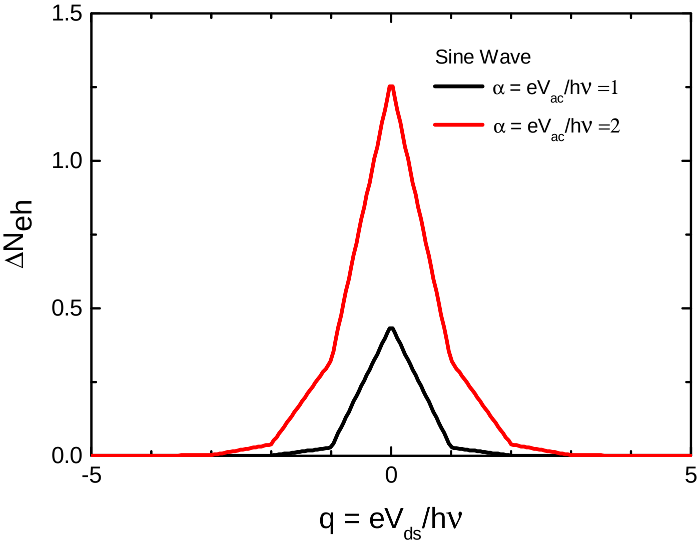

FIGURE 1.15 – Zero-temperature excess noise in the energy spectroscopy for sine-window pulses with amplitude $\alpha = n = 1$ and $\alpha = n = 2$. As defined in the main text, the injection procedure for each sine profile under study is recovered when the DC bias q is equal to the amplitude α.

when the temperature increases, as shown in Fig. 1.16.

Fig.1.17,1.18 and Fig.1.19 show the qualitative comparison between the typical pulse shapes under scruting : lorentzian injecting a few particles $\alpha = 1$ or 2 and a sine wave.

The way the total noise distribution with q evolves from the excess particle number at zero temperature is strictly calculable, and depends on a single parameter(θ_e). From an infinitely precise curve, the P_l distribution can be analyzed even for large θ_e, as can be expected in the “stair-like” structure of Fig.1.16. The main difficulty being the explosion of the required precision with θ_e. Such an analysis of the P_l distribution from a deconvolution of the experimental data at finite temperature was proposed and performed in [44] and [146] for the energy spectroscopy of sine and bi-harmonic wave with a flux transferring several charges per pulse.

The noise measurement might seem complex compared to a current measurement, but this drawback has to be compared with the possibility to characterize the underlying mechanism of photo-assisted transport. An energy-dependent scatterer with a small linear dispersion of the transmission probability $D(\varepsilon) = D_0 + \varepsilon \partial D / \partial \varepsilon$ would scatter for instance differently electrons and holes. How such an asymmetry would give information about the

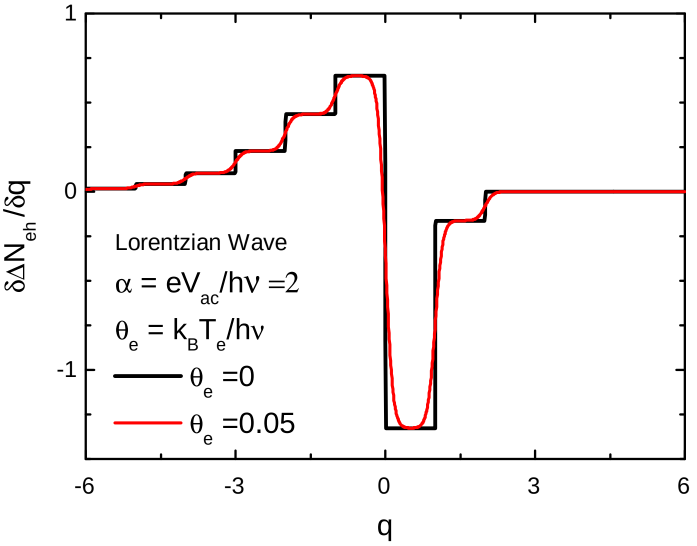

FIGURE 1.16 – Derivation of the excess noise in reduced units according to Eq. 1.29 at zero and finite temperature for a lorentzian voltage pulse with AC amplitude $\alpha = 2$ and arbitrary DC level q. At zero-temperature, the step size at each integer value for q probes $\mathrm{P}_{l=-q}(\alpha)$. The charge injection procedure is recovered at $\alpha = q$ only. At finite temperature(red curve), the excess noise probes a probability distribution influenced by the possibility of thermal energy exchange in the two reservoirs, but from which the photo-assisted processes can be still analyzed when $\theta_e << 1$.

particle distribution ? Unfortunately, the resulting excess current $< I_{ph} >$ compared to Eq. 1.25 does not provide information on the number of excited particles in the left lead. Using the same Fourier Transform property as in Eq. 1.22, we find that this current is proportional to the total power from the voltage pulse :

$$\begin{aligned} < I_{ph}(V_p) >^t &= \frac{e(h\nu)^2}{2h}\frac{\partial D}{\partial \varepsilon}\sum_{l=-\infty}^{+\infty}(l+q)^2 P_l \\ &= \frac{e^3}{h}\frac{\partial D}{\partial \varepsilon}\frac{< V_{ac}^2(t) >_t + V_{ds}^2}{2} \end{aligned} \tag{1.44}$$

However, using an experimental set-up with low-amplification range under 1kHz, Julie Dubois[37] used this current as a RF in-situ calibration. The impact of a similar non-linear term in the transmission probability while calculating the noise amplitude was also

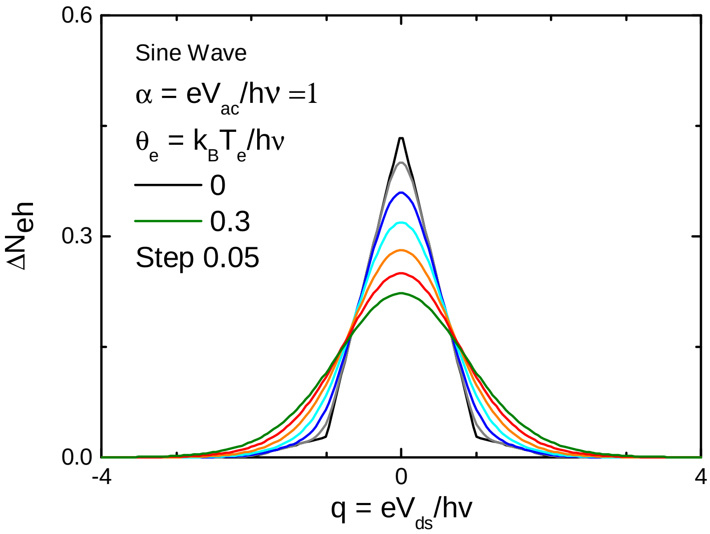

FIGURE 1.17 – Finite-temperature excess noise in the energy spectroscopy for voltage pulses with sine window and amplitude $\alpha = n = 1$. As defined in the main text, the injection procedure under study is recovered when the DC bias q is equal to the amplitude α.

addressed in her work.

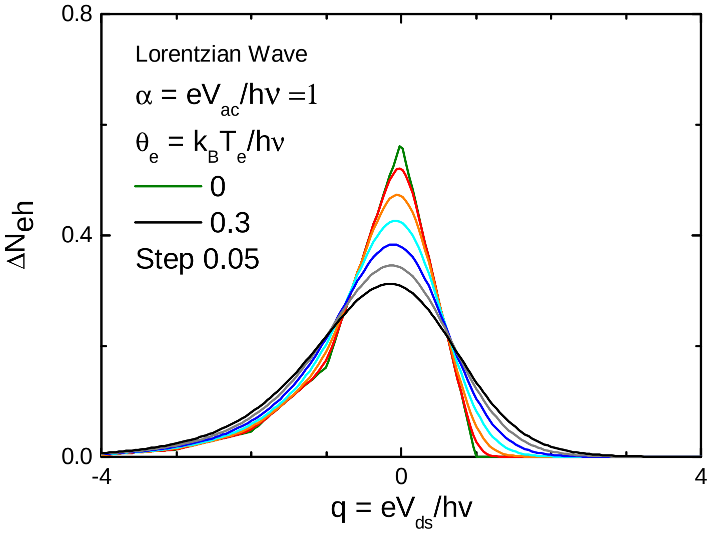

Figure 1.18 – Finite-temperature excess noise in the energy spectroscopy for voltage pulses with lorentzian shape and amplitude $\alpha = n = 1$. As defined in the main text, the injection procedure under study is recovered when the DC bias q is equal to the amplitude α.

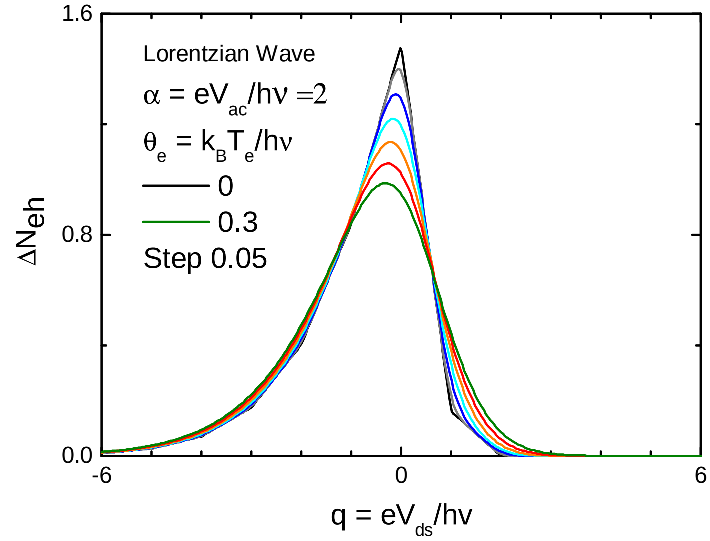

Figure 1.19 – Finite-temperature excess noise in the energy spectroscopy for voltage pulses with lorentzian shape and amplitude $\alpha = n = 2$. As defined in the main text, the injection procedure under study is recovered when the DC bias q is equal to the amplitude α.

1.6 Time-domain measurement

1.6.1 Time spectroscopy experiment

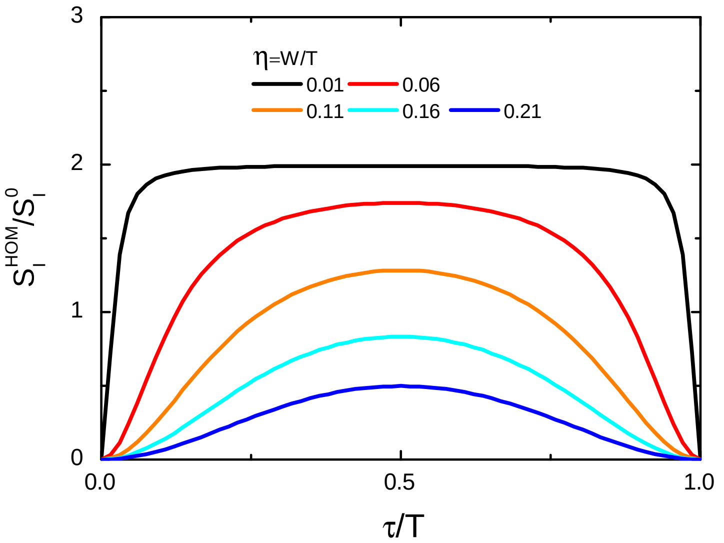

FIGURE 1.20 – Time-domain spectroscopy for train of lorentzian voltage pulses with various widths W compared to the period T and $\alpha = 1$. $\alpha = q = 1$. The noise is zero when the contacts are driven in phase (τ/T=0) and maximal when the separation between the two trains is half a period. If the repetition rate still allows for a complete time-separation of particles injected from the right and from the left, twice the noise of a single charge injection is found at $\tau/T = 1/2$.

Two critical aspects of the on-demand transfer of particles are lost in low-frequency statistical measurements : the injection time and the wave-packet time-extension. The total number of excitation is found when all the particles have transited back in one the contacts, not at intermediary time. Even if the energy distribution is in principle sufficient to rebuild the time-picture, it might be interesting to consider measurements giving a direct access to these quantities.

Signatures of these quantities are recovered when a voltage source $V_p(t{+}\tau/2)$ is connected to the right lead of the quantum conductor while the left lead is maintained at the $V_p(t{-}\tau/2)$. τ indicates a tunable time-delay between the two sources. The noise measurement is only sensitive to the voltage drop at the energy-independent scatterer. PASN calculations are equivalent to a single contact driven with a source ($V_p(t{-}\tau/2){-}V_p(t{+}\tau/2)$).

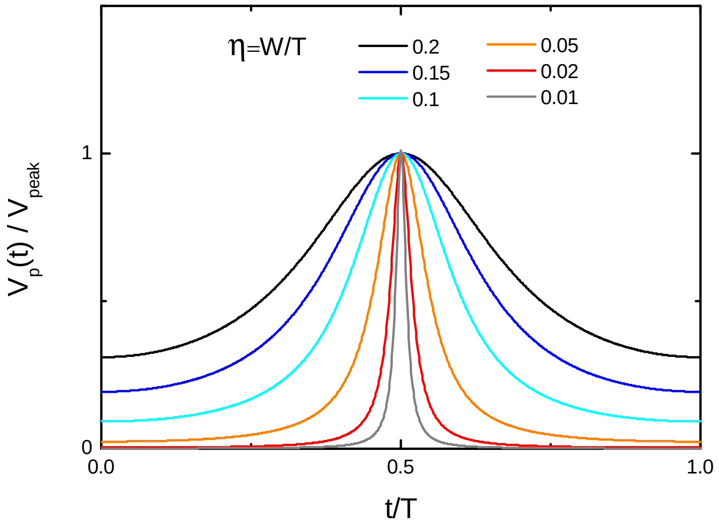

FIGURE 1.21 – Time-profile for various periodic trains of lorentzian voltage pulses as applied from a classical source on a contact. The separation of the voltage pulses in the time domain is lost for large W. As explained in the section 1.7, in that case the quantum wire whole excitation is still strictly made of a stream of single-particle excitations but these particles cannot be probed separately in the proposed experimental scheme. In the time-spectroscopy experiment, two sources of such voltages pulses are used to define the bias applied on the sample.

The PASN expression for any pulse shape $V_p(t)$ can be expressed from the original p_l decomposition of the phase term.

$$S_I^{HOM}(\tau)/S_I^0 = \sum_{k=-\infty}^{+\infty} |k||\Pi_k|^2(\tau) \tag{1.45}$$

With :

$$\Pi_k(\tau) = \sum_{l-\infty}^{+\infty} (p_l p^*_{l-k} e^{i2\pi\tau\nu l}) e^{-i2\pi\tau\nu k/2} \tag{1.46}$$

Fig. 1.20 represents the PASN amplitude S_I^{HOM} generated in this situation in reduced units for a lorentzian periodic pulses injecting one electron per period, and with different FWHM. The general shape has a few basic features. When τ is zero, the barrier is driven uniformly and there is no possibility for particle scattering to produce shot noise. Possible scattering events are all correlated through anti-bunching. When τ/T=0.5, the peaks from the two periodic trains of pulses are maximally separated and the noise shows a maximum. If $W \ll T$ there is no extension of each voltage peak over several periods (amplitude over time for the source pulses are plotted in Fig. 1.21 for direct comparison) and the noise maximum is exactly the PASN expected from two independent particles injected per period, alternatively emitted by the left and right contacts.[13]

1.6.2 Lorentzian pulses and quantum overlap

The link between the time-dependent electronic wave traveling in the conductor and the PASN is given by the comparison between $S_I^{HOM}(\tau)$ and the quantity 2(1-$C(\tau)$). $C(\tau)$ is the quantum overlap between two single excitation traveling above the Fermi sea emitted at different times.

$$C(\tau) = | < \psi^*(x, t + \frac{\tau}{2}) | \psi(x, t - \frac{\tau}{2}) > |^2 \tag{1.47}$$

The possibility to describe the excited Fermi sea with the creation of n right-moving electrons and n left-moving holes is a remarkable consequence of lorentzian pulses with $\alpha = n$. The wavefunction[14] for a transferred electron emitted from a pulse centered at time t_0 was obtained in [71].

$$\psi(x, t) = \sqrt{\frac{v_F}{2\pi}} \frac{i\sqrt{2W}}{x - v_F(t - t_0) + i v_F W} \tag{1.48}$$

The projection does not depend on the time t, and $C(\tau)$ is then exactly a lorentzian curve of FWHM $2W$ and $C(\tau = 0)$=1. S_I^{HOM} in that case is :

$$\begin{aligned} S_I^{HOM}(\tau)/S_I^0 &= \frac{8\beta^2 sin(\pi\nu\tau)^2}{1 - 2\beta^2 cos(2\pi\nu\tau) + \beta^4} \\ lim_{W\to 0} S_I^{HOM}(\tau)/S_I^0 &\sim 2(1 - \frac{1}{1 + (\tau/2W)^2}) \end{aligned} \tag{1.49}$$

---

[13] The delay-dependent shot noise suppression for colliding particles at a QPC from various sources in chiral edge channel was analyzed in [103] as a tool to compare quantum states produced in initially uncorrelated systems. The name spectroscopy is used. We consider in this work a system with bi-directional channels, and only voltage pulses.

[14] It can be obtained form the single-electron creation operator in Eq. 1.53. The right-moving states with linear dispersion are $\frac{exp(-i\varepsilon(t - x/v_F)/\hbar)}{\sqrt{2\pi\hbar v_F}}$.

The time-spectroscopy is a measure of the quantum overlap $| < \psi^*(x, t+\tau)|\psi(x, t) > |^2$, i.e. the size of wave-packet. We have introduced : $\beta = exp(-2\pi W/T)$. $W \to 0$ with fixed T leads to the regime where we can think of each period as a single event [15] The result can actually be extended to the quick repetition case when emitted electrons overlap over difference periods. It requires a slightly different definition for $C(\tau)$ based on the excited Fermionic Field instead of a single wavefunction. More details are provided in chapter 4. Eq.1.49 suggests a strong analogy with the Hong-Ou-Mandel experiment[62]. In the small W/T limit, close expressions have been obtained by Ol'khovskaya et al.[111] and by Jonckheere et al[69]. These works have been motivated by the single electron source demonstrated in [41] where single charges whose charge sign periodically alternates are emitted from an ac driven quantum dot capacitor and the trains of charges collide in a QPC. In the adiabatic ac drive limit, the wave packets mimic those emitted by lorentzian voltage pulses on a contact. The experimental demonstration of the indistinguishably of fermions from two such sources with a Hong-ou-Mandel experiment was performed recently[16].

The need to analyze the periodically-driven transport on all relevant timescales, and not only from average, is becoming more and more relevant. Among a more general trend towards GHz frequencies in mesoscopic systems, experimental advances in the field of on-demand electron sources are some of the motivation behind the introduction of Waiting-Time Distribution (WTD) for single-electron emitters[3] and quantized electrons pulses[30][2]. Theoretical developments also include new dedicated time-resolved numerical simulations[46].

From a noise measurement, we can therefore extract $| < \psi^*(x, t+\tau)|\psi(x, t) > |^2$ and measure the size of the wavepackets induced by lorentzian pulses. These properties are not true for periodic trains of lorentzian pulses with $\alpha \neq 1$ or other pulse shapes.

1.7 Leviton

We address in this part the properties of the states excited through lorentzian pulses, and their description as quasi-particles.

---

[15] The equivalence in Eq. 1.49 holds for $\tau \in]-T/2, T/2[$ and the result is identical with fixed W and $T \to \infty$.

1.7.1 Particle description of the excited state above the Fermi sea.

The treatment of the QPC independently at all energy levels reflects the use of a convenient basis to describe the scattering problem, and not the existence of several independent incoming objects. The difference is also seen when considering the time-domain. A description equivalent to the family of wave-function $exp(-i\varepsilon t/\hbar)$ is the decomposition into a time-dependent basis with states crossing the point $x = 0$ at time τ. Their wave-function are $\delta(\pm x/v_F - (t-\tau))$. On one hand, scattering events only relate states with the same τ and a single electron ends up divided into the two leads according to its decomposition over the basis $\delta(\pm x/v_F - (t-\tau))$. But measuring one electron in one lead at a certain time prevents from measuring it in the other lead at any other time. This is different from a state made of two particles being scattered independently, for which we expect a second charge to be observed later.

This thought experiment may lead us to study time-dependent quantum correlators of the form $< \delta\hat{\mathbf{I}}(t)\delta\hat{\mathbf{I}}(t+\tau) >^t$, whose Fourier Transform is probed in high-frequency noise measurements[16]. For instance, such experiments have been conducted with the already mentioned mesoscopic capacitor source where the injection mechanism reflected in “jitter noise” for some selected driving cycles[94][112]. Keeling et al.[71] have proposed a different approach. They have compared one-electron and two-electrons operators to analyze how the Fermi statistics block several particles from being excited after a quantized lorentzian pulse. Their proposal offers also interesting possibilities to discuss the successive injection of N electrons compared to the simultaneous injection of exactly N electrons. A detailed presentation can be found in[59]. We reproduce here the main ideas. We start with a single electron at an energy $|\varepsilon_0>$, alone in the vacuum. As already stated, the effect of a time-dependent voltage drop on this state can be calculated from the Schrödinger equation.

---

[16] See also calculations and references in [37].

$$
\begin{aligned}
|\phi_{exc.}> &= \sum_{l=-\infty}^{+\infty} p_l \hat{a}_L^\dagger(\varepsilon_0 + lh\nu)\hat{a}_L(\varepsilon_0)|\varepsilon_0> \\
&= \int_{-\infty}^{+\infty} d\varepsilon \delta(\varepsilon - lh\nu) \sum_{l=-\infty}^{+\infty} p_l \hat{a}_L^\dagger(\varepsilon_0 + \varepsilon)\hat{a}_L(\varepsilon_0)|\varepsilon_0> \\
&= \int_{-\infty}^{+\infty} \frac{d\varepsilon}{2\pi\hbar} \int_{-\infty}^{+\infty} dt e^{i(\varepsilon - lh\nu)t/\hbar} \sum_{l=-\infty}^{+\infty} p_l \hat{a}_L^\dagger(\varepsilon_0 + \varepsilon)\hat{a}_L(\varepsilon_0)|\varepsilon_0> \\
&= \int_{-\infty}^{+\infty} \frac{d\varepsilon}{2\pi\hbar} \int_{-\infty}^{+\infty} dt e^{i\varepsilon t/\hbar} e^{-i\phi(t)} \hat{a}_L^\dagger(\varepsilon_0 + \varepsilon)\hat{a}_L(\varepsilon_0)|\varepsilon_0> \\
&= \int_{-\infty}^{+\infty} d\varepsilon p_\varepsilon \hat{a}_L^\dagger(\varepsilon_0 + \varepsilon)\hat{a}_L(\varepsilon_0)|\varepsilon_0>
\end{aligned}
$$

$\hat{a}_L(\varepsilon)$ is the creation operator for a left-moving particle in the vacuum at energy ε. p_l does not exist unless $exp(-\phi(t))$ is periodic. p_ε exists in any situation. Here we are interested in lorentzian pulses with a flux e/h, applied at time t_m and FWHM $2\tau_m$. The photo-assisted scattering amplitudes p_ε can be decomposed in two parts, a Dirac function and p^{reg}, a continuous function for positive energy.

$$
\begin{aligned}
e^{-i\phi(t)} &= \frac{t + i(\tau_m + it_m)}{t - i(\tau_m - it_m)} \\
p_\varepsilon &= \delta(\varepsilon) - \frac{2\tau_m}{\hbar}\Theta(\varepsilon)e^{-\varepsilon(\tau_m - it_m)/\hbar} \\
p_\varepsilon &= \delta(\varepsilon) + p_\varepsilon^{reg}\Theta(\varepsilon)
\end{aligned}
$$

The problem with two indistinguishable electrons $|\varepsilon_0, \varepsilon_1>$ with initial energies ε_0 and ε_1, is straightforward if they are well-separated, i.e. if $\varepsilon_1 \gg \varepsilon_0$. They both move freely according to p_ε. They are shifted upwards in energy over a range $\sim \hbar/\tau_m$. If $|\varepsilon_0 - \varepsilon_1|$ is similar or inferior to this scale, the overlap starts to play a role and prevents some scattering events. Predictions about the final probability to have two excited electrons at energy $\varepsilon_3^F > \varepsilon_2^F$ both above the two initial energies $\varepsilon_2^F > \varepsilon_1 > \varepsilon_0$ involve operators $\hat{a}_L(\varepsilon_3^F)\hat{a}_L(\varepsilon_2^F)$. As already stated :

$$
U^\dagger \hat{a}_L(\varepsilon_{3,2}^F)U = \hat{a}_L(\varepsilon_{3,2}^F) + \int_{-\infty}^{\varepsilon_{3,2}^F} d\varepsilon' p_{\varepsilon'}^{reg} \hat{a}_L(\varepsilon_{3,2}^F - \varepsilon') \tag{1.50}
$$

Where U is the unitary operator which gives excited states on the right from initial states on the left. Following [71], we show

$$\hat{a}_L(\varepsilon_3^F)\hat{a}_L(\varepsilon_2^F)U|\varepsilon_0,\varepsilon_1 >= 0 \tag{1.51}$$

which makes all correlators with more than one particle above ε_1 vanish, proving that only one electron at a time can end above this level.

$$\begin{aligned}
\hat{a}(\varepsilon_3^F)\hat{a}(\varepsilon_2^F)U|\varepsilon_0,\varepsilon_1 > &= UU^\dagger\hat{a}_L(\varepsilon_3^F)UU^\dagger\hat{a}_L(\varepsilon_2^F)U|\varepsilon_0,\varepsilon_1 > \\
&= U\left(\hat{a}_L(\varepsilon_3^F) + \int_{-\infty}^{\varepsilon_3^F} d\varepsilon' p_{\varepsilon'}^{reg}\hat{a}_L(\varepsilon_3^F-\varepsilon')\right) \\
&\left(\hat{a}_L(\varepsilon_2^F) + \int_{-\infty}^{\varepsilon_2^F} d\varepsilon' p_{\varepsilon'}^{reg}\hat{a}_L(\varepsilon_2^F-\varepsilon')\right)|\varepsilon_0,\varepsilon_1 > \\
&= U\left(p_{\varepsilon_3^F-\varepsilon_1}^{reg}\hat{a}_L(\varepsilon_1) + p_{\varepsilon_3^F-\varepsilon_0}^{reg}\hat{a}_L(\varepsilon_0)\right) \\
&+ \left(p_{\varepsilon_2^F-\varepsilon_1}^{reg}\hat{a}_L(\varepsilon_1) + p_{\varepsilon_2^F-\varepsilon_0}^{reg}\hat{a}_L(\varepsilon_0)\right)|\varepsilon_0,\varepsilon_1 > \\
&= U\left(p_{\varepsilon_3^F-\varepsilon_1}^{reg}p_{\varepsilon_2^F-\varepsilon_0}^{reg}\hat{a}_L(\varepsilon_1)\hat{a}_L(\varepsilon_0) + p_{\varepsilon_3^F-\varepsilon_0}^{reg}p_{\varepsilon_2^F-\varepsilon_1}^{reg}\hat{a}_L(\varepsilon_0)\hat{a}_L(\varepsilon_1)\right)|\varepsilon_0,\varepsilon_1 > \\
&= U\left(p_{\varepsilon_3^F-\varepsilon_1}^{reg}p_{\varepsilon_2^F-\varepsilon_0}^{reg} - p_{\varepsilon_3^F-\varepsilon_0}^{reg}p_{\varepsilon_2^F-\varepsilon_1}^{reg}\right)\hat{a}_L(\varepsilon_1)\hat{a}_L(\varepsilon_0)|\varepsilon_0,\varepsilon_1 >
\end{aligned} \tag{1.52}$$

In the integral we have conserved only the energy available in the initial states. According to the last line, only one probability amplitude is left, which has a characteristic anti-symmetrical form in the exchange of the two final energies. But the property $p^{reg}(a+b) = p^{reg}(a)p^{reg}(b)$ makes this amplitude trivially zero. We see that the key properties of a lorentzian pulse are strikingly related : the absence of negative energy shift imposes the lorentzian shape and thus p^{reg}. In turn, p^{reg} are exactly the only distributions for which this "sum-product" law holds. When the initial system is the infinitely deep Fermi sea at zero-temperature $|\Phi_F>$, similar calculations can be used. The same result is then obtained : only one right-moving electron can be observed above the Fermi sea and reach the right reservoir. Operator U performs a single particle creation [17] described by :

$$A^\dagger(\tau_m, t_m) = \int_0^{+\infty} d\varepsilon \sqrt{\frac{2\tau_m}{\hbar}} e^{-\varepsilon(\tau_m - it_m)/\hbar}\hat{a}_L^\dagger(\varepsilon) \tag{1.53}$$

Keeling et al. linked this crucial property to a structural property : U is a rank-1 matrix.

---

[17] Charge conservation can be checked by considering the entire system. See [59]

At non-zero temperature, thermally excited holes and electrons would move according to the limited possibility offered by Eq. 1.52. Similarly a lorentzian pulse with $q = -1$ generates a single hole whose creation operator is :

$$B(\tau_m, t_m) = \int_{-\infty}^{0} d\varepsilon \sqrt{\frac{2\tau_m}{\hbar}} e^{-|\varepsilon|(\tau_m + it_m)/\hbar} \hat{a}_L(\varepsilon) \tag{1.54}$$

1.7.2 Multiple particle injection

Using a recurrence[71], the effect of N successive lorentzian pulses can be analyzed. For all pulses $q = 1$. We note their FWHM $2\tau_k$ and the center time $t = t_k$. We have $k \in [1, N]$ ans start with all t_k different. The right-moving excited state is :

$$U|\Phi_F > \to \prod_{l' > l, l \in [1,N]} \frac{\xi_l^* + \xi_{l'}}{\xi_{l'} - \xi_l} \prod_{k=1}^{N} A^\dagger(\tau_k, t_k)|\Phi_F > \tag{1.55}$$

where $\xi_l = \tau_l - it_l$. Exactly N electrons are excited above the Fermi level. Similarly, N lorentzian pulses with different widths τ_k and centered at different times t_k, but all with $q = -1$ give a final state with exactly N holes. Mixing pulses with $q = 1$ and $q = -1$ makes the final state non-deterministic for the number of particles, unless a large separation in time is used. The same recurrence but making each added of the N pulses ξ_l converging towards a single value ξ gives the excited state from a lorentzian with amplitude $\alpha = N$ pulse, i.e. sending $q = N$ charges.

$$U|\Phi_F > \to \prod_{k=1}^{N} \mathbf{L}_k^\dagger(\tau, t)|\Phi_F > \tag{1.56}$$

Where $\mathbf{L}_k^\dagger(\tau, t) = \sqrt{\frac{2\tau}{\hbar}} \int_0^\infty d\varepsilon \frac{(2\tau\varepsilon)^k}{\hbar^k k!} e^{-\varepsilon(\tau - it)/\hbar} \hat{a}_L^\dagger(\varepsilon)$
Unlike each $A^\dagger$, $\mathbf{L}_k^\dagger$ are not normalized wave-packets, but $\prod \mathbf{L}_k^\dagger$ is. The transition shows that electrons induced by well separated lorentzian pulses are detected with the same energy dispersion and almost independently, while electrons sent simultaneously pile up in energy. The last one has then a typical energy close to $N\varepsilon_{qp} \sim \hbar/2\tau$. In a realistic system with interactions, they still behave as quasi-particles with a finite typical lifetime τ_{qp} [29][48][153] [18] :

---

[18] See also AppendixB.

$$\tau_{qp}^{-1} \approx \frac{E_F}{2h}(\frac{N\varepsilon_{qp}}{E_F})^2 ln(\frac{E_F}{N\varepsilon_{qp}}) \tag{1.57}$$

This formula does not apply specifically to a Leviton, but to any quasi-particle. The remarkable additivity of lorentzian-induced electrons is analogous to one of the characteristic property for a Soliton [36] solution to a wave equation. The independent propagation -measurements are not independent- is a natural property for free electrons which extends the analogy further. Inducing N holes with "negative" lorentzian is similar. The state generated by a quantized lorentzian and previously referred to as "Coherent State of AC Current" has been called a leviton to emphasize this quasi-particle behavior. The same final state could be generated by a mesoscopic capacitor source driven in the so-called "adiabatic regime"[72].

Chapitre 2

Low-temperature cross-correlation detection with parallel high-mobility transistors (HEMT)

From their early successes to the most recent results [14][152][95], noise measurements in mesoscopic physics have relied on stable low-noise amplification and fast data acquisition. In this chapter we describe an experimental system dedicated to simultaneous cross-correlation measurements of voltage fluctuations in the MHz range and low-frequency current at very low-temperature in an helium-free cryostat (section 2.1). A 35 mK electronic temperature is found while noise powers of 10^{-30} A^2/Hz can be resolved in about 3 minutes.

The two-channels cross-correlation set-up is a convenient way to separate the sample voltage fluctuations from the parasitic amplification noise background. As explained in section 2.2, no knowledge or calibration of this unwanted noise is required and the analysis is greatly simplified. The choice of the MHz range results from the combination of several arguments. First, both the physics of DC and photo-assisted shot noise for energy between 10 mK and 1 K involve much shorter timescales, typically below the nanosecond. Thus, the zero-frequency white noise approximation can be used. At the same time, both the 1/f noise from mesoscopic samples and amplification devices can be neglected as their respective corner frequencies are exceeded. Finally, real-time data acquisition and numerical treatment in this frequency range are now possible with the association of personal computers and fast Analog to Digital Converters (ADC)(section 2.4).

Fine in-situ calibration of the amplification chain is presented in section 2.3. At the core of this set-up are cryoamplifiers based on commercial high-mobility pseudomorphic HEMT (pHEMT). As shown in previous works [34],[122], these transistors have ultra-low input-referred voltage noise down to the MHz range around 4 K and allow the implementation of home-made, efficient and low-cost cryoamplifiers. The concept is presented in section 2.5. We report in section 2.6 the performances obtained with our new design based on parallel Agilent ATF-34143 pHEMTs.

2.1 Description of the system

2.1.1 Overview

Fig. 2.1 shows a schematic view of the two measurement lines implemented in the cryostat. Tab. 2.1 lists the different temperatures at which each functional block is grounded.

The mesoscopic sample is represented as a resistor R_S and the randomly fluctuating current is represented as the source δI_S. This sample is a QPC and all calibrations are based on its physical properties. In the general context of this manuscript, this is the sample referred to as "B". Details can be found in Appendix B. We describe the system starting from the QPC and following the signal up to the ADC stage.

- Two passive resonant circuits (RESONATOR boards) Z_A and Z_B act both as pass-band filters and current-to-voltage converters. The resonant frequency is in the low MHz range : 2.5 MHz. The voltages seen at these resonators are respectively labeled V_A and V_B.
- 55-centimeters (measured : ~98 pF) coaxial lines connect the resonators to the cryoamplifiers (CRYOAMP board), thermalised at 4 K.
- Then, coaxial lines extend further (measured :~ 68 pF and ~ 70 cm) from the cryoamplifiers to a room temperature printed board (called SPLITTERs, see also [34]). The purpose of this board is to separate the incoming fixed DC polarization current used to select the transistor working point from the out-coming amplified signal to be analyzed.
- Additional room temperature amplification is provided by two NF SA-421F5 amplifiers with 46 dB of gain ($G_{NF} = 200$) and an input impedance of 1 MΩ[1].
- The amplified outputs V_1 and V_2 are then read on the synchronized input channels of a 50 Ω 8-bit Agilent digitizer and continuously accumulated at 20 MS/s.

---

[1] NF SA-421F5 are differential amplifiers. Here they are used with one grounded input.

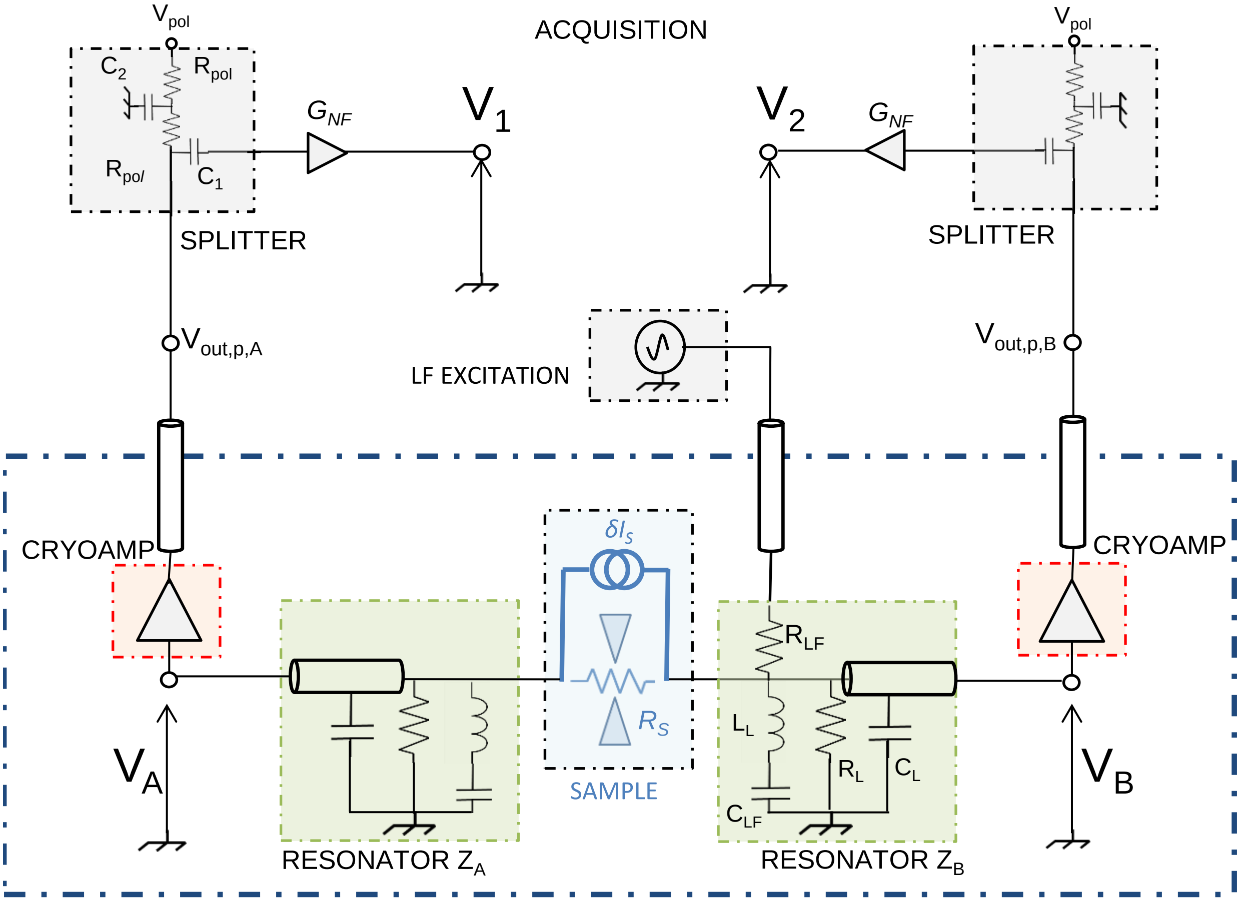

FIGURE 2.1 – Schematic representation of the low-temperature two-channel cross-correlation measurement system. The dotted dark blue box mark the helium-free cryostat. Except for the resistor R_{LF}, the two channels are entirely identical and labels are not repeated. CRYOAMP and LF-EXCITATION board are detailed in Fig. 2.2 and 2.7.

- Simultaneously, low-frequency are analyzed. An injection line dedicated to DC and kHz signal is directly connected on resonator B. Standard lock-in technique is used to extract the response in output signal V_1.
- Additional room-temperature filtering is provided by 7^{th}-order Tchebychev filters (Appendix E) with a cut-off frequency at 8.5 MHz.

Photographs of the lines inside the helium-free cryostat can be found in Appendix A.

Circuit Board	Temp.
SAMPLE	13 mK
RESONATOR	13 mK
CRYOAMP	4.1 K
SPLITTER	300 K
LF INJECTION	300 K

Table 2.1 – Thermal grounding points in the measurement set-up. Each stage temperature was monitored with calibrated thermometers. For the coolest parts, the electronic temperature was measured independently around 35 mK. See 2.3

2.1.2 General requirements for passive components

Electronic components were selected to maintain low-temperature accuracy and reliability, while being insensitive to the addition of high magnetic fields. This is the only possibility to achieve a full calibration. The thin-film resistors (all CMS with 0805-size) have been measured at 4 K and show little deviation from their room temperature values, under 5%. The only exception is the 11 Ω resistor RC1, with variations up to 15%. The resistors originate from several manufacturers. Following [34], we use a COILCRAFT 1812CS with $L_L = 22\,\mu$H, without magnetic core. Despite the absence of high-µ material, the low-temperature parasitic series resistance is expected to be low in the MHz range according to these previous results (a few Ω). All capacitors (also CMS with 0805-size) are based on the same dielectric (C0G/NP0) which was found to be extremely stable from room temperature to 4 K.

2.1.3 Cryo-amplifiers

Circuit

Full circuitry of the 2-HEMTs device is shown in Fig. 2.2. Upper and bottom lines are parallel and identical. Each contains one transistor. The board is realized by milling a 35 µm-50 µm-35 µm Copper-Insulator-Copper flexible P.C.B. [2]. The board size is $2.8\times1.8\,\mathrm{cm}^2$ and it was enclosed in a 2 mm-thick copper box as an electromagnetic shield.

Passive components can be divided in two groups : those which define the DC polarization point and those that contribute to the stability of the device at high frequencies.

---

[2] 2. Dielectric is a polyoxymethylene (POM) polymer. Data are available about its cryogenic thermal conductivity. [52]. Despite not knowing the exact crystalline structure of the material we use, we can expect a typical value at 4K of $\sim$10 $\mathrm{mWm^{-1}K^{-1}}$, close to the well-known Kapton[82].

Component	Value
R_L	2×5 kΩ in parallel
L_L	22 μH
C_L	190 pF
C_{LF}	2×4.7 nF
R_{LF}	200 kΩ
R_{pol}	1 kΩ
$C1$	22 nF
$C2$	2.2 nF
R_{C1}	11 Ω
R_{C2}	200 Ω
C_{C1}	22 nF
C_{C2}	5 pF
C_{C3}	100 pF

TABLE 2.2 – Passive components values. The line in the table separates the components of the CRYOAMP board from the others components. See Fig.2.1 ,2.2 ,and 2.7

R_{C2}=200 Ω is meant to impose the source-gate voltage directly from the drain-source current, eliminating the need for an extra line from room-temperature. This self-polarization resistor is heavily shunted by three 22 nF capacitors C_{C1} (cut-off ∼12 kHz). The lines were not matched to 50Ω and have a typical length of 1-2 cm, short enough to rule out any destructive interference between the two output waves in the MHz range. To prevent GHz waves from resonating, small discrete components R_{C1}, C_{C2} , C_{C3} have been placed all along the input and output paths as a precaution. We also have to consider the possibility for an extra capacitance to be added by the pattern on the PCB. The transmission line has a co-planar waveguide geometry with a ground parallel plane. The central connector has a width 0.2 cm, and the veins are roughly 300 µm-wide. Numerical simulations with a dedicated software indicate a low characteristic impedance (below 5 Ω) and capacitance per unit length below 10 fF/m. [3].

Polarisation

DC voltages can be measured at two points with a digital multimeter : $\mathrm{V_{dc,source}}$ and $\mathrm{V_{out,p}}$ for each line. The current flowing in each HEMT is then given as

$$\mathrm{I_{ds,hemt}} = \frac{1}{2}\frac{\mathrm{V_{dc,source}} - \mathrm{V_{out,p}}}{2\mathrm{R_{pol}}} \tag{2.1}$$

---

[3] The software is TX-LINE 2003$^{\mathrm{TM}}$. Based on room-temperature dielectric constant ∼4 for POM.

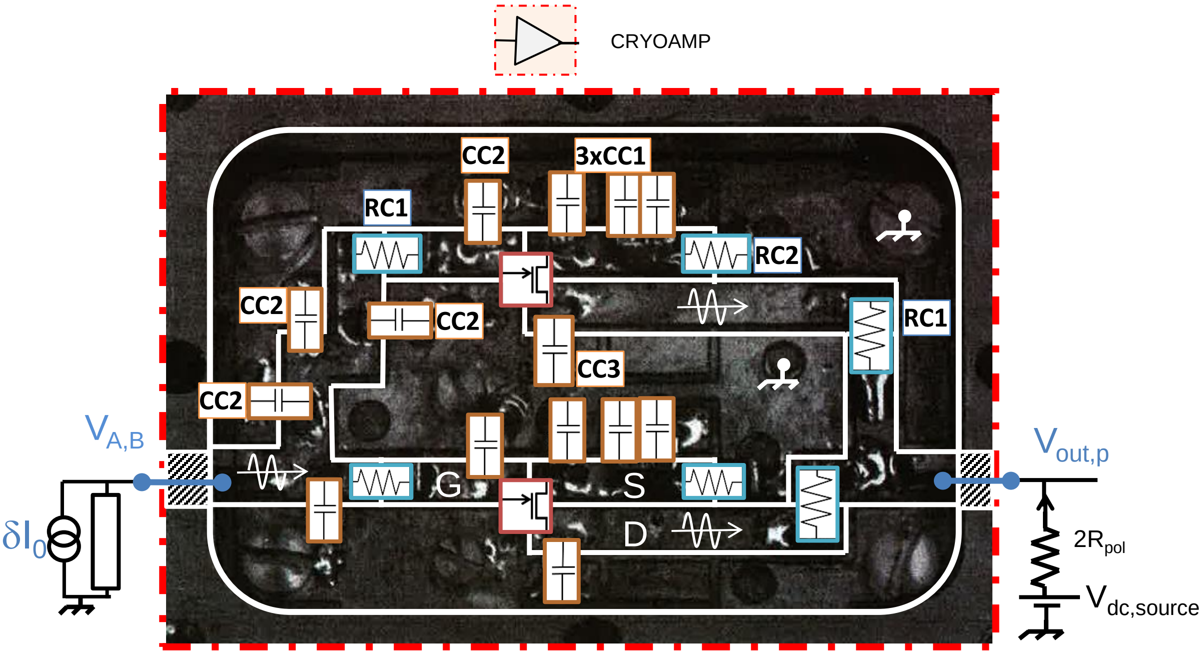

FIGURE 2.2 – Schematic representation of the 2-HEMT cryo-ampliplifier. Simplified version of the input and output circuits are represented. Stricly duplicated electronics has not been labeled on the bottom line. Real-size 1.8 cm×2.8 cm.

The drain-source voltage follows.

$$V_{\mathrm{ds,hemt}} = V_{\mathrm{out,p}} - I_{\mathrm{ds,hemt}}(R_{C1} + R_{C2}) \tag{2.2}$$

The I-V curve is presented in Fig. 2.3(a). It can be compared to similar curves obtained with a single HEMT and a 10-HEMTs device in Appendix F.

From these voltages we can evaluate the total dissipated power on the PCB : ∼ 2.2 mW per amplifier[4]. This is low enough to maintain proper operation of our 400 µW cryostat from CRYOCONCEPT™and preserve cooling power at all stages. In particular, the lowest temperature achieved, 12.5 mK was unchanged when powering the set-up. This low-consumption results from the high gate voltage V_{gs} ∼0.48 V used to deplete the 2DEG and the correspondingly low current, well below the typical 60 mA from the manufacturer.

The other quantity of interest is the output conductance (Fig. 2.3(b)). We have to

---

[4] Power dissipated in each HEMT plus in R_{C1} and R_{C2}.

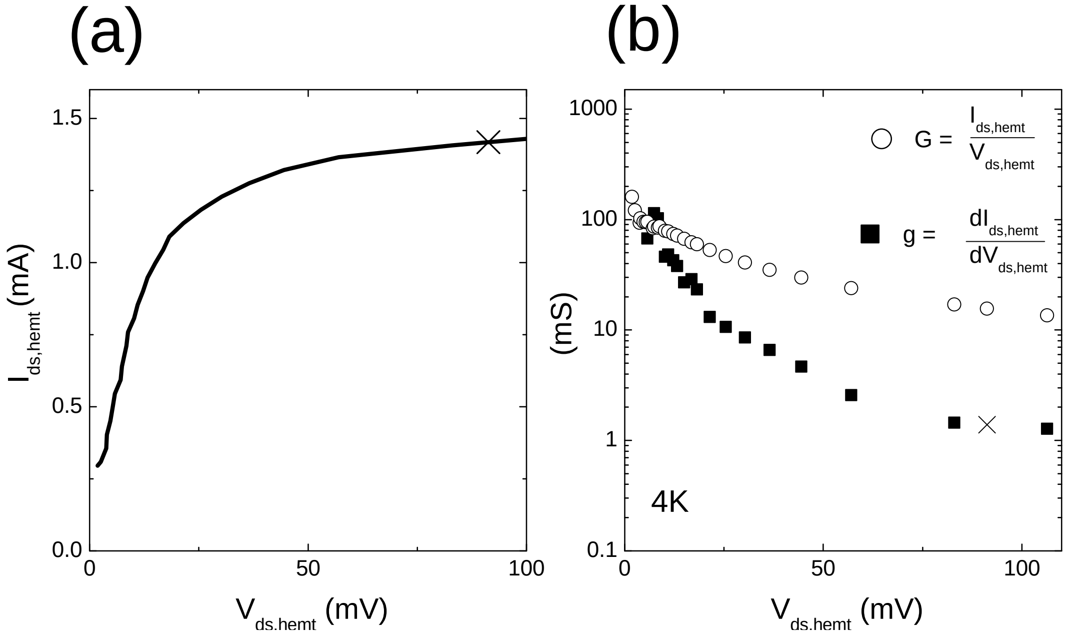

FIGURE 2.3 – On both (a) and (b), the cross marks the selected working point. (a) Drain current $I_{ds,hemt}$ as a function of drain-source voltage $V_{ds,hemt}$ for each self-polarized ATF-34143 in the 2-HEMT device. Measurement is performed in an He^4 bath. (b) Black dots represent $G(V_{ds,hemt})$ the non-linear conductance of the channel at 4K. Black squares represent the constrained differential conductance $g=dI_{ds,hemt}/dV_{ds,hemt}$.

distinguish three quantities. The non-linear channel conductance is $G(V_{ds,hemt}) \sim 16$ mS. The constrained differential conductance is $g=dI_{ds,hemt}/dV_{ds,hemt} \sim 1.4$ mS. Both are directly available from our I-V curve. Unfortunately, none is the differential conductance $g_{ds}=\partial I_{ds,hemt} \backslash \partial V_{ds,hemt}$, which would be obtained only at fixed V_g and was not measured for the proposed 2-HEMTs device. This last quantity should be in-between.

2.1.4 Crysotat thermalization

Techniques used in order to combine limited heat conduction from stage to stage and good thermalization of the electrons were fully reviewed in Julie Dubois's Phd thesis. They are not described here.

2.2 Cross-correlation

2.2.1 Cross-correlation and reliability

Starting essentially in the 90s, mesoscopic noise is now commonly measured by two techniques.

Auto-correlation

The basic rule when considering several sources of signal is that averaged power from uncorrelated systems are additive. Knowing this rule, the auto-correlation technique is straightforward. Voltage fluctuations are amplified, sampled, Fourier-transformed and averaged over time, often with a spectrum analyzer. Analog power detection is also possible, with adequate input filtering. In both case, the calibration of the noise power from all external sources allows to retrieve their contributions. With this technique and various amplification scheme, DC shot noise from QPC [121][91] or diffusive wires[138] have been measured.

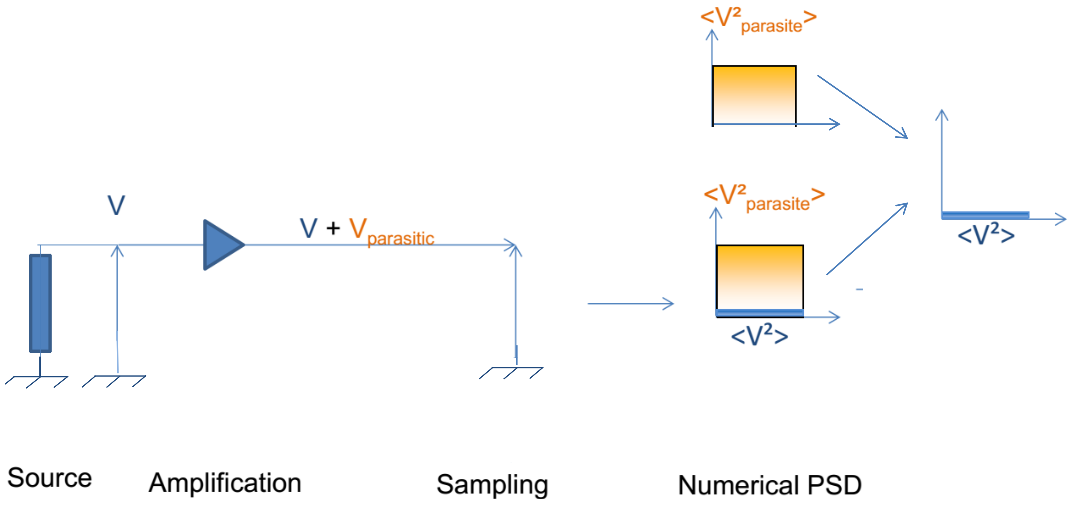

FIGURE 2.4 – Auto-correlation measurement.

Cross-correlation

Analogous to the four-point method commonly used to measure a resistance without being sensitive to the input resistance added by the connections between the voltmeter and the sample, the cross-correlation technique was introduced in order to improve the reliability of mesoscopic noise measurements. Proposed in [49], it requires two amplification lines. Voltage fluctuations are detected independently and the cross-correlated signal is computed. Uncorrelated sources affecting only one of the two lines are averaged to zero and do not require permanent calibration. This aspect is particularly useful when parasitic noise suffers from uncontrolled mid-term variations. It also reduces the impact of gain fluctuation and only noise current are correlated through the sample. When parasitic noise powers are much higher than the signal noise power, as is often the case, the signal-to-noise ratio is also reduced by a factor $\sqrt{2}$ [98]. Shot noise from QPC with integer[78] and fractional charges[126], diffusive wires[60] or chaotic cavities[108][109] were measured with this technique.

Eventually, many out-of-equilibrium noise measurements incorporate a slow time-modulation of the driving parameter. Roughly speaking, it may refer to a simple ”ON-OFF” comparison. A more elaborate possibility with sine-modulation is offered by lock-in detection of the modulated noise, as was used in [121][91].

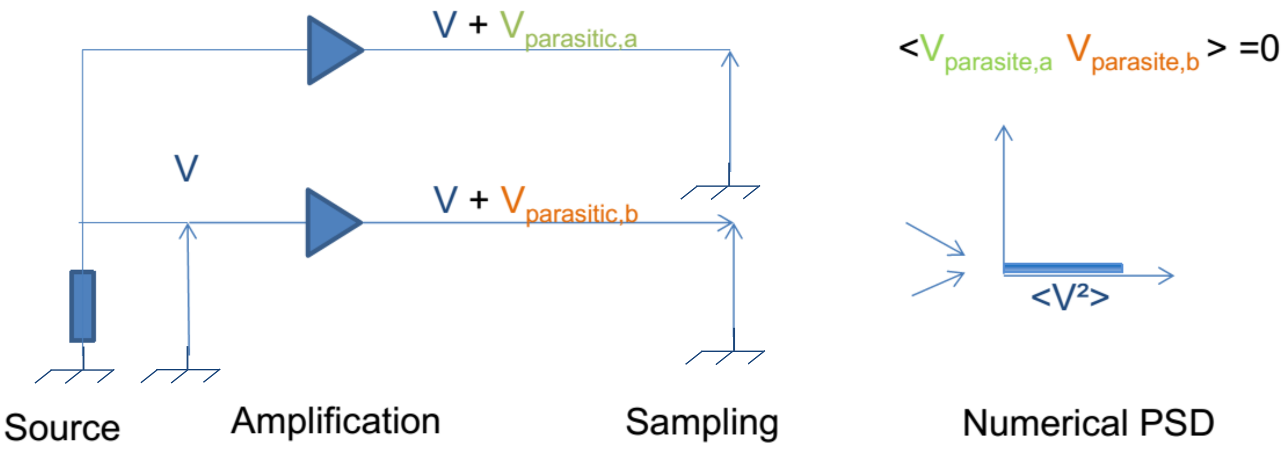

FIGURE 2.5 – Cross-correlation measurement.

2.2.2 Expression for cross and auto-correlated signal

In order to calibrate the amplification system, we follow the model in Fig. 2.6, where the details of the amplification line have been reduced to a single stage amplification. Similarly, the internal electronics of the cryo-amplifier is not represented. Both hypotheses have no consequence on the calibration. We introduce a set of new parameters to describe the cross-correlation measurement : total gains G_A,G_B and noise sources $\delta\mathrm{I}_{\mathrm{NA}}$, $\delta\mathrm{I}_{\mathrm{NB}}$, $\delta\mathrm{V}_{\mathrm{NA}}$, $\delta\mathrm{V}_{\mathrm{NB}}$. All these quantities might be frequency-dependent. The effective gains G_A,G_B also contain a capacitive part from all accumulated transmission coaxial wires and therefore have to be considered at first as complex numbers.

$$\begin{aligned} V_1 = &\quad G_A(\delta\mathrm{V}_{\mathrm{NA}} + \frac{Z_A Z_B}{Z_A + Z_B + R_S}\delta\mathrm{I}_{\mathrm{NB}} + \frac{Z_A R_S}{Z_A + Z_B + R_S}\delta\mathrm{I}_{\mathrm{S}} + \frac{Z_A(Z_B + R_S)}{Z_A + Z_B + R_S}\delta\mathrm{I}_{\mathrm{NA}}) \\ V_2 = &\quad G_B(\delta\mathrm{V}_{\mathrm{NA}} + \frac{(Z_A + R_S)Z_B}{Z_A + Z_B + R_S}\delta\mathrm{I}_{\mathrm{NB}} - \frac{Z_B R_S}{Z_A + Z_B + R_S}\delta\mathrm{I}_{\mathrm{S}} + \frac{Z_B Z_A}{Z_A + Z_B + R_S}\delta\mathrm{I}_{\mathrm{NA}}) \end{aligned}$$

Taking into account : Z_A=Z_B=Z, these equations can be simplified. We are more specifically interested in three different power amplitudes.

$$|V_1|^2 = \quad |G_A\delta\mathrm{V}_{\mathrm{NA}}|^2 + \frac{|G_A Z|^2}{|2Z + R_S|^2}(|Z|^2|\delta\mathrm{I}_{\mathrm{NB}}|^2 + |R_S|^2|\delta\mathrm{I}_{\mathrm{S}}|^2 + |Z + R_S|^2|\delta\mathrm{I}_{\mathrm{NA}}|^2 \tag{2.3}$$

$$|V_2|^2 = \quad |G_B\delta\mathrm{V}_{\mathrm{NB}}|^2 + \frac{|G_B Z|^2}{|2Z + R_S|^2}(|Z + R_S|^2|\delta\mathrm{I}_{\mathrm{NB}}|^2 + |R_S|^2|\delta\mathrm{I}_{\mathrm{S}}|^2 + |Z|^2|\delta\mathrm{I}_{\mathrm{NA}}|^2) \tag{2.4}$$

$$|\overline{V_1}V_2| = \quad \frac{\overline{G_A}G_B||Z|^2}{|2Z + R_S|^2}(Re(\overline{Z}(Z + R_S))(|\delta\mathrm{I}_{\mathrm{NA}}|^2 + |\delta\mathrm{I}_{\mathrm{NB}}|^2) - |R_S|^2|\delta\mathrm{I}_{\mathrm{S}}|^2) \tag{2.5}$$

$$\tag{2.6}$$

In the above equations, time-averaging is implicit. The first two equations define the auto-correlated signals and they are necessarily real and positive. The last one defines the cross-correlated signal. It is a real number, but only because two assumptions are verified. First we have supposed that our two resonators are identical. Second, G_A is very similar to G_B. In the experiment, the imaginary part is found to be close to zero : the phase difference is under 8°around 2.5 MHz. It was therefore completely negligible in the analysis since $\cos(8°) = 0.99$[5].

---

[5] At the same time, $\sin(8°) = 0.14$. A more accurate statement would be that the imaginary part is clearly observed, but does not add information.

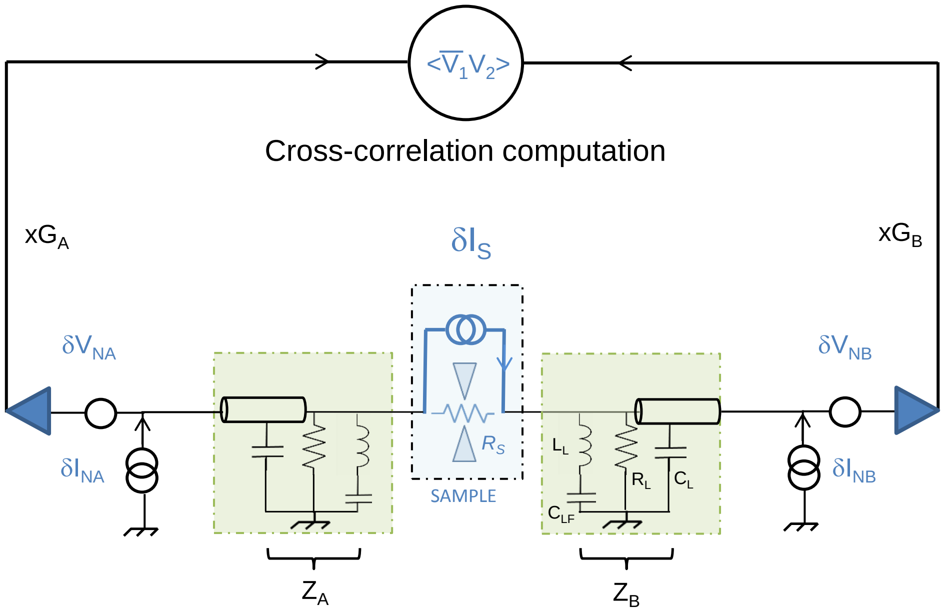

FIGURE 2.6 – Reduced model for Gain calibration.

Component	Value
R_{LF1}	47 kΩ
R_{LF2}	998 Ω
R_{LF3}	110M Ω
R_{LF4}	1M Ω
C_{LF1}	6.2 nF

TABLE 2.3 – DC and low-frequency injection circuit components.

2.3 Calibration

2.3.1 Low-Frequency : conductance measurements

Model

Fig. 2.7 and tab.2.3 detail the equivalent circuit for frequencies up to 20 kHz. The DC values of the resistors are all known, and we are left only with in-situ calibration of the product $G_{NF}G_{cryo}$. As R_{LF3}+R_{LF} $\gg$$\mathrm{R}_L$, the 497 Hz and 342 mVpp excitation $V_{LF,source}$ generates a virtually constant current $I_{LF} \sim 3.1\,\mathrm{nA}$ through the system, independent from R_S. Typically, when the the QPC is closed, this amounts to ∼8 µV on the sample, low enough to consider that we are measuring the differential conductance.

Eq. 2.7 gives the relation between R_S and the output $V_{LF,out}$.

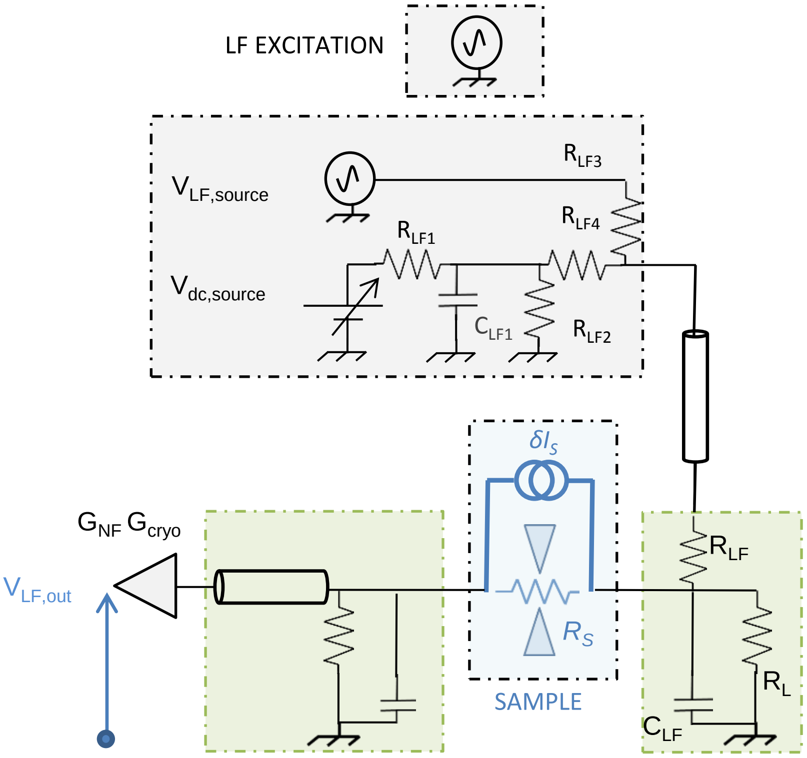

FIGURE 2.7 – Schematic representation of the low-frequency circuit. The DC tension is provided by the DAC auxiliary output of a EG&G 5210 Lock-in. The same Lock-in generates the 497 Hz $V_{LF,source}$ and extracts $V_{LF,out}$ from the amplified signal.

$$R_S(V_{ds}) = \frac{R_q}{D(V_{ds})} + R_c = G_{NF}G_{cryo}\frac{I_{LF}R_L^2}{V_{LF,out}} - 2R_L \tag{2.7}$$

R_c is the total resistance of all contacts and mesa in series with the QPC. $R_q = h/2e^2$, and $D(V_{ds})$ is the transmission. We extract $R_c \sim 450\,\Omega$ and $G_{NF}G_{cryo}$ ~720 by aligning the conductance plateau of the QPC with quantized value n/R_q. As Eq. 2.8 is linear in $1/D(V_{ds})$ and R_c, these two adjustable parameters are independent. The result is presented on Fig. 2.8.

A few technical details have to be mentioned. Facing the lack of clear plateau around $2/R_q$ and $3/R_q$, we choose to align first and fifth inflection on quantized values, as well-separated data points over the x-axis should normally reduce the error for a linear fit. Such an arbitrary choice limits the possibility for a mathematical definition of the error bar on

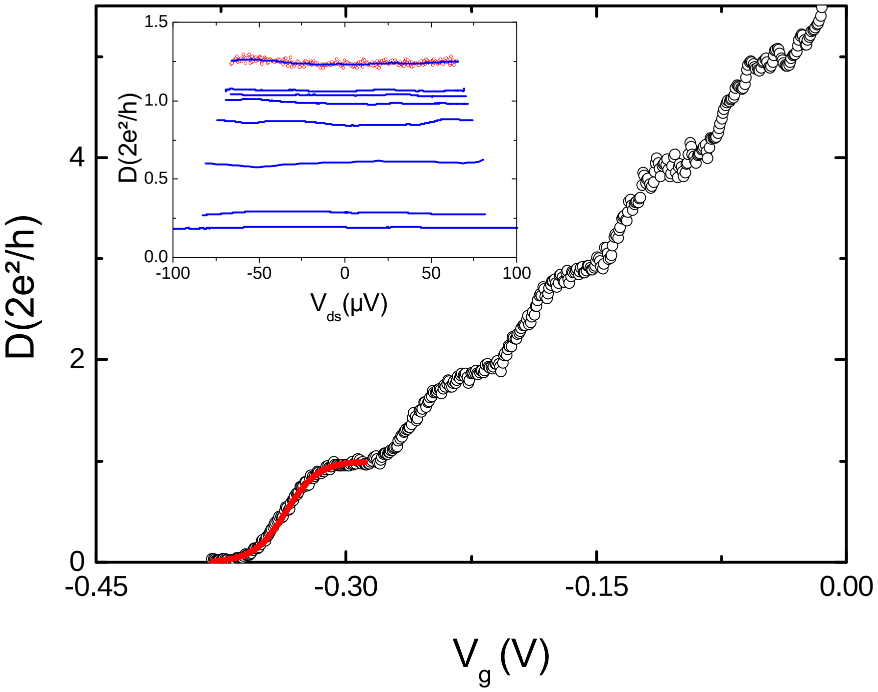

FIGURE 2.8 – (Main plot) Differential conductance measurement at zero bias for QPC "B" (black dots). Best Fit with least square method to evaluate the saddle point parameters (red line). (Inset) Differential conductance measurements under varying DC bias and fixed gate voltage (blue lines). Data sets have been smoothed : original data points for V_g=-0.267 V are displayed to illustrate the numerical treatment (red dots).

R_c. Values from 400 to 500 Ω are found satisfying. This large range does not affect the quality of the measurement of the differential conductance when $D < 1$, as the pinning of the first plateau, with a well-marked quantization, is actually self-calibrating.

Using this calibration, we measure the differential conductance under bias voltage for this sample (see inset Fig. 2.8) at a few selected gate voltage.

Saddle-point

As can be understood using the standard saddle-point model from Büttiker[23] [6] linking the energy dependence of channel transmissions and the potential geometry, short plateaus

---

[6] Also [79][50]

are usually associated with short gate constrictions. We review briefly this model. In Eq. 2.8, the electrostatic potential V_{elec}(x,y) is assumed to be governed by three parameters : the saddle-point $V_{g,\text{eff}}$, a characteristic energy describing lateral confinement $\hbar w_y$ and a characteristic scale for the barrier energy-dependence $1/\hbar w_x$. The x-direction is taken aligned with the sample. $V_{g,\text{eff}}$ is strongly associated with the gate voltage. From electrostatic considerations and the typical size of the split-gate pattern, the dependence $V_{g,\text{eff}}$ vs. V_g can reasonably be expected linear $V_{g,\text{eff}}=\beta V_g+V_0$ when displacing the gate voltage over a few plateaus only. Similarly, $\hbar w_y$-$\hbar w_x$ can often be taken as two constants.

$$V_{\text{elec}}(x,y) = V_{g,\text{eff}} - \frac{1}{2}m^* w_x^2 x^2 + \frac{1}{2}m^* w_y^2 y^2 \tag{2.8}$$

Considering free electrons, the transmission as a function of energy is found to be given by 2.9

$$D(\mathrm{E}_F + eV_{ds}) = \Sigma D_n(\mathrm{E}_F + eV_{ds}) \tag{2.9}$$

With :

$$D_n(\mathrm{E}_F + eV_{ds}) = \frac{1}{1 + e^{2\pi \frac{\mathrm{E}_F + eV_{ds} - V_{g,\text{eff}} - \hbar w_y (n+\frac{1}{2})}{\hbar w_x}}} \tag{2.10}$$

Consistent with the physics of quantum tunneling, 2.10 allows for transmission probability between 0 and 1. Short plateaus as for sample "B" appear when the barrier is smooth (small $1/\hbar w_x$) and/or confining energies are small. On Fig. 2.8, we have represented the best fit for a single plateau according to the following expression :

$$D_1(V_g) = \frac{1}{1 + exp(A(-V_g - B))} \tag{2.11}$$

Thus :

$$A = \frac{2\pi}{\beta \hbar w_x} = 103.4 \pm 0.2 V^{-1} \tag{2.12}$$

$$B = \frac{1}{\beta}[V_0 + \frac{\hbar w_y}{2}] = 336.32 \pm 0.02\$, mV \tag{2.13}$$

The energy separation between conductance channels ΔV_g, as measured using the gate values for which half integer multiple of $1/R_q$ are crossed, evolves from 80 mV to 60 mV. $A\Delta V_g/2\pi \eqsim$1.0–1.3 is an estimate of the typical ratio $\hbar w_y/\hbar w_x$. This ratio is is in agreement with the qualitative observation that plateaus are short (channel dimensions are close to the wavelength).

QPC geometry and consequences

Such a constriction is also expected to lead to a rather slow dependency $\partial D/\partial(eV_{ds})$ of the transmission with respect to electronic kinetic energy eV_{ds}, and thus displays only a limited non-linear behavior in the differential conductance under bias voltages. Still putting aside interactions, so-called self-biasing effects might reduce even further the impact of an increased (eV_{ds}) on the differential conductance for low bias.

Indeed, it was proved from conductance measurements in the presence of a bias eV_{ds} in the 1-10 mV rangethat the differential conductance tends to align with half quantum of $2e^2/h$[76][113]. This is the most visible sign that the barrier potential is affected by eV_{ds}. It may be interpreted within a simple model[50][97] as a sign of the voltage drop being symmetrical over the barrier, with the saddle point energy moving by $0.5V_{ds}$. This model predicts that $\partial D/\partial(eV_{ds})$ should be zero around $eV_{ds} = 0$. The behavior of $\partial D/\partial(eV_{ds})$ is made even more complicated by the presence of resonances or anomalies attributed to interaction[100]. But again, a short constriction tends to limit these effects.

In our case, the QPC sample "B" is about 80nm long and its design was inherited from the work of Bajjani et al. [156], for which minimization of interactions effects and 0.7 "Anomaly"[100] was intended (see also Appendix B). There is no sign of a strong zero-bias anomaly or 0.7 anomaly. Over about ±80–100 µV, the differential conductance is remarkably stable. The range D=0.2–0.3 is especially interesting, with fluctuations within $\pm 0.015/R_q$ and under ±5%.

2.3.2 DC shot Noise measurements

Model

If we consider a single noise source in parallel with the sample, all three equations in 2.5 are simplified and equivalent.

$$\frac{|\overline{V_1}V_2|}{|\overline{G_A}G_B|} = -\frac{|V_1|^2}{|G_A|^2} = -\frac{|V_2|^2}{|G_B|^2} = \frac{|Z(f_0)|^2}{|2Z(f_0)+R_S|^2}|R_S|^2|\delta \mathrm{I}_{\mathrm{S,V}_{ds}}|^2 \qquad (2.14)$$

The DC Shot Noise developed in the previous chapter is such a localized and tunable source. Its behaviour is well-established and depends on a set of universal properties : Fermi exclusion/statistics and quantum tunneling. Diffusive resistors in the hot electron regime offer a similar possibility[9]. The frequency scale over which the DC shot noise varies due to energy quantification has been verified[129][156][157]. At 10 µV (∼ 250 MHz) the amplitude difference DC–2.5 MHz is 0.1% at zero temperature, and this attenuation decreases linearly with higher bias. As the source can be considered a pure white noise, any comparison between the noise spectrum with V_{ds} switched on and V_{ds} switched off, thereafter called an ON-OFF measurement, provides the resonator shape (Fig. 2.9). The proposed best numerical fit contains three adjustable parameters :

$$P(f, V_{ds}) = \frac{A(V_{ds})}{1 + (f^2 - f_0^2)^2/(f\Delta_r)^2} \tag{2.15}$$

With :

$$\begin{aligned}
A(V_{ds}) &= |\overline{G_A} G_B| R_{eq}^2 |\delta \mathrm{I}_{\mathrm{S},\mathrm{V}_{ds}}|^2 \\
&= \text{-1.172E-15} \pm \text{6.4E-18 V}^2 \text{ /Hz} \\
f_0 &= \sqrt{\frac{1}{(2\pi)^2 L_L C_L}} = 2.520 \text{ MHz} \pm 1 \text{ kHz} \\
\Delta_r &= \frac{1}{R_{eq} C_L} = 423.6 \text{ kHz} \pm 4 \text{ kHz} \\
R_{eq} &= \frac{|Z(f_0)|}{|2Z(f_0) + R_S|} |R_S|
\end{aligned}$$

The resonant frequency f_0 and the bandwidth Δ_r are found identical for all V_{ds} over the ±90 µV Voltage range, as expected. We have neglected the line attenuation, [7] i.e. we have considered a constant gain over the frequency range 2–3 MHz. C_L is found from f_0 190 pF. From Δ_r we estimate the measurement impedance ∼2.2 kΩ, most likely reduced due to the finite resistance of L_L at f_0 (found ∼5Ω) [8]. The shape of the auto-correlation measurement in a ON-OFF situation is used as well. The two resonant frequencies are slightly different (2.49 MHz and 2.56 MHz), and the bandwidth is also about 423 kHz when the transmission

---

[7] Estimated from the asymptotic behavior of the noise away from the peak frequency to be about ±5%, expressed in % compared to the value at peak frequency. f_0 and Δ_r are found only slightly different if we use a linear correction of the Data. The difference in $A(V_{ds})$ is within the error bar. This is consistent with the Lorentzian Fit being already a very good assumption. See Fig. 2.9

[8] We also observe that C_{LF} is not entirely negligible at 2.5 MHz and acts as a slight reduction of L_L.

is $D = 0.32$ (and 406 kHz when $D = 0.2$).

Fixing the two shape parameters allows to save computation time, and increases the precision on the extracted amplitude. But the most time-efficient method is to avoid the best fit procedure and compute the average noise power over the bandwidth $f_{max} - f_{min}$. Fig. 2.10 illustrates the choice of a 1 MHz computation bandwidth and the corresponding signal-to-noise ratio [9].

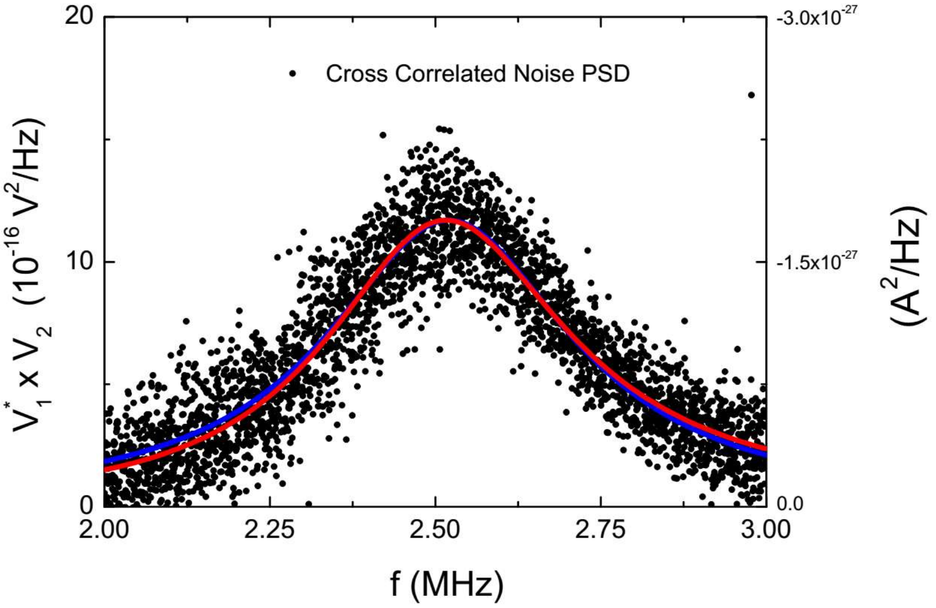

FIGURE 2.9 – Cross-correlated amplified noise spectral noise density filtered by the resonant circuit (black dots). The QPC with transmission 0.32 is biased with 90μV. The equilibrium noise spectrum has been substracted. Each data point corresponds to an average over 60000 PSD spectra. Best fit with exact shape (red curves) and Lorentzian approximation (blue curve). The original computed spectrum has a negative sign which has been removed.

DC shot Noise

Eq. 2.16 gives the ON-OFF current noise difference expected for a QPC at temperature T_e, under the bias V_{ds}, and with a transmission D.

---

[9] The averaging does not ideally represent a pure signal blurred by an independent gaussian noise. The optimum would have been with a shorter bandwidth : for $\arctan(x)/\sqrt{x}$, the maximum is at x$\sim$ 1.4. For $(\arctan(x)/\sqrt{x})/(1+\arctan(x)/x)$ it is x$\sim$ 2.7.

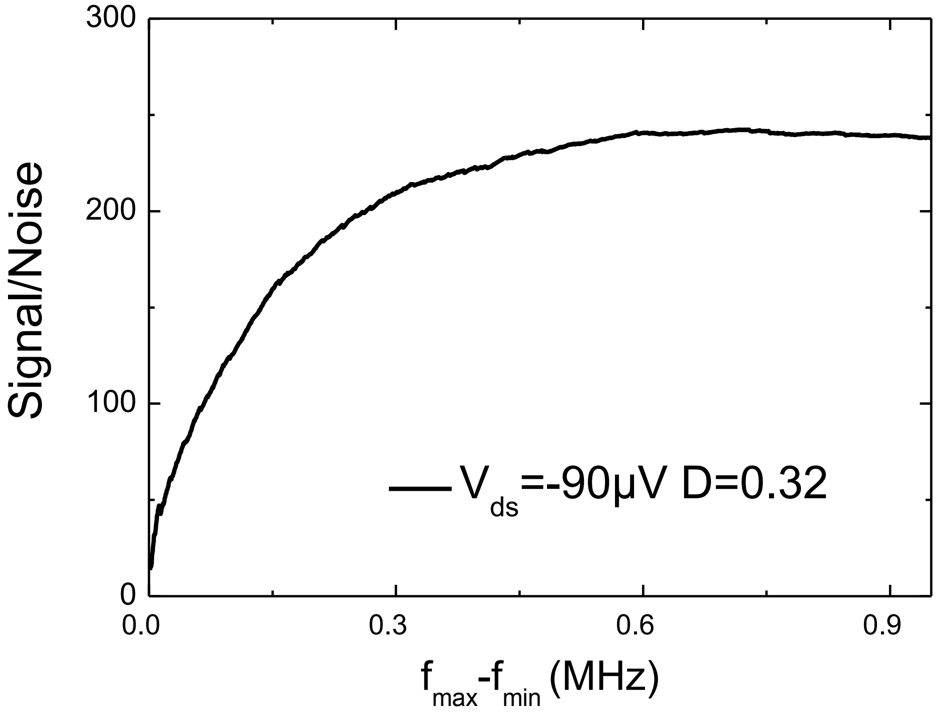

FIGURE 2.10 – Bandwidth and signal-to-noise ratio. Cross-correlated amplified noise spectral noise density is averaged over a symmetric bandwidth $f_{max} - f_{min}$ centered atf_0. This averaging defines the signal part of the ratio. The standard error from the difference between two V$_{ds}$=0("OFF") measurements defines the error part of the ratio. The QPC with transmission 0.32 is biased with 90μV. Each data point corresponds to an average over 60000 PSD spectra. This ratio is the same as the one extracted from the numerical least-square error $\approx$5E-18V^2/Hz and the peak amplitude A(V$_{ds}$) when the shape parameters are fixed.

$$|\delta \mathrm{I}_{\mathrm{S},\mathrm{V}_{ds}}|^2 = G_q D(1-D)[coth(\frac{eV_{ds}}{2k_BT_e})\frac{eV_{ds}}{2k_BT_e} - 1]4k_BT_e(V_{ds}) \tag{2.16}$$

G$_q$ denotes 1/R$_q$. D is the transmission, and is measured separately. The DC bias V$_{ds}$ is known. The (x)coth(x) dependance induces both a corner voltage which provides an accurate way to determine the temperature, and a linear regime where the noise increase is proportional to the bias. The work of Spietz and coauthor on the accuracy and universality of shot noise thermometry[135][136], illustrates this useful situation. The proportionality coefficient contains the gain : in order to separate it from the factor $D(1-D)$, two different transmissions are analysed $D = 0.20$ and $D = 0.32$ and the result is shown on Fig. 2.11.

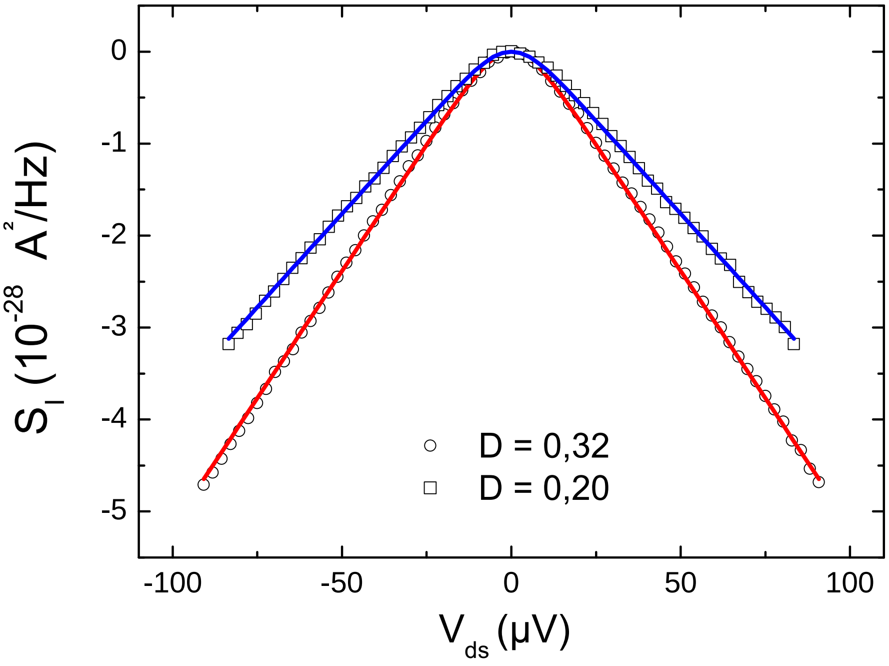

FIGURE 2.11 – Shot Noise DC with heating effect for low-transmission gain calibration. Two experimental transmissions are used $D = 0.2$ (square dots) and $D = 0.32$ (round dots). Each data point corresponds to an ON-OFF procedure and to thus twice 60000 PSD spectra. Fits with the same adjusted cross correlation gain and electronic base temperature are plotted (blue and red line). Heating effects are estimated using the model from Kumar et al. [78]

The Fit function in Fig. 2.11 takes into account small heating effects according to the formula in Eq. 2.17. Power dissipated in the sample due to Joule effect at the tunnel barrier and along the mesa flows to the two contacts where the electrons are maintained at the base electronic temperature. The non-equilibrium temperature $T_e(V_{ds})$ is reached in the vicinity of the constriction and governs the reservoirs distribution.

$$T_e(V_{ds}) = \sqrt{T_e(V_{ds} = 0)^2 + \alpha_{WF} V_{ds}^2} \tag{2.17}$$

The thermal conductance slowing down the output energy flow can be estimated from the measured electric resistance using the Wiedemann-Franz law. Equating output energy and Joule dissipation provides the temperature profile and the peak value at the constriction for all V_{ds}. According to the model introduced by Kumar et al. [78], we have :

$$\alpha_{WF} = \frac{6e^2}{\pi^2 k_B^2}\frac{R_c D G_q}{4}(1+\frac{R_c D G_q}{2}) \tag{2.18}$$

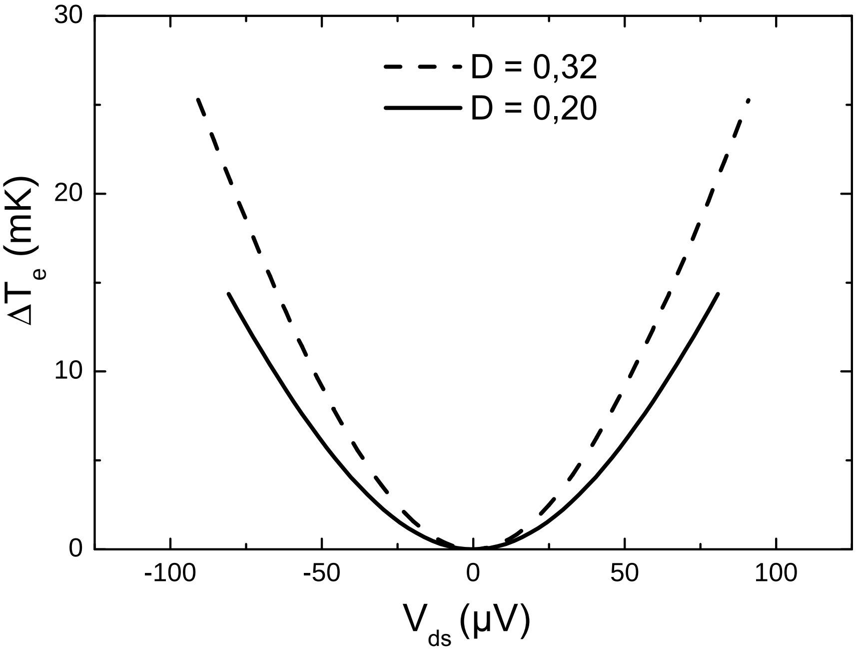

FIGURE 2.12 – Electron heating in noise calibration.

The cusp around V_{ds} =0 in Fig. 2.11 leads to a base electronic temperature of 35mK. The temperature increases corresponding to Eq. 2.17 are plotted on 2.12. We note that the excess noise calculated at 90 μV for $D = 0.32$ in those conditions is almost the same as a zero temperature theory $2eI_{ds}(1-D) = 4.9\text{E-}28\text{A}^2/\text{Hz}$. At the same time $4k_B\Delta T_e(V_{ds})G_q D$ $=3\text{E-}29\text{A}^2/\text{Hz}$. It means that $\sim$ 6% of the noise increase along V_{ds} is attributed to a change in the temperature, or equivalently that the gain is ∼3% lower in this model than without heating effects. The agreement between the two slopes and the measured factor $D(1-D)$ is good, and no additional fitting parameter[118] has to be included to take into account the 0.7 transmission "anomaly". This was expected both from the successive works of Roche et al.[123] and DiCarlo et al.[33] with such low transmissions, and the absence of clear 0.7 signature in the conductance.

$|\delta \mathrm{I}_{\mathrm{S},\mathrm{V}_{ds}}|^2$ and the measured PSD can now be interpreted and the cross-correlation gain $\overline{G_A}G_B$=613542 is retrieved. Using an Anritsu 69147B sine source, the post-amplification is observed separately (Appendix E). Thus -$\sqrt{\overline{G_{A,cryo}}G_{B,cryo}} = -4.6\,\mathrm{V/V}$ at the resonant frequency.

2.3.3 Johnson-Nyquist (JN) equilibrium noise measurements

Method

We check the consistency of the previously determined parameters (electronic temperature, measurement resistance, and gain) with Johnson-Nyquist (JN) equilibrium noise measurements. The QPC is at $D = 1$ to minimize the noise impact of any unwanted voltage perturbation on the sample. There are two difficulties. One is to separate thermal noise from the amplification noise. To do so, we consider again an "ON-OFF" experiment, and compare noise increases $\Delta|I(T_{RuO_2})|^2$ when biasing at different powers a heat source resistor (electrically separated from the sample circuit) situated on the 12.5 mK stage of the cryostat. We label each spectrum with the temperature measured with the already mentioned calibrated thermometer close to the cold fingers (Fig. 2.13 and 2.14).

The second difficulty is the weak link between the temperature at the cold fingers and the electronic temperature in the sample. Below 100 mK, phonons are extremely rare, and the dielectric insulators needed for electrical insulation impose a long thermal length. The electronic temperature decouples from the rest of the system and plateau above the cryostat base temperature. While stable at first, the noise increase is linear with the temperature rise ΔT_{RuO_2} when the coupling is restored. On Fig. 2.15, the asymptotic behavior of $\Delta|I(T_{RuO_2})|^2$ indicates a corner temperature at 34 mK, to be compared to the 35 mK temperature extracted from the shot noise.

Model

We make the assumption that the measurements resistors are at the same temperature than the mesoscopic resistor[10]. Eq. 2.5 for the"ON-OFF" JN measurements simplifies to :

---

[10] This assumption, based on the short distance between the components, has been indirectly confirmed thanks to the small CMS heating from Joule effect analysed in appendix C

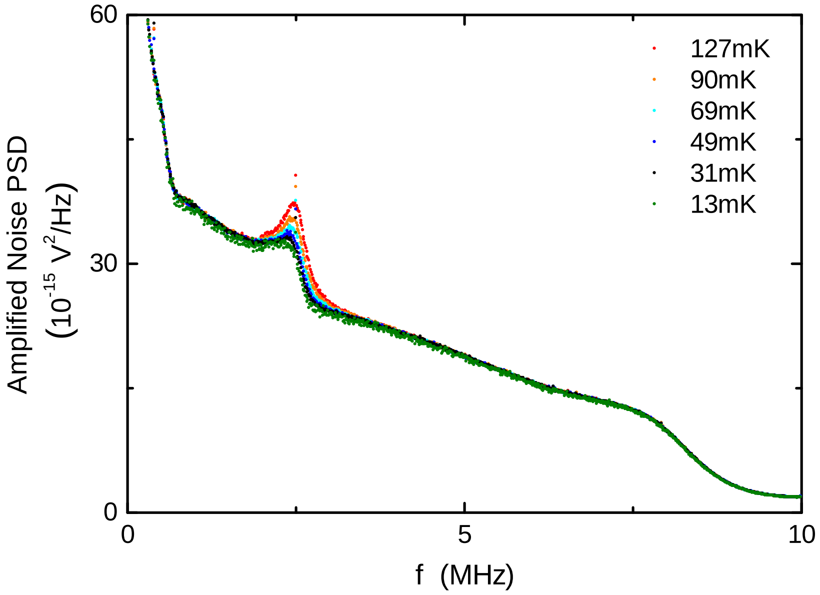

FIGURE 2.13 – Noise Increase with temperature evolution. Auto-correlation spectra from measurement line 1.

$$\frac{|V_1|^2}{|G_A|^2} = \frac{|V_2|^2}{|G_B|^2} = 4k_B\Delta T_e R_{eq,2} \tag{2.19}$$

With :

$$R_{eq,2} = Real(\frac{Z(Z+R_S)}{2Z+R_S}) \tag{2.20}$$

The peak value is extracted with a Lorentzian best fit (Fig. 2.16 and 2.17)). Resonant frequency and bandwidth confirm the parameters of the RLC, with again a constant shape for all measurements with the fixed transparency $D = 1$. A constant ratio 1.29 is found between peak values $|V_1|^2$ and $|V_2|^2$. This ratio is exactly the one observed when comparing amplification noise levels outside the resonant bandwidth (2.22). Thus $G_B = \sqrt{1.29}G_A$. We can now compare the temperature evolution from ΔT_{RuO_2} and ΔT_e in 2.19. The clear observed agreement confirms the gain extracted from the DC Shot Noise (See Fig. 2.18).

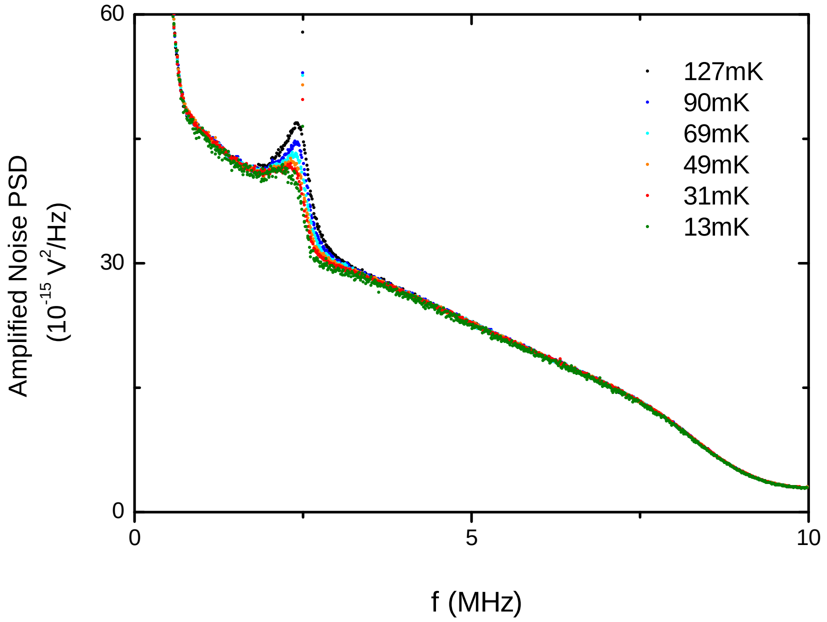

FIGURE 2.14 – Noise Increase and temperature evolution. Auto-correlation spectra from measurement line 2.

2.4 Data acquisition and real-time treatment

As already mentioned, the two output signals V_1 and V_2 (see Fig. 2.1) are DAC converted simultaneously and PSD spectra are computed. We use a 8-bit 50 mV-input-range digitizer from Agilent Instruments (Acquiris U1071A-HZ4) with a PCI-Express port and operate at a rate 20 MS/s. As long as the acquisition rate is superior to twice the top frequency of the resonator bandwidth, there is no additional gain in information. In our case, the Nyquist frequency 10 MHz is set to match the filter band pass and thus avoid aliasing. The memory size for each of the channel is twice N_s=65472 data points divided into two blocks : one can be read and processed while the other stores new incoming data. As long as we can treat the data fast enough, it allows for real-time continuous acquisition. The transfer rate of the PCI-Express port is not a limiting factor.

Time-consuming numerical operations are FFT-calculations and results saving. A C++ software program treats each block $V_1(t_i)/V_2(t_i)$ of N_s data. First, the FFT algorithm from the FFTW package[43] calculates the Fourier spectrum. Second the four PSD (both auto-

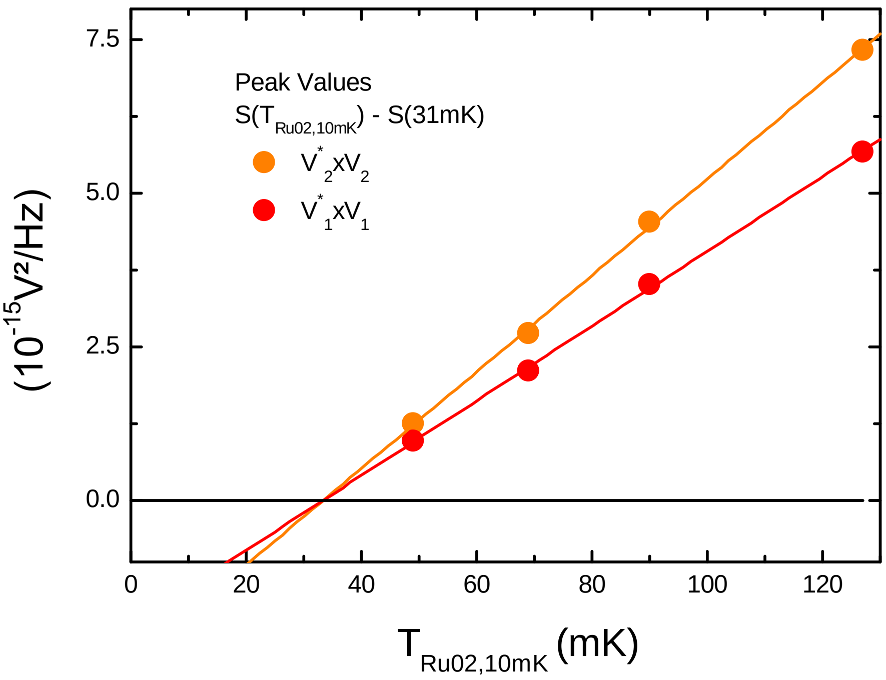

FIGURE 2.15 – Asymptotic behavior of the equilibrium noise and cryostat temperature.

correlations, real and imaginary part of cross-correlation) are computed for a selected N$_{PSD}$ number of frequency data points and N_{av} spectras are accumulated to provide the statistical average over time. The treatment duration for a single set of PSD spectras falls behind the acquisition time ∼3.3 ms when we save only the frequency points within 2 MHz around the resonant frequency (N$_{PSD}$=6600). This band, more than twice the RLC measurement circuit, is large enough to analyze simultaneously the signal from the sample (N$_{PSD}$=3240, 1 MHz around f$_0$, see Fig. 2.10) and the amplification stability from the noise background. Averaging over typically 20000 PSD (∼70 s), the procedure takes about 3% longer than the pure data acquisition. The frequency resolution is then 305 Hz. Test PSD spectra have been compared for consistency with the outputs of a HP89410A DC-10 MHz Vector Signal Analyzer.

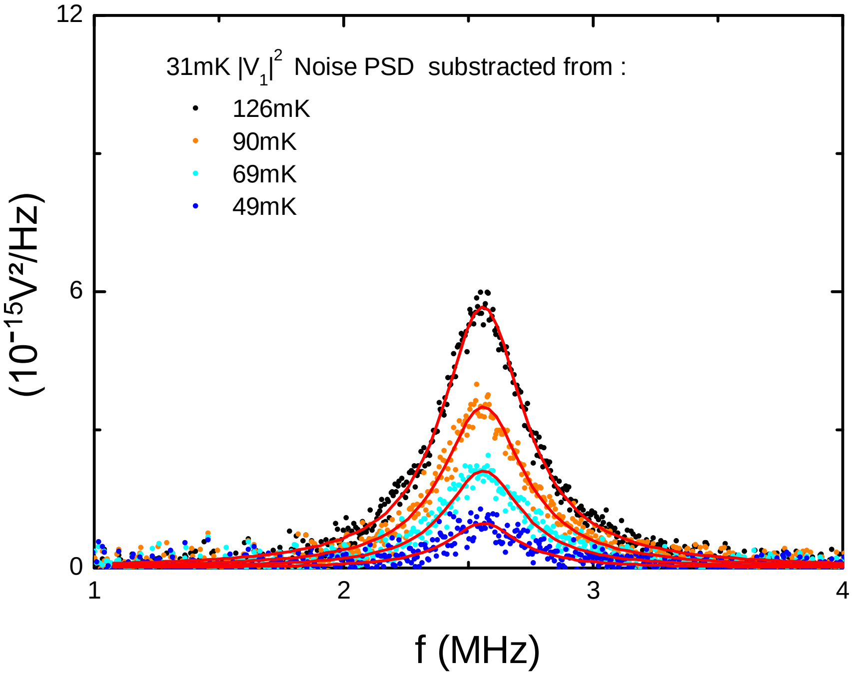

FIGURE 2.16 – Noise Increase and Heating. Measurement Line 1.

2.5 Benefits of parallel transistors

2.5.1 Transistor Parallelism

”Parallelizing” mutiple transistors is a common technique to improve the sensitivity of an amplification system while starting with an already available object. Examples of this situation at low-temperature have already included in the past a very large set of components : MESFETs [83], MOSFETs [74], rf-SETs [58] and a similar result exists for instance for SQUIDs [150], this time in series. Two main ideas are common to several of these works.

When exciting and measuring a sample in a sub-kelvin cryostat, the distance between the sample and room-temperature electronics can rapidly extends beyond 1 m. When the sample impedance is close to the quantum conductance $\approx 13\,\mathrm{k}\Omega$, the RC time constant generated by the coaxial line and various instruments input capacitance drops to a hundred of kHz. ”Passive” impedance matching, simply adding a smaller resistor in parallel with the sample has limited interest as it linearly reduces output voltage amplitude, thus cancelling

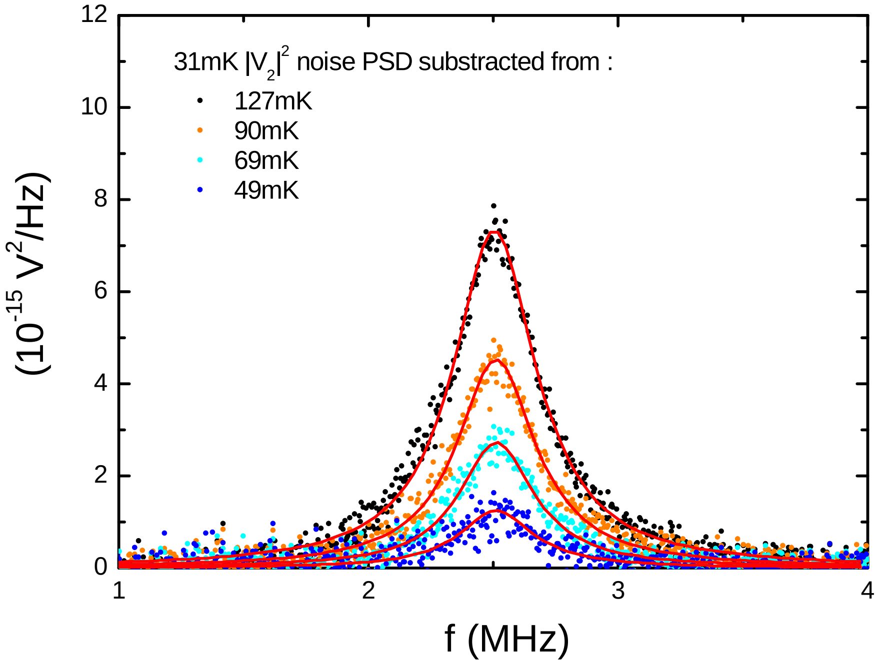

FIGURE 2.17 – Noise Increase and Heating. Measurement Line 2.

the larger available bandwidth[11]. Properly designed active devices have to be used to decouple input and output impedances. The other aspect of interest is the possibility to improve the noise performances. Both ideas have to be considered in the limitations associated with power consumption and space use in a cryostat.

2.5.2 Small signal model

To study how parallel transistors can allow for better sensitivity, we use a standard small signal model [63][149].

Fig. 2.19 represents the two most basic situations : a single HEMT compared to two HEMTs. All transistors are supposed identical and operate at a single working point described by the two intrinsic parameters : the transconductance $g_m = \partial I_{ds}/\partial V_g$ and the channel differential conductance $g_{ds} = \partial I_{ds}/\partial V_{ds}$. A signal source δI_0 generates a voltage over an input resistance Z_{RLC}. Noise sources from the HEMTs are divided in two categories : a first

---

[11] Still, an optimum value for a passive parallel resistance might exist if you consider the competition between the two kinds of amplifier noise sources : current sources and voltage sources.

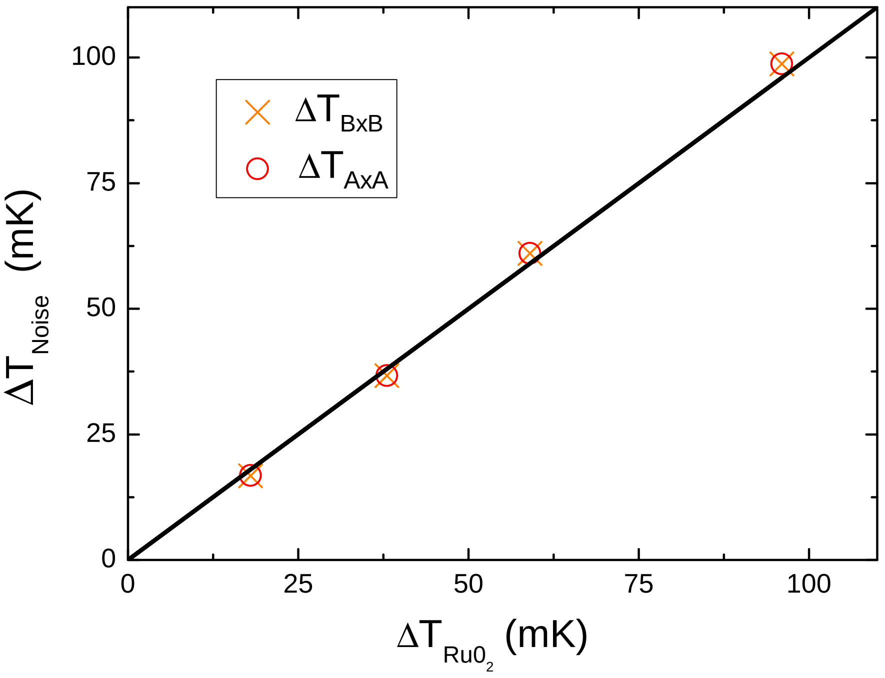

FIGURE 2.18 – Jonhson Nyquist noise temperature and thermometry.

noise current at the input δI_{N1} (δI_{N2}) and a second at the output δI_{V1} (δI_{V2}). The latter type of noise source can equally be represented by an input voltage source, as is often the case in commercial amplifiers Data Sheet. The circuitry shows a few obvious simplications. First, the output conductance has doubled for the 2-HEMT device and it can easily be inferred that the N-HEMT device will lead to a conductance Ng_{ds}. On the contrary, the input impedance is unchanged. Taking into account all sources, we can write Eq. 2.21 and compare the output voltages V_{out}, $V_{out,p}$.

$$V_{out} = A_{hemt}(Z_{RLC}(-\delta I_0 + \delta I_{N1}) + \frac{\delta I_{V1}}{g_m}) \tag{2.21a}$$

$$V_{out,p} = A_{hemt}(Z_{RLC}(-\delta I_0 + \delta I_{N1} + \delta I_{N2}) + \frac{\delta I_{V1} + \delta I_{V2}}{2g_m}) \tag{2.21b}$$

A_{hemt}, the intrinsic HEMT gain g_m/g_{ds}, appears identically in both equations and from this point of view, the choice of parallelizing transistors is neutral. This is because all cur-

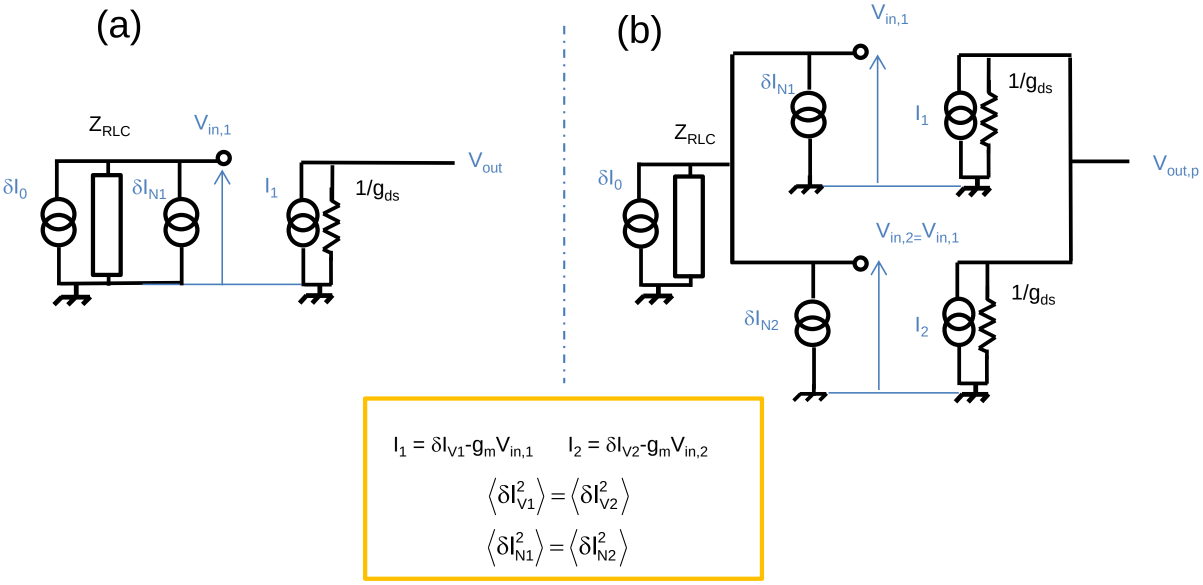

FIGURE 2.19 – Small signal model for ideal HEMT, with signal source and noise sources. (a) Single HEMT. (b) Two parallel HEMTs. (δI_{V1}, δI_{V2}) are independent drain-source, or channel, current noises. Drain-source currents can be converted in voltage noise source at the input, or input-referred voltage noise. (δI_{N1} , δI_{N2}) are indepedent gate-source current noises. The minus sign in terms $-g_m V_{in1,in2}$ reflects the "common source" geometry of the circuit.

rents from all HEMTs are phase-correlated. Taking the time-average power then provides Eq. 2.22 in which uncorrelated products have disappeared and power equality for noise sources has been considered.

$$< V_{out}^2 > = A_{hemt}^2 (Z_{RLC}^2 (\delta I_0^2 + < \delta I_{N1}^2 >) + \frac{\delta I_{V1}^2}{g_m^2}) \tag{2.22a}$$

$$< V_{out,p}^2 > = A_{hemt}^2 (Z_{RLC}^2 (\delta I_0^2 + 2 < \delta I_{N1}^2 >) + \frac{1}{2} \frac{< \delta I_{V1}^2 >}{g_m^2}) \tag{2.22b}$$

Starting with the comparison between Eq. 2.22(a) and 2.22(b), we can directly generalize the behaviour to a N-HEMTs device : noise power from current sources at the gate adds linearly, while noise power from channel sources follow a 1/N reduction. If the input-refered amplitude are equal, there is no interest in parallelisation. But, for a GaAs/AlGaAs heterostructure, the competition is more favourable to channel noise than gate noise. For instance, in [34], it was observed that no current noise from a single ATF-34143 could be seen when working with an input resistor of 2.5 kΩ at 290 mK (i.e. an additional 6.4E-27 A^2/Hz source, or 4E-20 V^2/Hz). At the same time, they report an estimate of 1.6E-19 V^2/Hz for input-referred channel noise. Considering the geometry of an ATF-34143 (gate area) and the 4 K temperature the two main gate-source current noise (leakage current and input impedance thermal noise) are indeed expected to be extremely small. Also implementing an ATF-34143, coworkers in [122] report 6.25E-28 A^2/Hz for gate noise and 4.9E-19 V^2/Hz for input-referred channel noise. Although noise generation is sensitive to the details of the implementation, parallelisation appears favourable. If the latter performances are reproduced with again a 2.5 kΩ impedance, up to 11HEMTs might be used.

For statistical measurements, it would mean a critical $1/\sqrt{11}$ reduction in measurement time.

2.6 System Performances

2.6.1 Electronic effective temperature

Helium-free cryostat combining pulse tube cryocooler and $\mathrm{He}^3/\mathrm{He}^4$ dilution stage to reach temperature down to 10mK have recently become more common. The possibility to maintain the cryostat base-temperature for arbitrarily long-time without operations forcing to stop the measurement is an obvious advantage when planning statistical analysis of large data-sets. But questions about electrical noise and mechanical vibrations in this new generation of systems have attracted attention. In the very same cryostat used in our current experiment, but with noise acquisition over a DC-200 kHz bandwidth and no cryogenic amplification stage, it was reported in 2012 by Julie Dubois[37] that the noise level observed over the kHz range (Fig. 2.20) in a cross-correlation PSD in this band was evolving synchronously with the rotary valve cycle.

Fig. 2.21 reproduces the results from her experiment. The rotary valve (Pulse Tube PT410 from Cryomech) cycle has a duration 660 ms and a clear peak in sound level can be used to trigger the acquisition card with a microphone. A more detailed DC Shot Noise experiment in the time window (about 100 ps) where the noise power was found at its lowest leads to ∼70 mK, compared to 110–120 mK for an experiment in normal conditions.

The introduction of cryo-amplifiers has coincided with a much lower electronic temperature 35 mK. The two observations are most likely to be correlated.

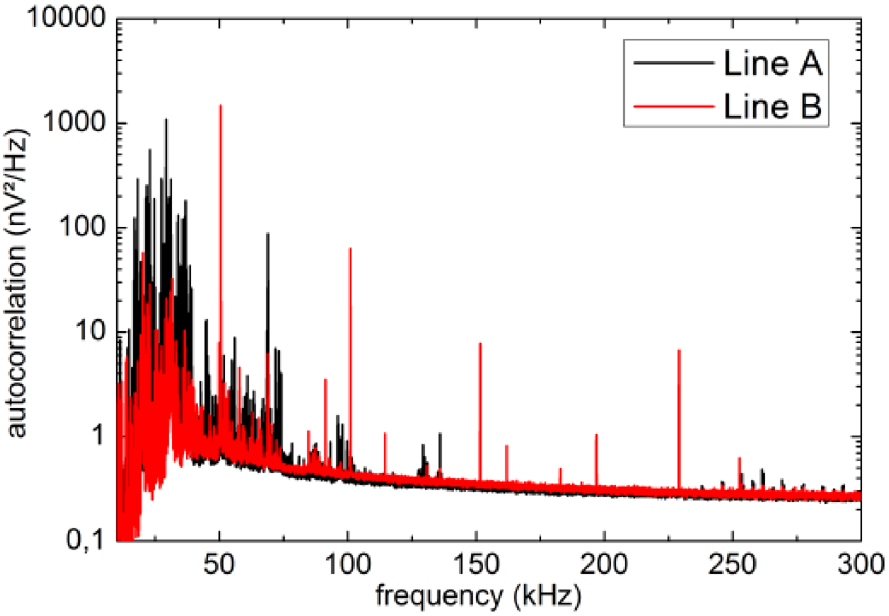

FIGURE 2.20 – Full Auto-correlations spectrum showing the amplified spectral noise density for acquisition line A (black) and B (red) with a full room-temperature amplification system (gain∼80000) and DC–200 kHz in the Cryoconcept Helium-free cryostat. Almost all peaks in the DC–50 kHz band were observed to disappear when the cryocooler was turned off. From [37].

If there is a slow random voltage bias, with a probability distribution P(V$_{parasite}$), Σ_VP(V$_{parasite}$)SN(V$_{parasite}$+V$_{ds}$) becomes the DC Shot Noise observed, where SN(V) is a short notation for the noise at DC bias V. As shown in [142], where the problem was studied for a STM this type of fluctuations appears as an higher electronic temperature. There is also the possibility for this noise power to dissipate energy. Both phenomena are prevented here because the range 6 kHz–100 kHz is grounded near the sample. To date, no experiment equivalent to the one undertook by J.Dubois has been conducted to verify the presence or absence of dependence with the slow driving of the rotary valve. The set-up electronic temperature now compares well with other noise measurements systems with broad band radio-frequency coaxial lines[156][44][94][130].

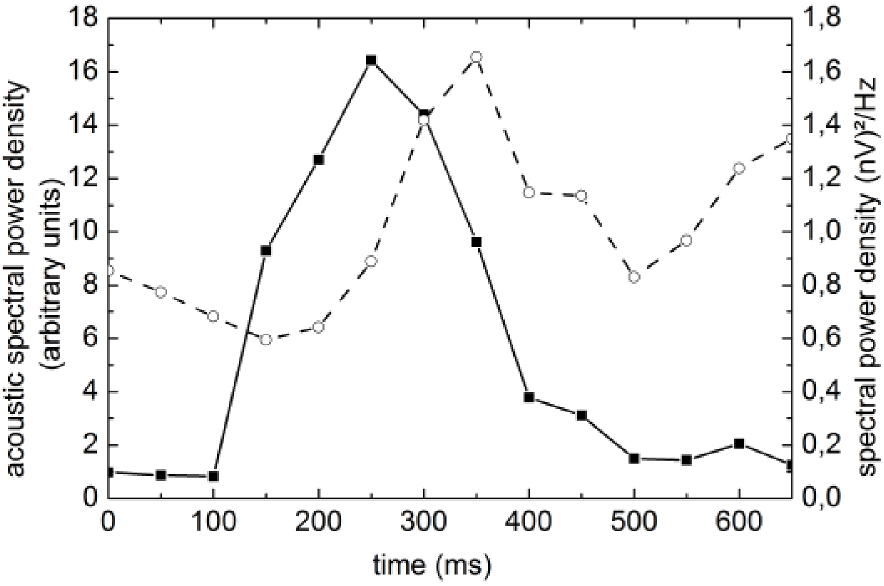

Figure 2.21 – Noise level over the band 1–20 kHz measured during a 65 ms time-window at different start time compared to the rotary valve cycle. (Dash line) Acoustic noise power of the pulse tube system. (Solid line) Amplified PSD averaged over a 65 ms time-window at different start time and measured from line B[37].

2.6.2 Input-referred voltage noise

Full auto-correlation PSD spectra with a pinched-off QPC (infinite resistor) are represented on Fig. 2.22. The inset emphasizes the low-frequency 100Hz–100kHz amplitude. From the model 2.6 and the corresponding set of equations 2.5, currents from the amplifier or the measurement resistor do not participate outside the resonator bandwidth. The total input-referred voltage noise is $0.26\,\mathrm{nV}/\sqrt{\mathrm{Hz}}$ at 2 MHz and $0.22\,\mathrm{nV}/\sqrt{\mathrm{Hz}}$ at 3 MHz. In both cases, the gain at 2.5 MHz is used for all frequencies with no attempt to compensate for the change in line capacitive filtering[12].

The white noise contribution from the post-amplification, about 8.5E-15 V^2/Hz can be extracted to obtain a proper picture of the cryo-amplifier performance. The difference in amplitude between line A and B is perfectly explained by the gain difference observed during the noise calibration Fig. 2.23. Using the mean value between the two extremities

---

[12] The slope in Fig. 2.22 is the signature of this capacitive effect.

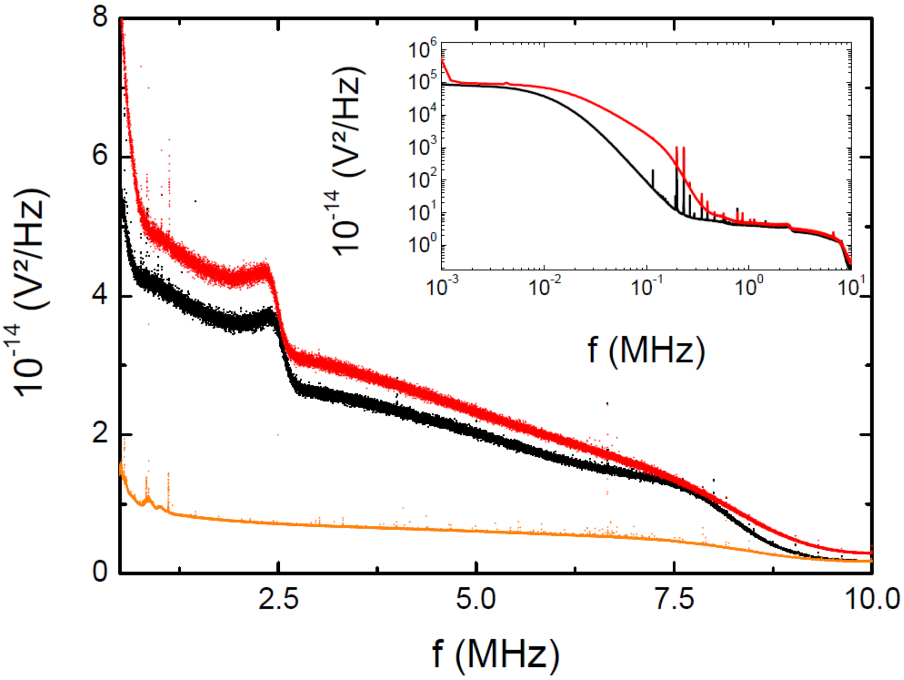

FIGURE 2.22 – Full auto-correlations spectra showing the amplified PSD for acquisition line 1 (red dots) and 2 (black dots). Each data point is an average over 5000 PSD spectra. Inset shows the low-frequency noise affecting low-frequency measurements. The QPC is kept pinched. Voltage-noise added by post-amplification with the commercial amplifiers is plotted for comparison (orange dots). Measured with 50000PSD spectra and a short circuit at the input.

of the resonance, the noise source is found to be $\sim$0.21 nV/$\sqrt{\text{Hz}}$.

To date, there is no available single-HEMT device at the same polarisation point and inserted in the same circuit, and this ultra-low noise level cannot be directly compared to the expected noise reduction $\sqrt{2}$ described in part 2.5. But many experimental details reported in[34]-final gain,polarization configuration, measurement frequency—which was also the basis for this work are close. They estimated the amplifier noise with a single ATF-34143 to be $\sim$0.4 nV/$\sqrt{\text{Hz}}$. Additionally, some geometries with more transistors have been fabricated, with a voltage-noise as low as $\sim$0.12 nV/$\sqrt{Hz}$ with 10 HEMTs. This last result strongly indicates that the origin of the noise reduction is the parallelism (see Appendix F for details about design and measures).

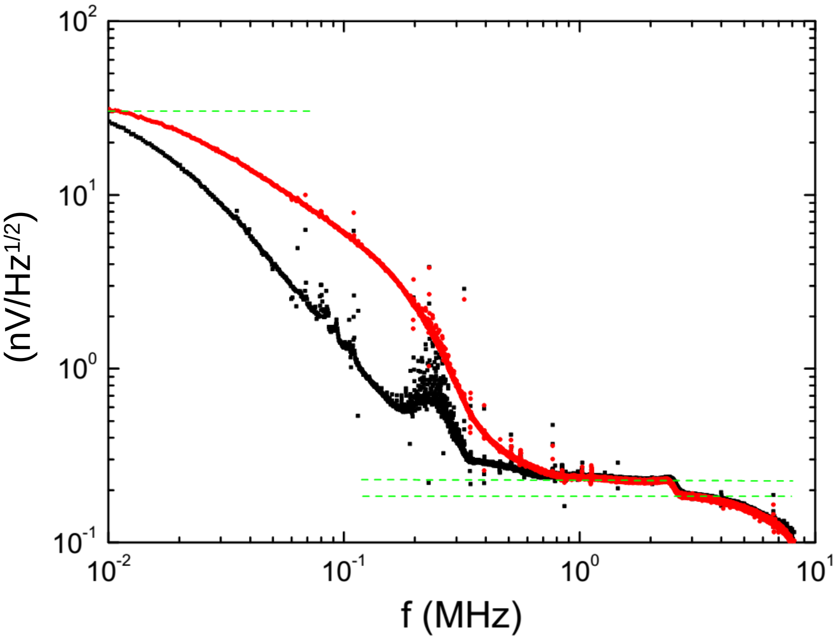

FIGURE 2.23 – Input-referred noise spectrum from 2-HEMT cryoamplifiers, for acquisition line A (red) and B (black). Dashed green lines mark the noise level at the boundaries of the resonance, where no noise current is present.

2.6.3 Resolution and integration time.

Voltage fluctuations from the amplification dominate the auto-correlation PSD spectrum in the MHz range. The histogram of the cross-correlation measurement data points after accumulating N_{av} PSD spectra is thus governed by their amplitude. Fig. 2.24 represents these histograms for the frequency data points in the cross-correlation equilibrium spectrum with $D = 0.32$ in the 2 MHz–3 MHz band for N_{av}=20000 and 40000 ($\sim$65 s and $\sim$110 s). As the noise would adopt the shape of the resonator for a single spectrum, we obtain an homogeneous measurement around zero by computing the difference $\Delta NoisePSD$ between two successive acquisitions. The standard deviation $\sigma_{i,j}$ behaves (see Tab. 2.6.3) according to :

$$\sigma_{1,2} = \sqrt{\frac{\sigma_{1,1}\sigma_{2,2}}{2}} \tag{2.23}$$

$\sigma_{i,j}$ is the standard deviation for the quantity $|V_i^* V_j|$, i and j being 1 or 2. In addition, $\sigma_{i,j}$ is well predicted from the total input-referred noise $0.24\,\mathrm{nV}/\sqrt{\mathrm{Hz}}$ as the amplitude and

$1/\sqrt{\mathrm{N}_{av}}$ as a reduction over time.

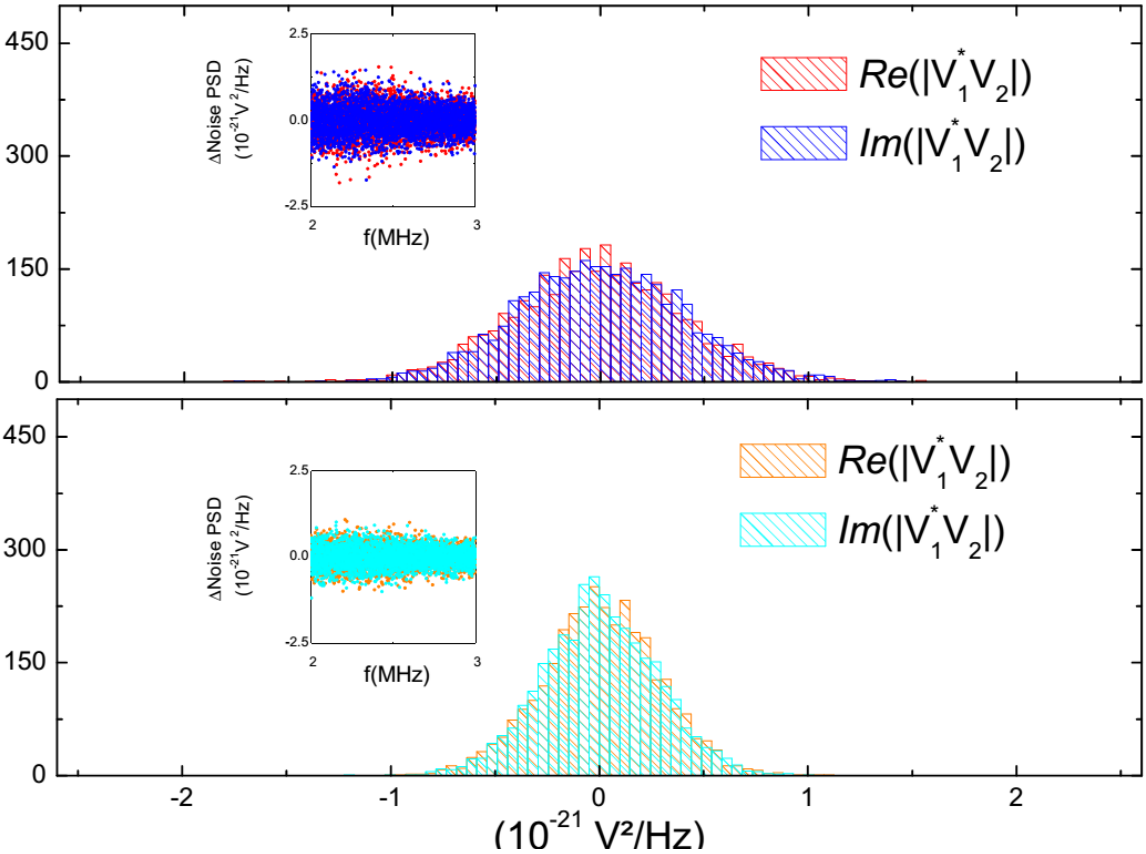

FIGURE 2.24 – Histograms of cross-correlation ON-OFF measurement with N_{av}=20000 (top part) and N_{av}=20000 (bottom part), and real (red-orange dots) and imaginary (blue-cyan dots). Data points are obtained from the difference $\Delta NoisePSD$ of two successive measurements in identical conditions (Insets). All results are input-referred to eliminate gain discrepancies.

Under those conditions, a source noise 1E-29A^2/Hz can be resolved with 680 spectra or in ∼2.2s.

2.6.4 Accuracy and ”ON-OFF” procedure

The ”ON-OFF” procedure takes twice this time while the error is multiplied by $\sqrt{2}$. Indeed, it requires two independent spectra instead of one. So 2.2 s×4 ∼ 8.8 s should be necessary to obtain the same error bar. However, the procedure is interesting because it maintains the statistical consistency of the results for long measurements. This is illustra-

Measurement	$\sigma_{i,j}$ N$_{av}$=20000	$\sigma_{i,j}$ N$_{av}$=40000
$\|V_1^* V_1\|$	5.8E-22	4.2E-22
$\|V_2^* V_2\|$	5.5E-22	3.8E-22
$Real\|V_1^* V_2\|$	4.1E-22	2.8E-22
$Im\|V_1^* V_2\|$	4.0E-22	2.8E-22

TABLE 2.4 – Standard deviation of ON-OFF measurement with N$_{av}$=20000 and N$_{av}$=20000. Data points are obtained from the difference $\Delta NoisePSD$ of two successive measurements in identical conditions. All amplitudes are input-referred in V^2/Hz to eliminate gain discrepancies.

ted in Fig. 2.25 by the repetition (∼160 times) of a typical PASN single measurement over ∼24 hours.

We are interested in the noise difference Δ_{ON-OFF} due to an additional voltage periodic pulse (”ON”) compared to a DC bias alone (”OFF”). While external controls are left unchanged, the base line clearly undergoes random, small and slow drifts. Whatever the source of change, in terms of relative deviation, it is limited : typically 0.25% with extreme change topping at 1.5%. But a huge bias is generated by the fact that the ”OFF” spectrum is two orders of magnitude bigger than Δ_{ON-OFF}. For instance, comparing absolute values at ”t∼0” for the ”OFF” spectrum and at t∼10 hours for the ”ON” spectrum, we might grossly underestimate Δ_{ON-OFF}. On the other hand, the precision is mechanically increased by the number of acquisitions, leading to a false feeling of accuracy. The ”ON-OFF” procedure strongly reduces this effect.

We propose a test to evaluate the choice of the slice size : N$_{av}$ ∼20000–50000 spectra. The variable to be followed is $|\Delta|\Delta_{ON-OFF}||$, the difference between two successive values of Δ_{ON-OFF}. As reported in Fig. 2.25, the accumulated error remains within the error bar and shorter slices are not needed to maintain the uncertainty close to the intrinsic level, determined by the relative amplitude of the drifts.

2.6.5 Current noise

We study equilibrium spectra. Following again Eq. 2.5 and the model in Fig. 2.6, we make the final assumption that any noise power not explained by Johnson-Nyquist thermal noise from one of the RLC and the sample or voltage fluctuations from the amplifiers observed outside the bandwidth is due to one of the noise source I$_{\mathrm{NA}}$ or I$_{\mathrm{NB}}$ From equilibrium

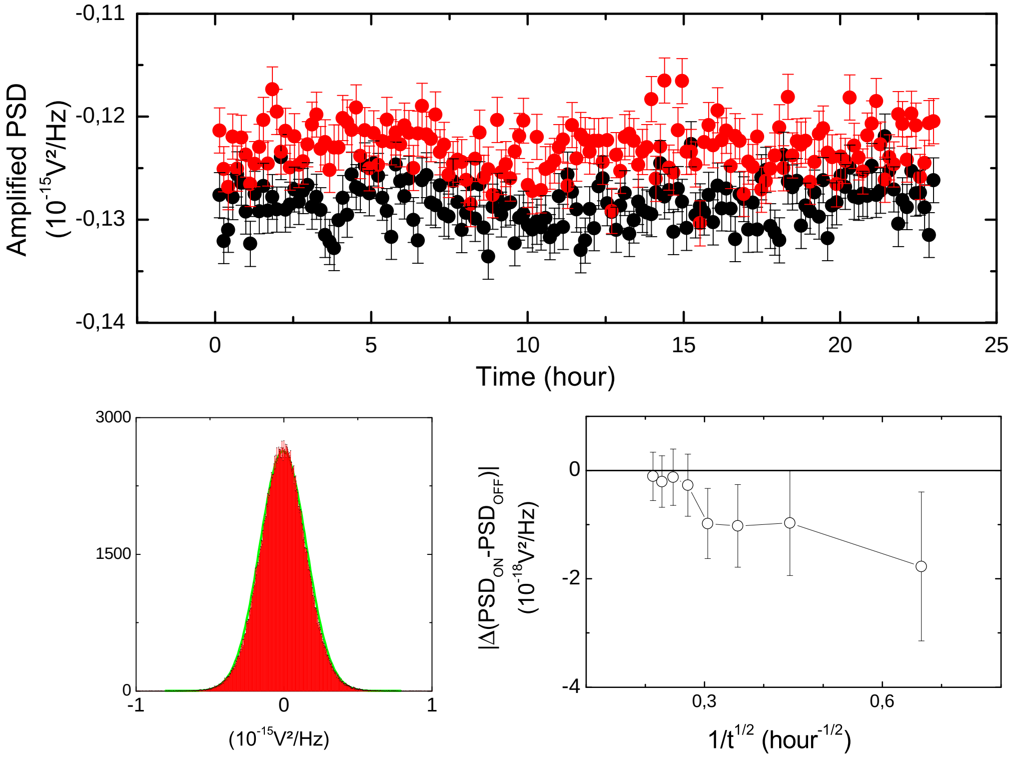

FIGURE 2.25 – "ON-OFF" measurement and long-term consistency. Three parameters are identical for all points : N_{av}=50000, D ∼0.34 and V_{ds} ∼20 µV. (TOP PART) "OFF" measurements (red dots) and "ON" measurements : a roughly Lorentzian pulse 4.8GHz is added (black dots). (BOTTOM PART,left) Histogram at t=23 hours with all "ON-OFF" data points (red) with Gaussian plot (green line). (BOTTOM PART, right) $|\Delta|\Delta_{on-off}||$ and its average over time. Error bar is the s.e.m from intermediary histograms at time t.

noise spectra at $D = 1$, we subtract the noise attributed to voltage fluctuations using a linear equation between the data points 2.0 MHz and 3.0 MHz. The thermal noise of all three resistors at 35 mK (R_S , and the resistive part of Z_A and Z_B) is subtracted using spectrum from Fig. 2.16, 2.17 or the equivalent for the Cross Correlation PSD. A linear renormalized amplitude is necessary to get 35 mK. The noise spectra to be explained are represented on Fig. 2.26, using input-referred amplitude.

$$|V_1|^2 = \frac{|G_A Z|^2}{|2Z+R_S|^2}(|Z|^2|\delta \mathrm{I_{NB}}|^2 + |Z+R_S|^2|\delta \mathrm{I_{NA}}|^2) \tag{2.24a}$$

$$|V_2|^2 = \frac{|G_B Z|^2}{|2Z+R_S|^2}(|Z+R_S|^2|\delta \mathrm{I_{NB}}|^2 + |Z|^2|\delta \mathrm{I_{NA}}|^2) \tag{2.24b}$$

$$|\overline{V_1}V_2| = \frac{\overline{G_A}G_B||Z|^2}{|2Z+R_S|^2}(Re(\overline{Z}(Z+R_S))(|\delta \mathrm{I_{NA}}|^2 + |\delta \mathrm{I_{NB}}|^2)) \tag{2.24c}$$

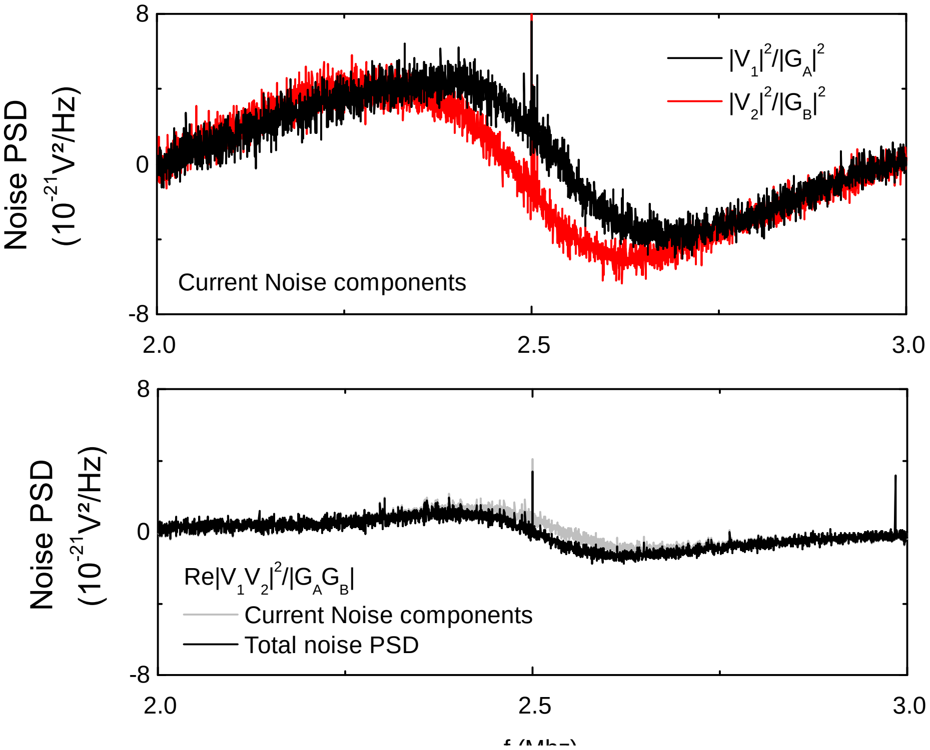

FIGURE 2.26 – Current noise components observed in the equilibrium spectra when $D = 1$ and in input-referred units for the two auto-correlations signal (top part) and the cross-correlated signal (bottom part, black line). The total noise PSD $|\overline{V_1}V_2|/\overline{G_A}G_B|$ including the thermal noise of all resistors at 35 mK is reproduced (bottom part, grey line). Typically 20000–40000 PSD spectra are averaged together.

According to the set of equations 2.24, the observed noise clearly does not originate from a pure white source : it display an anti-resonant behavior where a white noise would have induced a resonant PSD. However the frequency-dependence can be satisfyingly explained from a model taking into account a capacitive coupling between the output and the input of each HEMT, and the associated Miller effect. We present the model we used to check this in the next section.

If we focus for instance on the oscillation in the cross-correlation PSD, where the contribution $\mathrm{I_{NA}}$ / $\mathrm{I_{NB}}$ to the PSD are alternatively negative and positive, it seems possible to arbitrarily put this parasitic contribution close to zero by selecting a certain bandwidth to calculate the mean signal. This technique was not explored. In a typical experiment with a 2–3 MHz measurement bandwidth , the average power leads to an equivalent white noise source in the range 7–15 $\mathrm{fA}/\sqrt{\mathrm{Hz}}$, depending on the line. This value does not provide a complete characterization, but still allows to evaluate the typical deviation to be seen between two measurements at different transmissions.

It should be emphasized that if the mean value of the current noise integrated over the full bandwidth is small, it actually dominates the equilibrium noise PSD at 35 mK. To illustrate this, we reproduce here a typical noise measurements measured at 300 K (see Fig. 2.27), where the thermal noise dominates the signal and the typical peak from the RLC-filtering is obvious compared to Fig. 2.26.

2.6.6 Additional observations

A few other elements have also been observed :

- Cryo-amplifiers show a very small gain evolution when $V_{dc,source}$ is ON (see Fig. 2.7).
- At least one of the CMS resistors R_{LF} or R_L is heated through Joule effect when powering the $V_{dc,source}$ source and introduce a parasitic noise current increasing with $V_{dc,source}$.

Details are given in Appendix C. Both effects might be avoided in the future by modifying the low-temperature passive electronics surrounding the sample.

2.7 Miller effect ?

We use a small signal model in order to check the possible origin of the current noise observed in section 2.6.5. The anti-resonant shape in Fig. 2.26 is found to be indeed reproduced in presence of the Miller effect.

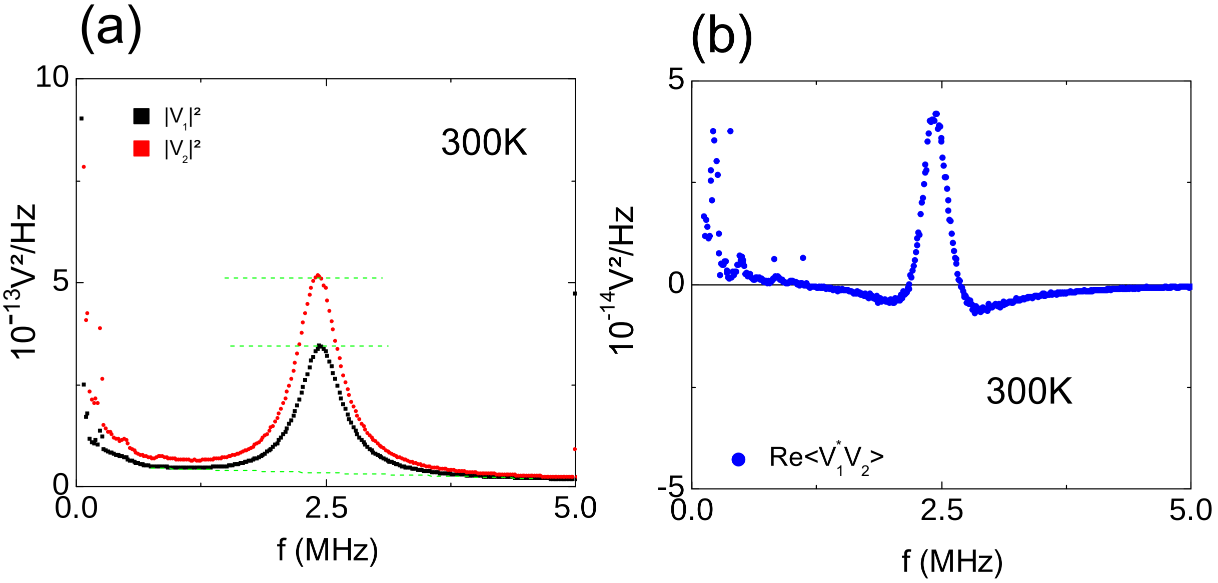

FIGURE 2.27 – 300K. Amplitudes are dominated by the thermal noise of the measured system (sample and resonators). At room temperature, the sample is a classical resonator(~18 kΩ). Estimating the gain from the auto, (gain ~ 0.25 and ~ 0.20 for respectively cryo-amplifiers A and B are found satisfying for all measurements at this temperature) and supposing 2 kΩ for the RLC reduced from skin effect in the inductance, the calculated amplitude for the cross measurement should be 3.8E-14 V^2/Hz at the resonance, in close agreement with the observed 4E-14 V^2/Hz. At such a low gain, the Miller effect is absent and at room temperature the thermal noise dominates any noise from the amplifiers.

2.7.1 Model

Discrepancies in single-transistor DC characteristics were found in early experiments to be reasonably small, both in current I_{ds} and in voltage V_{ds}. A single set of intrinsic parameters (g_m, g_{ds}) is therefore used in our model for all transistors. A detailed electronic model for an amplification chain is represented in Fig. 2.28 for two transistors. Compared to Fig. 2.1 and the full description of CRYOAMP board in Fig. 2.2, this model does not include passive components which are negligible in the MHz range, but incorporates the $C_{gd} = 0.16$ pF parasitic capacitor mentioned in the ATF-34143 Data Sheet from the manufacturer. Other parasitic elements (access resistance/inductance) were reviewed and found negligible in the MHz range, as expected from a device designed primarily for telecommunication application.

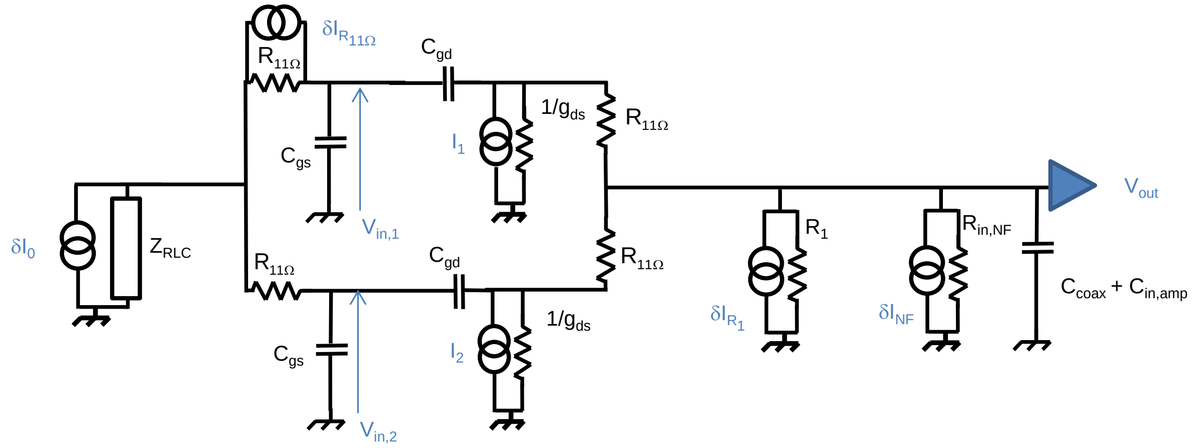

$I_1 = \delta I_1 - g_m V_{in,1}$ $C_{gd} = 0{,}16\text{pF}$ $\delta I_{NF} = 100\text{ fA}/\sqrt{\text{Hz}}$ $R_{in,NF} = 1\text{M}\Omega$

$I_2 = \delta I_2 - g_m V_{in,2}$ $C_{coax} + C_{in,amp} = 70\text{pF}+85\text{pF}$ $\delta I_{R_1} = \frac{4k_B T_{300K}}{1\text{k}\Omega} = 4\text{pA}/\sqrt{\text{Hz}}$

$\delta I_{R_{11\Omega}} = \frac{4k_B T_{4K}}{11\Omega} = 4.5\text{pA}/\sqrt{\text{Hz}}$

FIGURE 2.28 – Small signal model of amplification line with two parallel transistors in the MHz range.

On the left, the input impedance is simplified to a single RLC resonant circuit : the QPC is considered pinched, but the model can be extended without difficulties. All 5 pF resistors in parallel with the resonator are merged inside. The 5 pF capacitor singled out as C_{gs} cannot be merged due to the 11 Ω resistor. The central part contains two independent current sources replacing two polarised HEMTs. They may symbolize amplified signal or the HEMT channel noise (independent sources δI_1 and δI_2), depending on the situation under scrutiny. On the right, input impedance R_{NF}, input capacitance $C_{in,amp}$ and input noise δI_{NF} from the post-amplifier are represented, along with the resistor $R_1 = 1\,k\Omega$ from the SPLITTER board.

2.7.2 Absence of leakage current or thermal noise at the input

High mobility electron transistors based on GaAs/AlGaAs have several characteristics that make them suitable for low-temperature operation. These HEMTs are based on semiconductor heterostructures and carriers do not ”freeze out” as there is no competition between semiconductor bandgap and thermal energy. As the thermal energy available is low, low-temperature also reduces the leakage current. The parasitic parallel conductance in the donor region also decreases. These two characteristics are important as they are known to introduce current noise in amplification devices. They have attracted attention for quantum measurement and particle detectors and a short historic review of the technology can be found in [53].

2.7.3 Input resistor 11 Ω

We focus first on the two 11Ω resistors at the input. Due to the finite input impedance of the HEMT induced by $1/|C_{gs}\omega| \approx 13k\Omega$ at 2.5 MHz, a small fraction of each fluctuating current $\delta I_{R11\Omega}$ can circulate in Z_{RLC}. It can be shown to induce a small anti-resonant component (compared to the ideal RLC circuit) in the input voltage of the two HEMTs $V_{in,2}$ or $V_{in,1}$. But the typical amplitude cannot explain the dominant behavior of the noise current compared to the thermal noise of Z_{RLC}.

2.7.4 Output Noise and C$_{gd}$ coupling

Due to the parasitic capacitor C_{gd} (at 2.5 MHz we have $1/|C_{gd}\omega| \approx$400kΩ), a small fraction of each current I_1 and I_2 can circulate in Z_{RLC} and generate additional input voltages $V_{in,1}$ $V_{in,2}$. As I_1 and I_2 are function of $g_m V_{in,1}$ and $g_m V_{in,2}$, the effect is amplified by the intrinsic gain of the transistor. The typical amplitude and frequency-dependence to be observed in noise PSD are described by the set of equations 2.25 where the assumption $11\Omega \ll |Z_{RLC}|$ and $11\Omega \ll |1/g_{ds}|$ are considered valid. In that simplified situation, any source of noise $\delta I_{n,out}$ among $\{\delta I_1, \delta I_2, \delta I_{R1}, \delta I_{NF}\}$ leads to an output voltage which must respect the conditions :

$$\left\{ \begin{array}{llll} I_1 & +I_2 & & = -2g_m V_{in,1} + \delta I_{n,out} \\ V_{in,1} & = V_{in,2} & & = (I_1 + I_2)\dfrac{Z_{out} Z_{in}}{Z_{out} + Z_{in} + C_{gd}(\omega)^{-1}} \\ V_{out} & = & & (I_1 + I_2)\dfrac{Z_{out}(Z_{out} + C_{gd}(\omega)^{-1})}{Z_{out} + Z_{in} + C_{gd}(\omega)^{-1}} \end{array} \right. \tag{2.25}$$

We have written :

$$Z_{out} = R_{in,NF}//R_1//(C_{coax} + C_{in,amp})//g_{ds}^{-1}//g_{ds}^{-1} \qquad \approx (2g_{ds})^{-1}$$

$$Z_{in} = Z_{RLC}//C_{gs}//C_{gs} \tag{2.26}$$

$$C_{gd}(\omega) = j2\omega C_{gd} \tag{2.27}$$

We focus on the impact of a known white noise source $\delta I_{n,out}$:

$$\begin{cases} I_1 + I_2 & = \dfrac{Z_{out} + Z_{in} + C_{gd}(\omega)^{-1}}{Z_{out} + Z_{in}(1 + 2g_m Z_{out}) + C_{gd}(\omega)^{-1}} \delta I_{n,out} \\ V_{in,1} & = \dfrac{Z_{out} Z_{in}}{Z_{out} + Z_{in}(1 + 2g_m Z_{out}) + C_{gd}(\omega)^{-1}} \delta I_{n,out} \\ V_{out} & = \dfrac{Z_{out}(Z_{in} + C_{gd}(\omega)^{-1})}{Z_{out} + Z_{in}(1 + 2g_m Z_{out}) + C_{gd}(\omega)^{-1}} \delta I_{n,out} \end{cases} \tag{2.28}$$

In a frequency region outside the resonant bandwidth of Z_{RLC}, the PSD $|V_{out}|^2$ quickly reduces to a flat noise power filtered by the line through $|Z_{out}|$.

$$|V_{out,base}|^2 = |Z_{out}|^2 |\delta I_{n,out}|^2 \tag{2.29}$$

Inside the bandwidth we can on the contrary neglect Z_{out} compared to Z_{in} and the constant power is modulated by a frequency dependent factor.

$$|V_{out}|^2 = A(\omega)|V_{out,base}|^2 \tag{2.30}$$

We have :

$$\begin{aligned} A(\omega) & = |\frac{Z_{in} + C_{gd}(\omega)^{-1}}{Z_{in}(1 + 2g_m Z_{out}) + C_{gd}(\omega)^{-1}}|^2 \\ & \approx |\frac{1}{jZ_{in}(1 + 2g_m Z_{out})2C_{gd}\omega + 1}|^2 \end{aligned} \tag{2.31}$$

This situation is an example of the well-known Miller effect. This factor contains the anti-resonant behavior. The typical scale of the modulation around 1.0 it introduces depends on $2g_m Z_{out}$ (in practice the amplifier gain), and C_{gd}. As the input-referred noise observed outside the bandwidth was found to be ∼5E-20 V^2/Hz, a fluctuation up to ±10–15% would be necessary to explain Fig. 2.26. This is not achieved without supposing a larger coupling capacitor, typically C_{gd} ∼0.5 pF while the manufacturer indicates 0.2 pF.

The origin of this additional capacitance is not clear, but might arise from the PCB design.

2.8 Conclusion

In this chapter, we have built and fully analyzed two amplification chains from which a continuous cross-correlation measurement over a 450 kHz-bandwidth can be realized. Noise powers of 1E-30 A^2/Hz are resolved in a few minutes. The parasitic noise current is interestingly small, and the long-term stability is satisfying. This performances are achieved by improving previous measurement schemes based on auto-correlation and pHEMT with a design based on two parallel transistors. The QPC charateristic was measured at low-frequency while DC shot noise thermometry indicates an equilibrium electronic temperature of 35 mK.

Chapitre 3

RF Calibrations

In order to observe how a few charges are injected in a ballistic 1D coherent conductor under voltage pulses, the radio-frequency signal has to meet some requirements.

- We need to apply voltages pulses with a repetition frequency ν high enough that we collect a sizable amount of photo-excited charges. This argument concerns all parasitic noise sources : more photo-excited particles means a better signal to noise ratio. The argument can be also applied to the incoming thermally excited charges as a first indication, even if we know its effect to be more complicated (no averaging out). $\theta_e = k_B T_e / h\nu$ must be small.
- Closely related to the previous rule, we also need the energy of an observed particles in the noise to be mostly a consequence of an AC pulse. That way, its final state gives direct information on the photo-assisted processes without the need for numerical "deconvolution" as mentioned in section 1.5.2. Quantized energy shift have an amplitude hν competing with thermal energy $k_B T_e$. For the previously defined trains of voltage pulses like the periodic square or the sine wave, the final energy for each electron is directly set by the repetition frequency, for a Lorentzian pulse there is an intrinsic energy scale to consider too. It corresponds to the FWHM, shorter than the period. In all cases, we find also the condition $\theta_e = k_B T_e / h\nu \ll 1$.
- We need to know precisely the amplitude $\alpha = eV_{ac}/h\nu$ of the applied pulses to the sample, and its "shape" in order to interpret correctly the number of excess particles. The particularly steep slope of $\Delta N_{eh}(\alpha)$ as a function of the DC level "$q = e < V_p > /h\nu$" in some energy-windows suggests that errors might come from overestimating or underestimating q compared to α (see Fig. 1.14 and 1.15).

- The RF-line have to be designed to combine high-frequency transmission and proper operation of the cryostat.

In this chapter, we review the radio-frequency techniques used to generate, transmit and calibrate in-situ the signal applied to the QPC. The technical limitations to the frequency range are compared to the QPC and PASN physics.

3.1 Wideband DC–30 GHz coaxial lines overview

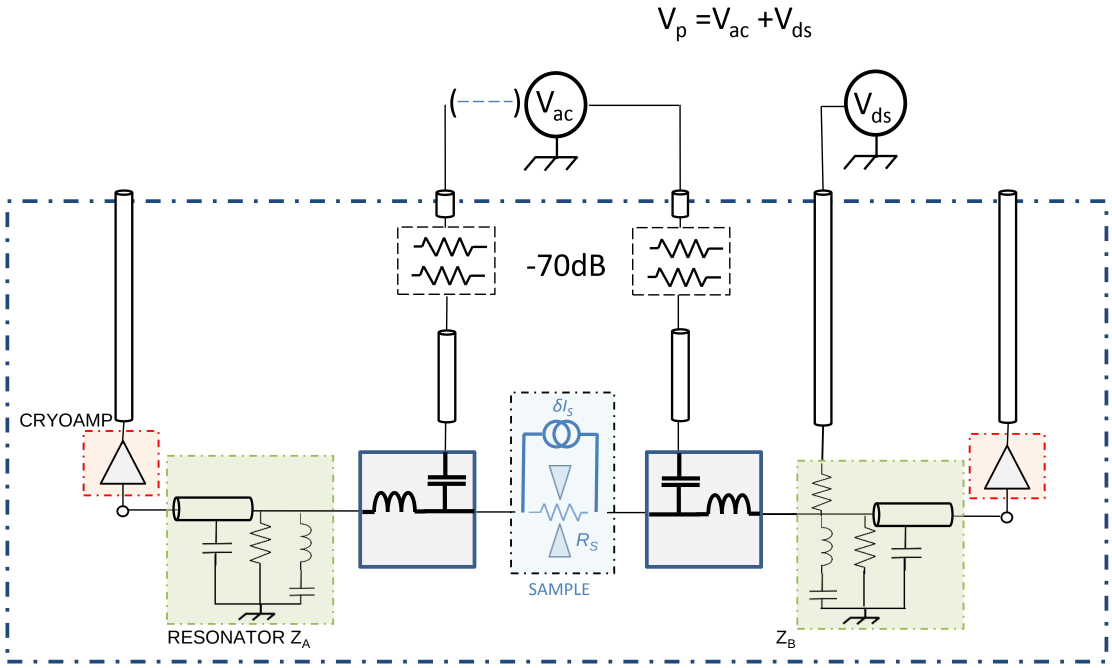

FIGURE 3.1 – RF Injection lines. The two lines are built from the same plan and can be both used. In practice, the detailed calibration reported here refers only to one of them, used for single pulse injection experiments.

As shown in Fig. 3.1, two coaxial lines with a total attenuation of -70 dB are implemented directly into the cryostat. They consist in a series of 2.2 mm diameter Cu-Ni wires short sections, with thermal grounding at each stage of the cryostat (see Appendix A). Attenuators are typically inserted at each stage. Namely -20 dB at 4 K, 1 K and 50 mK, plus -10 dB at the lowest temperature stage 12.5 mK. The power dissipated with pulses up to a few Volts peak-peak does not affect the cooling power of the cryogenic system. It was also checked by plugging only one line at a time that the equilibrium electronic temperature is not determined by thermal radiation along the RF lines. The sample has a huge resistance compared ($\geq$13 kΩ) to the 50 Ω characteristic impedance of these lines.

Anritsu K250 Bias Tee near the sample are used to combine RF injection and DC-10 MHz measurement. Below 4 K, these Bias Tee have a ~3 µH inductance and about 20-40 pF capacitance.

The distance between room-temperature parts and the sample is about 1 m.

3.2 Frequency selection

Using the full range and sensitivity of room-temperature sources, the available range and resolution for the amplitude at the contacts of the sample is easily verified to be large enough for our experiments. With 7.5 GHz and -73.3 dB, a room-temperature resolution of 1 mV leads to a resolution $\delta\alpha$=0.007, while a 2 Vpp range gives a top $\alpha \sim 7$. The bottom frequency is determined by the competition with the temperature. At 4 GHz and 35 mK $\theta_e \sim 0.18$. The top repetition frequency or energy-scale can be determined by several factors. With higher frequency, the current increases and more power is dissipated. As a consequence, the sample temperature also increases. The hypothesis of a constant transmission for all energies involved becomes less and less valid. According to the results of section 2.3.1, a 100 µV bias on the QPC at low-transmission induces typically a ±5% variation in the transmission. This corresponds to $eV/h = 24$ GHz. The top voltage applied to the sample for a Lorentzian pulse sending a single charge when it has a FWHM $2W$=30 ps is ~90 µV [1]. The average energy of the injected particle in that case is ~25 µV according to section 1.7. If we consider the periodic problem [2], the average energy can be checked to be the same. The top repetition frequency is also in that case a consequence of the technology used to generate the pulse shape and cannot be arbitrarily increased, as detailed after. The final argument is the limited coherence and lifetime of the electrons. Using formula Eq. 1.57 and with $E_F = 14.3$ meV, the lifetime of photo-excited particles at these energies is at least a few periods. In all cases it is much larger than the typical 0.3 ps spent in the 80 nm-scatterer by individual electrons. See also Appendix B.

---

[1] The power to be dissipated in the leads is then $<V_p^2 D/R_q>$, typically 10^{-14} W.

[2] $P_{-1} = \beta^2$, $P_{l>-1} = \beta^{2l}(1-\beta^2)^2$ and $\beta = exp(-2\pi W/T)$. The average energy is given by $< \varepsilon >= h\nu \sum_{l=1}^{+\infty} P_{l-1} l^2/2$

3.3 In-situ calibration

3.3.1 Photo-assisted shot noise

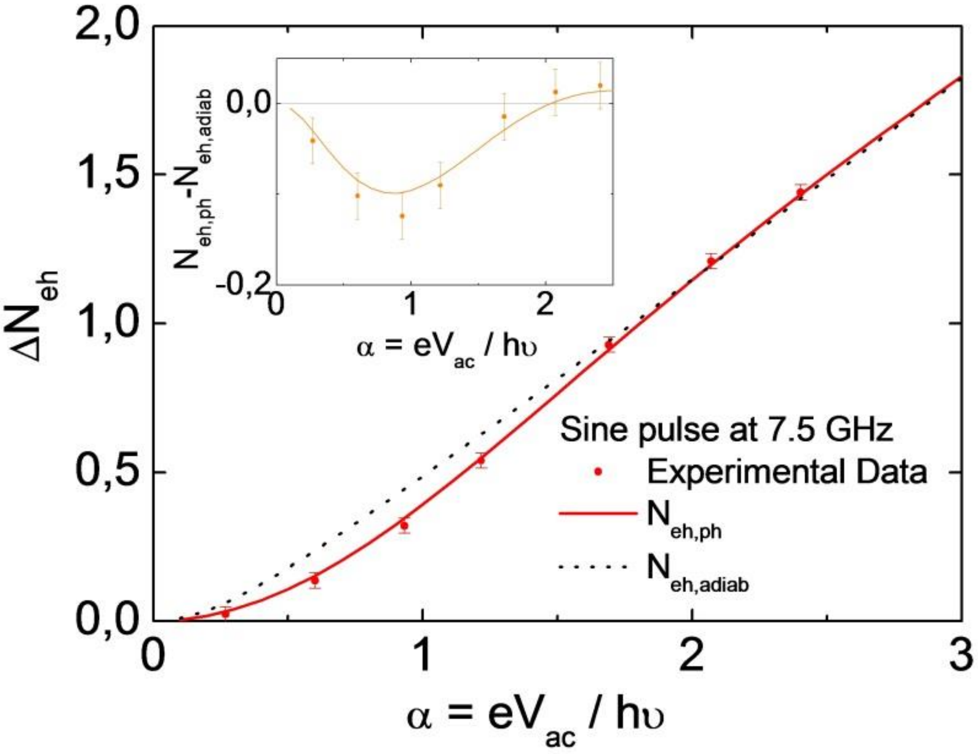

FIGURE 3.2 – In-situ calibration of AC amplitude at a single frequency 7.5 GHz. A single fit parameter is necessary to adjust the theory $\Delta N_{eh,ph}(\alpha)$ (red line) and the experimental data (red dots). The dash line represents the theoretical asymptotic behavior $\Delta N_{eh,adiab}(\alpha)$. As can be seen in the inset, the low-amplitude behavior shows the characteristic photo-assisted reduction. The difference between the experimental noise for AC-transport and adiabatic transport is negative.

In section 1.3 we have developed the photo-assisted shot noise induced by any kind of signal $V_{ac}(t)$. Here we are interested in the special case of a Sine Voltage, in the absence of added DC component.

$$V_p(t) = V_{ac}(t) = \frac{\alpha h\nu}{e} sin(2\pi\nu t) \tag{3.1}$$

As already mentioned, the photo-assisted probability distribution P_l is expressed through Bessel function $P_l = |J_l(\alpha)|^2$.

This situation has been studied in details in [120] and [130] and is now considered well-understood. The noise difference between the QPC at equilibrium T_e and the bias-driven system is a particular case of Eq.1.29 expressed as :

$$\Delta S_I(V_{ac}(t),0,T_e) = S_I^0 \Delta N_{eh}(\alpha,0,\theta_e) = S_I^0 \sum_{l=-\infty}^{+\infty} l \left[coth(\frac{l}{2\theta_e}) - 2\theta_e \right] \mathrm{J}_l^2(\alpha) \tag{3.2}$$

Eq.1.29 was previously written for the special case of a single conductance channel. The experiment is performed in a QPC where two channels defined by the spin coexist. Thus :

$$S_I^0 = 2D(1-D)\frac{2e^2}{h}h\nu \tag{3.3}$$

At zero temperature, the limit $\alpha \to +\infty$ is :

$$S_I^{adiab} = S_I^0 \; N_{eh,adiab} = 2e\frac{2e^2}{h}D(1-D)\frac{2V_{ac}}{\pi} \tag{3.4}$$

It can be proved to be identical to the noise obtained when calculating the average over a sinusoidal distribution of DC bias amplitude.

$$\begin{aligned} S_I^{moy} &= 2e\frac{2e^2}{h}D(1-D)\frac{1}{T}\int_0^T dtV_{ac}|sin(\frac{2\pi t}{T})| \\ &= 2e\frac{2e^2}{h}D(1-D)\frac{2V_{ac}}{\pi} \\ &= 2e\frac{2e^2}{h}D(1-D)\frac{2V_{ac}}{\pi} \end{aligned} \tag{3.5}$$

This limit and the identity between Eq.3.4 and 3.5 can be understood as follows. When the frequency ν is extremely slow, we expect the system to evolve adiabatically and the resulting noise to behave like a DC bias at any time. The long-term average is then given according to 3.5. The difference between Eq. 3.2 and 3.5 is important at small value $0 < \alpha < 1$ but rapidly vanishes. At finite temperature and beyond $\alpha > 2$, the adiabatic average becomes a very good assumption. The adiabatic approximation at finite temperature is defined as :

$$S_I^{adiab} = S_I^0 \ N_{eh,adiab} = 4k_BT_e\frac{2e^2}{h}D(1-D)\frac{1}{T}\int_0^T dt\left[\frac{eV_{ac}(t)}{2k_BT_e}coth(\frac{eV_{ac}(t)}{2k_BT_e})-1\right] \qquad (3.6)$$

Eq. 3.6 generalizes 3.5 to any AC voltage and temperature.

The effect of a DC bias on the system has been verified experimentally in section 2.3.2. As a consequence, the adiabatic regime and the direct comparison of DC and AC noise PSD provides information on α through the asymptotic behavior. It means we have access to the AC amplitude at frequency ν applied on the sample.

However, large bias are expected to affect the transmission, even if slightly, and additionally the electronic temperature through Joule effect increases with α. Correction to the fit function, however predictable, are more and more important. Fortunately, quantum effects around and below $\alpha = 1$ have a characteristic signature and the combination of the two limits offers a satisfying in-situ calibration of the applied signal. This procedure is exemplified in Fig. 3.2. The best Fit $\Delta N_{eh,ph}$ contains a single adjustable parameter, the attenuation coefficient η_ν between the output of the room-temperature RF source and the observed amplitude on the sample. Small heating effects are taken into account according to Eq. 2.17.

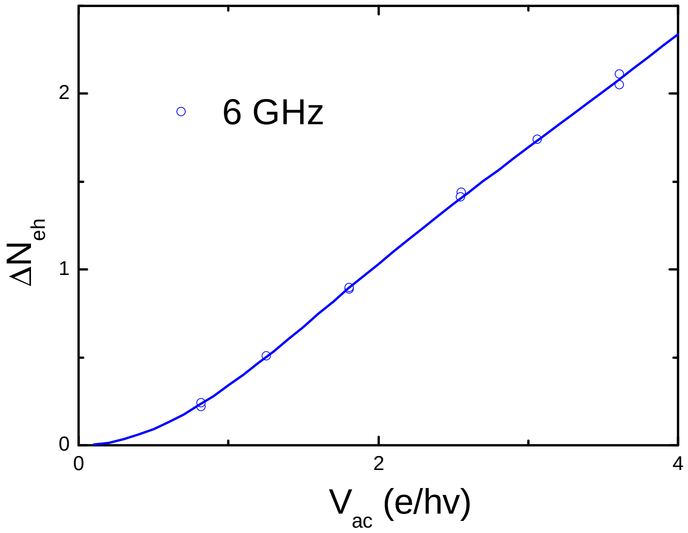

FIGURE 3.3 – In-situ calibration of AC amplitude at ν=6 GHz .

For the special case of Fig. 3.2, the frequency is 7.5 GHz. We can check how consistent is the experimental attenuation coefficient with known material constraints. The attenuation coefficient from the calibration is η_ν = -83.3 dB. -70 dB are known to be implemented inside the fridge, and -10 dB to be added at the input. We can therefore estimate the total losses at -3.3 dB. Two meters of 2.2 mm-diameter Cu-Ni coaxial wires are used to connect the source and RF lines. Given the length of coaxial wires, especially at room temperature, it indicates few reflections along the lines and at the sample contacts at this frequency.

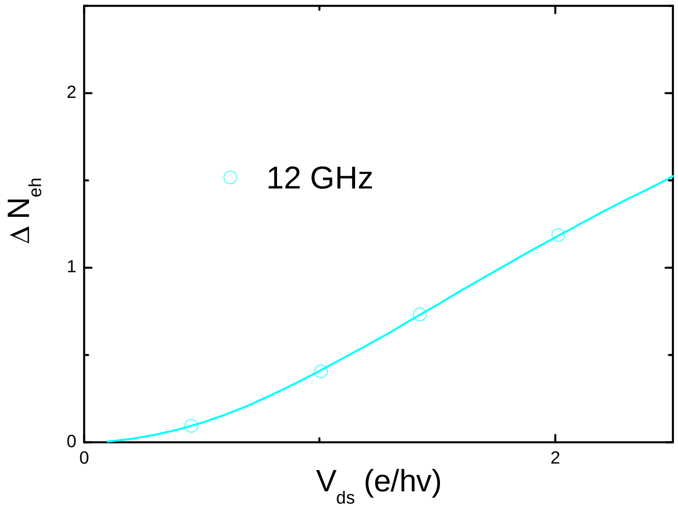

FIGURE 3.4 – In-situ calibration of AC amplitude at ν =12 GHz.

3.3.2 Harmonic by harmonic pulse generation

Applied Amplitudes

Several harmonics of the repetition frequency are usually involved in an AC bias, especially when the intrinsic timescale (rise time, FWHM ...) are much shorter than the period. While an oscilloscope can provide a time-domain picture of the pulse at room-temperature, such a tool is missing in-situ. We can reproduce separately the photo-assisted noise calibration proposed in the previous section at all the harmonics involved in the desired voltage pulse. Then we know the spectral content when they are applied simultaneously. This linear sum rule is true if the sample conductance shows negligible non-linearity with the bias. But this is insufficient. The response of the quantum conductor depends on the precise time-profile, and we have to know all the relative phases at the sample.

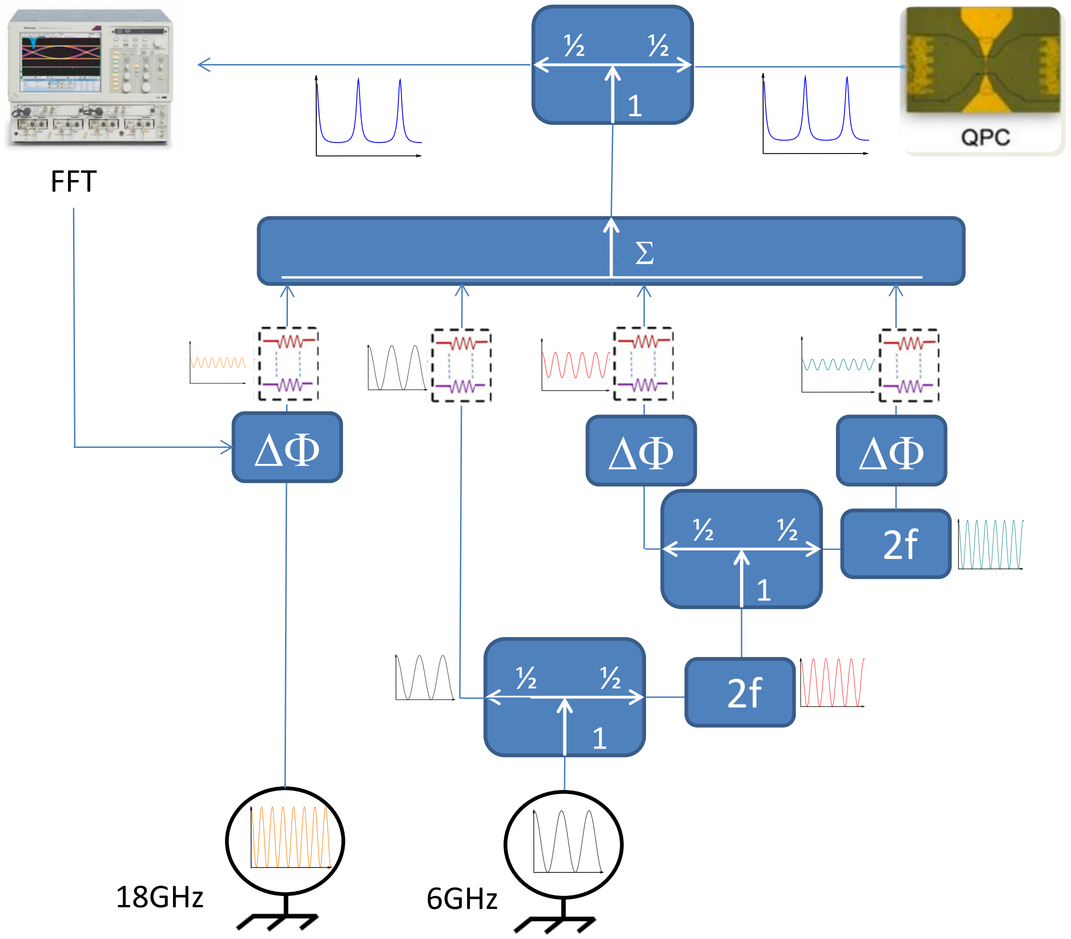

FIGURE 3.5 – 4-harmonic arbitrary pulse generation. Two Radio-frequency sources generate signals of arbitrary amplitude at ν_0 and $3\nu_0$. Phases are synchronized through the external clock reference of source $3\nu_0$. Two frequency doublers [4] with adjustable output amplitudes can be used to generate signals of arbitrary amplitudes at $2\nu_0$ and $4\nu_0$. Discrete small value attenuators are also inserted. An adequate number of phasers is used to select all relative phases mechanically. At one of the output of a 60 GHz power-divider, a reference signal is registered using a digital oscilloscope while the other output is send to the sample. The oscilloscope is used to perform a FFT and check the pulse, and if necessary resynchronize the two RF sources. The FFT might strongly differ from the target at the oscilloscope in order to compensate for the deformation in the lines.

Fig. 3.5 shows a setup dedicated to the combination of four-harmonics with arbitrary amplitude and arbitrary relative phases. The results of individual photo-assisted calibration

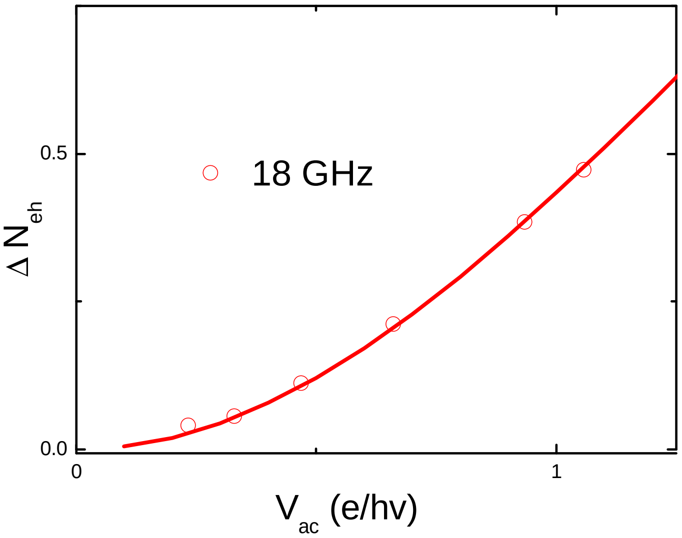

FIGURE 3.6 – In-situ calibration of AC amplitude at a 18 GHz

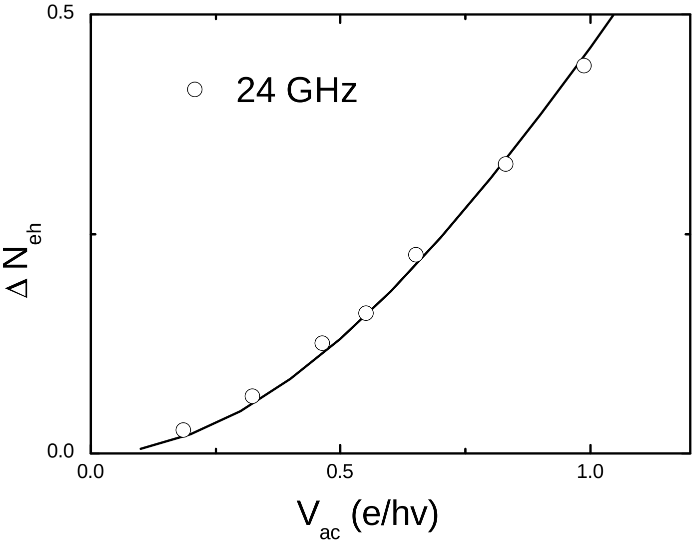

FIGURE 3.7 – In-situ calibration of AC amplitude at a 24 GHz.

for each multiple of $\nu_0 = 6$ Ghz are shown in Fig. 3.3, 3.4, 3.6 and 3.7. Note that $V_{ac} = e/h\nu$ does not refer to the same voltage in the four figures as they refer to different frequencies.

The conversion from noise PSD to the reduced unit ΔN_{eh} contains the same factor $1/\nu$. At zero temperature, all curves would look identical. The large value for α are less interesting when $\nu = 24\,\mathrm{GHz}$ as it implies higher voltage : α=1 is already $\sim 100\,\mu\mathrm{V}$.

The typical parameter used as an effective attenuation coefficient is the ratio between the amplitude detected at a DSA8200 Tektrnonix Digital Sampling Oscillator and on the sample. It does not depend on the way the signal is generated.

Control of all relative phases

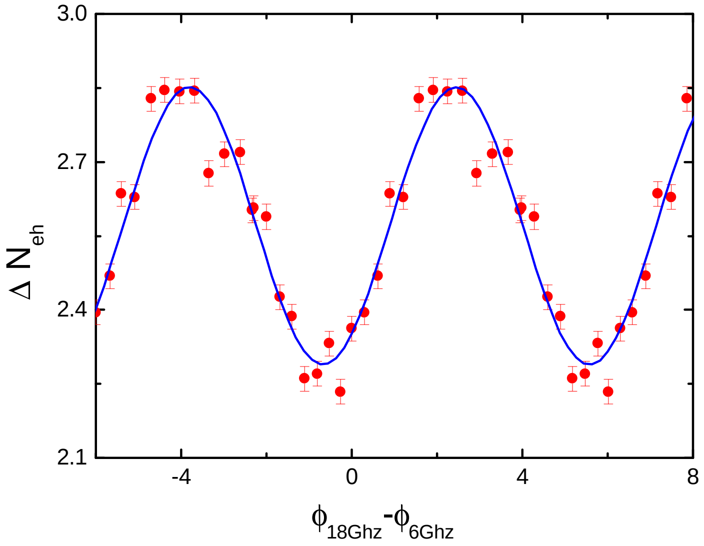

Figure 3.8 – Control of Relative Phase between third and first harmonic. $\nu_0 = 6\,\mathrm{GHz}$. Experimental parameters : $q = 0$, $\alpha_1 \sim 3.97$ and $\alpha_3 \sim 0.93$. This set of values gives large noise and large contrast. The best fit is a sine function with a single adjustable parameter : the phase.

A simple extension of the procedure used to calibrate in-situ amplitude using the photo-assisted shot noise can provide precise information on the relative phases between our four harmonics.

In section 3.3.1 we have seen in the specific case of a sine wave that the behavior for an increasing number of particles gets close to an adiabatic approximation.

This idea is true for any signal $V_p(t)$. We can therefore expect a predictable phase-dependence when applying simultaneously two frequencies and rotating one of them. This

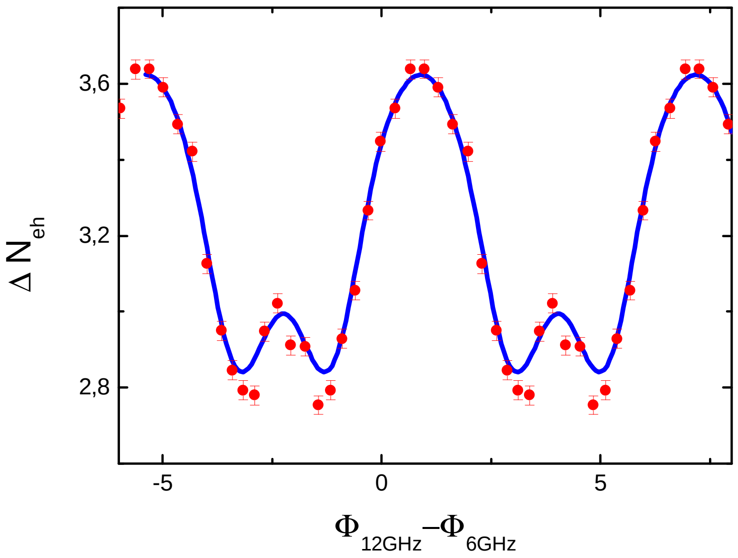

FIGURE 3.9 – Control of Relative Phase between second and first harmonic. $\nu_0 = 6\,\mathrm{GHz}$. Experimental parameters : q ~1.17, $\alpha_1 \sim 5.77$ and $\alpha_2 \sim 2.11$. This values gives large noise and large contrast. The best fit is based on a full photo-assisted calculation, with a single adjustable parameter : the relative phase induced along the line.

strategy was inspired by the work of Gabelli et al. [44]. Roughly :

$$S_I^{adiab} \propto \frac{h\nu_0}{eT}\int_0^T |q + \alpha_n cos(2\pi\nu_0 nt) + \alpha_m cos(2\pi\nu_0 mt + \delta\Phi_m + \Phi^0_{nm})| \tag{3.7}$$

q, α_n, α_m are voltage amplitudes. n and m are integer values. $\delta\Phi_m$ is a tunable phase while Φ^0_{nm} is a fixed value imposed by the lines. The objective is to compensate Φ^0_{nm} at the input in order to maintain the pulse shape on the pulse.

The basic example with $a = 0$, $n = 1$, $m = 3$ and $\alpha_1 \gg \alpha_3$ shows mostly a sine dependence with Φ_{nm}. Using a finite value for q allows to get a different noise when $\Phi^0_{nm} + \delta\Phi_m = 0$ or $\pm\pi$. This procedure is remarkably precise even with a limited knowledge on the applied amplitudes. Fig. 3.9, 3.8 and 3.10 shows the result for the case under scrutiny, in which three relative phase are necessary. The two RF sources in Fig. 3.5 were directly combined (doublers are turned off) and the phase difference labeled with the oscilloscope FFT. As this is a very precise measurement, we have duplicated periodically the experimental data to ease the fitting procedure.

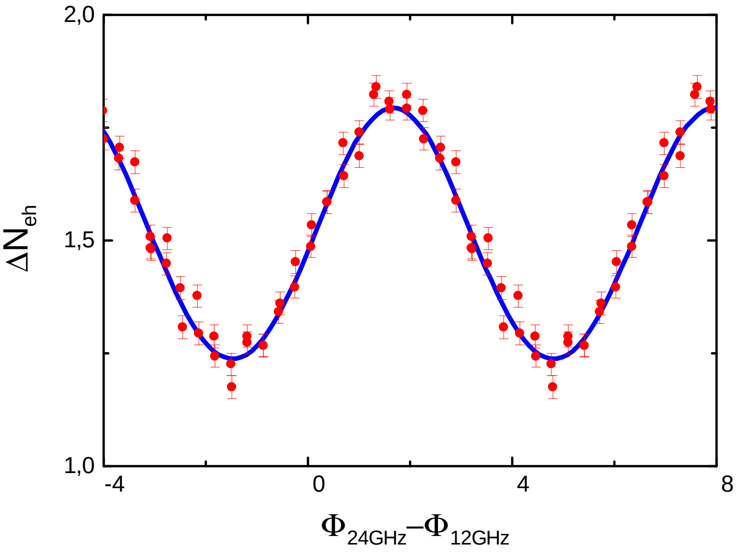

FIGURE 3.10 – Control of Relative Phase between second and fourth harmonic. $\nu_0 = 6\,\text{GHz}$. Experimental parameters : q ~1.17, $\alpha_2 \sim 1.81$ and $\alpha_4 \sim 0.68$. This values gives large noise and large contrast. The best fit is based on a full photo-assisted calculation, with a single adjustable parameter : the relative phase induced along the line.

3.3.3 Long-term stability

The digital sampling oscilloscope in Fig. 3.5 is used to perform continuously a FFT. Two types of drifts can be expected. First the internal ocsillators of the two RF sources cannot maintain phase-lock over long-time. Second, frequency doublers are active devices with small changes in the output. We have checked how well the output of the pulse generation was maintained over long-time. Fig. 3.11 describes the result for a section Lorentzian pulse at 6 GHz with a width $W/T = 0,09$. This pulse is intensively used in chapter 4 to 6.

All other harmonics are found negligible, proving the absence of uncontrolled components from non-linear effects in the active devices involved [5].

3.4 Commercial Arbitrary Waveform Generator

The procedure presented in the previous section allows simultaneously a very high degree of control on the shape applied to the QPC and a high-quality calibration. Lorentzian

---

[5] It does not imply that each channel is the source of purely one of the four harmonic.

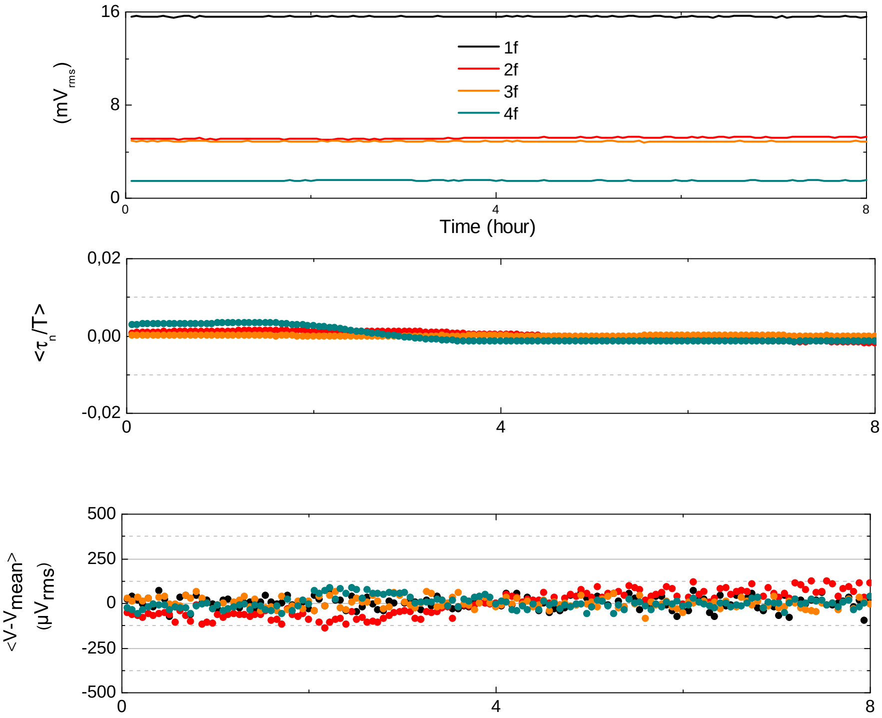

FIGURE 3.11 – Long-term stability of pulse generation. The top part shows the amplitude for the generation of the four first harmonics of single-particle Lorentzian train with a width $W/T = 0.09$ and 6 GHz, as observed at the input of the oscilloscope. Average amplitudes are set to compensate line defects. The deduced attenuation coefficient shows a behavior most likely dominated by resonances at 18 GHz and 24 GHz. The middle part shows the experimental deviation of the relative phase $2\pi\tau_n/T$ as observed at the oscilloscope input. After compensating the line defects, the zero value at the sample contacts is well-maintained. The bottom part shows the deviation of all amplitudes over time.

pulses with 4.8 GHz repetition frequency were also generated using a low-jitter Tektronix 24 GSample/s Arbitrary Waveform Generator (AWG) and a Digital to Analog Converter (DAC) synthesizer with output range 2 Vpp. Similarly square pulses at 4 GHz were generated using the same device. The final shape and amplitude applied on the sample was analyzed using the photo-assisted distribution observed in spectroscopy experiments. This is detailed in chapter 4. The AWG is appropriate for low GHz frequencies. The increased skin depth limits the coaxial losses and less pulse deformations are expected.

3.5 Conclusion

We have described the generation of voltage pulses with an amplitude ranging from 0 to a 100 μV and suitable for average current down to a fraction of a charge. Knowledge of the precise shape applied on the quantum conductor at 35 mK can be provided by PASN measurements. Our implementation of a four harmonic arbitrary combination source is used to obtain a Lorentzian pulse with a characteristic width $W/T = 0.09$. This situation implies a limited superposition of successive voltage pulses as the repetition rate is 6 GHz.

Chapitre 4

Minimal-excitation states for electron quantum optics using levitons [1]

We present in this chapter a set of measurements to verify the core prediction of Levitov et al.[90] : a Lorentzian voltage pulse with quantized flux realizes a clean single-particle injection in a quantum wire due to the particular distribution of photo-assisted processes occurring in the system. As described in chapter 1, three type of experiments are conducted and various pulse shapes are compared. First, in section 4.1 shot noise spectroscopy enables to analyze the photo-assisted probability distribution at all energies. Then, in section 4.2 we compare the total noise found when attempting an arbitrary charge injection using different time-profile for the voltage pulse. As a last characterization, we verify in section 4.3 the presence of a characteristic time-profile absent in particle-counting experiment using the proposed time-spectroscopy. It indicates that on-demand injection is indeed performed.

4.1 Shot Noise Spectroscopy

Following the presentation in chapter 1, we analyze the excess noise power appearing from the application of a signal $V_p(t) = V_{ac}(t) + V_{ds}$ compared to the DCSN from the constant bias V_{ds}.

In both situations the incoming current is $q = eV_{ds}/h\nu$ in charges/period. Experimental data are subtracted between the two measurements to obtain ΔN_{eh}.

V_{ac} is defined by a shape and expressed in units of α, V_{ds} in units of q charges/period. The signal corresponds to a pulsed charge injection procedure when $q = \alpha$. The distribu-

---

[1] Results reviewed in this chapter are presented in [39]

tion of photo-assisted processes in periodic trains of sine-window pulses, square pulse and Lorentzian pulses are all found to behave qualitatively and quantitatively as expected.

4.1.1 Sine pulse

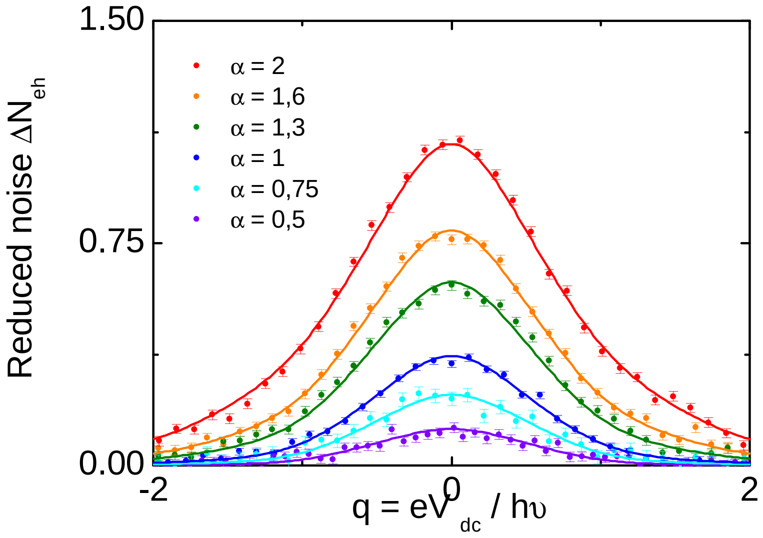

FIGURE 4.1 – Sine 7.5 GHz Energy Spectroscopy. QPC transmission D ∼0.33. Typically 40000 PSD are averaged together for each point. In addition a 2-point window adjacent averaging was performed along each curves.

The oscillating signal is defined as :

$$V_p(t) = \frac{qh\nu}{e} + \frac{\alpha h\nu}{e} cos(2\pi\nu t) \tag{4.1}$$

At zero temperature, an identical number of excess particles per pulse ΔN_{eh} must be found at all frequencies. At finite temperature, the noise also depends on the parameter θ_e. At base temperature 35 mK [2] and ν =7.5 GHz, 16 GHz and 24 GHz we have respectively θ_e =0.1, 0.05 and 0.03. At these values, the photo-assisted processes are dominating the structure of the observed energy spectroscopy, except for very small α and 7.5 GHz. See

---

[2] The temperature increase from the Joule effect in our experiments is commented in section 4.1.4.

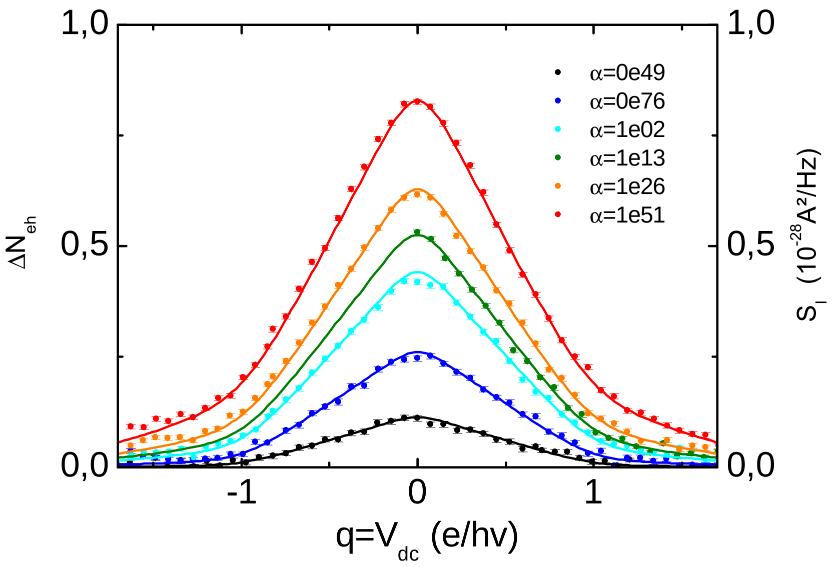

Figure 4.2 – Sine Wave 16 GHz Energy Spectroscopy. QPC transmission D ∼0.33 or ∼0.24. Typically 60000 PSD are averaged together for each point.

Fig. 4.1, 4.2 and 4.3. A clear signature of the quantum dynamics is the rapid change of slope in all curves near $q = \pm 1$, which cannot be explained without quantized energy shift.

$P_l(\alpha)$ are given by the square value of Bessel function, and there is no adjustable parameters after the in-situ calibration. As mentioned in section 4.1.4, the final agreement for simultaneously large q and α is found when taking into account small corrections from the Joule effect. As expected, a symmetric distribution of photo-absorption and photo-emission processes is found.

4.1.2 Square pulse

Definition and generation

A square pulse is defined as :

$$\begin{aligned} V_p(t) &= -\frac{\alpha h\nu}{e} + \frac{qh\nu}{e} && if \quad 0 \leq t < 0.5T \\ &= \frac{\alpha h\nu}{e} + \frac{qh\nu}{e} && if \quad 0.5T \leq t < T \end{aligned}$$

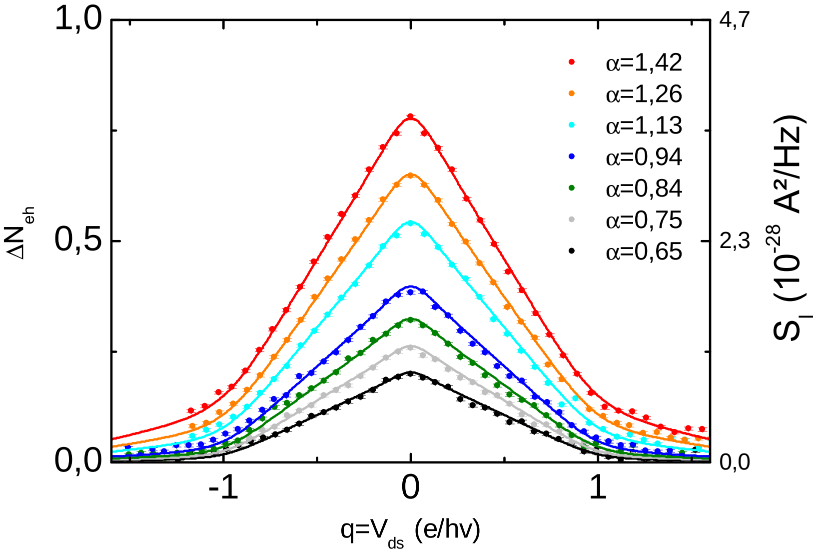

FIGURE 4.3 – Sine Wave 24 GHz Energy Spectroscopy. QPC transmission D ∼0.24. Typically 60000 PSD are averaged together for each point.

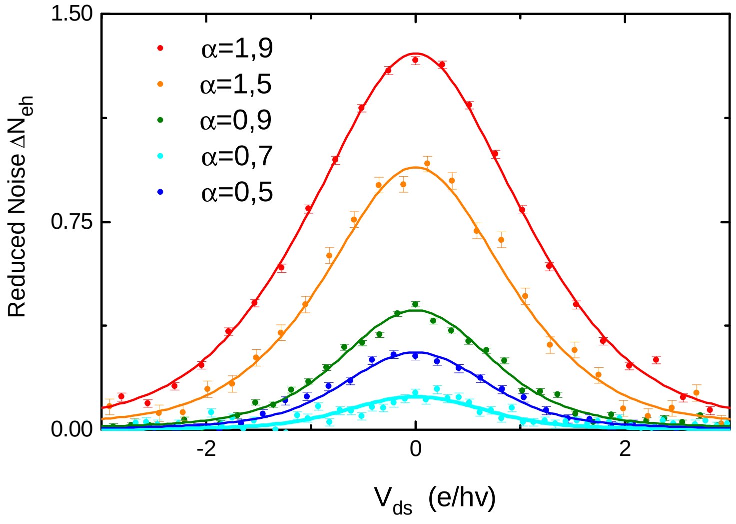

FIGURE 4.4 – Square 4 GHz Energy Spectroscopy. QPC transmission D∼0.34

The Fourier Series of such a time-window contains only the DC average and odd multiple of ν.

$$V_p(t) = \frac{4\alpha h\nu}{e\pi} \sum_{l=0}^{+\infty} \frac{sin(2\pi(2l+1)\nu t)}{2l+1} + \frac{qh\nu}{e} \tag{4.2}$$

The rise-time slows down and the ripple amplitude increase when cutting off high frequencies. This leads to select a rather low repetition rate 4 GHz. The Joule heating is not expected to be important, one of the advantage of working with a low-current. 4 GHz = 16µV. Even so, $\theta_e \sim 0.18$ and singularities in the slope are rounded. Fig. 4.4 shows the energy spectroscopy experiment for the pulse square generated by the RF source Tektronix AWG 7122b. The amplitude is changed through a set of discrete passive attenuators DC–18 GHz, and the full range of the device is used[3]. The fit curve is based on an ideal square pulse 4 GHz.

There is an adjustable parameter : the pulse amplitude α. The overall agreement between the theory and the experimental data is remarkably good.

A few more arguments indicate that the partially unknown pulse deformations do not significantly alter this measurement. First their is an experimental reason. Two very similar attenuation coefficients in the RF injection line are found at 4 GHz and 12 GHz using a mono-frequency PASN experiment. It shows that at least the first and third harmonics are applied to the sample contacts with the correct harmonic ratio defining a square pulse. The second comes from the numerical analysis of the difference between the pure square pulse and its truncated Fourier Series as soon as 3ν. While absolute differences in the noise power could have been detected with our experimental error bars, they correspond to very small relative variation in ΔN_{eh} and no qualitative change.

Comments

The P_l distribution can be calculated for the ideal square pulse when $\alpha = q$ is an integer. It has three characteristics, qualitatively associated with the asymptotic behavior $\lim_{l=\pm\infty} P_l(\alpha) \sim (\alpha^2/l^2 - \alpha^2) \rightarrow (\alpha/l)^2$[4]. It can be compared to the squared Bessel functions for $\alpha \ll l$, which behave as $\sim \alpha^{2l} 1/(4l!)^2$.

- The average energy for excited holes/electrons is high compared to a smooth shape, and the variance is broad.
- The distribution of photo-assisted processes is symmetrical.

---

[3] According to the manufacturer, the rise time 20%–80% is 35 ps.

[4] $P_l(\alpha) = 0$ if $l - n$ is even and not 0

- ○ Injecting n charges leads to a diverging number of excess particles with increased n

From the agreement between Fig.4.4 and theory, we can confirm directly the two first points, while the last one is analyzed in section 4.2.

4.1.3 Lorentzian pulses

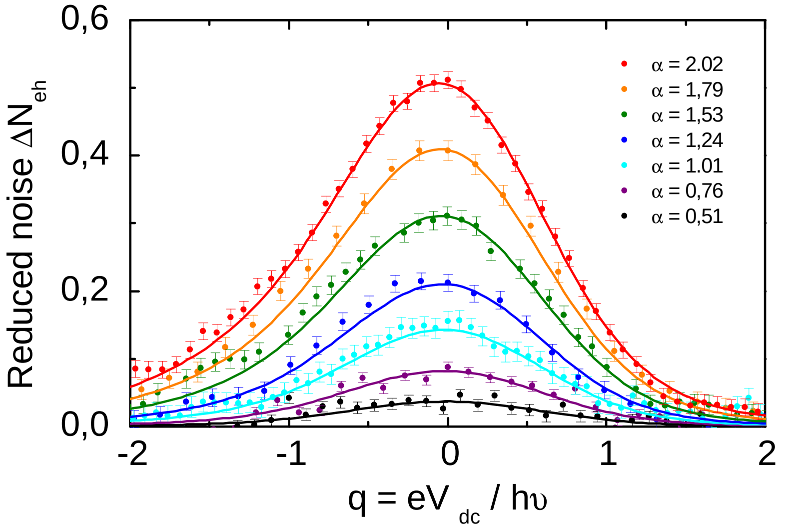

FIGURE 4.5 – Lorentzian 4.8 GHz Energy Spectroscopy $W/T = 0.183$. The QPC transmission is D∼0.33.

Two experiments are presented. A first Lorentzian pulse Applied using the AWG generator with width $W/T = 0.183$ and 4.8 GHz is analyzed in Fig. 4.5. The FWHM $2W/T$ and amplitude α are calibrated using the spectroscopy results. The agreement is good, and the fit parameters are consistent with the AWG resolution and known RF line transmission. The second pulse with W/T=0.09 and 6 GHz (Fig. 4.6) was obtained by combining 4 fully calibrated harmonics as described in chapter 3. Both experiments show the characteristic asymmetry between negative and positive value for "q". Changing the applied signal to a negative pulse sending "holes" reverse the figure. The steep slope is the first signature of a very small probability to affect the Fermi Sea while transferring a non-negligible number of particles. The difference between non-integer and integer charge transfer is theoretically expected to be weak and is considered in section 4.2.

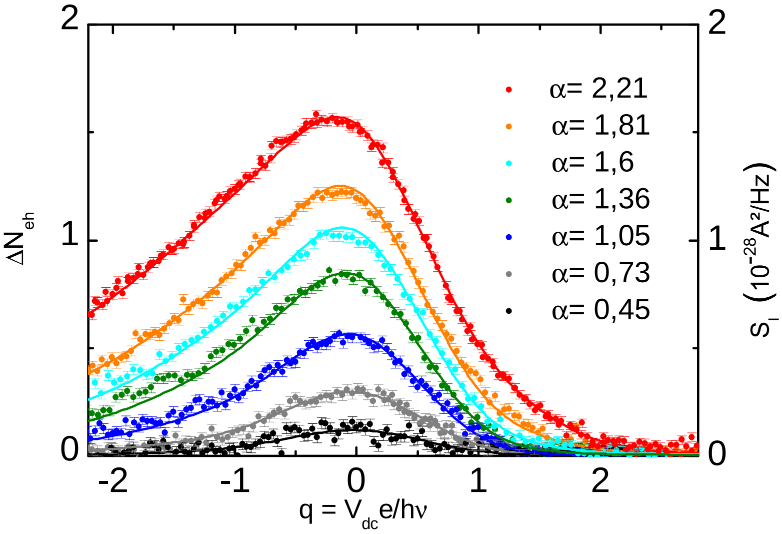

FIGURE 4.6 – Lorentzian pulse with width $W/T = 0.09$ and 6 GHz. The QPC transmission is D∼0.19

4.1.4 Effects of temperature increase

Details about the model

All theoretical curves used to interpret the experimental data take into account the possibility for the Joule effect to induce a temperature increase according to :

$$T_e(V_{ds} + V_{ac}(t)) = \sqrt{T_e(V_{ds} = 0)^2 + \alpha_{WF}(V_{ds}^2 + < \overline{V_{ac}(t)^2} >^t)} \tag{4.3}$$

With α_{WF} derived ab initio and given as :

$$\alpha_{WF} = \frac{6e^2}{\pi^2 k_B^2} \frac{R_c D G_q}{4} (1 + \frac{R_c D G_q}{2}) \tag{4.4}$$

It was found that small discrepancies between the experimental data and the theoretical expectations could be well accounted for using a value of α_{WF} based not on the total resistance R_c measured for the mesa and the contacts in series with the QPC, but on a slightly different resistance. The experimental R_c was 400Ω and the best agreement was found with 600Ω. The difference might be a consequence of an error on R_c (see method and comment in section 2.3). There is no clear answer about this issue to date. However, we show in this section that this leave all relevant conclusions unaffected.

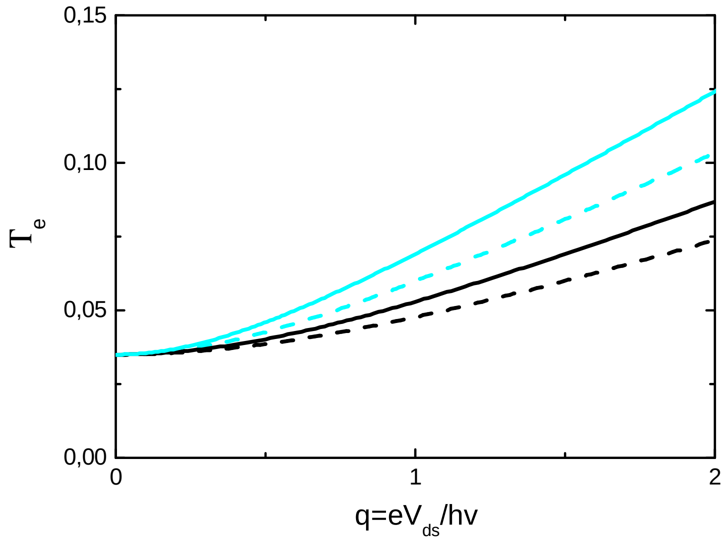

FIGURE 4.7 – Temperature increase as appearing in the proposed model for the experimental data. The signal is a "sine" pulse at 16 GHz(black line) or 24 GHz(blue line), both represented only with $\alpha = q$. The temperature appearing in the proposed model for the DC Shot Noise experiment with the same average current is represented with the dashed line.

In previous work with QPC, for instance [78] or [37], the tunable transmission has been used extensively to validate the model for the heating effect through the noise increase under DC bias when no shot noise can occur (on each conductance plateau). In section 2.6.6, we mentioned the presence of an additional noise power from the Joule effect in the measurement resistor. It prevents this method, as it evolves also with the DC bias [5]. A measurement with power from a GHz excitation only might solve this issue. Indeed this signal do no reach the measurement resistor (see Fig. 3.1).

The temperature increase appearing in the proposed model for the 16 GHz sine wave, 24 GHz sine wave, and 6 GHz lorentzian pulse with W/T=0.09 are plotted in Fig.4.7 and 4.8. These are the experiments in which charge injection is performed with a significant Joule Power.

---

[5] See Appendix C.

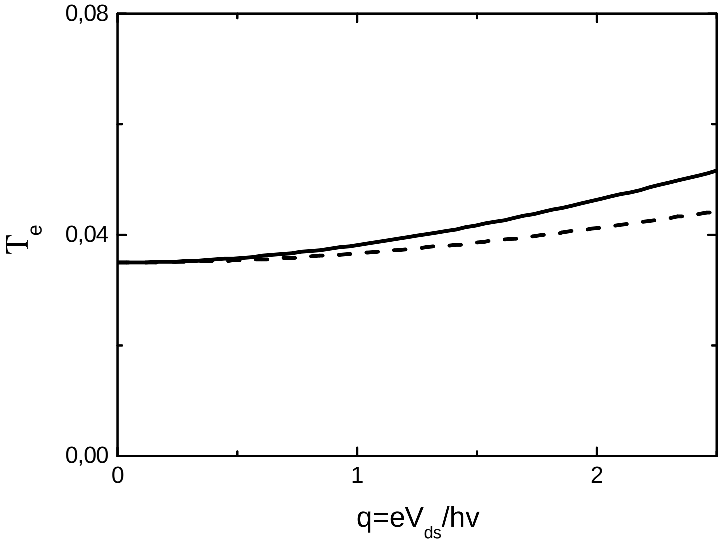

FIGURE 4.8 – Temperature increase as appearing in the proposed model for the experimental data (black line). The signal is a periodic train of Lorentzian pulses at 6 GHz and width W/T=0.09 and is represented only with $\alpha = q$. The temperature appearing in the proposed model for the DC Shot Noise experiment with the same average current is represented with the dashed line.

Do we have to consider the thermal noise of the reservoirs ?

We consider in this work an experimental subtraction between data from a noise measurement with an AC pulse and data from a measurement with a DC bias only. As such, one of the most important point is the small amplitude of the temperature increase between the two situations. Otherwise, the thermal noise of the reservoirs $4k_BT_eD^2G_q$, normally rejected thanks to the ON-OFF subtraction, would start to play a role. We can use the model to evaluate this quantity in our experiences. The injection excess noise analyzed in the next section for the Lorentzian pulse with $q = \alpha$=1 is about $\sim 10^{-29}$A^2/Hz whereas the impact from the change in experimental temperature would be about $\sim 10^{-31}$A^2/Hz. The predicted temperature is about 40 mK[6].

If we consider the two sinusoidal AC signals, the situation is also acceptable. We find a noise increase possibly due to a change in temperature of typically $\sim 10^{-30}$A^2/Hz (at 16 GHz) or $\sim 2 \times 10^{-30}$A^2/Hz (at 24 GHz) when the excess noise to be explained is respec-

---

[6] This prediction is typical for values of R_c from 400Ω to 600Ω.

tively $\sim 2 \times 10^{-29} \mathrm{A}^2/\mathrm{Hz}$ or $\sim 3 \times 10^{-29} \mathrm{A}^2/\mathrm{Hz}$. Therefore, the temperature increase cannot be misinterpreted as the dominant effect.

4.2 Charge injection

We now analyze the excess noise level[7] associated to an on-demand charge injection using voltage pulses. It corresponds for all pulses to the case $\alpha = q$.

4.2.1 Comparison between pulse shapes

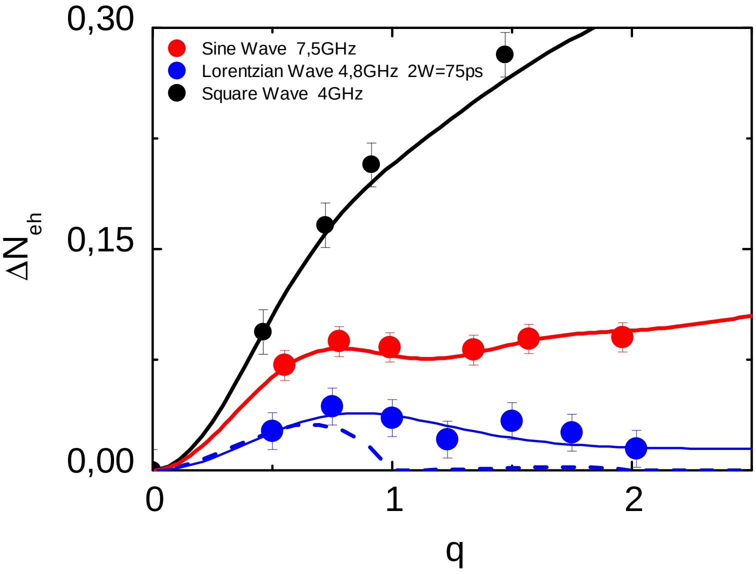

FIGURE 4.9 – Arbitrary Charge Injection.

We report on Fig. 4.9 the noise level associated to the square pulse 4 GHz, the sine wave 7.5 GHz and the Lorentzian pulse 4.8 GHz. Due to the temperature, the noise level is only an estimate of the number of particles undergoing photo-assisted energy change. However three different behaviors appear clearly. The square pulse shows a rapidly increasing number of excess particles with no trace of plateauing. This number stabilizes at an intermediary level for the sine-wave. Eventually, the Lorentzian pulse stabilize at an even lower level[8]

---

[7] Extended technical information about the error bar can be found in Appendix G.

[8] The presence of small unexplained variations does not allow to confirm the asymptotic behavior, but

All these noise levels are in good agreement with the model for these shapes and energies. These three pulses belong to three different categories of pulse injection. The distribution of the $P_l(\alpha)$ has for each family a different evolution with the number of photons "l". A more quantitative analysis is possible and proposed at the end of next section.

4.2.2 High characteristic energy and quantum signatures

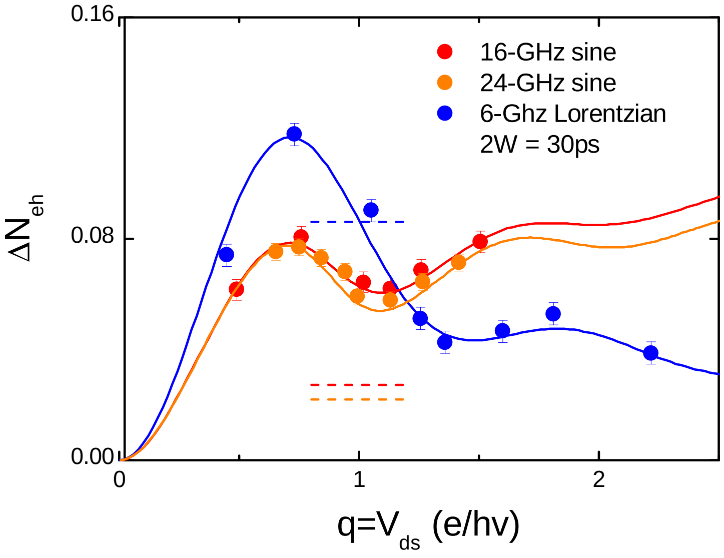

FIGURE 4.10 – Signature of orthogonality catastroph. Full lines indicate the PASN theory including the Joule effect for the 16 GHz(red) sine wave, 24 GHz sine wave(orange) and 6 GHz Lorentzian pulse(blue). Dash lines show the noise level explained by the mechanism in Eq. 4.5 and experimental data are marked with dots.

We consider now a second set of experiments. We report on Fig.4.10 the noise level associated to two sine waves at 16 GHz and 24 GHz, and a Lorentzian pulse 6 GHz and W/T=0.09. They have in common a small ratio θ_e and, in the case of the Lorentzian pulse, a high typical energy $2W/\hbar$ compared to the temperature scale.

---

the observed number of excess particles per pulse is still compatible with a vanishing excess noise for high currents.

Overview

In reduced units (both vertical and horizontal scales contain a factor $1/\nu$), the two experimental curves for sine waves are mostly identical. This shows that the number of particles is not a property of the AC amplitude, but of the average charge per pulse (or equivalently the flux per pulse). As the agreement with the theoretical expectations indicates, the slightly higher noise level for the 16 GHz-wave can be explained by the lower ratio between the thermal energy $k_B T$ and the typical energy $\mathrm{h}\nu$. While both pulse shapes lead to local maxima an minima, the general behavior is clearly different, especially when we consider the asymptotic trend for an increasing current.

Local minima

All three curves show a local minimum. It is well-marked and slightly above $q = 1$ for the two sine excitations. It is around $q = 1.4$ for the Lorentzian pulse. The existence of such extrema was commented in section 1.4. They are the consequence of the opposition between the charge being a finite quantity carried by individual particles and the continuous control on the average transmitted charge allowed by the voltage. When trying to inject an arbitrary charge from a given set of carriers, a complex combination must be used. This point is analyzed in [84][90]. The sharp inversion point near $q = n$ reflects a dynamical analog of the Anderson orthogonality catastrophe[4].

To be precise, the zero temperature theory predicts a minimal number of excess particles at integer values for $q = \alpha$. As the agreement with the model indicates, both the displacement of this minimum toward higher values q=α of and the contrast are well-explained by finite-temperature PASN theory. This was commented in details in section 1.4.3, and we have applied here the previously developed arguments. Qualitatively, there is a finite probability for the photo-excited particles in the left reservoir to stay close to the Fermi level. In that case, they are partitioned according to the presence or absence of thermally excited particles from the other reservoir. Similar oscillations were observed very recently with an Al/Al oxide/Al tunnel junction[45].

Pulse shape and clean/unclean charge injection

When analyzing the evolution of the noise level introduced by finite temperature, we have determined the weight $\omega(l, q, \theta_e)$ of each of the probability P_l.

$$\begin{aligned}\Delta N_{eh}(\alpha,q,\theta_e)-\Delta N_{eh}(\alpha,q,0) &= \sum_{l=-\infty}^{+\infty}((l+q)coth(\frac{l+q}{2\theta_e})-qcoth(\frac{q}{2\theta_e})-|l+q|+|q|)\mathrm{P}_l \\ &= \sum_{l=-\infty}^{+\infty}\omega(l,q,\theta_e)\mathrm{P}_l \qquad (4.5)\end{aligned}$$

Eq. 4.5 defines the partition noise of the thermal excitations emitted by the right-hand reservoirs[9], which must appear even in the absence of photo-emission, i.e. even for a Lorentzian pulse. As we are in the regime $q/\theta_e \gg 1$, it depends only on two quantities confirmed by the energy spectroscopy. Near $q = 1$, this extra contribution is :

$$\Delta N_{eh}^{extra} = 2\theta_e P_{-1} \qquad (4.6)$$

For the Lorentzian pulse in Fig. 4.10, the observed noise 0.09 ± 0.01 can be entirely explained by this contribution $2\theta_e e^{-4\pi w\nu}$=8.6% ($T_e = 39$ mK according to section 4.1.4). This is not the case for the two sine waves at 16 GHz and 24 GHz. $\Delta N_{eh}^{extra} \sim 2\theta_e J_{-1}(\alpha)^2$=2.3% and 2.6% (with T_e =52 mK and 68) does not explain the observed ΔN_{eh} 6% and 6.4%.

Although the noise level at $q = \alpha = 1$ is higher for the studied Lorentzian pulse than for the sine waves, their excess noise levels before and beyond this value follow two different trends. It corroborates the two different interpretations for this noise level. For a sine wave, it is stable since hole-creation, described by the series $P_{l<-n}(n)$, does not tend to zero.

Eventually, it is interesting to notice that despite the difficulty to observe quantum oscillations with the charge, a similar analysis for the pulses in Fig.4.9 shows also a remarkable agreement with the theory. The finite noise 3.7± 1.2% found for the 4.8 GHz Lorentzien at $q = 1$ can be explained by $\Delta N_{eh}^{extra} \sim 2\theta_e e^{-4\pi w\nu} \sim 3.4\%$ ($W/T = 0.183$ and $\theta_e = 0.17$). By contrast, we expect $\Delta N_{eh}^{extra} \sim 2\theta_e J_{-1}(\alpha)^2$ to be about 3.9% for the sine wave 7.5 GHz, which cannot accounts for the observed 8%.

These results demonstrates all the main aspects of pulsed injection down to a few particles : the typical energy of the excited particles, their statistical distribution, the minimal noise with integer charges and the absence of photo-emission processes for a Lorentzian pulse. These are all the ingredients needed for the minimal-excitation state existence, the Leviton.

---

[9] See details in chapter 1 and Eq.1.41

4.2.3 Effects of shape approximation ?

Applied Voltage

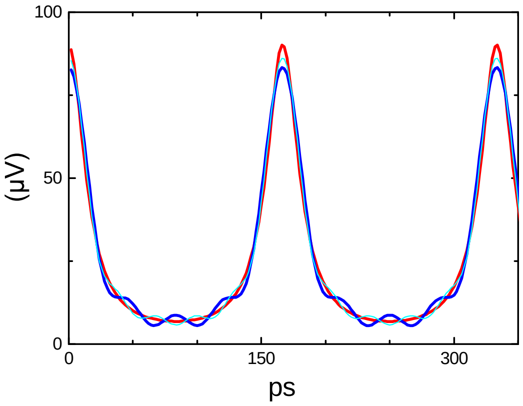

FIGURE 4.11 – Applied voltage modifications for a Lorentzian with low-pass filtered harmonic content and $W/T = 0.09$. Unfiltered signal (red line). Cut-off frequency at 4.5ν (dark blue line). Cut-off frequency at 5.5ν (cyan blue line).

In this section we use additional numerical simulation in order to compare the pure Lorentzian pulse and the approximation with the first four harmonics only. A periodic train of Lorentzian pulses has the following Fourier decomposition :

$$V_p(t) = \alpha \left(1 + 2 \sum_{l=1}^{+\infty} cos(2\pi l \nu t) e^{-2\pi \nu l w} \right) \tag{4.7}$$

The weight of high harmonics decrease exponentially. The width W/T is the key parameter to evaluate how important is the truncated part. For instance with W/T=0.183, the term $l = 2$ brings correction whose amplitude is limited to 13% of the total amplitude from the two lower harmonics. With W/T=0.09, we are at 7% when $l = 4$ and 3.5% when $l = 5$. This is illustrated in Fig. 4.11.

Zero and Finite Temperature temperature

The excess noise for the 4-harmonics is quantitatively very close to the ideal pulse when W/T=0.09, with a level of injected particles very close to zero at integer value of q. Note that the choice of an arbitrary number of frequencies has no effect on the average value.

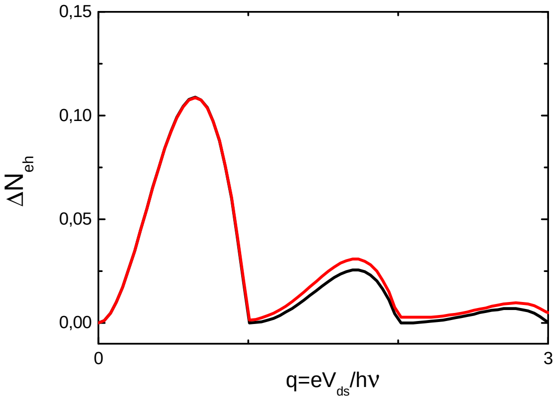

FIGURE 4.12 – Excess number of particles when attempting repeated charge injection from a pulse. Calculated excess noise for a pure Lorentzian with W/T=0.09(black line) and a partially transmitted pulse with cut-off frequency 4.5ν (red line). $T_e = 0$

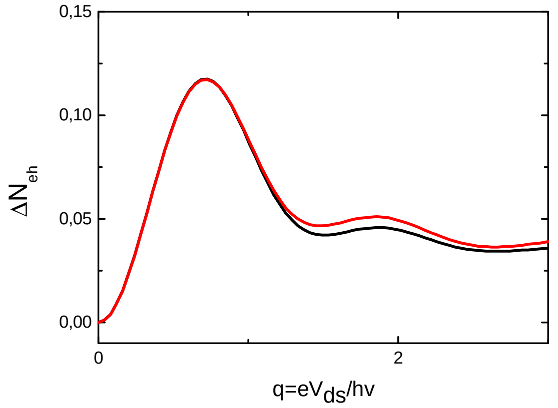

FIGURE 4.13 – Excess number of particles when attempting repeated charge injection from a pulse. Calculated PASN excess noise for a pure Lorentzian W/T=0.09 (black line) and a partially transmitted pulse with cut-off frequency 4.5ν (red line). The temperature scale $\theta_e = 0.12$ reflects the experimental situation.

The difference is especially difficult to observe in a experiment at finite temperature and in presence of Joule heating. Given the error bars achieved for the results proposed in the next section, these small differences from the ideal case are unfortunately unrealistic to discuss. The situation is summarized by numerical simulations in Fig.4.12 and 4.13.

4.3 Time-domain noise spectroscopy

4.3.1 Experimental Results

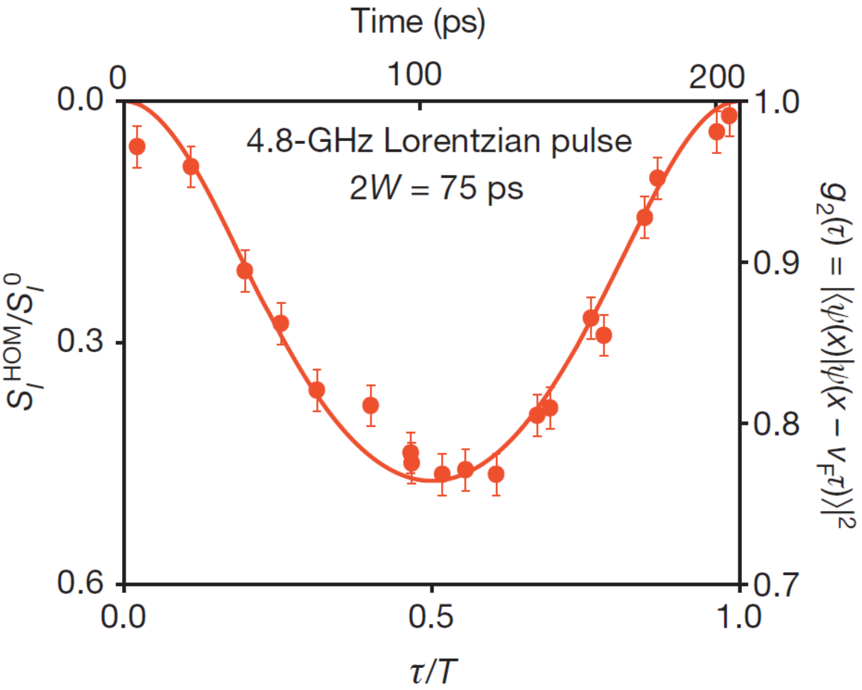

FIGURE 4.14 – Quantum overlap from time-spectroscopy. Lorentzian pulse 4.8 GHz with width W/T 0.183. QPC transmission D=0.3

Finally, to get time-domain information on the Leviton wave-packets, we perform the time-spectroscopy as presented in section1.6. It requires to use a DC–18 GHz power-divider and a phase-shifter in order to send the 4.8 GHz pulse simultaneously on the two contacts with a controlled time-delay. Fig. 4.14 shows that the expected time-dependency is indeed observed in the noise. It reflects the time extension of the on-demand injection. When the two contacts are driven in phase, the Fermi sea is in the same state on both sides of the scatterer and no Fermion can be randomly partitioned : all scattering events must associate two electrons through anti-bunching. On the contrary, the largest separation induce the maximal noise.

Using the 4.8 GHz Lorentzian generated from the Tektronix AWG sacrificed good time-separation of charge pulses for the possibility to have a similar AC signal on both lines, i.e. for the possibility to control all meaningful frequencies. The two lines are known to be only partially identical in practice. The transmissions are close for the first two harmonics, but the third frequency 14.4 GHz (with a very small influence on the P_l distribution for W/T=0.183) was almost not transmitted by the second line. The theoretical curve on Fig.4.14 is based on identical ideal Lorentzians at finite temperature. In the newt section, we show that this measurement is not only a proof of on-demand injection, but also a measurement of the quantum overlap between Levitons.

4.3.2 Wavepacket Interpretation and train of Levitons

When we are applying N successive Lorentzian pulses, strictly N electrons are transferred. But the total wavefunction is not the sum of the independently excited wave-functions. In the time-spectroscopy experiment with a repetition frequency small compare to the typical width of the pulses, we are not measuring a single wave-packet, but a property of the total wave-function. Despite this, we show here that the quantity appearing in the noise measurement Fig. 4.14 is still a quantum overlap. It proves that the time-spectroscopy gives exactly the time-extension of a train of Leviton-like excitation.

As demonstrated in section 1.2.2 using the Floquet formalism, all states are scattered from the energy window $[(l-1)h\nu, lh\nu]$ to the energy window $[(m-1)h\nu, mh\nu]$ with probability amplitude p_{l-m}. The basis inside each window can be chosen according to our need. Following the calculations proposed in [38], we use the wave-packets description from Martin and Landauer[96]. Instead of the continuous variable $\varepsilon_0 \in [-h\nu, 0]$ we use the number $n \in \mathbb{Z}$ and replace the wavefunction $e^{-i(t-x/v_F)(\varepsilon_0+lh\nu)/\hbar}$by the orthogonal wave-packets $\varphi_{n,l}(t-x/v_F)$ [10].

$$\varphi_{n,l}(t-x/v_F) = \frac{1}{\sqrt{2\pi\hbar v_F}} \frac{sin(\pi(u-n))}{\pi(u-n)} e^{-i2\pi(l+1/2)(u-n)} \tag{4.9}$$

With u=$(t-x/v_F)/T$.

The quantity which gives information on the probability amplitude to find a particle at a point x and at time t is the Fermionic field operator.

---

[10] The unitary transformation is defined by :

$$\varphi_{n,l}(t-x/v_F) = \frac{1}{h\nu}\int_{-h\nu}^{0} d\varepsilon_0 \;\; e^{i\varepsilon_0 2\pi n} e^{-i(t-x/v_F)(\varepsilon_0+lh\nu)/\hbar} \tag{4.8}$$

Using the annihilation operators $\hat{a}^0_l$ associated to φ^F_l and acting on the Fock states in the reservoirs, this operator in the absence of pulse is :

$$\hat{\Psi}^0(t - x/v_F) = \sum_l \varphi^F_l(t - x/v_F)\hat{a}^0_{l,n} \tag{4.10}$$

$$= \sum_l \sum_n \varphi_{n,l}(t - x/v_F)\hat{a}^0_{l,n} \tag{4.11}$$

In the presence of a pulse it is :

$$\hat{\Psi}(t - x/v_F) = \sum_l \sum_n \sum_k \varphi_{n,l}(t - x/v_F)p_k\hat{a}^0_{l-k,n} \tag{4.12}$$

Where we have used the fact that the ac potential does not mix wave-packets of different values of n. We can now calculate the quantum overlap between two train of pulses with a delay $\theta = \tau/T$.

$$< \hat{\Psi}^\dagger(u + \frac{\theta}{2})|\hat{\Psi}(u - \frac{\theta}{2}) >=$$

$$\int_0^1 du \sum_{l'l} \sum_{nn'} \sum_{kk'} \overline{\varphi_{n',l'+k'}(u + \frac{\theta}{2})}\varphi_{n,l+k}(u - \frac{\theta}{2}) < \hat{a}^{0\dagger}_{l',n'}\hat{a}^0_{l,n} >$$

We have $< \hat{a}^{0\dagger}_{l',n'}\hat{a}^0_{l,n} >= (2\pi\hbar v_F)\delta_{nn'}\delta_{ll'}f_l$. The factor f_l is zero if $l > -1$. We can subtracts the correlations in the Fermi Sea (i.e. the amplitude also found from the same calculation without ac potential), we find :

$$| < \hat{\Psi}^\dagger(u + \frac{\theta}{2})|\hat{\Psi}(u - \frac{\theta}{2}) > - < \hat{\Psi}^{0\dagger}(u + \frac{\theta}{2})|\hat{\Psi}^0(u - \frac{\theta}{2}) > |^2$$

$$= |\frac{sin(\pi\theta)}{\pi\theta}|^2 C(\tau) \tag{4.13}$$

Where :

$$C(\tau) = |\sum_{l=-\infty}^{-1} e^{i2\pi l\theta} \sum_k (P_k - \delta_{k,0})e^{i2\pi k\theta}|^2 \tag{4.14}$$

The factor $|sin(\pi\theta)/\pi\theta|^2$ corresponds to the overlap over the x-axis between two electrons spread over an energy window $[-h\nu, 0]$and delayed by τ. It prevents the calculated operator from being periodic, which does not correspond to a possible measurement. Summing over all $(\theta = \theta_0 + m)$, we can observe that this term gives a constant factor equal to 1. The calculation is written for any photo-assisted distribution P_k after a purely ac voltage. As in previous calculations, the outcome of a charge pulse with a finite average voltage can be found using a shifted Fermi sea. When the average voltage imposes an integer number of transferred charges per pulse n, we can equivalently use the occupation numbers $P_k^{tot} = P_{k-n}$.

Using the P_k amplitude for a Lorentzian pulse with $\alpha = n = 1$[11], we have :

$$\begin{aligned}
P_k^{tot} =& 0 && for\ \ k < 0 \\
P_0^{tot} =& exp(-4\pi W/T) = \beta^2 && \\
P_k^{tot} =& \beta^{2(k-1)}(1-\beta^2)^2 && for\ \ k > 0
\end{aligned}$$

And thus :

$$C(\tau) = \frac{(1-\beta^2)^2}{1 - 2\beta^2 cos(2\pi\tau\nu) + \beta^4} \tag{4.15}$$

This quantity appears in the time-spectroscopy noise for the train of Lorentzian pulses $\alpha = 1$ derived in Eq. 1.49.

This generalization shows that the proposed time-spectroscopy has measured the quantum overlap of a train of Levitons :

$$\frac{S_I^{HOM}}{S_I^0} = 2(1 - C(\tau)) \tag{4.16}$$

The finite-temperature does not change this interpretation. This counter-intuitive result is shown in chapter 6 and compared to experiments.

4.4 Conclusion

We have investigated the excited particles resulting from a voltage pulse in a coherent conductor and how their number depends on the pulse shape. The distribution of photo-assisted process predicted from quantum transport theory has been compared to expe-

---

[11] See Section 1.4.1

riments for square pulses, sine pulses and lorentzian pulses. The quantization of photo-assisted energy-shifts and charge granularity can be observed, demonstrating that they determine the system state. The observed PASN can be completely understood in all cases by taking into account the finite temperature. The suppression of photo-emission for a Lorentzian pulse with quantized flux compared to all other situations can thus be confirmed from the noise level when the transmitted charge per pulse is 1. The energy and time-domain distribution for the excitation wave-packet both agree with the leviton expected properties. Our experiments have achieved less than $\sim 1\%$ of extra excitation, which makes our system an on-demand source suitable for interference experiments with a few electrons.

Chapitre 5

Toward a full tomography of a quantum state with photo-assisted shot noise : leviton

In chapter 4, energy spectroscopy, electron-hole content analysis and time-spectroscopy are combined to bring evidence for the formations of the minimal excitation state, the leviton. The current fluctuations in these experiments are fully described by the probability distribution $\{P_l = |p_l|^2\}$.

But a quantum state such as the leviton can only be fully described by the set of complex probabilities amplitudes or by the knowledge of the energy density matrix, which involves the quantities $p_l\overline{p_{l'}}$ $(l \neq l')$, obviously not limited to the set $\{P_l = |p_l|^2\}$. Finding these coefficients is the purpose of a Quantum State Tomography (QST).

Over the years, experimental schemes have been found which have allowed to perform such a QST on various families of degrees of liberty : atomic orbitals[5], light field [134], vibrational modes of a molecule[40], discrete levels of atoms in a potential well[85]. Recent results with an entangled spin-photon qubit[31] illustrates the high interest of such a measurement in quantum information with solid state qubits[92]. The key step of preparing a system in a controlled and reproducible way must include all phases, and two-states entanglement is characterized through the density matrix.

In order to reconstruct the orbital states of an electron in a quantum conductor, the DC shot noise combined with tunable beam-splitters has been proposed by Samuelsson et al.[127]. A PASN-based scheme analogous to an Optical Homodyne Tomography[134] for the output state of a mesoscopic capacitor source is detailed in [55]. This could probe the decoherence along a short chiral edge channel. Here, a similar idea is applied to the simplified geometry of a QPC with a spin-degenerate channel, and we analyze the excited Fermi sea after a voltage pulse on a contact.

In section 5.1, we indicate how the full matrix $\overline{p_l}p_{l'}$ can be extracted from noise measurements. In section 5.2 we report our experimental results for a Lorentzian pulse at 6 GHz with a FWHM $2W = 30\,\mathrm{ps}$ and sending one electron, in order to achieve the full characterization of leviton. As explained in the last section 5.3, these measurements should allow to reconstruct the energy density matrix.

5.1 Principle

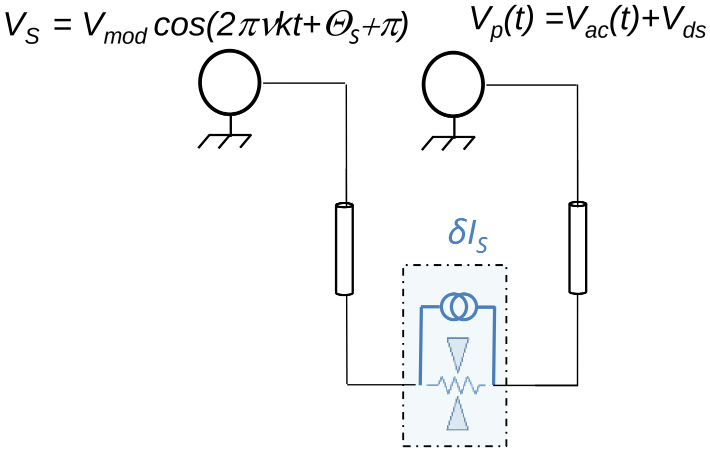

Figure 5.1 – Principle of a tomography experiment. A first voltage source is used to apply a pulse $V_p(t)$ on a contact. A purely harmonic source $V_S(t)$is connected to the second contact, with a small peak-peak amplitude $2V_{mod}$ compared to $V_p(t)$. The QPC has a transmission between 0 and 1 in order to generate shot noise.

Single electron properties in a periodically AC-driven conductor are expressed through the transformation of the right-moving annihilation operator.

$$\hat{a}_L^F(\varepsilon', l) = \sum_{m=-\infty}^{+\infty} p_{l-m}\delta(\varepsilon' - \varepsilon'')\hat{a}_L(\varepsilon'', m) \tag{5.1}$$

We consider the set-up in Fig. 5.1. A periodic voltage $V_p(t)$ applied to the left contact with an arbitrary DC level $q = eV_{ds}/h\nu$.

The transmission is selected between 0 and 1 in order to generate shot noise.

The bias at the scatterer is modulated using a second voltage source connected to the right contact. This signal $V_S(t) = V_{mod}cos(2\pi k\nu t + \Theta_S + \pi)$ is purely harmonic, it has a small peak-peak amplitude compared to the pulse and its average is zero. k is a strictly positive integer and ν is the pulse repetition frequency. The phase Θ_S can be changed.

5.1.1 Small amplitude development

Under the usual assumption of energy-independent transparency, the noise can be calculated as if a single voltage source $V_p(t) - V_S(t)$ was connected to the left contact, and no voltage applied to the the right contact.

The scattering amplitude are therefore associated with :

$$\tilde{p_l} = \frac{1}{T}\int_0^T dt e^{-i\phi(t)} e^{il2\pi\nu t} e^{i\int_0^t 2\pi k\eta_k\ cos(2\pi k\nu t+\Theta_S+\pi)} \tag{5.2}$$

$$\tilde{p_l} = \frac{1}{T}\int_0^T dt e^{-i\phi(t)} e^{il2\pi\nu t} e^{-i\eta_k\ sin(2\pi k\nu t+\Theta_S)} e^{i\eta_k\ sin(\Theta_S)} \tag{5.3}$$

η_k is $V_{mod}\, e/(hk\nu)$ with e the elementary charge and h the Planck constant. η_k is the scale of the modulation in e/period. The last phase factor $e^{i\eta_k\ sin(\Theta_S)}$ plays no role and it will be dropped from now on. Indeed, the energy-spectroscopy experiment is only sensitive to $|\tilde{p_l}|$. To maintain consistency with the previous chapters, we maintain the definition of the p_l distribution as the Fourier components of the phase variation $exp(-i\phi(t))$ under the AC part of the pulse only. We note $\tilde{p_l}$ these components in the modulated situation. We develop the last exponential factor in Eq. 5.3 to the first order in η_k. After integration :

$$\tilde{p_l} = p_l - \frac{\eta_k}{2}(p_{l+k}e^{i\Theta_S} - p_{l-k}e^{-i\Theta_S}) \tag{5.4}$$

We know from chapter 1 that a noise spectroscopy will provide the quantities :

$$|\tilde{p_l}|^2 = |p_l|^2 - \eta_k Re\left(\overline{p_l}(p_{l+k}e^{i\Theta_S} - p_{l-k}e^{-i\Theta_S})\right) \tag{5.5}$$

Where again we have kept only the first order in η_k.

5.1.2 Expressions

We show in this section how we can extract full information about the complete numbers p_l when varying the phase Θ_S and the frequency $k\nu$ of the additional modulation. Calculations are first presented at zero temperature.

The noise difference (positive or negative) in presence or absence of the additional voltage modulation is found from Eq. 1.26.

$$\Delta S_I^{Tomo}(q) = S_I^0 \sum_{l=-\infty}^{+\infty} |l+q| \left[|\tilde{p}_l|^2 - |p_l|^2 \right] \tag{5.6}$$

We can extract individually each term in the sum using the second derivative along q at $l = -q$, imitating Eq. 1.28. Only two values for Θ_S give independent information : 0 and $\pi/2$. They provide respectively :

$$\begin{aligned} \Theta_S &= 0 && \rightarrow -Re(\overline{p_l}p_{l+k} - \overline{p_{l-k}}p_l) && = A_{l,k} \\ \Theta_S &= \frac{\pi}{2} && \rightarrow -Im(-\overline{p_l}p_{l+k} + \overline{p_{l-k}}p_l) && = B_{l,k} \end{aligned}$$

We are interested in products $p_l\overline{p'_l}$[1]. Each line has the same structure : the difference between two identical products $p_l\overline{p'_l}$ shifted by k. If we sum $A_{l,k} + A_{l-k,k}$, i.e. the first line when $q = -l$ and the first line $q = -l + k$, two terms are compensated. We can repeat the operation with $A_{l-2k,k}$ and so on. High-energy transition under a finite-energy bias are unlikely. Physical consistency induces the existence of a cut-off frequency $mh\nu$ beyond which all products $\overline{p_{l-nk}}p_{l-nk-k<m}$ are negligible. Once this value is reached, we are left with only one term. The second line offers the same possibility. In the end :

$$p_l\overline{p_{l+k}} = -\sum_{r=0}^{r=+\infty} A_{l-rk,k} - i\sum_{r=0}^{r=+\infty} B_{l-rk,k} \tag{5.7}$$

5.1.3 Leviton wave-function analysis

If we implement the experimental protocol proposed in the previous section with an arbitrary pulse, we probe the single-electron correlation function of the system. The special case of the leviton is particularly interesting. For this situation, the scheme is analog to a single-particle QST. Indeed, as there is no hole and only one electron, its wave-function is

---

[1] The closely related density matrix is described in section 5.3

measured. We develop in this section the corresponding calculations. The photo-assisted amplitudes are labelled p_l^{Lev}.

First, the periodicity reduce the number of frequencies to be measured to a discrete set. The exponential law obeyed by the quantity p_l^{Lev} reduces also the number of frequency with a relevant statistical weight. Additionally, we also benefit from $p_{l<-1}^{Lev} = 0$. Finite-temperature is expected to introduce a statistical smearing discussed at the end.

We have for a leviton :

$$\begin{aligned}
p_{l<-1}^{Lev} &= 0\\
p_{l=-1}^{Lev} &= -\beta\\
p_{l>-1}^{Lev} &= \beta^l(1-\beta^2)
\end{aligned}$$

With $\beta = exp(-2\pi W/T)$. The amplitudes p_l^{Lev} have all the same phase (except the minus sign for l=-1), and they have been chosen real with no loss of generality. It corresponds to the choice of one pulse centered at t=0 and the flux chosen zero at t=0 (it makes $\phi(t)$ an odd and periodic function). We have the noise derivative :

$$\frac{\partial}{\partial q}\frac{\Delta N_{eh}^{Tomo}(q,\Theta_S)}{\eta_k} = \frac{\partial}{\partial q}\frac{\Delta S_I^{Tomo}(q)}{S_I^0\eta_k} = 2cos(\Theta_S)\sum_{l=-k-\tilde{q}}^{-\tilde{q}-1} p_l^{Lev}p_{l+k}^{Lev} \tag{5.8}$$

Where $\tilde{q}$ is the closest integer value inferior to q. All measurements with Θ_S in phase quadrature add zero noise to the first order in η_l. As $p_{l<-1}^{Lev} = 0$, the extraction algorithm takes a simplified form. Starting from $1 < q < 2$, we expect to find 0. Then, with $0 < q < 1$, we expect $p_{-1}^{Lev}p_{k-1}^{Lev}$. With $-1 < q < 0$ we extract $p_0^{Lev}p_k^{Lev}$, and so on. How the finite temperature affects noise amplitudes and slope can be evaluated as in section 1.4.3. If we compare expectations at finite temperature and zero temperature we have :

$$\Delta S_I^{Tomo}(q,\theta_e) - \Delta S_I^{Tomo}(q,0) = S_I^0\sum_{l=-\infty}^{+\infty}\left[(l+q)coth(\frac{l+q}{2\theta_e}) - |l+q|\right](|\tilde{p}_l|^2 - |p_l^{Lev}|^2) \tag{5.9}$$

The typical weight function $xcoth(x) - |x|$ have been analyzed in Fig. 1.12. The signal at each integer value of q [2] is typically shifted by $2\theta_e(|\tilde{p}_{-q}|^2 - |p_{-q}^{Lev}|^2)$ as long as $q/2\theta_e \ll 1$.

---

[2] This time the behavior near $q = 0$ does not requires a different formula. See section 1.4.3. The sign of the shift is directly given by the difference $|\tilde{p}_{-q}|^2 - |p_{-q}^{Lev}|^2$.

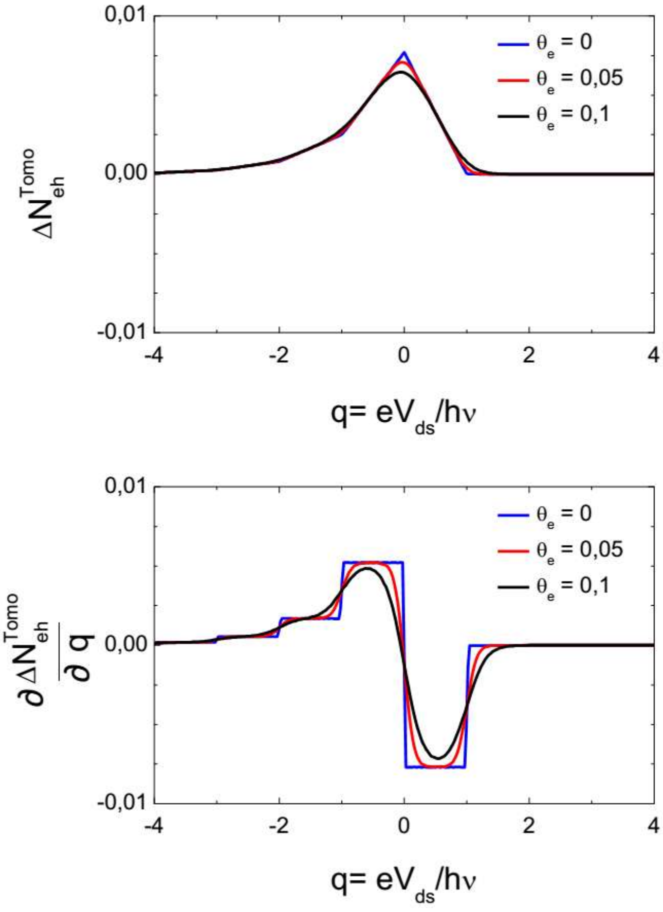

FIGURE 5.2 – PASN calculations for the minimal single-electron excitation and a sine modulation at various temperature θ_e =0, 0.05 and 0.1 (blue, red and dark curves). The sine wave amplitude is $\eta_{k=1} = 0.01$ with its frequency identical to the pulse frequency. The Lorentzian with amplitude $\alpha = 1$ has a width $W/T = 0,09$. The noise difference in reduced units ΔN_{eh}^{Tomo} between the noise found in presence and absence of the modulating signal is plotted at the top, its derivative at the bottom.

However, the proposed algorithm is based on the change of slope rather than the noise level. How the temperature affects this quantity is illustrated in Fig. 5.2.

Slopes in the DC sweep are minimally affected by θ_e when q is half-integer. The error when using the entire interval $[\tilde{q}, \tilde{q}+1]$ to evaluate Eq. 5.8 is typically bounded by the changes at the extremities.

5.2 Experimental Results

5.2.1 Experimental Set-up

The system for RF generation proposed and fully calibrated in chapter 3 is adapted to send a small phase-locked sine wave on the second contact of the QPC. The amplitude of this signal is a consequence of the pick-up method, and the amplitude on the sample is first approached using the attenuation coefficient in the lines and eventually slightly adjusted on the measurement. The path difference is modified through a phase-shifter. An active switch is used to turn ON or OFF the modulation signal.

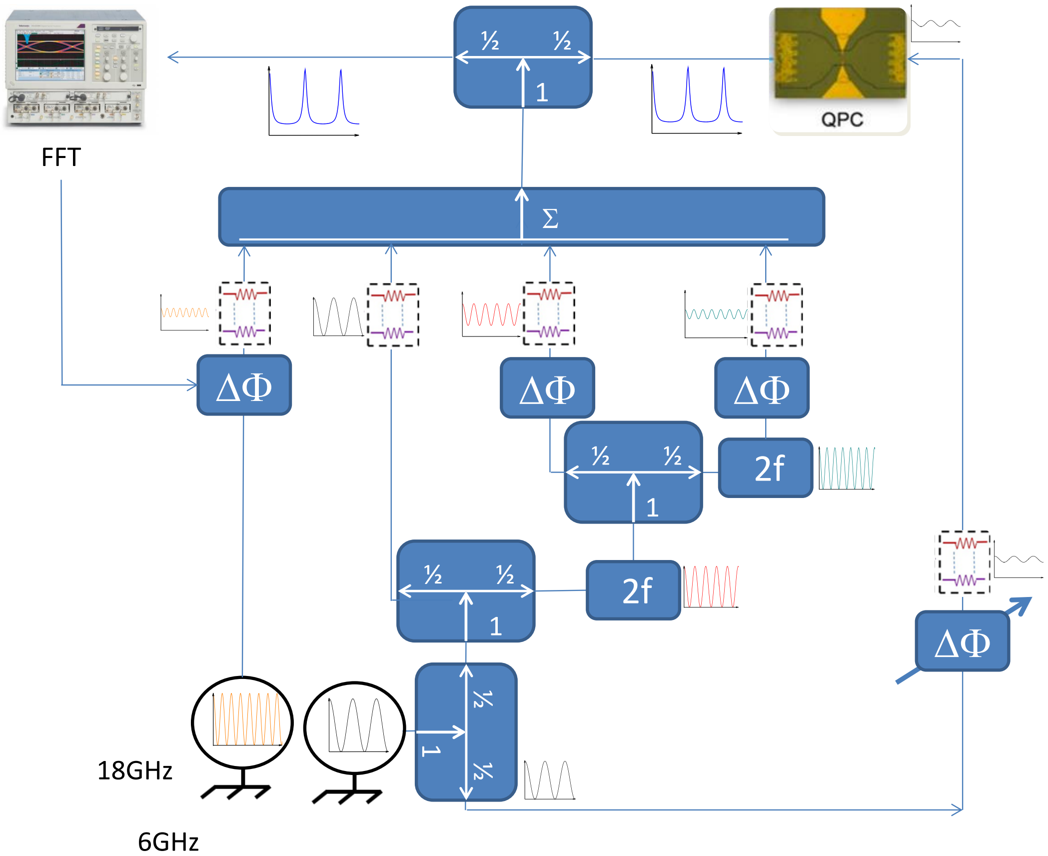

Figure 5.3 – RF generation for QST. The Lorentzian pulse(QPC left-contact) with cut-off frequency 4ν is generated using the compensation system of chapter 3. A phase-locked signal(QPC right-contact) at frequency $k\nu$ is picked up at the appropriate point in the line (for instance, the case $k = 1$ is represented on the figure). The modulation signal is filtered (pass-band or low-pass) to eliminate undesired harmonics on this side.

5.2.2 Phases

Experimental determination of the in-situ phase

We use modulation signal with frequencies $k\nu$, with $k = 1$ or $k = 2$. We perform first a complete sweep of the room temperature phase Φ for both frequencies. The typical ON-OFF difference between the noise level with or without modulated signal is plotted on Fig. 5.4 and 5.5.

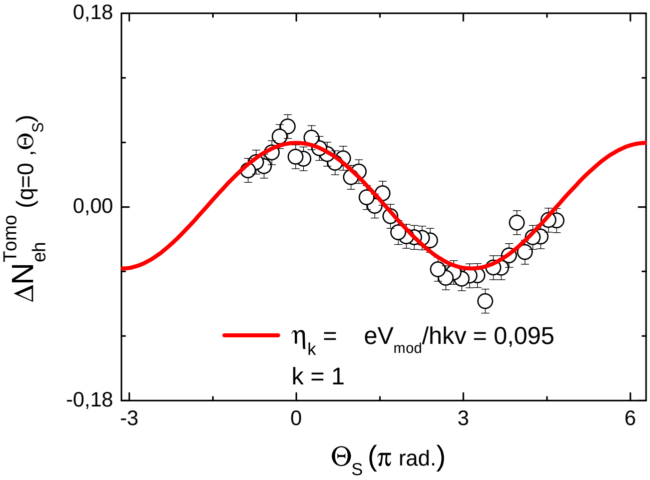

FIGURE 5.4 – Phase sweep. A Lorentzian ν=6 GHz, α=1 and a width $W = 0.09T$ is applied to the left contact of a QPC. A small harmonic signal at frequency ν is applied on the second contact. The reported noise amplitude is the difference between the experiment with and without this additional signal. The phase Θ_S on the contact is adjusted using a best fit based on the PASN calculation (red line). The QPC transmission is $D \sim 0.2$. The temperature should be stable for all measurements at $T_e \sim 37mK$ ($V_S(t)$ induces very limited power changes).

The results are in very good agreement with the theory and the cosine response $cos(\Theta_S)$ is observed. Finite-temperature is taken into account. Only one fitting parameters is introduced, the fixed difference introduced by the transmission lines between the room-temperature phase of the signal sources and Θ_S on the sample.

Analysis

Here we have to comment on a slight difference between the protocol proposed in the previous section and this adjustment with a best fit. If the applied phase Θ_S was known

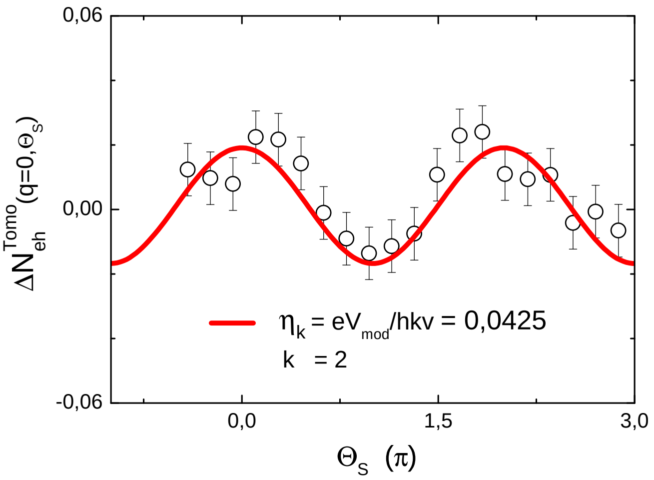

Figure 5.5 – Phase sweep. A Lorentzian ν=6 GHz, α=1 and with width $W = 0.09T$ is applied to the left contact of a QPC. A small harmonic signal at frequency 2ν is applied on the second contact. The reported noise amplitude is the difference between the experiment with and without this additional signal. The phase Θ_S on the contact is adjusted using a best fit based on the PASN calculation (red line). The QPC transmission is D ~0.25. The temperature should be stable for all measurements at $T_e \sim 37mK$ (V_S induces very limited power changes).

at first, we could confirm that all p_l^{Lev} are real from the absence of additional noise when $\Theta_S = \pi/2$. For experimental reasons, we favor another approach : we deduce Θ_S from this absence of noise. Experiments both in previous chapters and in the next section indicates the consistency of this choice[3].

5.2.3 DC sweep

We now perform the bias sweep when $\Theta_S = 0$. Fig. 5.6 show the experimental data points from the ON-OFF comparison, and the theoretical expectations based on PASN theory when we work with the first harmonic. Starting from $q = 2$, the noise variation is extremely low and does not start to increase until very close to $q = 1$. This is the sign of thermal effects rather than photo-assisted effects, and the slope is close to zero, as expected.

---

[3] However, it could have been avoided for instance by measuring the rectification of the AC current from two large Sine potentials at 6 Ghz and $k \times 6$ GHz, one applied on each contact. Indeed, it provides a phase-dependent measurable DC current. This purely classical effect has been mentioned in chapter 1. It is based on transmission non-linearities and applied power only, which is easily verified to vary as $cos(\Theta_S)$.

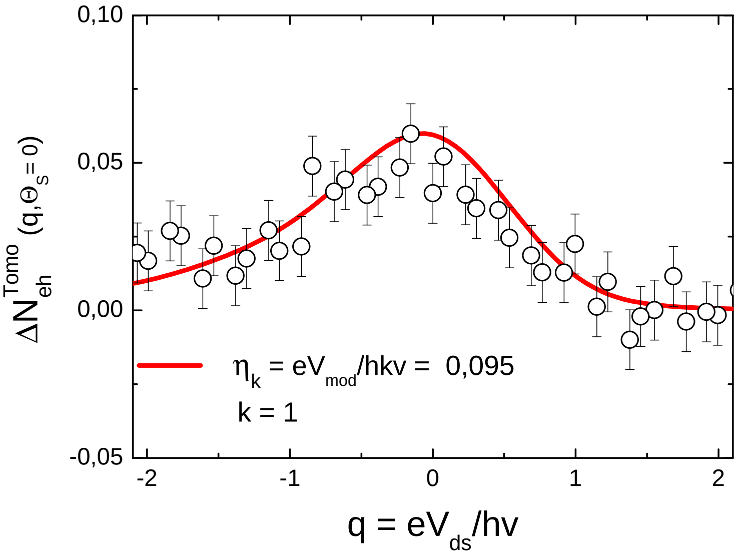

FIGURE 5.6 – Noise variations (black circles) when a Lorentzian $\alpha = 1$ is modulated with a small sine wave at frequency ν and with amplitude $\eta_{k=1} = 0.095$. The DC level is varied from $q = -2$ to 2. QPC transmission is D ∼0.2 and the temperature evolve from ∼37 mK to ∼42 mK when $|q|$=2. These effects are included in the PASN calculations (red line).

The slope is negative between $0 < q < 1$, which indicates that there is a difference in sign between p_0^{Lev} and p_{-1}^{Lev}. The rest cannot be analyzed without quantitative evaluation.

Fig. 5.7 shows now the experimental data points from the ON-OFF when we work with the second harmonic ($k = 2$). It confirms the conclusion about the change of sign between p_{-1} and p_1. We note that the low-level in both figure makes us very sensitive to parasitic events (far-away data points) and that the incertitude on the most interesting quantity, the slope in each section is affected. ΔN_{eh}^{Tomo} =0.01 at 6 GHz is equivalent to a noise variation $10^{-30} A^2/Hz$ when $D = 0.2$. At this point, we note that the p_l distribution must explain simultaneously all spectroscopy in this section and also 4.6 in chapter 4. How they could be combined in order to increase the precision on the p_l measurement is not precisely known. The set of measurements $k = 0$, $k = 1$ and $k = 2$ is also incomplete[4]. However, the general agreement between expectations and results is promising.

---

[4] In practice, the outputs of incomplete statistical measurements are usually compared to test density matrices, and the one which gives the best agreement with the results is chosen[28].

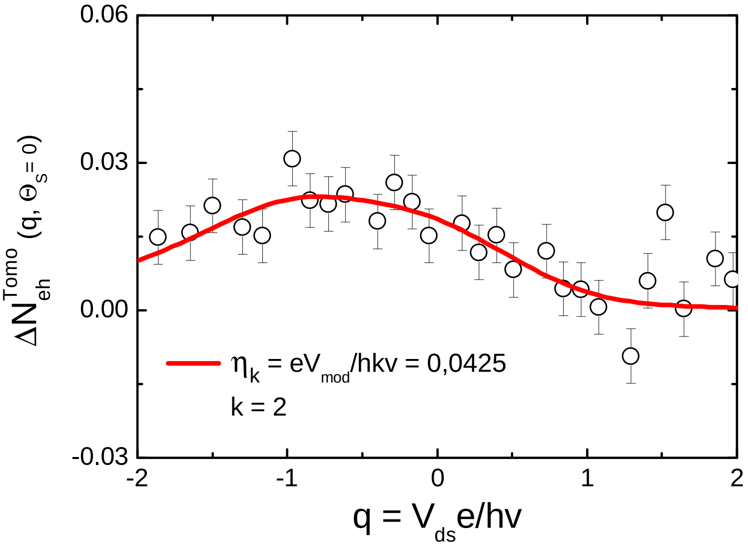

FIGURE 5.7 – Noise variations (black circles) when a Lorentzian $\alpha = 1$ and $W/T = 0.09$ is modulated with a small sine wave at frequency 2ν and amplitude $\eta_{k=2} = 0.0425$. The DC level is varied from $q = -2$ to 2. QPC transmission is D ∼0.2 and the temperature evolves from ∼37 mK to ∼42 mK when $|q|$=2. These effects are included in the PASN calculations (red line).

5.2.4 Note on method and reproducibility.

To eliminate the effect of small random drifts in the measurement systems and samples, and also spurious events modifying the transmission, the ON-OFF experimental comparison is used with typically 4 ON-OFF cycles of 20000 successive PSD for each data points (with the full 400 kHz bandpass). The experiment is also repeated several times. A single point with no AC signal to get the DCSN was always taken before changing to another value of q. That way we can check without ambiguity the system state. Fig. 5.8 shows this DCSN and the PASN from the leviton pulse only (state ”OFF”) during the measurement $k = 2$. Small deviations between ”passages” are consistent with changes in transmission, and can be precisely used to convert the noise in reduced units if necessary. For instance, to obtain Fig. 5.9, three measurements have been combined with a 3 points adjacent-averaging. The original data are on Fig. 5.9.

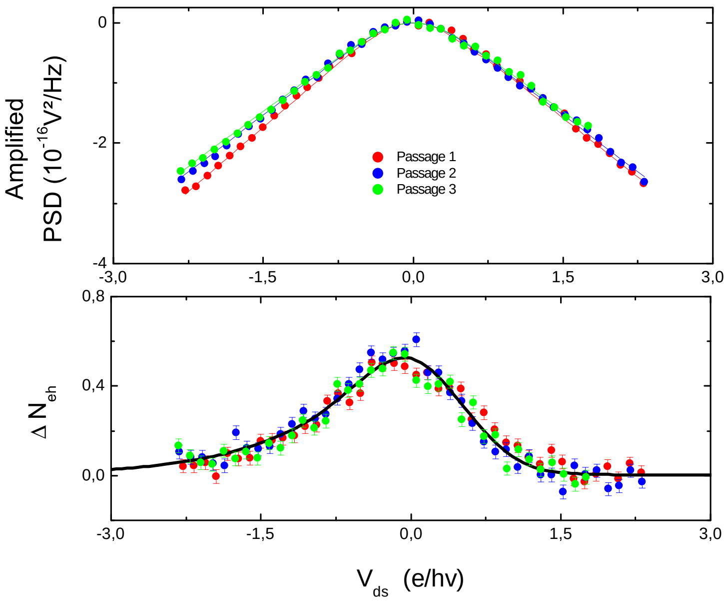

FIGURE 5.8 – Measurements checks during QST. DCSN (top part) and PASN from the leviton pulse (bottom part) are used to check the state of the system along the long-time averaging. Curves showing unexplained inconsistencies at this level have been eliminated.

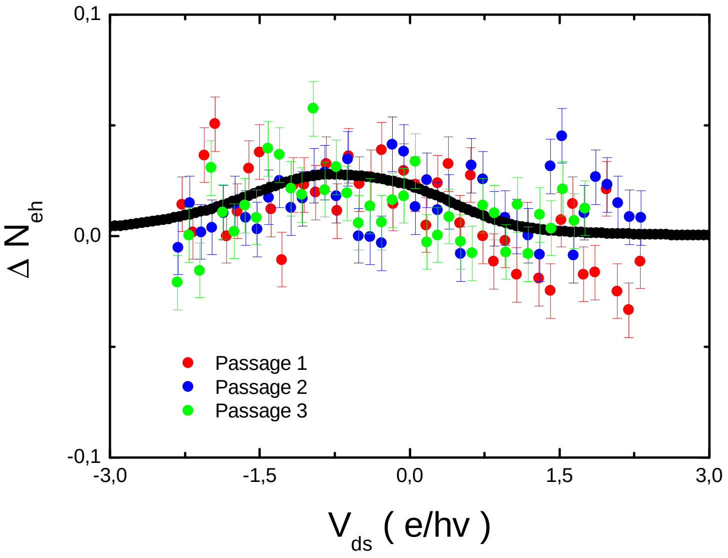

FIGURE 5.9 – Data post-treatment for QST. These three independents measurements are combined to obtain Fig. 5.7.

5.3 Toward a complete tomography

Our measurements could lead to a complete QST. The determination of the entire set of scattering amplitude $\overline{p_l'}p_l$ described in the previous section does not give directly the relation between the noise measurement and the fermionic correlator $< \varphi(t')^\dagger|\varphi(t) >$. This quantity is the analog of the electrical field correlator $< E^+(t')|E^-(t) >$ usually measured in quantum optics QST[93]. This quantity in the Floquet formalism was first derived by Grenier et al. in [55]. $< \varphi(t')^\dagger|\varphi(t) >$ can be decomposed into Fourier components :

$$
\begin{aligned}
&\langle \varphi^\dagger(t')|\varphi(t)\rangle - \langle \varphi^{\dagger 0}(t')|\varphi^0(t)\rangle = \\
&\quad = \int_{-\infty}^{+\infty}\int_{-\infty}^{+\infty} \frac{d\omega'}{2\pi}\frac{d\omega}{2\pi} e^{i(\omega' t' - \omega t)} \left[\sum_{ll'} \overline{p_{l'}}p_l \langle a^\dagger(\hbar\omega' - l')a(\hbar\omega - l)\rangle - \langle a^\dagger(\hbar\omega')a(\hbar\omega)\rangle\right] \\
&\quad = \int_{-\infty}^{+\infty} \frac{d\omega}{2\pi} e^{i((\omega - k2\pi\nu)t' - \omega t)} \sum_{lk} \overline{p_{l-k}}p_l \left[\frac{1 - sign(\omega - l2\pi\nu)}{2} - \delta_{k,0}\frac{1 - sign(\omega)}{2}\right] \\
&\quad = \sum_k e^{-ik2\pi\nu t'} \int_{-\infty}^{+\infty} \frac{d\omega}{2\pi} e^{i\omega(t' - t)} \sum_l \overline{p_{l-k}}p_l \left[\frac{1 - sign(\omega - l2\pi\nu)}{2} - \delta_{k,0}\frac{1 - sign(\omega)}{2}\right] \\
&\quad = \sum_k e^{-ik2\pi\nu t'} \int_{-\infty}^{+\infty} \frac{d\omega}{2\pi} e^{i\omega(t' - t)} G_{k,\hbar\omega}
\end{aligned}
$$

From Eq. 5.6 and 5.5 we have :

$$
\frac{\partial}{\partial q}\frac{\Delta S_I^{Tomo}(q)}{-2S_I^0\eta_k}|_{-q_0,\Theta_S} = \sum_l Re(e^{i\Theta_S}\overline{p_{l-k}}p_l)\frac{(1 - sign(h\nu q_0 - lh\nu))) - (1 - sign(h\nu(q_0 - k) - lh\nu))}{2}
$$

Measuring the noise for the angles $\Theta_S = 0$ and $\Theta_S = -\pi/2$ gives :

$$
\frac{\partial}{\partial q}\frac{\Delta S_I^{Tomo}(q)}{-2S_I^0\eta_k}|_{-q_0,0} + i\frac{\partial}{\partial q}\frac{\Delta S_I^{Tomo}(q)}{-2S_I^0\eta_k}|_{-q_0,-\frac{\pi}{2}} = G_{k,h\nu q_0} - G_{k,h\nu(q_0-k)} \qquad (5.11)
$$

The reconstruction of the Fourier components $G_{k\neq 0,\omega}$ follow the same pattern as the matrix $\overline{p_{l'}}p_l$. Starting an energy $-h\nu q_{cf}$ lower than the largest non-negligible photo-emission process, we measure the noise derivative once in every window $[h\nu(-q_{cf} + rk), h\nu(-q_{cf} + (r + 1)k]$ with the in-phase and out-of-phase modulation signals at frequency $kh\nu$. $G_{k=0,\hbar\omega}$ is simply the occupation number of holes and electrons, whose measurement was described in the energy spectroscopy section.

$$G_{k\neq 0,h\nu q_0} = \sum_{r=0}^{+\infty}\left[\frac{\partial}{\partial q}\frac{\Delta S_I^{Tomo}(q)}{-2S_I^0\eta_k}|_{-q_0+kr,0} + i\frac{\partial}{\partial q}\frac{\Delta S_I^{Tomo}(q)}{-2S_I^0\eta_k}|_{-q_0+kr,-\frac{\pi}{2}}\right] \tag{5.12}$$

This reconstruction has not been attempted on the leviton yet.

Chapitre 6

Interferences at a beam-splitter for Lorentzian pulses applied on a hot Fermi Sea.

It was shown in section 4.3.2 that the interference pattern observed in the time-spectroscopy experiment can be directly related to the determination of the quantum overlap :

$$| < \hat{\Psi}^{\dagger}(u+\tfrac{\theta}{2})|\hat{\Psi}(u-\tfrac{\theta}{2}) > - < \hat{\Psi}^{0\dagger}(u)|\hat{\Psi}^{0}(u) > |^2$$

between two states generated by Lorentzian pulses with a delay τ. In this chapter, we extend the analysis of this experiment and discuss thermal effects. As shown in [38], a key signature of the photo-assisted distribution after a Lorentzian pulse can be observed when varying the electronic temperature in the sample : time-dependence and temperature-dependence decouples in the PASN. The origin of this property is reviewed in section 6.1 and the experimental results presented in section 6.2.

6.1 Separation of time delay and temperature dependence.

Fig. 6.1 shows PASN calculations for the time-spectroscopy experiment with two counter-propagating trains single-electron Lorentzian pulses, one delayed by $\theta = \tau/T$. at various temperature. We can observe the expected bell shape indicating more or less fermionic anti-bunching. The maximum amplitude is reached when particles in each contacts are injected at maximum time-separation and the partition noises pile up. Thus the excess PASN amplitude decreases with temperature, as does the noise for a single pulse.

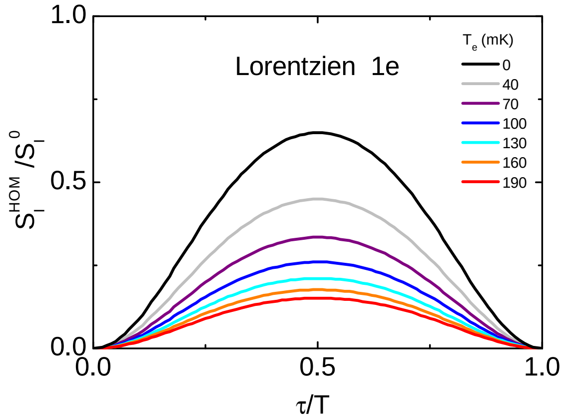

FIGURE 6.1 – Excess PASN calculations for the single-electron Lorentzian pulses time-spectroscopy at finite temperature T_e. Frequency is 4.8 GHz and $W/T = 0,183$.

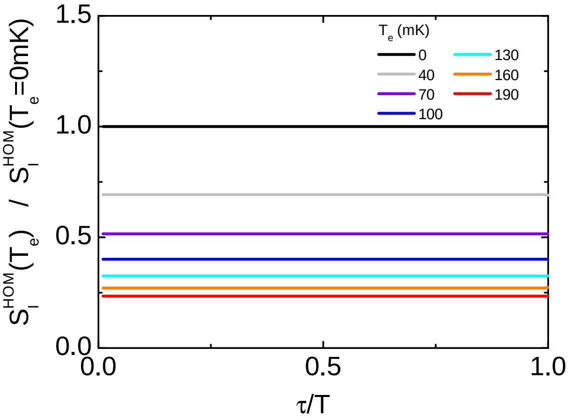

FIGURE 6.2 – Ratio of excess PASN calculations for the single-electron Lorentzian pulses time-spectroscopy at various electronic temperatures T_e. Frequency is 4.8 GHz and $W/T = 0,183$.

The PASN expression for any pulse shape $V_p(t)$ is expressed from the original p_l decomposition of the acquired phase amplitude $exp(-i\phi(t))$ according to Eq. 1.45 :

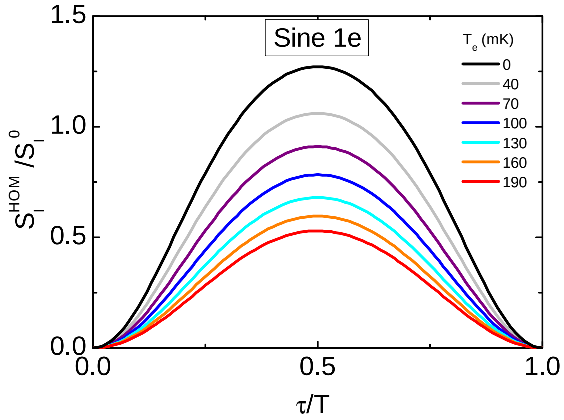

FIGURE 6.3 – Excess PASN calculations for the single-electron sine pulses time-spectroscopy at finite temperature T_e. Frequency is 7.5 GHz.

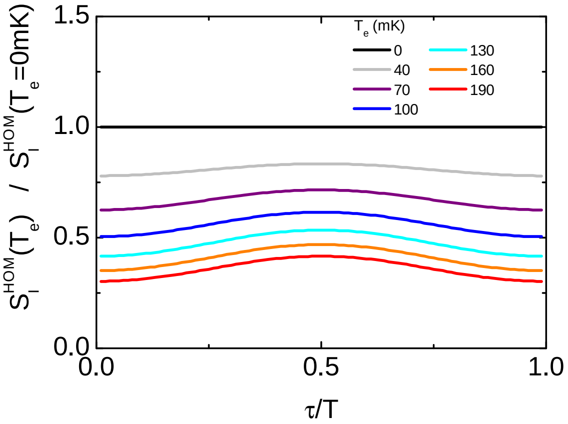

FIGURE 6.4 – Ratio of excess PASN calculations for the single-electron sine pulses time-spectroscopy at various electronic temperatures T_e. Frequency is 7.5 GHz.

$$S_I^{HOM}(\tau)/S_I^0 = \sum_{k=-\infty}^{+\infty} |k||\Pi_k|^2(\tau) \tag{6.1}$$

With :

$$\Pi_k(\tau) = \sum_{l-\infty}^{+\infty} (p_l p_{l-k}^* e^{i2\pi\tau\nu l}) e^{-i2\pi\tau\nu k/2} \tag{6.2}$$

Because of the symmetry in the voltage difference $V_p(t-\tau/2)-V_p(t+\tau/2)$. The shot noise computation actually reduces to :

$$S_I^{HOM}(\tau)/S_I^0 = 2\sum_{k=1}^{+\infty}|k||\Pi_k|^2(\tau) \tag{6.3}$$

The finite temperature PASN is then :

$$S_I^{HOM}(\tau,\theta_e)/S_I^0 = 2\sum_{k=1}^{+\infty}|k|coth(\frac{k}{2\theta_e})|\Pi_k|^2(\tau) \tag{6.4}$$

In section 1.4.1 we have calculated the probability distribution of photo-assisted processes for a train of Lorentzian voltage pulses transferring one electron each. We have defined the AC part of the pulse as :

$$V_{ac}(t) = \frac{h\nu}{e}\frac{cos(2\pi u)-e^{-2\pi\eta}}{cosh(2\pi\eta)-cos(2\pi u)} \tag{6.5}$$

From which we have derived p_l^{Lev}. It implies the quantities $|\Pi_k^{Lev}(\tau)|^2$:

$$\begin{aligned}|\Pi_0^{Lev}(\tau)|^2 &= |\frac{1-(2-e^{i2\pi\nu\tau})\beta^2}{1-\beta^2e^{i2\pi\nu\tau}}|^2\\ |\Pi_{k\geq 1}^{Lev}(\tau)|^2 &= \beta^{2k}(1-\beta^2)^2\left|\frac{e^{i2\pi\nu\tau}-1}{1-\beta^2e^{i2\pi\nu\tau}}\right|^2\end{aligned}$$

Where we have $\beta = exp(-\pi W/T)$. We see that $|\Pi_{k\geq 2}^{Lev}(\tau)|^2 = \beta^{2(k-1)}|\Pi_1^{Lev}(\tau)|^2$, a property inherited from the exponential law in p_l^{Lev}. Therefore in the sum in Eq. 6.3, the time-dependence and the temperature dependence can be separated. This is illustrated by Fig. 6.2. It means that the time extension of the quantum wavepacket, described using the correlator $C(\tau)$ in chapter 4.3.2, is measured at any temperature, if yet with a rapid decrease in resolution.

This situation is also remarkable among voltages pulses. For instance, it can be verified that the Bessel function do not allow this variable separation. While the PASN noise observed in a time-spectroscopy experiment with two sine pulses on each contact (Fig. 6.3) shows a bell shape and a decrease in amplitude with temperature, this evolution is not identical at all time τ (Fig.6.4). Unfortunately, if the exponential law in $p_{l\geq 0}^{Lev}$ is clearly a sufficient condition, there is no derivation to date of what are the necessary conditions. We do not know whether it is unique or not.

6.2 Experimental results

The temperature test is based on the same experimental parameters as used to verify the time-extension of the injected charge packet corresponding to the Leviton in chapter 4.3.

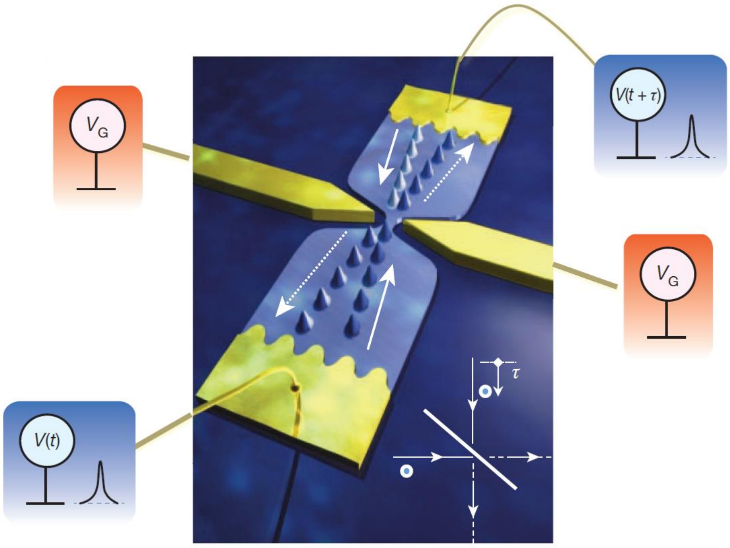

FIGURE 6.5 – Time-spectroscopy principle. Two single-electron Lorentzian pulses are applied to the contacts with a delay τ. See chapter 1 for details.

Pulse generation

We use a DC–18 GHz power-divider and a phase-shifter in order to send the 4.8 GHz pulse simultaneously on the two contacts with a controlled time-delay. The pulse is generated with an AWG generator. The noise level with a single connected contact confirms the pulse amplitude and width, one electron per period and $W/T = 0,183$.

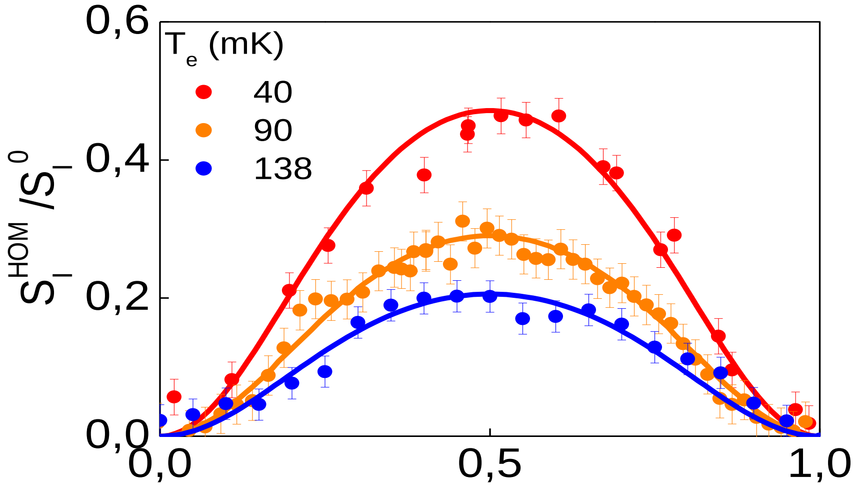

FIGURE 6.6 – Temperature dependence of the excess noise associated to dephased single-electron Lorentzian pulses.

Temperature

The electronic temperature has been previously observed through Jonhson-Nyquist noise measurement to follow closely the fridge temperature when the cryogenic system is above 35 mK. As indicated in section 2.3.3, the system temperature is monitored through a calibrated thermometer close to the last stage cold fingers. Here, in addition to the base temperature, at which the cryogenic system indicates $T_{Ru02} = 12.5\,mK$, we measure at $T_{Ru02} = 90\,mK$ and $T_{Ru02} = 140\,mK$.

Evolution with temperature increase

Fig. 6.6 shows the difference between the noise in presence of the AC signal and the equilibrium noise at the three attempted temperature, in reduced units (QPC transmission 0.3–0.35). All three curves agree with PASN calculation. As expected the top level of excess noise decreases rapidly with the temperature, and the amplitude (adjusted to obtain a best fit) is consistent with the thermometer indications. Fig. 6.7 shows the ratio between the experimental data at 90 mK and the theory at zero temperature.

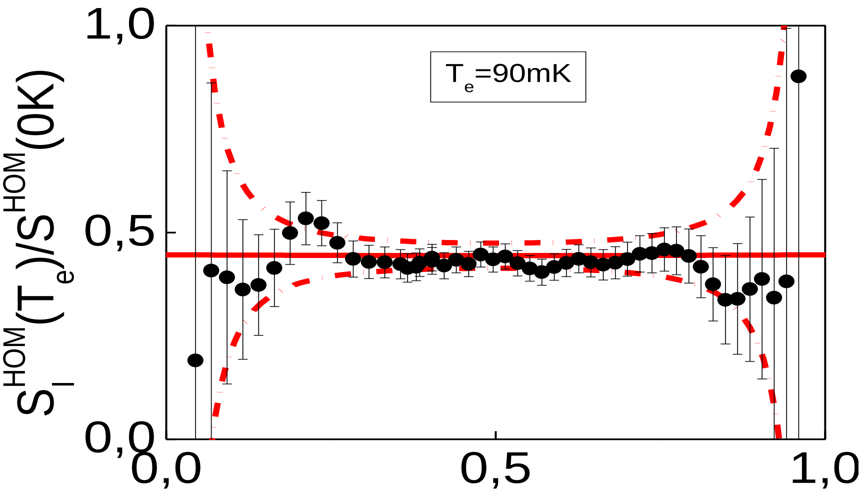

FIGURE 6.7 – Experimental test of the PASN temperature dependence for minimal-excitation interference at a beam splitter. Experimental excess noise for a single-electron pulse at each contact at 40 mK is divided by the zero-temperature PASN calculation.

Chapitre 7

Conclusion and Perspectives

7.1 Conclusion

In this work, we have investigated with low-frequency PASN measurements the on-demand injection of N indistinguishable electrons in a quantum conductor using voltage pulses applied on the contacts. A QPC realized from an high-mobility 2DEG in a GaAs/AlGaAs heterostructure has been used as a one-dimension coherent conductor with tunable transmission and we have applied sub-nanosecond pulses of various shapes.

The main achievement presented in this manuscript is the first experimental demonstration of the prediction from Levitov, Lesovik and collaborators on the effect of a Lorentzian pulse with quantized flux $e/h \int_{-\infty}^{+\infty} V_p(t)dt = 1$. We show that such a pulse injects a single electron in the system without additional perturbation of the Fermi sea. The quantum state of this single-particle excitation, called a Leviton, is well-defined and the emission time can be selected. The typical energy of the particle is set through the sharpness of the pulse in the time-domain.

In the first chapter we have reviewed the theory of AC transport in ballistic one-dimensional coherent conductor. We have focused on a periodic excitation at frequency ν and used the appropriate Floquet formalism. The effect of such periodic pulses on a quantum wire can be described by a set of photo-assisted finite energy transitions $lh\nu$ (with l an integer), with probability amplitudes p_l associated to the emission (if $l < 0$) or absorption ($l > 0$) of l photons. The theory shows that the particular behavior of the Lorentzian pulse results from the absence of photo-emission process : the formation of a hole in the Fermi sea is impossible. If the wire is perfectly transmitting, a single electron travels from one reservoir to the other on top of the Fermi sea. Remarkably, applying the sum of N such pulses transfers exactly N electrons simultaneously. This situation implements a reliable on-demand source with adjustable electron number. Their energy is controlled through the sharpness of the pulse in the time-domain. This case is unique among pulse shape and only true for a quantized flux. Any other pulse transfer both electrons and holes. The only other possibility to transfer particles from one side to the other without creating any hole is with the use of a DC current, which obviously does not perform on-demand injection.

We rely on low-frequency PASN measurements since the noise level at zero temperature is directly proportional to the number of quasi-particles injected in a partially transmitting quantum conductor. On the contrary, a current measurement is proportional to the injected charge, and cannot be sensitive to neutral electron-hole pairs. If zero temperature could be achieved, the experimental signature of an unperturbed Fermi sea during a train of lorentzian pulses would be the absence of excess shot noise ΔN_{eh} compared to a DC voltage injecting on average one electron for each pulse. By analyzing the effects of a realistic temperature, we show how the photo-assisted distribution can still be determined as long as photo-assisted energy-windows are not mixed by the thermal distribution, i.e when $\theta_e = k_B T_e / h\nu \ll 1$. Furthermore, the noise is a versatile tool which can be used to give detailed information about the complete energy distribution of the excited particle (energy-spectroscopy), and the wave-packet extension in the time-domain (time-spectrocopy).

In chapter 2, we have presented and fully studied the noise measurement set-up. We demonstrate the possibility to build a low-cost real-time noise detection set-up resolving spectral-density of $\sim 10^{-30}\,\mathrm{A}^2/\mathrm{Hz}$ in about 3 minutes. This is achieved by combining the well-known cross-correlation technique with the use of HEMTs mounted in parallel in a home-made cryo-amplifier. The high stability over time and low-amplification noise was found highly suitable for the detection of a few particles per pulse. Implemented in a $400\,\mu\mathrm{W}$ Helium-Free cryostat, the lowest electronic temperature extracted through shot noise thermometry is $T_e = 35\,\mathrm{mK}$. In an important improvement compared with previous realizations in our group, the noise acquisition is performed in the MHz range. The parasitic mechanical vibrations induced by the dry cryostat pulse tube are avoided.

As short voltage pulses are applied to a QPC, the calibration of the RF transmission lines is necessary. This is presented in chapter 3. It exploits PASN measurements and benefits from the high sensitivity of the noise detection. This offers a precise in-situ tool to understand the radio-frequency signal actually arriving at the QPC. The calibration includes not only the transmitted amplitude, but all relative phases. This leads to the possibility to compensate the defects of the transmission lines when necessary. We can thus propose a 15-picosecond-wide Lorentzian pulse and a repetition rate $\nu = 6\,\mathrm{GHz}$, with all four first harmonics completely monitored and with tunable amplitude. The quasi-particle has a typical energy of $25\,\mu\mathrm{V}$ and thermal effects are limited ($\theta_e = k_B T_e / h\nu \sim 0.12$). Eventually, for all pulse shapes, the understanding of the applied signal at several harmonics separately is one of the key components in the experimental demonstration of the PASN theory for voltage pulses.

The demonstration of the minimal excitation state, the Leviton, has been presented in chapter 4, where the injection of a few electrons in the quantum conductor is tested with various pulse shapes, pulse frequencies and pulse amplitudes. Results for all situations are in very good agreement with the PASN shot noise theory at finite temperature and including small calculable self-heating effects. Energy-domain experiments using shot noise spectroscopy demonstrate the clear symmetrical distribution of photo-emission and photo-absorption for square and sine pulses. On the contrary, lorentzians pulses of any amplitude pulses are shown to induce a limited number of photo-emission process compared with photo-absorption process. Changes of slope in the excess noise spectroscopy ΔN_{eh} as a function of the voltage $\mathrm{V}_{ds} = qh\nu/e$ reflect the quantized energy shifts in these process. They appear at multiple of $h\nu$ and are particularly well-marked with sine-wave at ν =16 GHz and ν =24 GHz (i.e. $\theta_e \sim 0.05$). When we consider $\Delta N_{eh}(q)$ as a function of the transferred charge q, we observe local maxima and minima, as predicted by Levitov et al. These quantum oscillations are a dynamical analog of the Anderson Orthogonality Catastroph (AOC). At zero temperature, minima are expected at integer values of q, while at finite-temperature the position is shifted due to predictable thermal effects. The observed positions agree with the model. The noise level observed at $q = 1$ informs us on the quantity of effectively injected electrons and holes when trying to inject a single electron. The finite level of excess particle per pulse 0.09 ± 0.01 for the 15-picosecond lorentzian is entirely taken into account by the anti-bunching of thermally-excited particles near the Fermi level. It shows the suppression of photo-emission for such a quantized pulse with the correct shape. In contrast the noise level cannot be explained by thermal excitations only for a sine pulse, or a square pulse. The time-spectroscopy completes the picture and probes the wavepacket extension in the time-domain. Analogous to an Hong-Ou-Mandel experiment, it gives the quantum overlap of the injected particle wave-function $| < \psi^*(t + \frac{\tau}{2}) | \psi(t - \frac{\tau}{2}) > |$ through τ-delayed lorentzian pulse collisions on the QPC. The expected lorentzian τ-dependence has been found. All these elements characterize the on-demand injection of Levitons.

The two last chapters are additional characterizations of the properties of Levitons. Calculations from Grenier et al. indicate the possibility to use noise measurements in order to perform a Quantum State Tomography (QST) on single-electron excitations. In this experiment, a periodic train of Lorentzian pulses generating successive Levitons interferes with a small harmonic excitation at frequency $k\nu$, with k an integer. The noise level probes the coherence between photo-assisted process at different energies p_l and p_{l+k}. It provides all products $\overline{p_l}p_{l+k}$ in the Floquet scattering matrix, hence the possible reconstruction of the density matrix over energy. Measurements at $k = 1$ an $k = 2$ have been performed, both in very good agreement with expectations, and could soon provide a QST.

Eventually, a last property of lorentzian pulses is tested in chapter 6. The PASN interference pattern at a beam-splitter for τ-delayed single-electron pulses applied on a hot Fermi Sea is proportional at any temperature to $1 - | < \psi^*(t + \frac{\tau}{2})|\psi(t - \frac{\tau}{2} > |$. This is a non-trivial consequence of the exponential law in the energy-distribution of the Leviton. This has been verified at 40 mK, 90 mK and 140 mK.

7.2 Prospects

This realization of an on-demand electron source opens new ways to build quantum experiments requiring synchronization of a controlled number of electrons. Like other recently available sources[1][15][41][61][99], it should participate to the transposition of quantum optics experiments from photons to electrons propagating in nanostructures. From this point of view, it has several interesting properties. The Leviton state is close in energy to the Fermi level and is therefore expected to show a coherence length of a few µm. The quantum wave-function is also directly controlled, independently from nano-lithographied structure. The simultaneous emission of two—or more— indistinguishable electrons is also remarkably straightforward.

By many aspects, the quantized Lorentzian pulse and the associated quantum state are a fundamental problem of quantum mechanics. Their dynamics is a remarkable consequence of the properties of the Fermi statistics. The mechanism might be reproducible with any Fermion in low-temperature condensed matter. The use of fractional-charge states described by the Luttinger theory as carriers has already been discussed in[68][71] and atomic Leviton[19] could be envisioned as well. The effect of interactions on a periodic source of voltage pulses injected in one of two co-propagating quantum Hall edge channels has been analyzed theoretically[54]. This theory could be tested with noise measurements similar to those presented in this manuscript. The use of a 15-Tesla supra-conductive coil is therefore planned in the near future.

Edge states in the quantum Hall Effect are similar to wave-guides for electrons. As proposed in [10] and used in recent experiments[154], a flying qubit can be defined by the distribution of a traveling electron between two possible channels. In addition of being a new test of AC quantum transport theory, the injection of electrons with voltage pulses in such a system has therefore application to quantum information processing[106].

Eventually, PASN measurements down to the detection of a single particle per GHz pulse could also test the feasibility of the recently proposed ”optimal entangler”[132]. In this problem, a time-dependent barrier switches the transmission of a quantum wire from 0 to 1 and back to 0 with minimal noise current when the time-profile has a particular shape. A split-gate QPC with GHz pulses applied on the gates is a good candidate and measurements have been recently started by B. Roche under the direction of C. Glattli and P. Roulleau.

Appendices

Annexe A

Additional Technical Information

A.1 Phase Shifters.

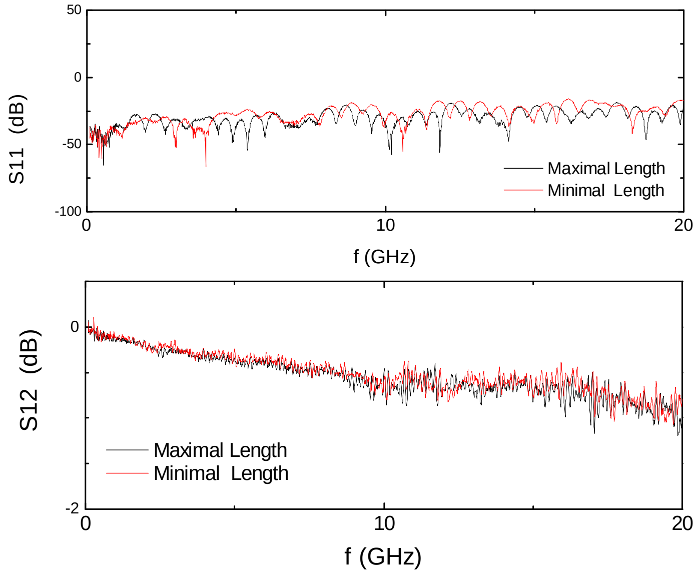

FIGURE A.1 – RF Phase shifters and pulse deformation. Transmission of a DC-18Ghz ARRA inc.$^{\mathrm{TM}}$model 9425A observed in the two extreme optical path lengths.

When performing time-spectroscopy (as in chapter 4 and 6) and noise tomography (as in chapter 5) a key hypothesis is the absence of deformation of a pulse when modifying the circuit in order to modify the phase. We have analyze our mechanical Phase Shifters using a Vectorial Network Analyzer.

A.2 Cryogenic System

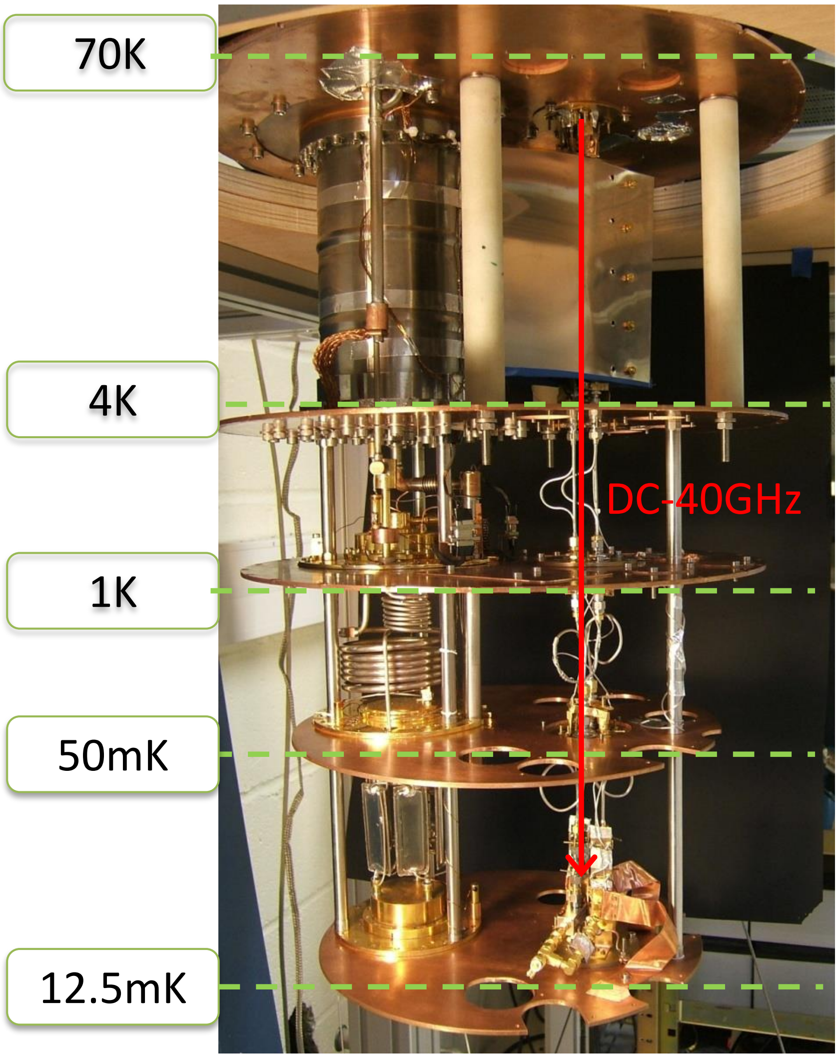

FIGURE A.2 – Cryogenic System. Helium-Free 400μW with base temperature 12.5mK from Cryoconcept^{TM}. The Photo adapted from [37]. Distances between the stage are -from 70K to 12.5mK- 25cm-10cm-15cm-15cm.

Annexe B

Quantum Point Contact

In this chapter we review the now well-established physics[144] of QPC [151][145] from their fabrication to the possibility to use them as a test system for the Levitov et al. prediction. Most of these requirements are shared by all PASN experiments.

When a constriction between two large conductors is narrow enough to be comparable to the electronic wavelength λ_F, a QPC is defined. While several techniques might be used, we focus on depleted 2DEG and split gates (section B.1). The next part B.2 contains a brief description for each of the different nanofabrication steps involved. How the requirements for the pulsed single-electron source are fulfilled is developped in section B.3.

Sample ”B” is the sample used for the calibration in chapter 2 and 3, the main results in chapter 4, and additional results in chapter 5. It was provided by the Laboratoire de Photonique et des Nanostuctures (L.P.N) in Marcoussis (France). The fabrication was performed by Yong Jin. The GaAS-AlGaAs wafer for the so-called sample ”A” mentioned in chapter 4, was supplied by Werner Wegscheider from ETHZ Zürich and the nanolithography performed by Julie Dubois in our group's facilities in Saclay. Sample ”C” was used for photo-assisted shot noise experiments. The GaAS/AlGaAs wafer was supplied by I. Farrer and D.A. Ritchie from the Cavendish in Cambridge. The nanolithography was performed by Yodchay Jompol, also in Saclay. Concepts of fabrication are basically the same for all samples. When numeric values are given without additional precision, they refer to sample ”B”.

Sample	A	B	C
mobility μ_e $10^6\,\mathrm{cm^2/Vs}$	2	0.4	2.5
density n_e $10^{15}\,\mathrm{m^{-2}}$	1.4	4	1.9

B.1 2DEG

GaAS and $\mathrm{GaAs}_x\mathrm{Al}_{1-x}$, where x defines the Aluminium mole fraction and is typically around 30%, are semiconductor crystals with only a slitghly different lattice constant, a convenient property to build a multilayer heterostructure without crystalline defects. On the other hand, their energy gap difference can be made significantly large : 1.424 eV and ~1.424+1.247× eV for respectively GaAS and $\mathrm{GaAs}_x\mathrm{Al}_{1-x}$ [133]. As is often found interesting in semiconductor physics, electronic densities near the interface, where the conduction and valence bands bend, can be engineered using dopants. Restricting n-type Si impurities from modulation-doping to the wide-band gap material[35], Störmer et al.[141] managed to trap electrons at a single interface in the electrostatic well generated by the balance between the field from the ionized dopants and the bands discontinuities (Fig. B.1). The well is only a few nanometers large, and the momentum in the perpendicular direction is quantized. When looking at the energy separaration, one finds typically a few meV (See for instance simulations for an approximately triangular well : [53]). At low temperature, only the fundamental level is occupied. The spatial separation between donors and charge carriers leads to enhanced elctronic mobility μ_e. Over the year (Fig. B.2), improved control of impurities and defects in the material has lead to μ_e now exceeding $10^7\,\mathrm{cm^2/Vs}$[140][117].

On top of the GaAs-AlGaAs heterostructure defining the quantum well, a thin second GaAs layer is now commonly grown : the cap-layer. It reduces the leak of carriers to preferred surface states that might affect the transport properties of the gas. In the end, for sample ”B”, the 2DEG is 35 nm-deep, on sample ”A” 100 nm, and for sample ”C” 90 nm. Tab. B.1 contains the specifications for all 2DEG.

B.2 Nanofabrication

The split-gate geometry (Fig. B.3) was introduced to control the appearance of a 1D conductor in a 2DEG([158] [143]). Starting with the buried 2D gas, two gates are patterned on top of the heterostucture. Under the effect of a strong negative voltage, the conductive interface is depleted and the gas is forced to adopt locally the gates shape. The separation between the two gates is rather small and the induced electrostatic potential defines two

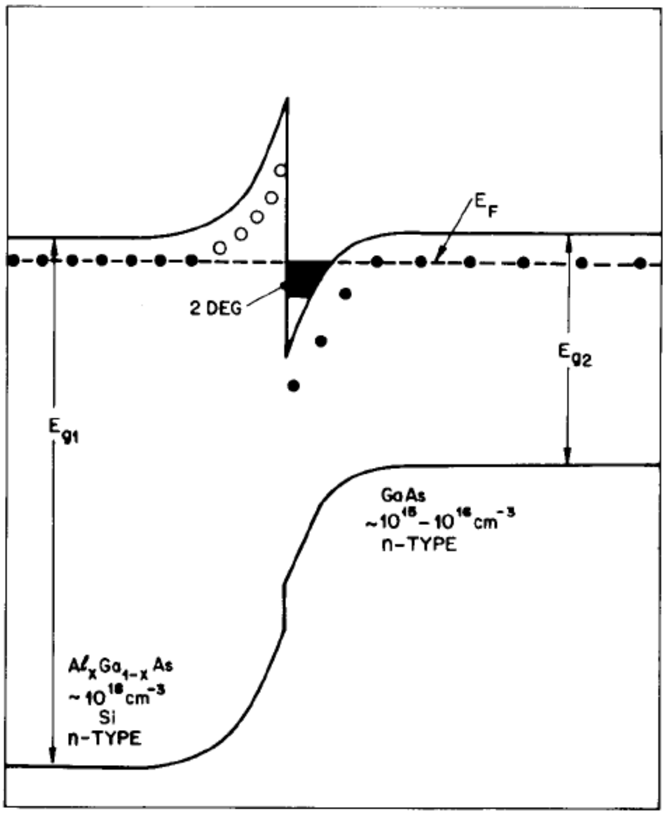

FIGURE B.1 – A two-dimensional electron gas (2DEG) can be created at the interface between two layers with different energy gaps. The 2DEG is fabricated from a GaAS-GaAs$_x$Al$_{1-x}$ heterostructure grown by Molecular Beam Epitaxy and modulation-doping. Si donors are ionized and the elecrostatic field compensates the diffusion current from the low-gap to the wide-gap conductance band : a potential well is established at the interface. From Störmer et al. [141].

wide 2D region, called the reservoirs, and a channel. The channel behaves as a ballistic waveguide when its length is reduced below the electron mean free path l_e. The comparison between the width of the constriction W_c and the wavelength λ_F gives the number of modes which can exists : $W_c/2\lambda_F$. The capacitive coupling between the gates and 2DEG electronic density is used to tune the waveguide width and modulate transmissions down to a single partially reflecting mode[151][145]. Recently, Iqbal et al.[64] have shown large-scale tunability (factor 1 to 3) in the lentgh with the combination of several gates with independant bias. We review in this section the three nanofabrication steps involved for all samples : mesa etching, ohmic contacts deposition and gate deposition.

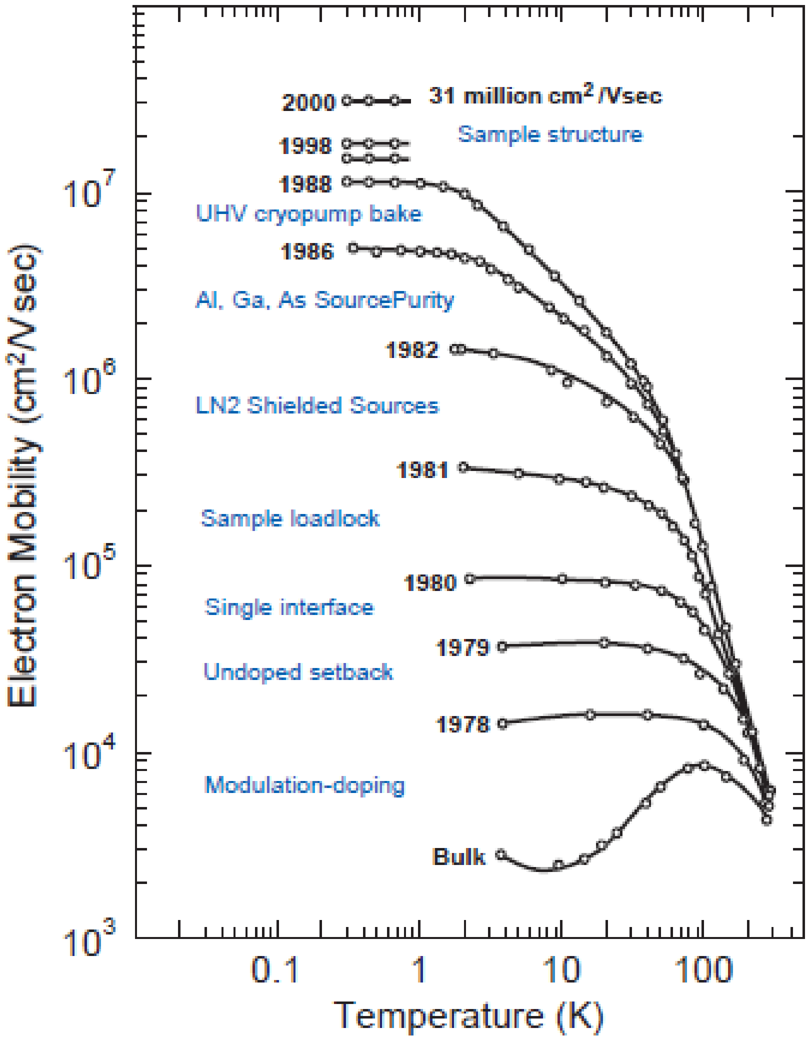

Figure B.2 – History of improvements in the mobility of electrons in GaAs, annotated with the technical innovation responsible for the improvement. From Pfeiffer et al.[116].

B.2.1 Mesa etching

Mesa can be seen on Fig.B.5 and B.7 as the slighlty darker greenish region in the middle of sample "B". It defines the region over which a 2DEG exists. Starting with an homogeneous MBE-grown wafer, wet etching is used to selectively remove the top layers from the wafer where the gas must be destroyed. Minimising the final 2DEG surface reduce the possibility for electrons to leak from the top-gate to the gas. The shape is also decided to minimize

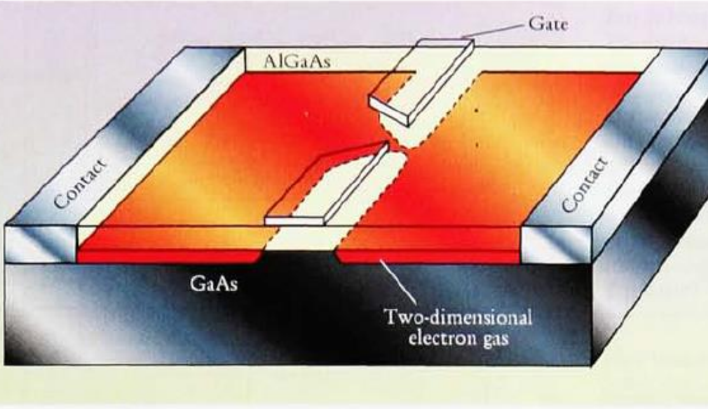

FIGURE B.3 – Density modulation of a 2DEG with a pair of top gates : the split-gate geometry. From the historical review of Van Houten et al.[144].

the resistance (large width and short length when possible) along currents trajectories through the sample. For sample "B", the total mesa length is about 80 µm, short enough to limit mesa resistance. Sample "A" is slightly shorter, about 70 µm. Sample "C", for which the room for two QPC forming a cavity had to be left, is much longer : 800 µm. But its typical width is also increased and the total resistance due the mesa (without contacts) is estimated to be 400 Ω (Fig. B.8)

B.2.2 Contact deposition

Reliable low-resistive ohmic (linear I-V characteristic) contacts are crucial for precise measurements, as their physics must not mask the mesoscopic behaviour under scrutiny. Contacts are needed to reach the buried 2DEG. Deposition of gold metallic contacts on the semiconducting substrate surface, a few 30 nm-100 nm away from the gas, leads to a Skottky barrier. Such a barrier is increasingly insulating at low-temperature when $k_B T$ becomes significantly less than the barrier height. These energy barriers are known to result from a combination of intrinsic properties of the two materials in contacts (Skottky-Mott theory) and surface states properties (Bardeen theory [8]). The most commonly used technique in GaAs has long been the diffusion of the eutectic alloy AuGeNi through the semiconductor crystal [20]. Contacts orientation compared to the crystallographic axes has been observed to strongly affect the quality of the resistance[70][51]. A meander-like or, as in our case, a crennel-like shape prevents this while increasing the effective perimeter of the contact zone. See Fig. B.7 for sample "B". At the core of the process, the atomic diffusion [21][57] is a strongly inhomogeneous process and the selection of optimal parameters (annealing time, temperature and alloy composition) asssociated with a certain 2DEG depth still attracts attention[75]. Optical or electronic lithography is used to pattern the contact. Au, Ge and Ni are evaporated from a single bullet containing a eutectic ratio for Au anf Ge, (∼13%-∼82%) and a small amount of Ni, used to improve the wetting properties of the melted alloy. The metal layer is annealed under N2/H2 gas atmosphere at about 450-470°C.

B.2.3 Gate deposition

The number of transmitting channels in the constriction is given by the ratio $E(2W_c/\lambda_F)$, where W_c is the width of the constriction. Typically the electrostatic walls must be separated by about 40 nm to obtain a single channel. To be able to reach this length without applying large voltages on the gate(thus limiting leakages), the two patterned metallic gates must be deposited with a separation of about 300 nm. E-beam lithography is required to reproduce this design with a satisfying precision.

B.3 Implementing the Levitov geometry

How does a QPC in a 2DEG corresponds to the 1D ballistic coherent conductor modelled in Levitov prediction ?

Parabolic band structure approximation

Most quantities describing the quantum states existing in the GaAS 2DEG are obtained, both qualitatively and quantitatively, using a parabolic dispersion relation for free in-plane quasi-particle with an isotropic effective mass m_*=0.067 m_e. Expression and values are given in Tab. B.3 for all QPC. From this relation, we see that the minimum Fermi energy E_F is tycally ∼8 meV, and therefore the Fermi temperature T_F is always above 46 K. These quantities are much higher than the effective energy for photo-assisted and thermally-excited quasiparticles (about 100 µV and 35 mK) considered during the study of pulsed injection. The velocity dispersion for electronic waves around the Fermi Energy is therefore negligible, especially considering the small length of the 2D reservoirs. For sample "B", on which the most energetic waves were send, a 100 µV electron has a speed

Property		Sample		
Name	Expression (2D)	"A"	"B"	"C"
Fermi Energy E_F (meV)	$\frac{\pi\hbar^2}{2m^*}\mathrm{n}_e$	5	14.3	6.8
Fermi Temperature T_F(K)	$\frac{\mathrm{E}_F}{k_B}$	60	170	80
Fermi velocity v_F (kms^{-1})	$\frac{\hbar}{\sqrt{2\pi}m^*}\sqrt{\mathrm{n}_e}$	162	274	199
Wavelenght λ_F (nm)	$\sqrt{\frac{2\pi}{\mathrm{n}_e}}$	67	40	58
Mean free path l_{el} (µm)	$\frac{h\mu_e\sqrt{\mathrm{n}_e}}{\sqrt{2\pi}e}$	12	4	18
Collision time τ_{el} (ps)	$\frac{\mathrm{l}_{el}}{\mathrm{v}_F}$	76	15	95
Resistance per square $\mathrm{R}_\square$ (Ω)	$\frac{1}{en_e\mu_e}$	22	39	13
Plasmon Frequency at λ_p=40 µm (Ghz)	$\sqrt{\frac{e^2n_e}{2m^*\varepsilon_{eff}}\frac{1}{\sqrt{40\,\mu_m}}}$	350	580	400

TABLE B.1 – Main Physical Properties for a 2DEG in the parabolic band structure approximation.

only 0.3% superior to a Fermi-level quasiparticule. Most theoretical calculations neglects the difference between phase and group-velocity in cold 2DEG.

Ballistic transport through the QPC

Small-size, low-dimension, low-disorder and low-temperature samples have led to a thorough study and classification of the quantum decays to be associated with the Boltzmann equation of transport. The electron mean free path l_{el} represents the distance an electron can travel without scatterisng on an impurity. These events do not affect the electronic coherence or the electron energy. We can compare l_{el} to the channel length imposed by the gate, from 80 to 300 nm. The worst situation is found when l_{el} ∼4 µm for the "low" mobility sample "B". Even in this case, the transport in the channel is clearly ballistic.

At the same time, the transport must be considered diffusive for the whole 2DEG as the reservoirs are larger than l_{el}. The transport over the mesa beyond the ballistic region surrounding the QPC and toward the contact is described using the Resistance per square $R_\square$. If we translate l_{el} into a free travel time τ_{el} (ps), we can see that the frequency of elastic scattering events becomes of the same order than the pulse period in PASN experiment around 10 GHz, but without consequences on the sub-poissonian behavior of shot noise as the coherence is conserved.

Transfer duration and instant scattering

An important assumption in the work of Levitov et al. is the instant scattering of electrons on the barrier. An electron impinging the scatterer at τ=0 and spending a time $\delta\tau$ in the channel must see the barrier as a fixed object. This limit is only possible if the potential is varying slowly compared to $\delta\tau$. With the length L_{qpc} of the QPC "B" 80 nm, the time spend in the constriction by a free electron travelling at v_F can be estimated ~0.3ps. Fig. B.4 represents the voltage drop as a function of time for the case of the pulse generating the single Leviton at 6 GHz and W=0.09ν. We see that the sharpest variation is limited to a relative amplitude $\Delta V_{vol}/V_{max}$ ~1.5%, but flux accumulation is actually smoother. Considering all experiments, the worst situation corresponds to the case of a 24 GHz sinewave : $\Delta V_{vol}/V_{max} \sim 4\%$.

Plasmons

No collective response of the electron gas to the electromagnetic field is expected as can be checked by calculating the plasmon frequency [139][11] in the sample.

Lifetime and coherence

Phonons are rare at sub-Kelvin temperature. Experiments[153] on two-dimensional systems have confirmed that phase breaking at is then due to electron-electron scattering, largely dominant compared to electron-phonon scattering. The theory of these collisions was developed by Chaplik[29] and Giuliani et al. [48].

For particles with energies E much lower than the temperature $\Delta = E - E_F \ll k_B T_e \ll E_F$

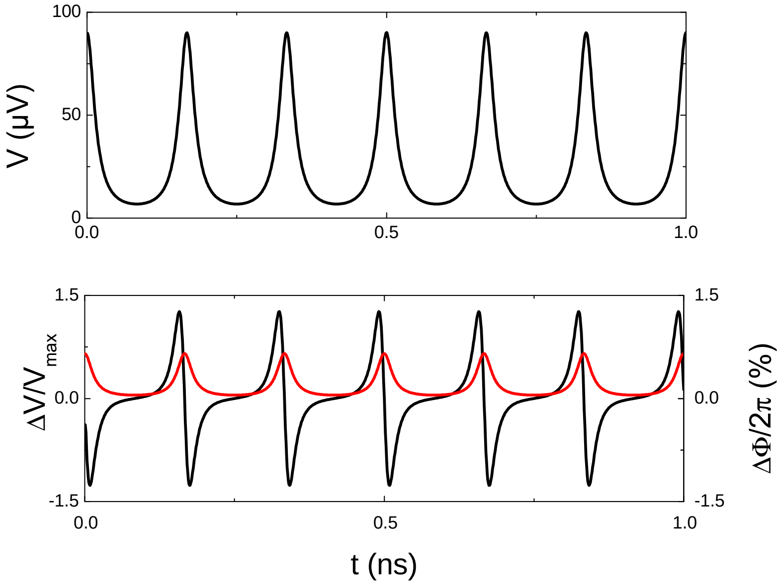

FIGURE B.4 – Voltage fluctuation and transfert time.

(Top) Time-profile of the voltage drop over the QPC for pulse generating the single Leviton at 6 GHz and W=0.09ν.

(Bottom) Relative amplitude variation during the ~0.3 ps transfert time for an electronic wave over the 80 nm channel of QPC "B" for the voltage drop (black) and phase accumulation (red).

$$\frac{1}{\tau_{in}(\Delta)} \approx -\frac{E_F}{h}(\frac{k_BT_e}{E_F})^2 \left[ln(\frac{k_BT_e}{E_F}) - ln(\frac{q_{TF}^{2D}}{p_F}) - ln(2) - 1\right] \tag{B.1}$$

Here, $q_{TF}^{2D} = 2me^2/(\varepsilon_r\hbar^2)$ is the 2D Thomas-Fermi screening wave vector, $p_F^2 = \sqrt{2m^*E_F}/\hbar$, m^* is the effective electronic mass, and ε_r is the dielectric constant (12.7 for GaAs). With 40mK we find typically $200 - 500ns$ for all samples. As the transport is diffusive at this timescale, a coherent length l_ϕ can be calculated according to :

$$l_\phi = l_{el}\sqrt{\frac{\tau_{in}}{\tau_{el}}} \tag{B.2}$$

l_ϕ is about 500–600 µm for all samples. For excited particles from GHz pulses, the energy scale is larger than k_BT_e. If $k_BT_e \rightarrow 0K$ $\Delta = \varepsilon - E_F \gg E_F$:

$$\frac{1}{\tau_{in}(\Delta)} \approx \frac{E_F}{2h}(\frac{\Delta}{E_F})^2 \left[ln(\frac{\Delta}{E_F}) - \frac{1}{2} - ln(\frac{2q_{TF}^{2D}}{p_F})\right] \tag{B.3}$$

With $100\,\mu V$, we find respectively for sample A,B, and C 0.5 ns, and 1.3 ns and 0.7 ns. The coherence is thus preserved beyond a few periods in our experiments.

Within the picture of Fermi quasi-particles, this collision time gives the lifetime of an electronic excitation at this energy.

Sample ”B”

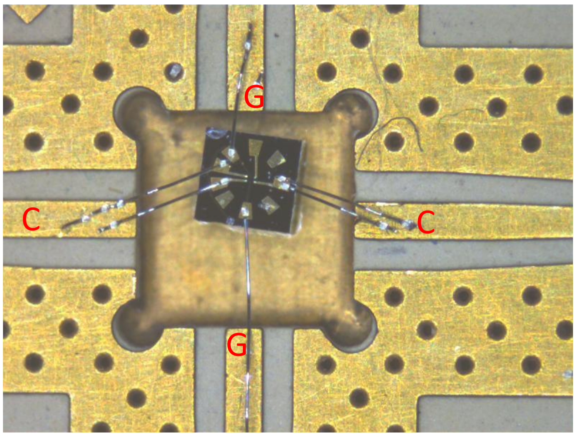

Figure B.5 – Optical image of Sample ”B” attached to the sample holder (background). Label G and C are respetively Gates and Ohmic contacts. Bonding wires are in aluminium and measure about 1 mm - diameter 100 µm. From calculations based on a simplified geometry, we expect typically 0.5 nH and 25 fF of parasitic inductance and capacitance to the ground for each contact to be added by bonding wires/pads. As they are not screened by any ground plane, the two bounding wires should allow for a capacitive shunt of the resistive QPC. The situation can be compared to sample ”A” , for which no such long bonding wires were needed. In both case, radio-frequency amplitudes were calibrated in-situ to account for all attenuation processes at the same time.

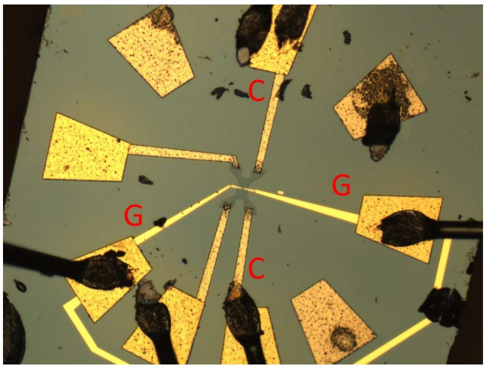

Figure B.6 – Optical image for Sample ”B”. Two bonding wires are used for each contact pad to decrease the parasitic inductance/resistance. Real-size 1 mm×1 mm

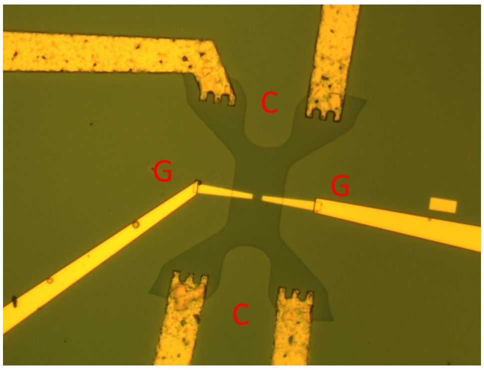

FIGURE B.7 – Label G and C are respectively Gates and Ohmic contacts. Mesa, contacts and gate pattern are inherited from the work of Bajjani et al. [7][156]. The split-gate is too thin near the tip end to be observed. Real size : 120x200µm.

Sample "C"

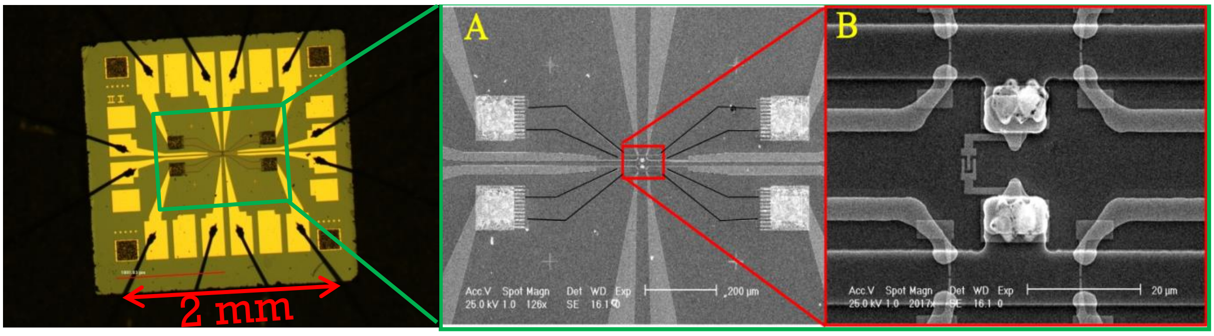

FIGURE B.8 – Images of Sample "C" : optical microscopy (left) and electronic microscopy (center and right).

Sample "A"

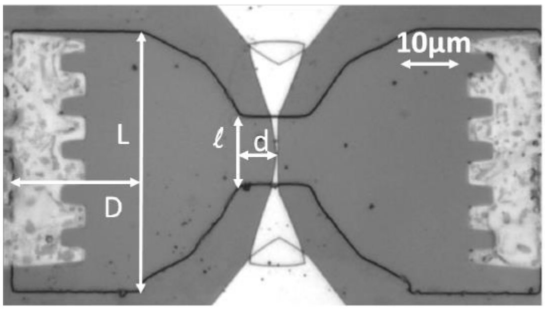

FIGURE B.9 – Electronic microscopy image of mesa and metallic deposition pattern for sample "A". Dimensions are L= 50 µm,D = 25 µm, l= 12 µm,d = 1 µm. Adapted from [37].

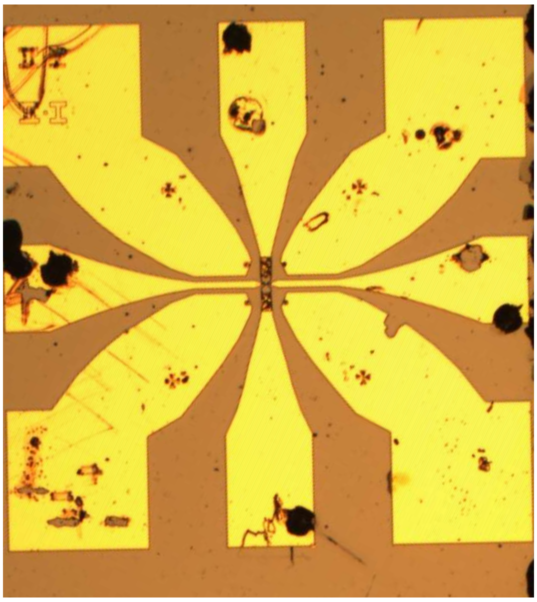

FIGURE B.10 – Optical microscopy image of four-way coplanar waveguide pattern for sample "A" (gold on GaAs). Dimensions : 2 mm×2 mm.

Annexe C

Additional effects from the set-up

In this appendix, we give additional details about the calibration and understanding of the cross-correlation noise measurement set-up described in chapter2. In particular, we produce quantitative information about the elements mentioned but not developed in section 2.6.6. The hypothesis of a small Joule Heating of the measurement resistors is debated and the consequences are discussed.

C.1 Joule Heating of measurement resistors

C.1.1 Observation and possible interpretation

The complete nomenclature of the measurement set-up can be found in chapter2. See 2.1,2.2, and 2.7. Below, Fig.C.1 represents a simplified version where the QPC is pinched, and only one line is observed. We measure the difference between the noise PSD at equilibrium and the noise PSD when a DC current flows through R_{LF} and R_{L}. Such a current exists each time we polarize the quantum conductor. In an ideal situation, no difference is expected. Thin film resistors R_{LF} and R_{L} are large and diffusive conductors under a 1-200 µV bias at 35 mK and display no shot noise. This is not what we have observed. A typical noise PSD is shown in Fig.C.2. It has all the signatures of an additional white noise source in parallel with R_{L}, i.e. seen through the pandbass filter Z_B.

A numerical best fit of the shape confirms this idea.

We consider two effects :

- Gain deviations
- Additional thermal noise from low-temperature electronics

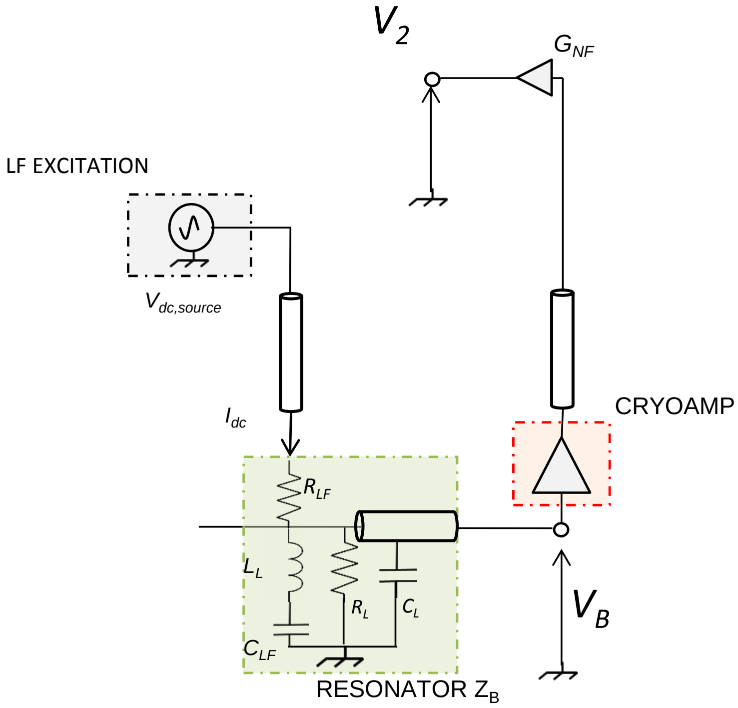

FIGURE C.1 – Joule Heating generation in measurement resistors. The current I_{dc} used to generate a bias on the quantum conductor also circulates in the resistors R_{LF} and R_L. When the QPC is pinched, we can observe how it affects the sample measurement.

We apply a large range of source bias $V_{dc,source}$ and analyze the noise PSD $< V_2^* V_2 >$ over Δf_w=2-3 MHz.

C.1.2 Best fit and parameters extraction

The proposed best numerical fit for each noise PSD as a function of bias V_{ds} on R_L contains four adjustable parameters :

$$P(f, V_{ds}) = P_{w,0}(V_{ds}) + \frac{A(V_{ds})}{1 + (f^2 - f_{0,B}^2)^2/(fd)^2} \tag{C.1}$$

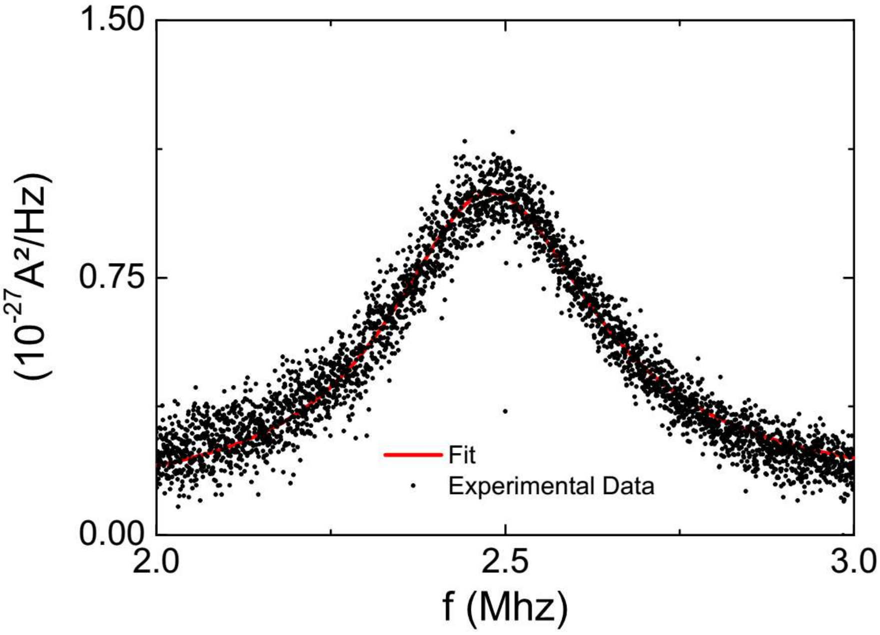

Figure C.2 – Joule Heating typical Noise PSD.

With :

$$
\begin{aligned}
A(V_{ds}) &= |\overline{G_A}G_B|R_{eq}^2|\delta \mathrm{I}_{\mathrm{L,V}_{ds}}|^2 \\
f_{0,B} &= \sqrt{\frac{1}{(2\pi)^2 L_L C_L}} \\
d &= \frac{1}{R_{eq}C_L} \\
R_{eq} &= |Z_B(f_{0,B})|
\end{aligned}
$$

As can be seen in Fig.C.3, the resonant frequency f_{0_B} and the bandwidth d are found identical for all V_{ds} over the $\pm 125\,\mu\mathrm{V}$ Voltage range, as expected. It confirms the existence of a noise source $|\mathrm{I}_{\mathrm{L,V}_{ds}}|^2$ in parallel with R_L.

C.1.3 Gain deviations with bias voltage

A change in gain could occur if the working point of the cryo-amplifiers was shifted in the process. A closer analysis of the DC circuit shows that the gate voltage V_g is displaced

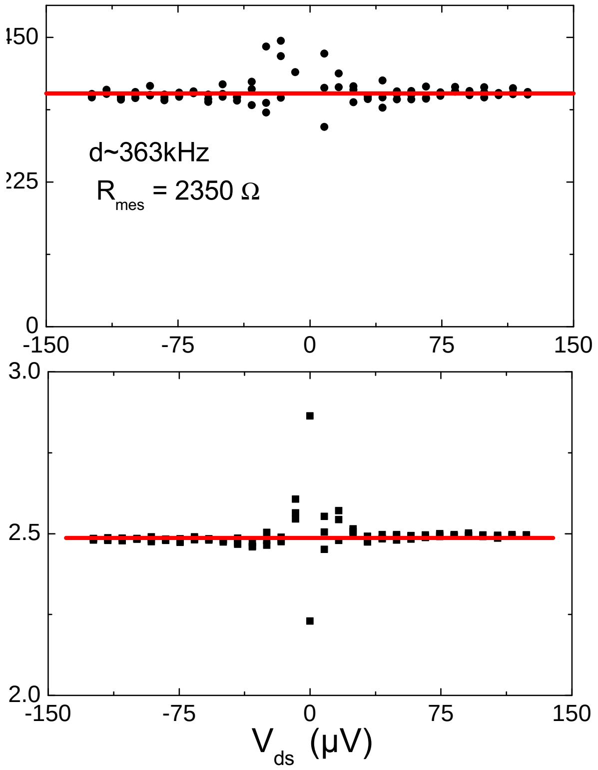

FIGURE C.3 – Passband Filtering of Joule Heating Noise. The numerical least-square method fails as the noise is too low to see a peak, leading to the random points near V_{ds}=0. The error bar becomes quickly as small as the plotted data dot.

by $-V_{ds}$. The typical amplitude for V_g is -280 mV, and the gain is very sensitive to small changes in the working point in this region (the gain moves typically from almost 0 to -5 V/V over 30 mV). When comparing any noise PSD with the equilibrium spectrum V_{ds}=0, the main effect of a small change in the gain is a change in the baseline from the cryo-amplifiers noise-voltage. This is why we have introduced the fitting parameter $P_{w,0}(V_{ds})$, which separates this frequency-independent [1] effect from the filtered current noise power $|\mathrm{I}_{\mathrm{L},\mathrm{V}_{ds}}|^2$. The extracted noise power is shown in Fig.C.4.

We interpret $P_{w,0}(V_{ds})$ as a change in gain :

$$P_{w,0}(V_{ds}) = [G^2_{cryo}(V_{ds}) - G^2_{cryo}(V_{ds} = 0)]G^2_{NF}|\delta V_{NB}|^2 \qquad \text{(C.2)}$$

As can be seen in Fig.C.4, the drift is extremely small. Extrapolating to 30 mV, we would

---

[1] As long as post-amplification and line-filtering do not evolve. This is true over 2-3 MHz.

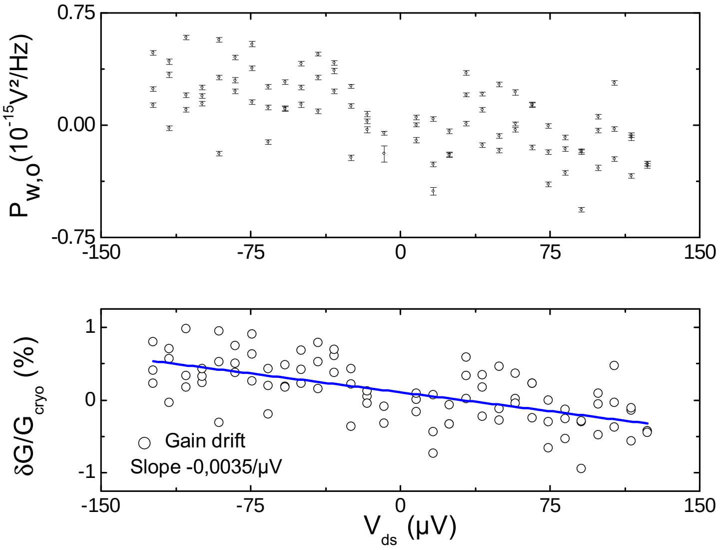

FIGURE C.4 – Gain deviations with bias voltage.

expect a change of about 100% in the gain, remarkably close to the proposed estimate using the I-V polarization curves.

C.1.4 Effective model for Joule Heating and parameters

Amplitude $A(V_{ds})$ is converted in a temperature increase on R_L. As R_LF is 100 times larger than R_L, the temperature would have to be 100 times larger to produce the same current noise. The effective temperature is shown in Fig.C.5. The experimental datas show a few interesting features. First it does not evolve at low-bias, then increases rapidly. Near 75 µV, the slope starts to decrease. For instance, a best fit with a single adjustable parameter and imitating the thermalization of thin film diffusive resistors in[138] produce such a behavior :

$$\frac{\partial^2 T_e^2(x)}{\partial^2 x^2} = -\frac{2V_{ds}^2}{\lambda_L L^2} - a(T_e^5(x) - T_{ph}^5) \tag{C.3}$$

With λ_L the Lorenz number, L=1 mm, and T$_e(x)$ is the electronic temperature along the resistor. T_{ph} is the crystal temperature : it imposes the conductor equilibirum temperature, which was most likely 35 mK according to Johnson-Nyquist measurements. The two term on the right-hand are meant to correspond to the dissipated Joule power and a phonon-electron thermal exchange term. a=4E11 is found (see Fig.C.5). We lack information to discuss further the relevance of this model, and check how realistic is the factor a. We therefore need an experimental scheme which allows to reject this noise in any situation. This is developed in the next section.

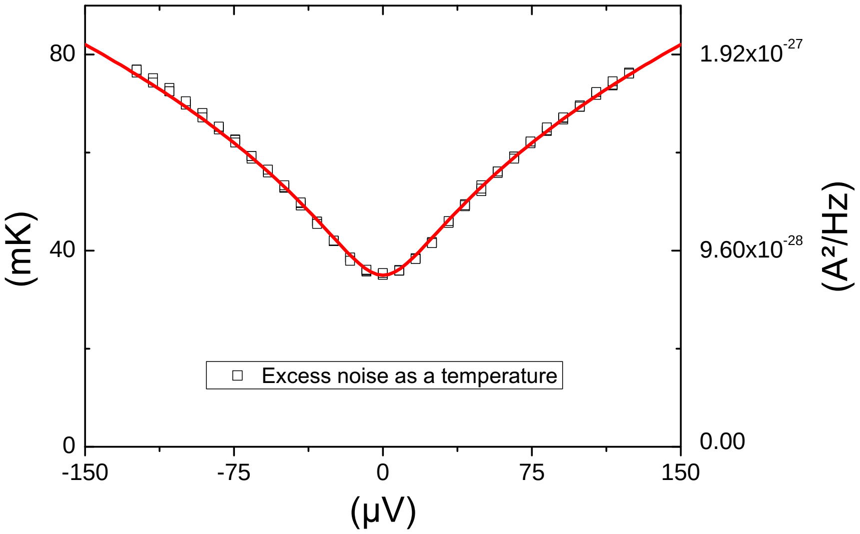

FIGURE C.5 – CMS effective temperature as a function of the applied bias voltage. Experimental data(square) and fit(red line).

C.1.5 Consequences

The CMS does not show any increase in temperature when a RF signal is applied from line B in the typical range of power necessary for few electrons pulses (a few pW on R_L, similar to the range explored with V_{ds}). It is confirmed by the perfect superposition shown in Fig.C.6 of the noise increase as seen in the two auto-correlation PSD and the cross-correlation PSD for a typical noise spectroscopy of an AC-pulse. The parameter γ is used to normalize the three amplitudes according to the gain difference between the lines.

Nonetheless, it must be underlined how the calibration based on the DC shot noise proposed in chapter2 has to be modified to fully take into account this effect. Basically a localized noise source enters in the noise along the shot noise from the sample. The key point is the fact that contrary to a source of noise localized in parallel with the sample, a source in parallel with one of the measurement resistor does not appear identically in

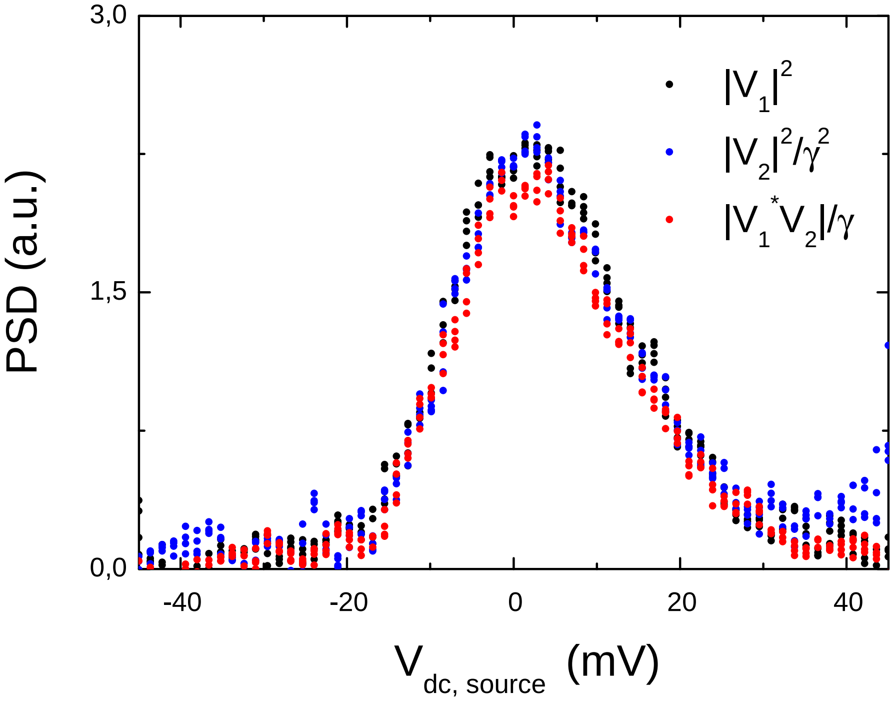

FIGURE C.6 – Typical noise spectroscopy of a Lorentzian pulse with D∼0.25.

all three PSD $|V_1|^2$, $|V_2|^2$, and $Re|\overline{V_1}V_2|$. Schematically, we have two independent sources $|\mathrm{I}_{\mathrm{L},\mathrm{V}_{ds}}|^2$ and $|\mathrm{I}_{\mathrm{s},\mathrm{V}_{ds}}|^2$ leading to power amplitude p and $|\mathrm{V}_{\mathrm{s},\mathrm{V}_{ds}}|^2$ in $|V_2|^2$. Here the variable V_{ds} is no longer the bias on the polarized R_L but on the sample R_S.

$$\begin{aligned}
\frac{|V_2|^2}{|G_B|^2} &= p + |\mathrm{V}_{\mathrm{s},\mathrm{V}_{ds}}|^2 \\
\frac{|V_1|^2}{|G_B|^2} &= \gamma^{-2}(\alpha^2 p + |\mathrm{V}_{\mathrm{s},\mathrm{V}_{ds}}|^2) \\
\frac{|\overline{V_1}V_2|}{|G_B|^2} &= \gamma^{-1}(\alpha p - |\mathrm{V}_{\mathrm{s},\mathrm{V}_{ds}}|^2)
\end{aligned} \tag{C.4}$$

α contains the voltage divider created by the measurement bridge. It does not depend on V_{ds}. Whatever the amplitude of $|\mathrm{I}_{\mathrm{L},\mathrm{V}_{ds}}|^2$, α, p, there is no adjustable parameters left and we can extract precisely the meaningful $|\mathrm{V}_{\mathrm{s},\mathrm{V}_{ds}}|^2$ and continue the Shot Noise analysis as usual(γ must be known or estimated as in section 2.3.3). See Fig.C.7 and C.8

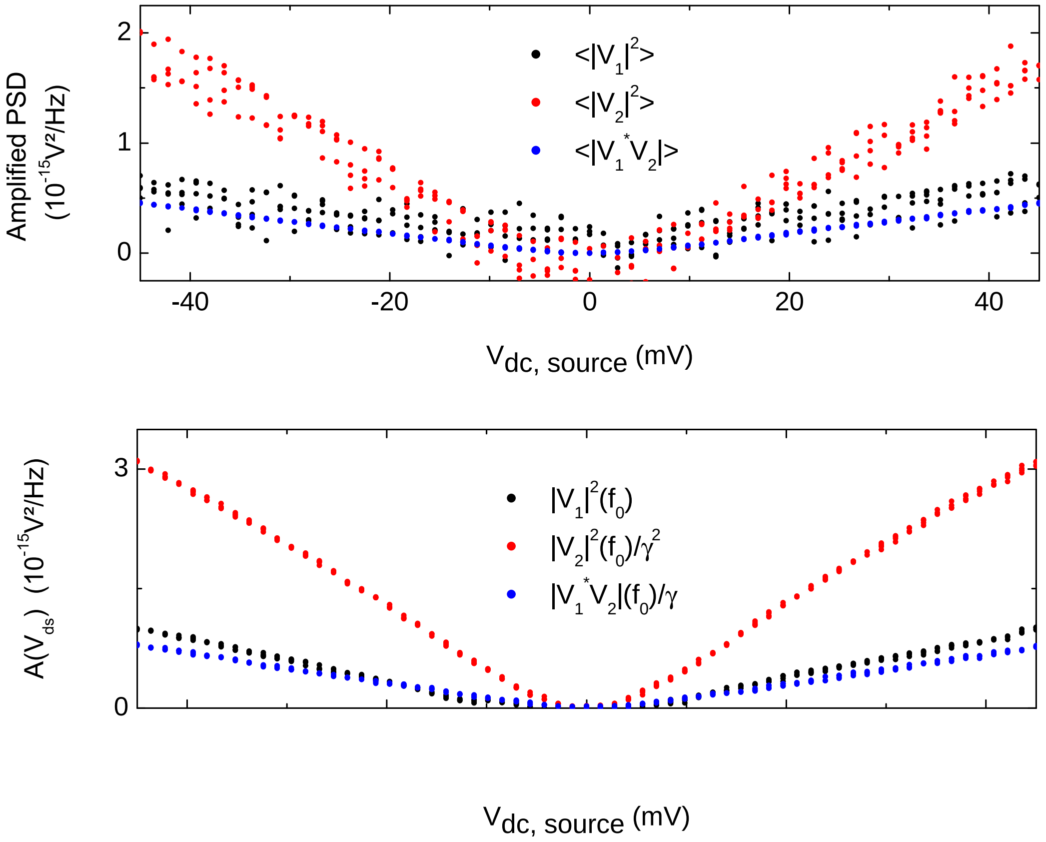

FIGURE C.7 – DC shot noise measurement with D∼0.25 as appearing in the different available PSD $|V_1|^2$(black), $|V_2|^2$(red), and $Re|\overline{V_1}V_2|$(blue). The Top part shows data points using the average over 2-3 MHz and 40000 repeated PSD single measurements. The quality of the auto-correlations measurements is much lower than the cross-correlations measurements. Interestingly, the extraction of the peak amplitude $A(V_{ds})$ using a least square algorithm and C.1 appears to be equally good for all the different available PSD, as shown in the Bottom part. It shows that this random error can be entirely explained by change in the voltage noise of each amplifier and removed. Looking closely at the untreated data points, parallel lines appear. The noise changes might not be fully random and have an underlying "flicker" structure.

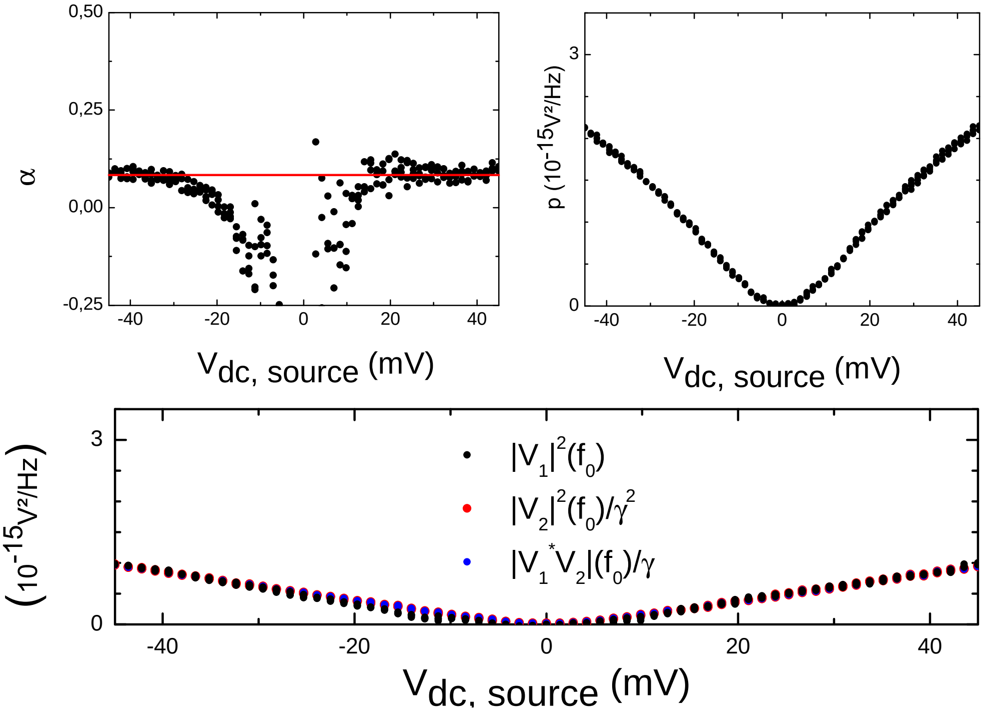

FIGURE C.8 – Full separation of the parasitic noise power "p" and DC Shot noise from the mesoscopic sample using the model C.4. Despite difficulties at low bias which could be reasonably associated to a very small and uncontrolled gain drift between the two measurements lines, the large signal for large bias allows a very satisfying extraction of the sample Signal.

C.2 Noise-level from post-amplification

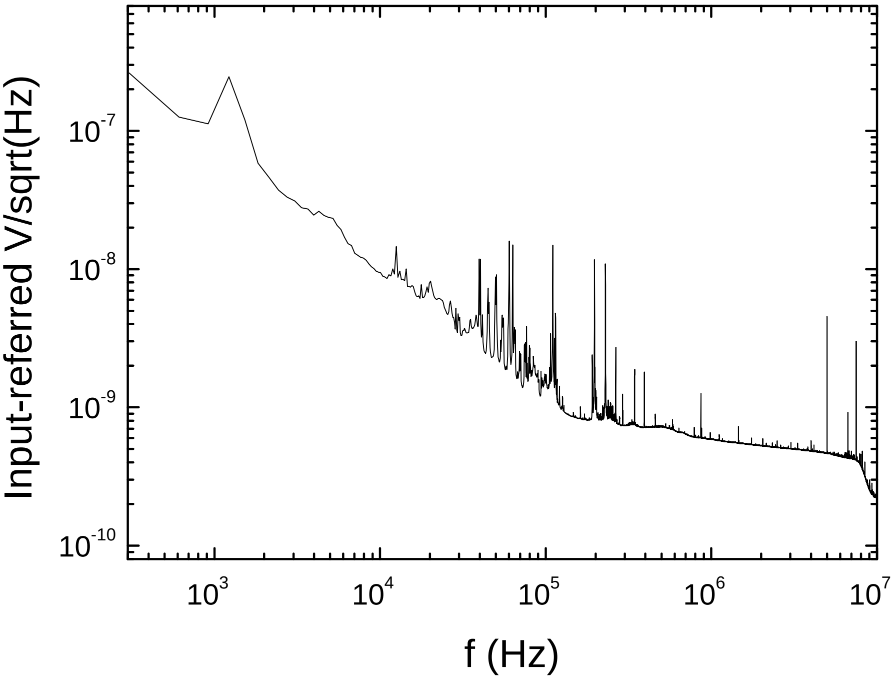

FIGURE C.9 – Input-referred spectral noise density from post- amplification. The amplifier model is NF SA421SA. A short circuit is placed at the input of the splitter board. The white noise observed in the range 1-10 MHz is in agreement with manufacturers specifications.

C.3 Acquisition Card input-noise

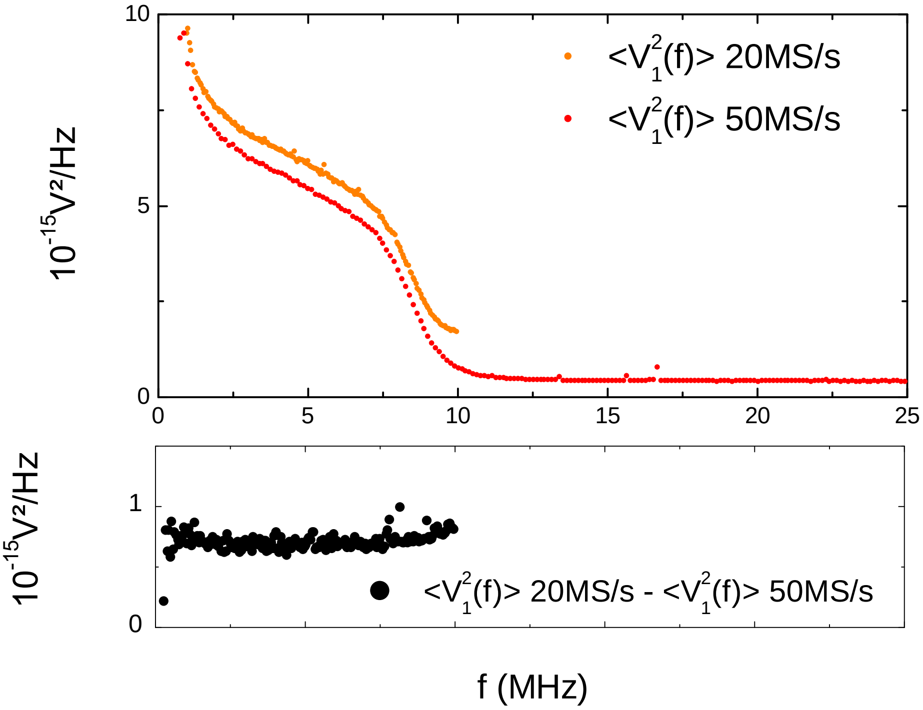

FIGURE C.10 – (top) Amplified spectral noise density from post-amplification filtered and then measured with two different sampling rate. (orange dots) 20 MS/s. (red dots) 50 MS/s. The Nyquist frequency moves accordingly from 10 MHz to 25 MHz. (bottom) Amplified spectral noise density at 50 MS/s substracted from 20 MS/s. Flatness and amplitude beyond 12 MHz indicates an excess white noise from the acquisition process, either physical or numerical. The upward translation is strictly equal to the one expected from integrating the white noise beyond 10 MHz on a shorter frequency range.

Annexe D

Chip-carrier High frequency design

This part is entirely reproduced from Julie Dubois Phd thesis for information purpose. The PCB dscribed here is used in single-electron pulsed source measurement in chapter 2,3 4 and 5.

To maintain a 50 Ω impedance and avoid unwanted reflections along the line, a particular attention has been paid to the design of the sample holder, which is used to adapt coaxial line with a typical 2.2 mm diameter to the sample size. Losses and grounding have been anticipated. The chip-carrier substrate is a 381 µm thick Rogers TMM10 laminate, with 17,5 µm thick copper lines. The dielectric constant is chosen close to the sample material (9.2 at 10 GHz). Copper conductors defining the lines are gold-plated (2 µm) to prevent oxydation. A thick copper plate of 1 mm is also bound to the circuit background using silver loaded conductive adhesive to form the center "pocket" where the sample is placed (Fig.D.1,D.3 andD.4). Via-holes with a diameter of ∼200 µm are regularly drilled in the laminate, they are filled/plated with copper and gold to ensure conductivity. The center socket is a 2.2 mm square, with clearance holes at the corners. Rosenberger 18s101-40ml5 right-angle mini-SMP connectors are placed on each soldering footrint detailed in Fig. D.3 (transmistting up to 40 GHz).

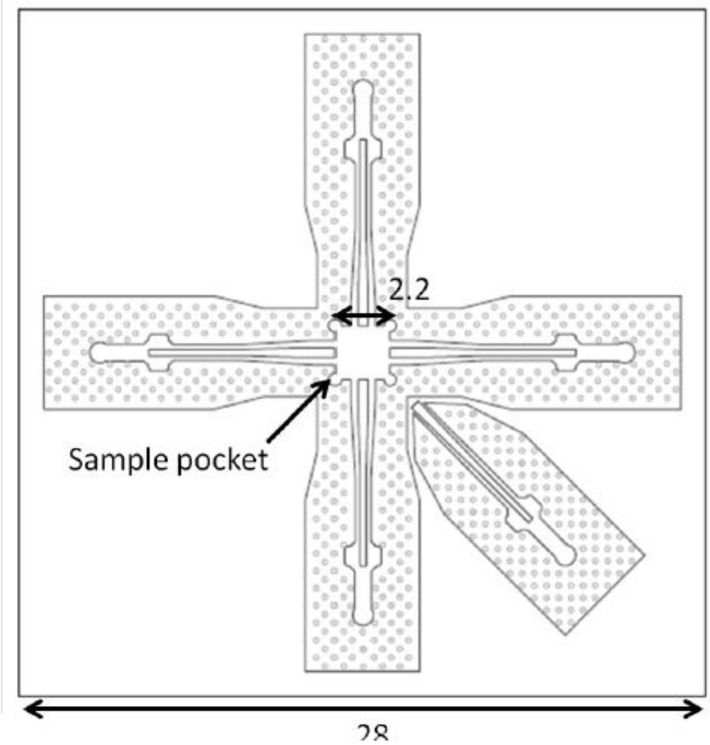

FIGURE D.1 – Sample holder. Dimensions are in mm.

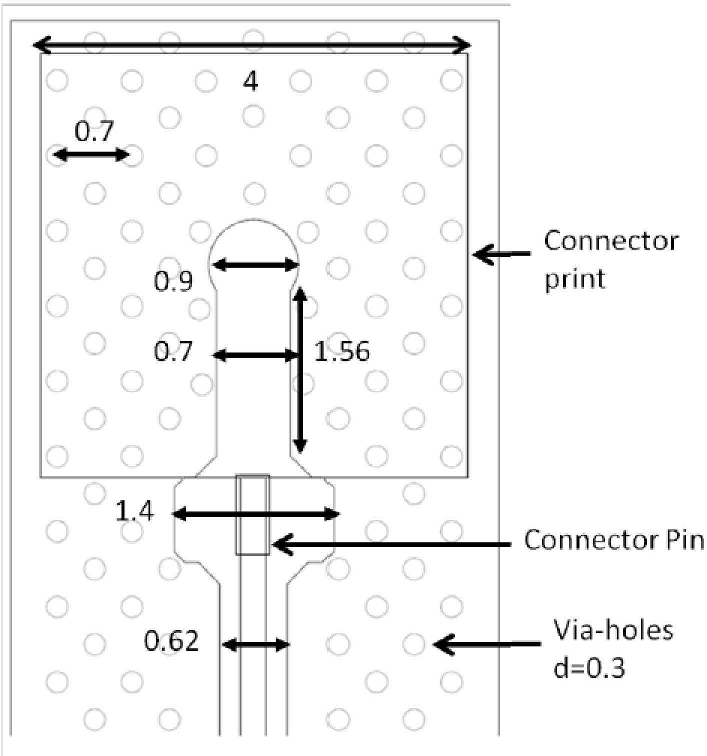

FIGURE D.2 – Sample holder connectors.

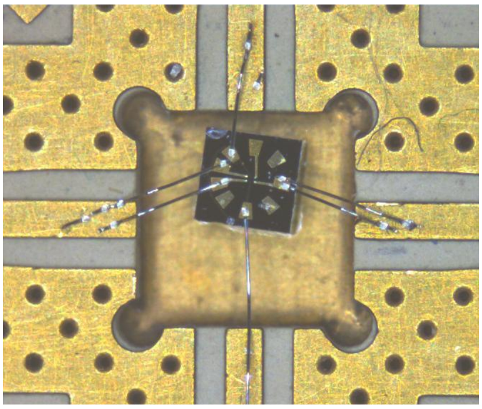

FIGURE D.3 – Position and bonding of sample "B".

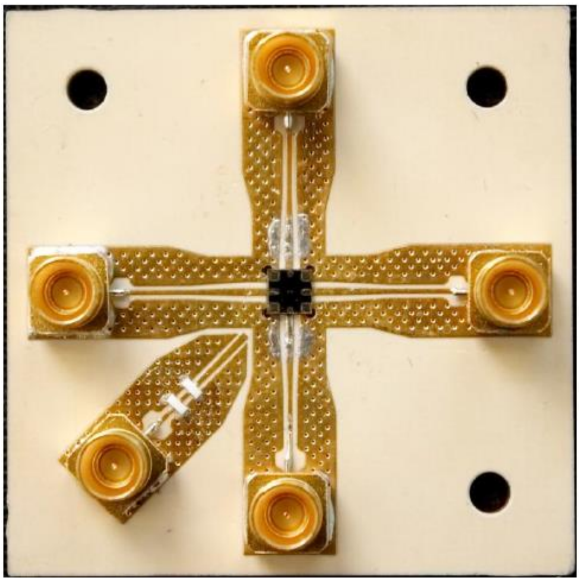

FIGURE D.4 – Position and bonding of sample "A".

Annexe E

Filters

Acquisition is performed at 20 MS/s. A low-pass filter with cut-off under the Nyquist frequency 10 MHz is needed. The geometry of this filter is designed to follow a 7^{th}-order Thebytchev pattern [137] adapted to a 50 Ω coaxial line (Fig. E.1). A small 10Ω resistor is added in order to erase ripple over 1 MHz-4 MHz. For this calibration, a RF source Anritsu 69147B is used to generate a -20 dBm excitation signal. In order to obtain directly the transmission function of the last stage of the circuit, the signal is send at the NF amplifiers output point (see Fig. 2.1) . The obtained transmission (Fig. E.2) is in good agreement with expectations. The DC attenuation corresponds to the drop over the 10 Ω resistor. The negative slope from 0 to 8 MHz corresponds to the increasing resistance of all three inductors : roughly 1(5) Ω at DC(10 MHz), see manufacturers Datasheet : Würth Electronik Ferrite CMS). Thus the 46 dB-gain of room-temperature amplification is slightly reduced to a factor 165 at 2.5 MHz. The cut-off frequency is 8.5 MHz and the roll-off, -26 dB between 2.5 and 12.5 MHz, strongly limits aliasing.

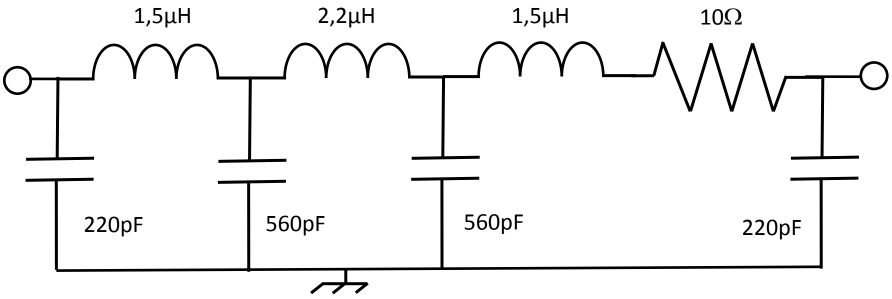

FIGURE E.1 – Schematic representation of room temperature filtering.

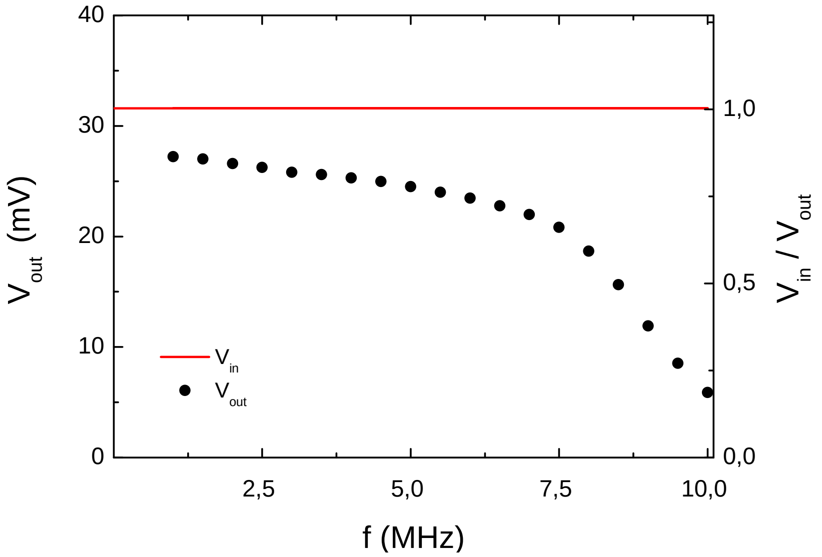

FIGURE E.2 – Filter calibration with Agilent Acquiris card.

Annexe F

ATF-34143 DC characteristic

F.1 1 HEMT

Fig. F.1 represents the set-up used to obtain the DC characteristic of an ATF-34143 pHEMT.

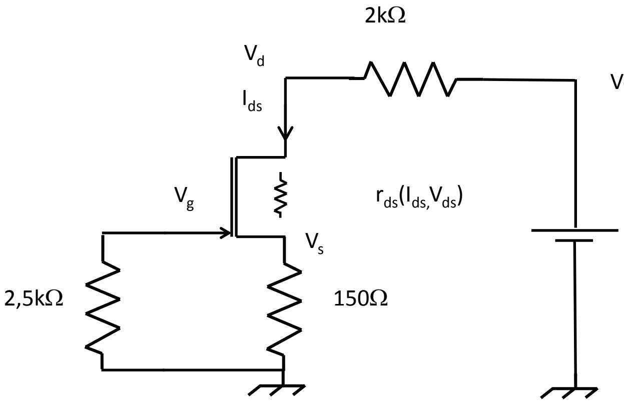

FIGURE F.1 – Set-up for I-V measurement for a self-polarised ATF-34143. Tensions V_{ds} and V_{gs} are respectively $V_d - V_s$ and $V_g - V_s$.

The value $150\,\Omega$ for the polarization resistor is close, but not identical, to the one in the parallel two-HEMTs device described in chapter 2. As shown in Fig. F.2a, room temperature and 4 K I-V curves differ and the quantitative analysis must be done at low-temperature. We note that both I-V curves show a lower saturation current than found in [34]. As mentioned in [122], the constrained relation $V_{gs}(I_{ds}) = -150 I_{ds}$ when changing V_{dc} prevents from deducing the differential conductance g_{ds} of the HEMT channel using the characterictic curve only. The constrained differential conductance $g(I_{ds}, V_{ds}(I_{ds})) = dI_{ds}/dV_{ds}$ at 4 K is plotted together with G(I,V_{ds})= I_{ds}/V_{ds} in Fig. F.2b.

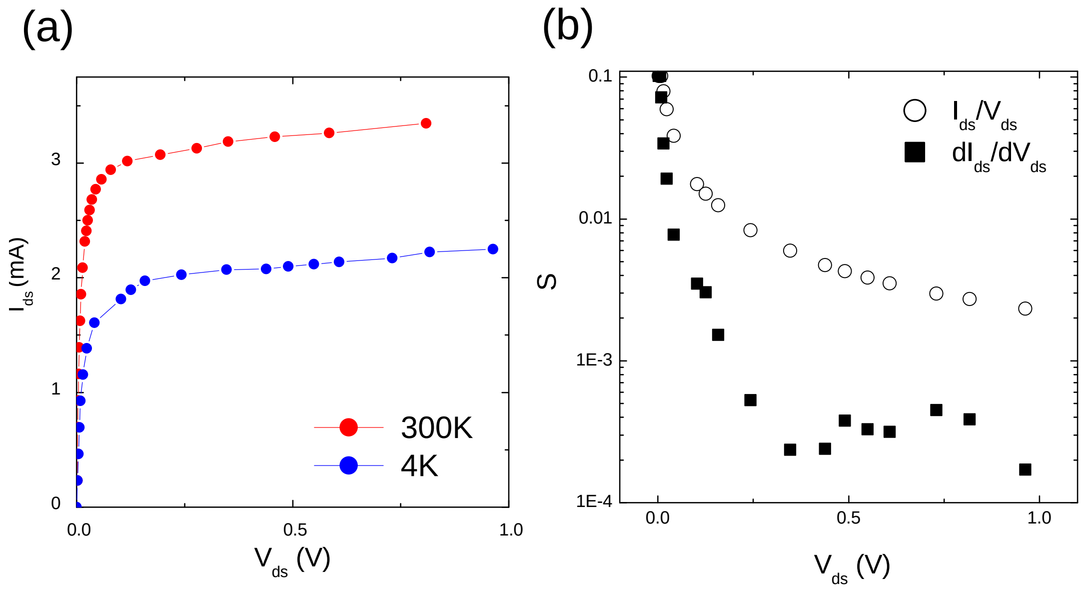

FIGURE F.2 – (a) Drain current I_{ds} as a function of drain-source voltage V_{ds} for a self-polarised ATF-34143. The red curve is a room temperature measurement, while the blue curve corresponds to a measurement in an He^4 bath. Values are derived from $I_{ds}(V_{dc})$ measurement. (b) Black dots represent G(I,V_{ds})=I_{ds}/V_{ds}, the non-linear conductance of the HEMT channel at 4 K. Black squares represent the constrained differential conductance g(I_{ds},$V_{ds}(I_{ds})$)=dI_{ds}/dV_{ds} at 4 K. Fluctuations in square points are a direct consequence of numerical derivation with scarce data points.

If the HEMT intrinsic gain $A_{hemt} = g_m/g_{ds}$, associated with g_m the transconductance, can be measured separately at a selected polarisation current, a reverse analyis can in principle provide g_{ds}. Indeed, using the relation between A_{hemt} and partial derivatives of $V_{ds}(I_{ds}, V_{gs})$ and inserting the constrained equation for V_g, we obtain equation F.1 :

$$g(I_{ds}, V_{ds}(I_{ds})) = \frac{dI_{ds}}{dV_{ds}} = \frac{1}{1/g_{ds} + A_{hemt} 150\Omega} \tag{F.1}$$

Compared to g_{ds}, that could be measured in a fixed-V_{gs} I-V characteristic, g is reduced since an increase in I_{ds} increase channel pinching.

Looking at equation F.2, we note that the power consumption P_w is easily maintained below 2 mW ($V_{ds} < 0.6\,\mathrm{V}$). If needed, using a polarisation resistance larger than 150Ω should lower the saturation current and decrease power consumption. This is exemplified by the system tested in the next section.

$$P_w = I_{ds}V_{ds} + \frac{I_{ds}^2}{150\Omega} \tag{F.2}$$

F.2 10 HEMTs with self-polarisation 1 kΩ

A test was conducted with 10 HEMTs in parallel.

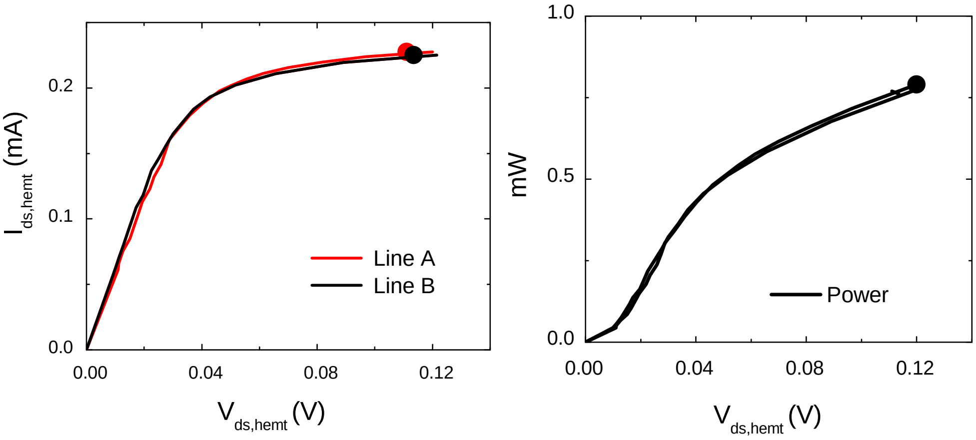

FIGURE F.3 – (a) Drain current I_{ds} as a function of drain-source voltage V_{ds} for a each ATF-34143 in a 10-HEMTs amplifier. Two prototypes were tested, leading to the red and black curves, both in an He^4 bath. Values are derived from the total $I_{ds}(V_{dc})$ measurement, and then interpreted as an individual I-V curve. A dot marks on each curve the polarisation point used for the noise calibration. (b) Total power consumption.

Compared to the 2-HEMTs devices studied in chapter2, each polarisation resistors has been changed to 1 kΩ before duplicating the pattern. This method strongly limits change in total power consumption : instead of being multiplicated, it has decreased. The device was tested with a DC shot noise experiment with a QPC and the noise voltage was

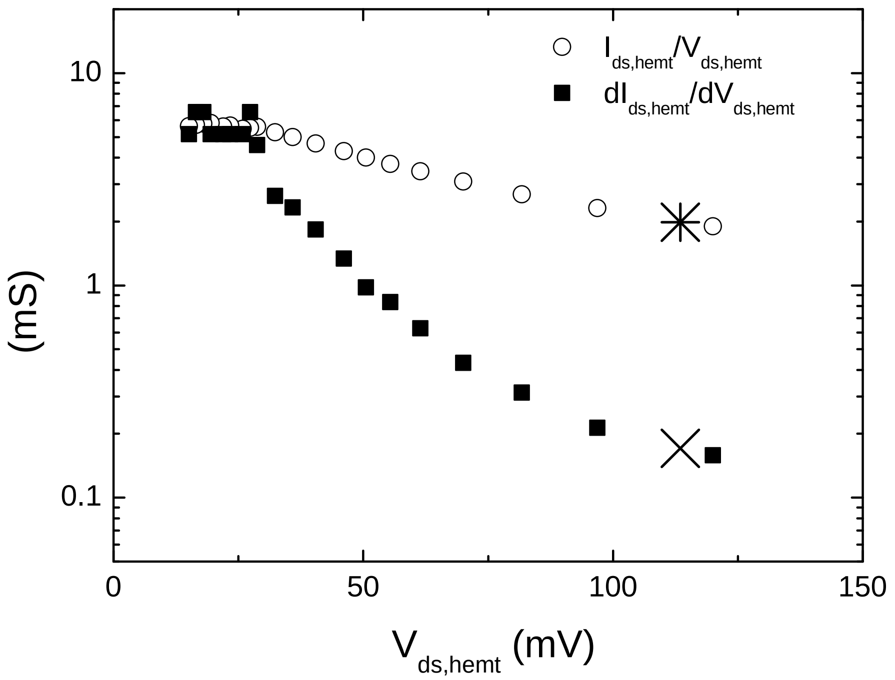

FIGURE F.4 – Black dots represent G(I,V_{ds})=I_{ds}/V_{ds}, the non-linear conductance of the HEMT channel at 4 K. Black squares represent the constrained differential conductance g(I_{ds},$V_{ds}(I_{ds})$)=dI_{ds}/dV_{ds} at 4 K. Fluctuations in square points are a direct consequence of numerical derivation with scarce data points. The polarisation point at which a noise measurement was attempted is marked with a star(cross) shape on the G(g) curve.

almost identical to the 2-HEMTs device with approximately $0.19\,\mathrm{nV}\sqrt{Hz}$ at the input, for approximately the same gain ∼ 5.3, in apparent contradiciton with the expected process. But the use of 1 kΩ change dramatically the polarisation point and the system does not equate the theoretical "parallelising" operation that would have lead to a reduced noise voltage. Noise current was observed but not evaluated.

F.3 10 HEMTs with self-polarisation 250 Ω

Compared to the 2-HEMTs devices studied in chapter2, each polarisation resistors has been changed to a lower quality resistor(thick film) expected to be 200 Ω but found around 250 Ω at low temperature. The I-V characteristicF.6 shows a significantly lower saturation current than with 200 Ω, the change being consistent with the drop already observed[1] in sectionF.1 from 150Ω to 200 Ω.

The duplicated pattern was also modified, with less components along the input path. Fig. F.6 shows the pattern we used.

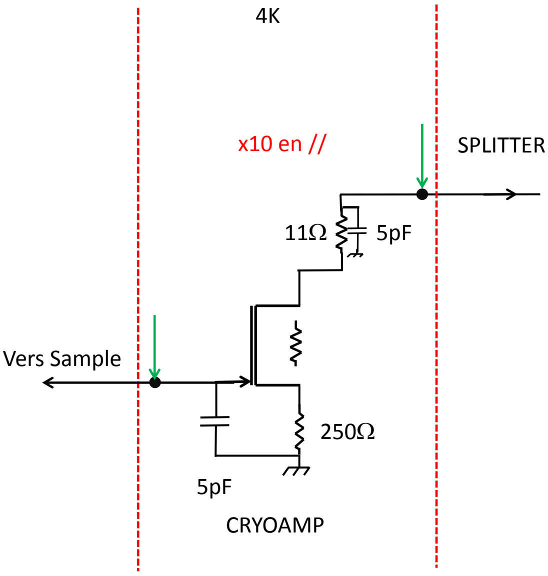

FIGURE F.5 – 10-HEMTs amplifier duplicated pattern. The green arrow indicates the common input and output points for the 10 parallels circuits.

As expected, the power consumption increase.

The device was tested with a DC shot noise experiment with a QPC. The best gain with long-term stability was found to be lower than the device described in 2, with about -1.6 V/V when $V_{dc,source} = 17.75\,V$ as a maximum. The cause of this lack of stability is still unknown. In this situation, the input-referred noise from the room-temperature amplification stage was found to be dominating and no significant acceleration of statistical measurements resulted. But the input-referred contribution to the voltage noise from the cryo-amplifiers was close to $\sim 0.12\,\text{nV}/\sqrt{Hz}$ the expected value being $\sim 0.09\,\text{nV}/\sqrt{Hz}$.

Noise current was observed but not precisely investigated. If we reproduce the method developed in chapter2 where the noise power measured outside the resonant bandwidth was subtracted to determine the amplitude of the source correlated to the sample conductance,

---

[1] Systematic tests with a set of resistance with small increase +10 Ω in the range 100-300 Ω but with a single ATF-35143 instead of ATF-34143 produce a similar evolution.

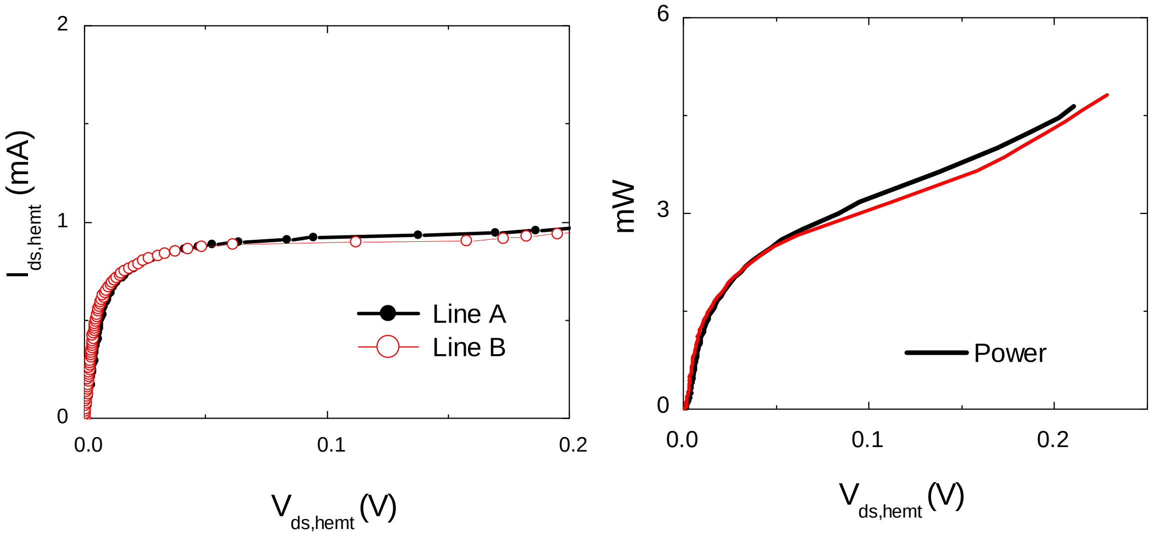

FIGURE F.6 – (a) Drain current I_{ds} as a function of drain-source voltage V_{ds} for a each ATF-34143 in a 10-HEMTs amplifier with self-polarisation 250 Ω. Two exemplaries were tested, leading to the red and black curves, both at 4 K. Values are derived from the total $I_{ds}(V_{dc})$ measurement, and then interpreted as an individual I-V curve. (b) Total power consumption for each cryo-amplifier.

we see an oscillation with a relative amplitude up to 25% of the baseline. It indicates a larger Drain-Gate coupling than with 2 HEMTs in parallel, as expected.

Annexe G

Data extraction

In order to extract the noise level corresponding to the situation in which charge injection is attempted from noise spectroscopy measurements with the lowest possible error bar, a least-square algorithm was used. The procedure involves a best fit with the following shape :

$$\Delta N_{eh}(q) = ae^{-(q-b)/c} + de^{-(q-f)/g} \tag{G.1}$$

This form is inspired by the asymptotic tails observed in section 1.4.3. It seems to avoid any obvious over-fitting, as the final residual distribution has a variance in agreement with the unavoidable noise from the amplification. For the sake of transparency, we have are gathered here a few curves which exemplified the procedure.

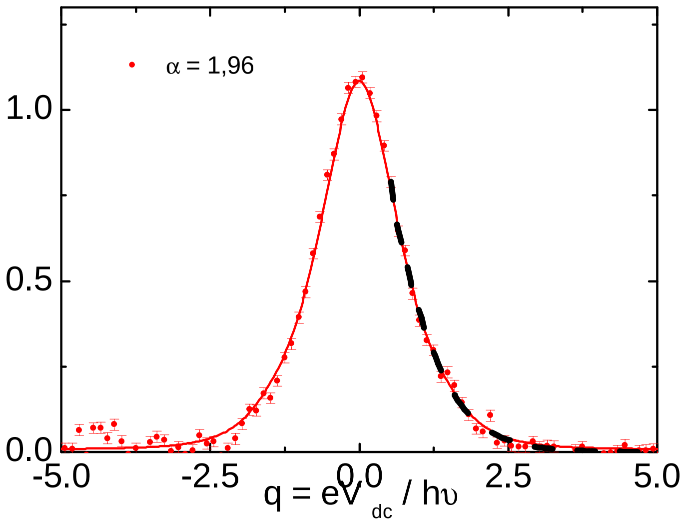

FIGURE G.1 – From sinus 7.5 GHz.

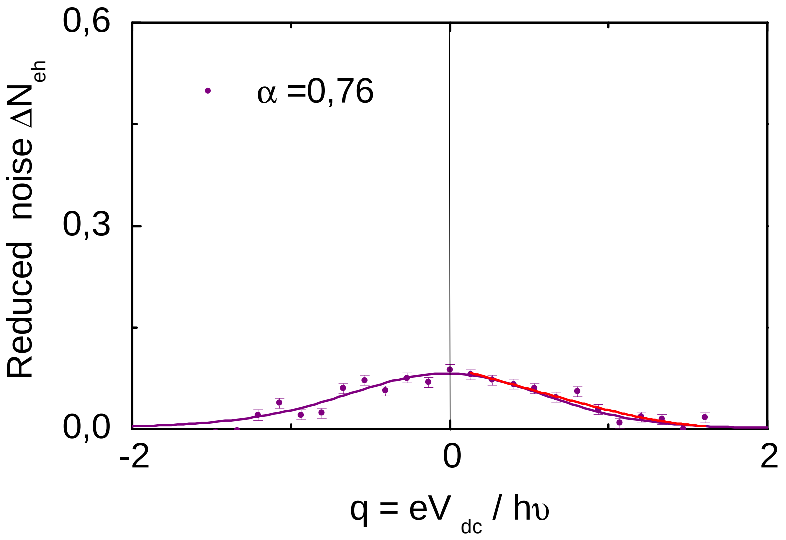

FIGURE G.2 – From Lorentzian 4.8 GHz energy spectroscopy experiment.

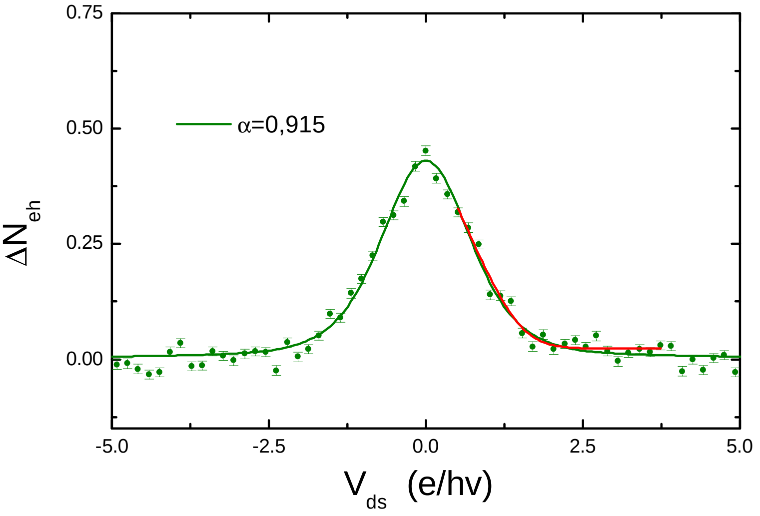

Figure G.3 – From Square 4 GHz energy spectroscopy experiment.

Annexe H

Second Order Expression in QST

In this appendix, additional elements are collected to comment on the impact of a first order development in η_k for the tomography experiment.

$$\tilde{p_l} = \frac{1}{T}\int_0^T dte^{-i\phi(t)}e^{il2\pi\nu t}e^{i\int_0^t 2\pi k\eta_k\ cos(2\pi k\nu t+\Theta_S+\pi)} \tag{H.1}$$

$$\tilde{p_l} = \frac{1}{T}\int_0^T dte^{-i\phi(t)}e^{il2\pi\nu t}e^{-i\eta_k\ sin(2\pi k\nu t+\Theta_S)}e^{i\eta_k\ sin(\Theta_S)} \tag{H.2}$$

We develop to the second order in η_k the above expression.

$$\tilde{p_l} = (1-\frac{\eta_k^2}{4})p_l - \frac{\eta_k}{2}(p_{l+k}e^{i\Theta_S} - p_{l-k}e^{-i\Theta_S}) + \frac{\eta_k^2}{8}(p_{l+2k}e^{i\Theta_S} + p_{l-2k}e^{-i\Theta_S}) \tag{H.3}$$

We know from chapter 1 that a noise spectroscopy will provide the quantities :

$$\begin{aligned}|\tilde{p_l}|^2 =&(1-\frac{\eta_k^2}{2})|p_l|^2 - \eta_k Re\left(\overline{p_l}(p_{l+k}e^{i\Theta_S} - p_{l-k}e^{-i\Theta_S})\right)\\ &-\frac{\eta_k^2}{4}Re\left(\overline{p_l}(p_{l+2k}e^{i\Theta_S} - p_{l-2k}e^{-i\Theta_S})\right) - \frac{\eta_k^2}{4}|p_{l+k}e^{i\Theta_S} - p_{l-k}e^{-i\Theta_S}|^2\end{aligned}$$

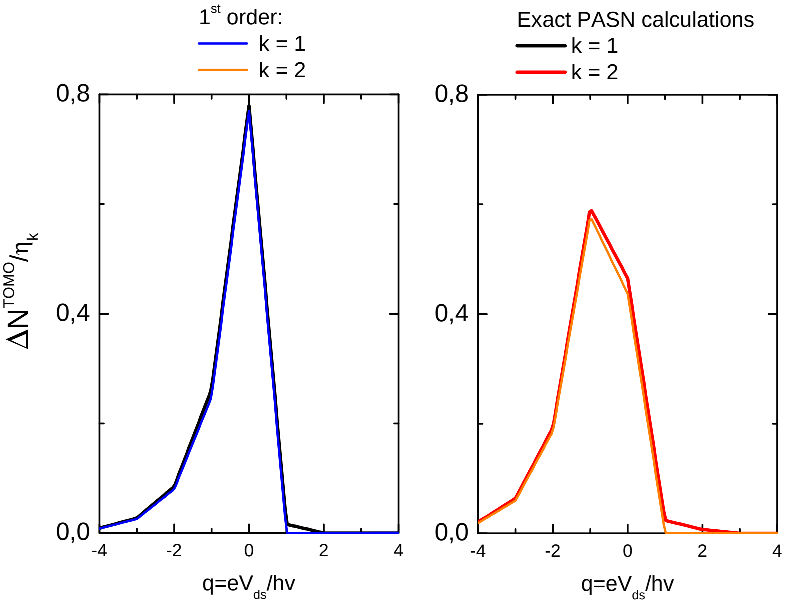

FIGURE H.1 – Exact PASN calculation and first order development in η_k for the tomography DC sweep for a Leviton W/T=0.09. $\Theta_S = 0$ and the amplitude $\eta_1 = 0.095$ and $\eta_2 = 0.0425$ corresponds to experimental values. See chapter 5. Results are divided by η_k for comparison.

Annexe I

Table of Symbols

Symbol	Definition
D	QPC Transmission
e	elementary charge
h	Planck Constant
k_B	Boltzmann Constant
T, ν	Period, Frequency
N_e, N_h, N_{eh}	Number of electron/hole/particles injected per pulse when $D = 1$
Q_e	Number of injected charges
q	$eV_{ds}/h\nu$
$V_p(t)$	Voltage Pulse
$V_{ac}(t)$	AC Voltage
V_{ds}	DC Voltage
S_I^0	$2\frac{e^2}{h}D(1-D)h\nu\times$nb. channels
L_s	Sample size
L, R	Left or Right
$T_e = \theta_e h\nu/k_B$	Electronic temperature
$\mu_{L,F}$	Electro-chemical Potential
E_F	Fermi Energy
$f_{L,R}(\varepsilon)$ or $f_{L,R}$	Energy Distribution
$\tilde{f}_{L,R}(\varepsilon)$ or $\tilde{f}_{L,R}$	Excited Energy Distribution
S_I^{DCSN}, S_I^{PASN}	DC Shot Noise, Photo-Assisted Shot Noise
$\hat{\mathbf{I}}(t)$	Current operator
$\hat{a}_{L,F}(\varepsilon)/\ \hat{b}_{L,F}(\varepsilon)$	Injected/reflected annihilation operator
$\hat{a}/\hat{b}_{L,F}(\varepsilon, l)$	Annihilation operator with semi-discrete index
$\hat{a}^F/\hat{b}_{L,F}(\varepsilon)$	Excited annihilation operator

Table I.1 – List of symbols

Symbol	Definition
$\phi(t)$	Voltage flux
R_c	Contacts and Mesa series resistance
P_l, p_l	Photo-assisted probability, probability amplitude l
p_l^{Lev}	Periodic leviton probability amplitude
$\tilde{p}_l$	Modulated pobability amplitude (QST)
$\alpha = eV_{ac}/h\nu$	AC voltage amplitude in reduced units
$\hat{\mathbf{P}}(\varepsilon)$	Floquet scattering matrix
$\Delta N_{eh}(T_e, q, \alpha)$	Excess PASN in reduced units
$W, W/T = \eta$	FWHM and duty cycle
$I_{ph}(V_p)$	Photocurrent
$\Pi_k(\tau)$	Photo-assisted amplitude k (time-spectroscopy) experiment
$C(\tau)$	Wave function single-particle time-overlap
β	$e^{-2\pi W/T}$
$(\Delta)S_I^{HOM}$	Time spectroscopy experiment (excess) noise
$(\Delta)S_I^{TOMO}$	QST experiment (excess) noise
v_F	Fermi velocity
p^{reg}	Regular part of isolated leviton photo-assisted distribution
$V_S(t)/V_{mod}/\Theta_S$	Modulation signal/amplitude/phase(QST)
η_k	Modulation reduced amplitude (QST)
η_ν	RF attenuation at frequency ν

Table I.2 – List of symbols

Acronym	Definition
QPC	Quantum Point Contact
QST	Quantum State Tomography
PASN	Photo-Assisted Shot Noise
PSD	Power Spectral Density
FCS	Full Counting Statistics
2DEG	2-dimensional Electron Gas
FWHM	Full Width at Half-Maximum
AOC	Anderson Orthogonality Catastrophe
RF	Radio-Frequency
WTD	Waiting Time Distribution
HEMT	High Electronic Mobility Transistor
ADC	Anolog to Digital Conversion
DAC	Digital to Analog Conversion

Table I.3 – Acronym List

Bibliographie

[1] F. J. Ahlers, O. F. O. Kieler, B. E. Sağol, K. Pierz, and U. Siegner. Quantized acoustoelectric single electron transport close to equilibrium. Journal of Applied Physics, 100(9) :093702+, November 2006. 148

[2] Mathias Albert and Pierre Devillard. Waiting time distribution for trains of quantized electron pulses, January 2014. 39

[3] Mathias Albert, Christian Flindt, and Markus Büttiker. Distributions of Waiting Times of Dynamic Single-Electron Emitters. Physical Review Letters, 107(8), August 2011. 39

[4] P. Anderson. Infrared Catastrophe in Fermi Gases with Local Scattering Potentials. Physical Review Letters, 18(24) :1049–1051, June 1967. 22, 114

[5] J. Ashburn, R. Cline, P. van der Burgt, W. Westerveld, and J. Risley. Experimentally determined density matrices for h(n=3) formed in collisions from 20 to 100 kev. Physical Review A, 41(5) :2407–2421, March 1990. 123

[6] D. Bagrets and F. Pistolesi. Frequency dispersion of photon-assisted shot noise in mesoscopic conductors. Physical Review B, 75(16) :165315+, April 2007. 11

[7] Eva Z. Bajjani. Bruit de grenaille quantique électronique et statistique de photons micro-ondes. PhD thesis, Université Pierre et Marie Curie - Paris VI, September 2009. 166

[8] John Bardeen. Surface States and Rectification at a Metal Semi-Conductor Contact. Physical Review, 71(10) :717–727, May 1947. 159

[9] N. Bergeal, F. Schackert, L. Frunzio, D. E. Prober, and M. H. Devoret. Mesoscopic resistor as a self-calibrating quantum noise source. Applied Physics Letters, 100(20) :203507+, 2012. 60

[10] A. Bertoni, P. Bordone, R. Brunetti, C. Jacoboni, and S. Reggiani. Quantum Logic Gates based on Coherent Electron Transport in Quantum Wires. Physical Review Letters, 84 :5912–5915, June 2000. 149

[11] A. S. Bhatti, D. Richards, H. P. Hughes, D. A. Ritchie, A. C. Churchill, M. P. Grimshaw, and G. A. C. Jones. Excitations of a drifting 2DEG. Solid-State Electronics, 40(1-8) :719–723, January 1996. 162

[12] H. Birk, M. J. M. de Jong, and C. Schönenberger. Shot-Noise Suppression in the Single-Electron Tunneling Regime. Physical Review Letters, 75 :1610–1613, August 1995. 2

[13] Laure-Hélène Bize-Reydellet. Bruit quantique électronique et photons micro-ondes. PhD thesis, Université Pierre et Marie Curie, Université Pierre et Marie Curie, August 2003. 9

[14] Ya Blanter and M. Büttiker. Shot noise in mesoscopic conductors. Physics Reports, 336(1-2) :1–166, September 2000. 1, 45

[15] M. D. Blumenthal, B. Kaestner, L. Li, S. Giblin, T. J. B. M. Janssen, M. Pepper, D. Anderson, G. Jones, and D. A. Ritchie. Gigahertz quantized charge pumping. Nature Physics, 3(5) :343–347, April 2007. 2, 148

[16] E. Bocquillon, V. Freulon, J. M. Berroir, P. Degiovanni, B. Plaçais, A. Cavanna, Y. Jin, and G. Fève. Coherence and Indistinguishability of Single Electrons Emitted by Independent Sources. Science, 339(6123) :1054–1057, March 2013. 2, 39

[17] E. Bocquillon, F. D. Parmentier, C. Grenier, J. M. Berroir, P. Degiovanni, D. C. Glattli, B. Plaçais, A. Cavanna, Y. Jin, and G. Fève. Electron Quantum Optics : Partitioning Electrons One by One. Physical Review Letters, 108(19) :196803+, May 2012. 2, 17

[18] Erwann Bocquillon, Vincent Freulon, François D. Parmentier, Jean-Marc Berroir, Bernard Plaçais, Claire Wahl, Jérome Rech, Thibaut Jonckheere, Thierry Martin, Charles Grenier, Dario Ferraro, Pascal Degiovanni, and Gwendal Fève. Electron quantum optics in ballistic chiral conductors. Annalen der Physik, 526(1-2) :1–30, January 2014. 2

[19] Jean-Philippe Brantut, Jakob Meineke, David Stadler, Sebastian Krinner, and Tilman Esslinger. Conduction of Ultracold Fermions Through a Mesoscopic Channel. Science, 337(6098) :1069–1071, August 2012. 148

[20] Norman Braslau. Ohmic contacts to GaAs. Thin Solid Films, 104(3-4) :391–397, June 1983. 159

[21] R. A. Bruce and G. R. Piercy. An improved Au-Ge-Ni ohmic contact to n-type GaAs. Solid-State Electronics, 30(7) :729–737, July 1987. 160

[22] M. Büttiker. Absence of backscattering in the quantum Hall effect in multiprobe conductors. Physical Review B, 38(14) :9375–9389, November 1988. 2

[23] M. Büttiker. Quantized transmission of a saddle-point constriction. Physical Review B, 41(11) :7906–7909, April 1990. 57

[24] M. Büttiker. Scattering theory of thermal and excess noise in open conductors. Physical Review Letters, 65(23) :2901–2904, December 1990. 10

[25] M. Büttiker. Scattering theory of current and intensity noise correlations in conductors and wave guides. Physical Review B, 46(19) :12485–12507, November 1992. 14

[26] M. Büttiker, Y. Imry, R. Landauer, and S. Pinhas. Generalized many-channel conductance formula with application to small rings. Physical Review B, 31(10) :6207–6215, May 1985. 1, 6

[27] M. Büttiker, A. Prêtre, and H. Thomas. Dynamic conductance and the scattering matrix of small conductors. Physical Review Letters, 70(26) :4114–4117, June 1993. 11

[28] V. Buzek, G. Drobny, R. Derka, G. Adam, and H. Wiedemann. Quantum State Reconstruction From Incomplete Data, May 1998. 132

[29] A. V. Chaplik. Energy Spectrum and Electron Scattering processes in Inversion Layers. Journal of Experimental and Theoretical Physics, 33(5) :856+, November 1971. 43, 162

[30] David Dasenbrook, Christian Flindt, and Markus Büttiker. Floquet Theory of Electron Waiting Times in Quantum-Coherent Conductors, November 2013. 39

[31] Kristiaan De Greve, Peter L. McMahon, Leo Yu, Jason S. Pelc, Cody Jones, Chandra M. Natarajan, Na Y. Kim, Eisuke Abe, Sebastian Maier, Christian Schneider, Martin Kamp, Sven Höfling, Robert H. Hadfield, Alfred Forchel, M. M. Fejer, and Yoshihisa Yamamoto. Complete tomography of a high-fidelity solid-state entangled spin–photon qubit pair. Nature Communications, 4, July 2013. 123

[32] Michel H. Devoret, Daniel Esteve, and Cristian Urbina. Single-electron transfer in metallic nanostructures. Nature, 360(6404) :547–553, December 1992. 2

[33] L. DiCarlo, Y. Zhang, D. McClure, D. Reilly, C. Marcus, L. Pfeiffer, and K. West. Shot-Noise Signatures of 0.7 Structure and Spin in a Quantum Point Contact. Physical Review Letters, 97(3) :036810+, July 2006. 65

[34] L. DiCarlo, Y. Zhang, D. T. McClure, C. M. Marcus, L. N. Pfeiffer, and K. W. West. System for measuring auto- and cross correlation of current noise at low temperatures. Review of Scientific Instruments, 77(7) :073906+, 2006. 46, 48, 73, 76, 188

[35] R. Dingle, H. L. Störmer, A. C. Gossard, and W. Wiegmann. Electron mobilities in modulation-doped semiconductor heterojunction superlattices. Applied Physics Letters, 33(7) :665–667, 1978. 156

[36] Drazin. Solitons an introduction, 1989. 44

[37] J. Dubois. Towards a n-electron source based on Lorentzian voltage pulses. PhD thesis, University Pierre et Marie Curie, CEA Saclay, October 2012. 33, 40, 73, 74, 75, 110, 154, 167

[38] J. Dubois, T. Jullien, C. Grenier, P. Degiovanni, P. Roulleau, and D. C. Glattli. Integer and fractional charge Lorentzian voltage pulses analyzed in the framework of photon-assisted shot noise. Physical Review B, 88(8), August 2013. 1, 5, 22, 119, 137

[39] J. Dubois, T. Jullien, F. Portier, P. Roche, A. Cavanna, Y. Jin, W. Wegscheider, P. Roulleau, and D. C. Glattli. Minimal-excitation states for electron quantum optics using levitons. Nature, 502(7473) :659–663, October 2013. 103

[40] T. Dunn, I. Walmsley, and S. Mukamel. Experimental Determination of the Quantum-Mechanical State of a Molecular Vibrational Mode Using Fluorescence Tomography. Physical Review Letters, 74(6) :884–887, February 1995. 123

[41] G. Fève, A. Mahé, J. M. Berroir, T. Kontos, B. Plaçais, D. C. Glattli, A. Cavanna, B. Etienne, and Y. Jin. An On-Demand Coherent Single-Electron Source. Science, 316(5828) :1169–1172, May 2007. 2, 17, 39, 148

[42] Lukas Fricke, Michael Wulf, Bernd Kaestner, Vyacheslavs Kashcheyevs, Janis Timoshenko, Pavel Nazarov, Frank Hohls, Philipp Mirovsky, Brigitte Mackrodt, Ralf Dolata, Thomas Weimann, Klaus Pierz, and Hans W. Schumacher. Counting Statistics for Electron Capture in a Dynamic Quantum Dot. Physical Review Letters, 110 :126803+, March 2013. 2

[43] M. Frigo and S. G. Johnson. The Design and Implementation of FFTW3. Proceedings of the IEEE, 93(2) :216–231, February 2005. 67

[44] Julien Gabelli and Bertrand Reulet. Shaping a time-dependent excitation to minimize the shot noise in a tunnel junction. Physical Review B, 87(7), February 2013. 19, 32, 74, 99

[45] Gabriel Gasse, Lafe Spietz, Christian Lupien, and Bertrand Reulet. Observation of Quantum Oscillations in the Photo-assisted Shot Noise of a Tunnel Junction, June 2013. 114

[46] Benoit Gaury, Joseph Weston, Matthieu Santin, Manuel Houzet, Christoph Groth, and Xavier Waintal. Numerical simulations of time resolved quantum electronics, July 2013. 39

[47] G. Gershon, Yu, E. V. Sukhorukov, and M. Reznikov. Detection of Non-Gaussian Fluctuations in a Quantum Point Contact. Physical Review Letters, 101(1) :016803+, July 2008. 2

[48] Gabriele F. Giuliani and John J. Quinn. Lifetime of a quasiparticle in a two-dimensional electron gas. Physical Review B, 26(8) :4421–4428, October 1982. 43, 162

[49] D. C. Glattli, P. Jacques, A. Kumar, P. Pari, and L. Saminadayar. A noise detection scheme with 10 mK noise temperature resolution for semiconductor single electron tunneling devices. Journal of Applied Physics, 81(11) :7350–7356, 1997. 53

[50] L. I. Glazman, G. B. Lesovik, D. E. Khmel'nitskii, and R. I. Shekhter. Reflectionless quantum transport and fundamental ballistic-resistance steps in microscopic constrictions. JETP Letters, 48(4) :238–241, August 1988. 57, 59

[51] Oktay Göktaş, Jochen Weber, Jürgen Weis, and Klaus von Klitzing. Alloyed ohmic contacts to two-dimensional electron system in AlGaAs/GaAs heterostructures down to submicron length scale. Physica E : Low-dimensional Systems and Nanostructures, 40(5) :1579–1581, March 2008. 159

[52] D. Greig, R. Jakeways, and M. Sahota. The low-temperature thermal conductivity of a polyoxymethylene "crystal". The Journal of Chemical Physics, 68(3) :1104–1107, 1978. 48

[53] Emile Gremion. Transistor balistique quantique et HEMT bas-bruit pour la cryoélectronique inférieure à 4.2 K. PhD thesis, Université Paris Sud XI, 2008. 85, 156

[54] Ch Grenier, J. Dubois, T. Jullien, P. Roulleau, D. C. Glattli, and P. Degiovanni. Fractionalization of minimal excitations in integer quantum Hall edge channels. Physical Review B, 88(8), August 2013. 13, 149

[55] Ch Grenier, R. Hervé, E. Bocquillon, F. D. Parmentier, B. Plaçais, J. M. Berroir, G. Fève, and P. Degiovanni. Single-electron quantum tomography in quantum Hall edge channels. New Journal of Physics, 13(9) :093007+, September 2011. 13, 123, 135

[56] Charles Grenier. Optique quantique électronique. PhD thesis, ENS Lyon, CNRS : UMR5672 – École Normale Supérieure (ENS) - Lyon 46 allée d'Italie 69007 Lyon France, June 2011. 2

[57] R. P. Gupta and W. S. Khokle. Gallium-vacancy-dependent diffusion model of ohmic contacts to GaAs. Solid-State Electronics, 28(8) :823–830, August 1985. 160

[58] S. Gustavsson, D. Gunnarsson, and P. Delsing. Cryogenic amplifier for intermediate source impedance with gigahertz bandwidth. Applied Physics Letters, 88(15) :153505+, 2006. 69

[59] Fabian Hassler, Bruno Kung, Gordey B. Lesovik, Gianni Blatter, Vladimir Lebedev, and Mikhail Feigel'man. Single-Particle Excitations Generated by Voltage Pulses. In AIP Conference Proceedings, pages 113–119. AIP, 2009. 40, 42

[60] M. Henny, S. Oberholzer, C. Strunk, and C. Schönenberger. 1/3-shot-noise suppression in diffusive nanowires. Physical Review B, 59(4) :2871–2880, January 1999. 53

[61] Sylvain Hermelin, Shintaro Takada, Michihisa Yamamoto, Seigo Tarucha, Andreas D. Wieck, Laurent Saminadayar, Christopher Bäuerle, and Tristan Meunier. Electrons surfing on a sound wave as a platform for quantum optics with flying electrons. Nature, 477(7365) :435–438, September 2011. 2, 148

[62] C. K. Hong, Z. Y. Ou, and L. Mandel. Measurement of subpicosecond time intervals between two photons by interference. Physical Review Letters, 59(18) :2044–2046, November 1987. 39

[63] Paul Horowitz and Winfield Hill. The Art of Electronics. Cambridge University Press, 2 edition, July 1989. 70

[64] M. J. Iqbal, De, D. Reuter, A. D. Wieck, and C. H. van der Wal. Split-gate quantum point contacts with tunable channel length. Journal of Applied Physics, 113(2) :024507+, 2013. 157

[65] D. A. Ivanov, H. W. Lee, and L. S. Levitov. Coherent states of alternating current. Physical Review B, 56(11) :6839–6850, September 1997. 1, 2, 5, 20, 21

[66] Yang Ji, Yunchul Chung, D. Sprinzak, M. Heiblum, D. Mahalu, and Hadas Shtrikman. An electronic Mach–Zehnder interferometer. Nature, 422(6930) :415–418, March 2003. 2

[67] J. Johnson. Thermal Agitation of Electricity in Conductors. Physical Review, 32(1) :97–109, July 1928. 9

[68] T. Jonckheere, M. Creux, and T. Martin. Time-controlled charge injection in a quantum Hall fluid. Physical Review B, 72 :205321+, November 2005. 148

[69] T. Jonckheere, J. Rech, C. Wahl, and T. Martin. Electron and hole Hong-Ou-Mandel interferometry. Physical Review B, 86(12), September 2012. 2, 39

[70] M. Kamada, T. Suzuki, F. Nakamura, Y. Mori, and M. Arai. Investigation of orientation effect on contact resistance in selectively doped AlGaAs-GaAs heterostructures. Applied Physics Letters, 49(19) :1263–1265, 1986. 159

[71] J. Keeling, I. Klich, and L. S. Levitov. Minimal Excitation States of Electrons in One-Dimensional Wires. Physical Review Letters, 97(11) :116403+, September 2006. 1, 38, 40, 42, 43, 148

[72] J. Keeling, A. V. Shytov, and L. S. Levitov. Coherent Particle Transfer in an On-Demand Single-Electron Source. Physical Review Letters, 101(19) :196404+, November 2008. 2, 44

[73] Klitzing, G. Dorda, and M. Pepper. New Method for High-Accuracy Determination of the Fine-Structure Constant Based on Quantized Hall Resistance. Physical Review Letters, 45(6) :494–497, August 1980. 2

[74] Y. Kondo, S. Fukano, A. Ninomiya, and T. Ishigohka. Cryogenic Low-Voltage/High-Current DC Power Source Using Multi-Parallel-Connected MOSFETs. Applied Superconductivity, IEEE Transactions on, 19(3) :2337–2340, June 2009. 69

[75] E. J. Koop, M. J. Iqbal, F. Limbach, M. Boute, B. J. van Wees, D. Reuter, A. D. Wieck, B. J. Kooi, and C. H. van der Wal. On the annealing mechanism of AuGe/Ni/Au ohmic contacts to a two-dimensional electron gas in GaAs/AlxGa1-xAs heterostructures. Semiconductor Science and Technology, 28(2) :025006+, February 2013. 160

[76] L. P. Kouwenhoven, B. J. van Wees, C. J. P. M. Harmans, J. G. Williamson, H. van Houten, C. W. J. Beenakker, C. T. Foxon, and J. J. Harris. Nonlinear conductance of quantum point contacts. Physical Review B, 39 :8040–8043, April 1989. 59

[77] Alex Kozhevnikov. Electron dynamics and coherence effects in mesoscopic hybrid normal metal-superconductor devices. PhD thesis, Yale, ProberLab Yale, 2001. 18

[78] A. Kumar, L. Saminadayar, D. Glattli, Y. Jin, and B. Etienne. Experimental Test of the Quantum Shot Noise Reduction Theory. Physical Review Letters, 76(15) :2778–2781, April 1996. 2, 9, 53, 63, 64, 110

[79] L. D. Landau and L. M. Lifshitz. Quantum Mechanics Non-Relativistic Theory, Third Edition : Volume 3. Butterworth-Heinemann, 3 edition, January 1981. 57

[80] R. Landauer and Th Martin. Equilibrium and shot noise in mesoscopic systems. Physica B : Condensed Matter, 175(1-3) :167–177, December 1991. 9

[81] Rolf Landauer. Johnson-Nyquist noise derived from quantum mechanical transmission. Physica D : Nonlinear Phenomena, 38(1-3) :226–229, September 1989. 9

[82] Jason Lawrence, A. B. Patel, and J. G. Brisson. The thermal conductivity of Kapton HN between 0.5 and 5 K. Cryogenics, 40(3) :203–207, March 2000. 48

[83] Adrian Tae Jin Lee. A low-power-dissipation broadband cryogenic preamplifier utilizing GaAs MESFETs in parallel. Review of Scientific Instruments, 64(8) :2373–2378, 1993. 69

[84] H. W. Lee and L. S. Levitov. Orthogonality catastrophe in a mesoscopic conductor due to a time-dependent flux, December 1993. 22, 114

[85] D. Leibfried, D. Meekhof, B. King, C. Monroe, W. Itano, and D. Wineland. Experimental Determination of the Motional Quantum State of a Trapped Atom. Physical Review Letters, 77(21) :4281–4285, November 1996. 123

[86] G. Lesovik and L. Levitov. Noise in an ac biased junction : Nonstationary Aharonov-Bohm effect. Physical Review Letters, 72(4) :538–541, January 1994. 2, 14

[87] G. B. Lesovik. Current fluctuations in an ideally conducting contact. JETP Letters, 70(3) :208–215, August 1999. 10

[88] L. S. Levitov. The Statistical Theory of Mesoscopic Noise, October 2002. 10

[89] L. S. Levitov and G. Lesovik. Charge distribution in quantum shot noise. JETP Letters, 58(3) :225–235, August 1993. 2, 9, 10

[90] Leonid S. Levitov, Hyunwoo Lee, and Gordey B. Lesovik. Electron counting statistics and coherent states of electric current. Journal of Mathematical Physics, 37(10) :4845–4866, 1996. v, vii, 1, 2, 5, 20, 21, 103, 114

[91] R. C. Liu, B. Odom, Y. Yamamoto, and S. Tarucha. Quantum interference in electron collision. Nature, 391(6664) :263–265, January 1998. 2, 52, 53

[92] Yu-xi Liu, L. Wei, and Franco Nori. Tomographic measurements on superconducting qubit states. Physical Review B, 72(1), July 2005. 123

[93] A. I. Lvovsky. Continuous-variable optical quantum-state tomography. Reviews of Modern Physics, 81(1) :299–332, March 2009. 135

[94] A. Mahé, F. D. Parmentier, E. Bocquillon, J. M. Berroir, D. C. Glattli, T. Kontos, B. Plaçais, G. Fève, A. Cavanna, and Y. Jin. Current correlations of an on-demand single-electron emitter. Physical Review B, 82(20), November 2010. 40, 74

[95] T. Martin. Course 5 Noise in mesoscopic physics, volume 81, pages 283–359. Elsevier, 2005. 1, 45

[96] Th Martin and R. Landauer. Wave-packet approach to noise in multichannel mesoscopic systems. Physical Review B, 45(4) :1742–1755, January 1992. 9, 119

[97] L. Martin-Moreno, J. T. Nicholls, N. K. Patel, and M. Pepper. Non-linear conductance of a saddle-point constriction. Journal of Physics : Condensed Matter, 4(5) :1323+, February 1992. 59

[98] Jacques Max. Méthodes et techniques de traitement du signal et applications aux mesures physiques. Masson, 1981. 53

[99] R. P. G. McNeil, M. Kataoka, C. J. B. Ford, C. H. W. Barnes, D. Anderson, G. A. C. Jones, I. Farrer, and D. A. Ritchie. On-demand single-electron transfer between distant quantum dots. Nature, 477(7365) :439–442, September 2011. 2, 148

[100] A. P. Micolich. What lurks below the last plateau : experimental studies of the 0.7*2e2/h conductance anomaly in one-dimensional systems. Journal of Physics : Condensed Matter, 23(44) :443201+, November 2011. 59

[101] M. Moskalets and M. Büttiker. Floquet scattering theory of quantum pumps. Physical Review B, 66(20) :205320+, November 2002. 12

[102] M. Moskalets, P. Samuelsson, and M. Büttiker. Quantized Dynamics of a Coherent Capacitor. Physical Review Letters, 100(8) :086601+, February 2008. 2

[103] Michael Moskalets and Markus Büttiker. Spectroscopy of electron flows with single- and two-particle emitters. Physical Review B, 83(3) :035316+, January 2011. 38

[104] B. A. Muzykantskii and Y. Adamov. Scattering approach to counting statistics in quantum pumps. Physical Review B, 68 :155304+, October 2003. 10

[105] I. Neder, N. Ofek, Y. Chung, M. Heiblum, D. Mahalu, and V. Umansky. Interference between two indistinguishable electrons from independent sources. Nature, 448(7151) :333–337, July 2007. 2

[106] Michael A. Nielsen and Isaac L. Chuang. Quantum Computation and Quantum Information : 10th Anniversary Edition. Cambridge University Press, 10 anv edition, January 2011. 2, 149

[107] H. Nyquist. Thermal Agitation of Electric Charge in Conductors. Physical Review Online Archive (Prola), 32(1) :110–113, July 1928. 9

[108] S. Oberholzer, E. Sukhorukov, C. Strunk, C. Schönenberger, T. Heinzel, and M. Holland. Shot Noise by Quantum Scattering in Chaotic Cavities. Physical Review Letters, 86(10) :2114–2117, March 2001. 53

[109] S. Oberholzer, E. V. Sukhorukov, and C. Schönenberger. Crossover between classical and quantum shot noise in chaotic cavities. Nature, 415(6873) :765–767, February 2002. 53

[110] William D. Oliver, Jungsang Kim, Robert C. Liu, and Yoshihisa Yamamoto. Hanbury Brown and Twiss-Type Experiment with Electrons. Science, 284(5412) :299–301, April 1999. 2

[111] S. Ol'khovskaya, J. Splettstoesser, M. Moskalets, and M. Büttiker. Shot Noise of a Mesoscopic Two-Particle Collider. Physical Review Letters, 101(16) :166802+, October 2008. 39

[112] F. D. Parmentier, E. Bocquillon, J. M. Berroir, D. C. Glattli, B. Plaçais, G. Fève, M. Albert, C. Flindt, and M. Büttiker. Current noise spectrum of a single-particle emitter : Theory and experiment. Physical Review B, 85(16), April 2012. 40

[113] N. K. Patel, L. Martin-Moreno, M. Pepper, R. Newbury, J. E. F. Frost, D. A. Ritchie, G. A. C. Jones, J. T. M. B. Janssen, J. Singleton, and J. A. A. J. Perenboom. Ballistic transport in one dimension : additional quantisation produced by an electric field. Journal of Physics : Condensed Matter, 2(34) :7247+, August 1990. 59

[114] Morten Pedersen and Markus Buttiker. Scattering theory of photon-assisted electron transport. Physical Review B, 58(19) :12993–13006, November 1998. 2, 11, 14

[115] J. P. Pekola, O. P. Saira, V. F. Maisi, A. Kemppinen, M. Möttönen, Yu, and D. V. Averin. Single-electron current sources : towards a refined definition of ampere, September 2012. 2

[116] Loren Pfeiffer and K. W. West. The role of MBE in recent quantum Hall effect physics discoveries. Physica E : Low-dimensional Systems and Nanostructures, 20(1-2) :57–64, December 2003. 158

[117] Loren Pfeiffer, K. W. West, H. L. Stormer, and K. W. Baldwin. Electron mobilities exceeding $10\hat{7}$ cm$\hat{2}$/v s in modulation-doped gaas. Applied Physics Letters, 55(18) :1888–1890, 1989. 156

[118] D. Reilly. Phenomenological model for the 0.7 conductance feature in quantum wires. Physical Review B, 72(3) :033309+, July 2005. 64

[119] B. Reulet, J. Senzier, and D. E. Prober. Environmental Effects in the Third Moment of Voltage Fluctuations in a Tunnel Junction. Physical Review Letters, 91(19) :196601+, November 2003. 2

[120] L. H. Reydellet, P. Roche, D. Glattli, B. Etienne, and Y. Jin. Quantum Partition Noise of Photon-Created Electron-Hole Pairs. Physical Review Letters, 90(17) :176803+, April 2003. 2, 14, 18, 93

[121] M. Reznikov, M. Heiblum, Hadas Shtrikman, and D. Mahalu. Temporal Correlation of Electrons : Suppression of Shot Noise in a Ballistic Quantum Point Contact. Physical Review Letters, 75(18) :3340–3343, October 1995. 2, 9, 52, 53

[122] A. M. Robinson and V. I. Talyanskii. Cryogenic amplifier for ˜ 1 MHz with a high input impedance using a commercial pseudomorphic high electron mobility transistor. Review of Scientific Instruments, 75(10) :3169–3176, 2004. 46, 73, 188

[123] P. Roche, J. Ségala, D. Glattli, J. Nicholls, M. Pepper, A. Graham, K. Thomas, M. Simmons, and D. Ritchie. Fano Factor Reduction on the 0.7 Conductance Structure of a Ballistic One-Dimensional Wire. Physical Review Letters, 93(11) :116602+, September 2004. 65

[124] Preden Roulleau, F. Portier, P. Roche, A. Cavanna, G. Faini, U. Gennser, and D. Mailly. Direct Measurement of the Coherence Length of Edge States in the Integer Quantum Hall Regime. Physical Review Letters, 100(12) :126802+, March 2008. 2

[125] Valentin Rychkov, Mikhail Polianski, and Markus Büttiker. Photon-assisted electron-hole shot noise in multiterminal conductors. Physical Review B, 72(15) :155326+, October 2005. 14, 15

[126] L. Saminadayar, D. Glattli, Y. Jin, and B. Etienne. Observation of the e/3 Fractionally Charged Laughlin Quasiparticle. Physical Review Letters, 79(13) :2526–2529, September 1997. 53

[127] P. Samuelsson and M. Büttiker. Quantum state tomography with quantum shot noise. Physical Review B, 73(4), January 2006. 123

[128] R. Schoelkopf, A. Kozhevnikov, D. Prober, and M. Rooks. Observation of Photon-Assisted Shot Noise in a Phase-Coherent Conductor. Physical Review Letters, 80(11) :2437–2440, March 1998. 2, 14, 18

[129] R. J. Schoelkopf, P. J. Burke, A. A. Kozhevnikov, D. E. Prober, and M. J. Rooks. Frequency Dependence of Shot Noise in a Diffusive Mesoscopic Conductor. Physical Review Letters, 78(17) :3370–3373, April 1997. 60

[130] R. J. Schoelkopf, P. Wahlgren, A. A. Kozhevnikov, P. Delsing, and D. E. Prober. The radio-frequency single-electron transistor (RF-SET) : A fast and ultrasensitive electrometer. Science (New York, N.Y.), 280(5367) :1238–1242, May 1998. 74, 93

[131] W. Schottky. Über spontane Stromschwankungen in verschiedenen Elektrizitätsleitern. Annalen der Physik, 362(23) :541–567, 1918. 9

[132] Y. Sherkunov, Jin Zhang, N. d'Ambrumenil, and B. Muzykantskii. Optimal electron entangler and single-electron source at low temperatures. Physical Review B, 80(4) :041313+, July 2009. 149

[133] Michael Shur. Handbook series on semiconductor parameters. World Scientific, 1996. 156

[134] D. Smithey, M. Beck, M. Raymer, and A. Faridani. Measurement of the Wigner distribution and the density matrix of a light mode using optical homodyne tomography : Application to squeezed states and the vacuum. Physical Review Letters, 70(9) :1244–1247, March 1993. 123

[135] Lafe Spietz, K. W. Lehnert, I. Siddiqi, and R. J. Schoelkopf. Primary Electronic Thermometry Using the Shot Noise of a Tunnel Junction. Science, 300(5627) :1929–1932, June 2003. 62

[136] Lafe Spietz, R. J. Schoelkopf, and Patrick Pari. Shot noise thermometry down to 10 mK. Applied Physics Letters, 89(18) :183123+, 2006. 62

[137] Michael Steer. Microwave and RF Design : A Systems Approach. SciTech Publishing, enlarged edition, April 2010. 185

[138] Andrew Steinbach, John Martinis, and Michel Devoret. Observation of Hot-Electron Shot Noise in a Metallic Resistor. Physical Review Letters, 76(20) :3806–3809, May 1996. 52, 173

[139] Frank Stern. Polarizability of a Two-Dimensional Electron Gas. Physical Review Letters, 18(14) :546–548, April 1967. 162

[140] Stormer. Nobel Lecture : The Fractional Quantum Hall Effect, 1998. 156

[141] H. L. Stormer. Two-dimensional electron gas at differentially doped GaAs-AlxGa1-xAs heterojunction interface. Journal of Vacuum Science and Technology, 16(5) :1517+, September 1979. 1, 156, 157

[142] Hélène L. Sueur and Philippe Joyez. Room-temperature tunnel current amplifier and experimental setup for high resolution electronic spectroscopy in millikelvin scanning tunneling microscope experiments. Review of Scientific Instruments, 77(12) :123701+, 2006. 74

[143] T. Thornton, M. Pepper, H. Ahmed, D. Andrews, and G. Davies. One-Dimensional Conduction in the 2D Electron Gas of a GaAs-AlGaAs Heterojunction. Physical Review Letters, 56(11) :1198–1201, March 1986. 156

[144] Henk van Houten and Carlo Beenakker. Quantum Point Contacts. Physics Today, 49(7) :22+, 1996. 155, 159

[145] B. van Wees, H. van Houten, C. Beenakker, J. Williamson, L. Kouwenhoven, D. van der Marel, and C. Foxon. Quantized conductance of point contacts in a two-dimensional electron gas. Physical Review Letters, 60(9) :848–850, February 1988. 2, 155, 157

[146] Mihajlo Vanević and Wolfgang Belzig. Control of electron-hole pair generation by biharmonic voltage drive of a quantum point contact. Physical Review B, 86(24), December 2012. 32

[147] Mihajlo Vanević, Yuli Nazarov, and Wolfgang Belzig. Elementary charge-transfer processes in mesoscopic conductors. Physical Review B, 78(24) :245308+, December 2008. 23

[148] Mihajlo Vanević, Yuli V. Nazarov, and Wolfgang Belzig. Elementary Events of Electron Transfer in a Voltage-Driven Quantum Point Contact. Physical Review Letters, 99(7) :076601+, August 2007. 14, 22

[149] S. Weinreb, J. C. Bardin, and H. Mani. Design of Cryogenic SiGe Low-Noise Amplifiers. Microwave Theory and Techniques, IEEE Transactions on, 55(11) :2306–2312, November 2007. 70

[150] R. P. Welty and John M. Martinis. A series array of DC SQUIDs. Magnetics, IEEE Transactions on, 27(2) :2924–2926, March 1991. 69

[151] D. A. Wharam, T. J. Thornton, R. Newbury, M. Pepper, H. Ahmed, J. E. F. Frost, D. G. Hasko, D. C. Peacock, D. A. Ritchie, and G. A. C. Jones. One-dimensional transport and the quantisation of the ballistic resistance. Journal of Physics C : Solid State Physics, 21(8) :L209+, March 1988. 2, 155, 157

[152] Ya. Recent Advances in Studies of Current Noise, November 2005. 1, 45

[153] A. Yacoby, U. Sivan, C. Umbach, and J. Hong. Interference and dephasing by electron-electron interaction on length scales shorter than the elastic mean free path. Physical Review Letters, 66(14) :1938–1941, April 1991. 43, 162

[154] Michihisa Yamamoto, Shintaro Takada, Christopher Bäuerle, Kenta Watanabe, Andreas D. Wieck, and Seigo Tarucha. Electrical control of a solid-state flying qubit. Nature Nanotechnology, 7(4) :247–251, March 2012. 149

[155] Yu, G. Gershon, D. Shovkun, Levitov, and M. Reznikov. Measurement of Counting Statistics of Electron Transport in a Tunnel Junction. Physical Review Letters, 95(17) :176601+, October 2005. 2

[156] E. Zakka-Bajjani, J. Ségala, F. Portier, P. Roche, D. Glattli, A. Cavanna, and Y. Jin. Experimental Test of the High-Frequency Quantum Shot Noise Theory in a Quantum Point Contact. Physical Review Letters, 99(23) :236803+, December 2007. 59, 60, 74, 166

[157] E. Zakka-Bajjani, J. Segala, F. Portier, P. Roche, D. C. Glattli, A. Cavanna, and Y. Jin. Observation of the shot noise singularity in a quantum point contact. Physica E : Low-dimensional Systems and Nanostructures, 40(5) :1697–1699, March 2008. 60

[158] H. Zheng, H. Wei, D. Tsui, and G. Weimann. Gate-controlled transport in narrow gaas/al_xga_1-xas heterostructures. Physical Review B, 34(8) :5635–5638, October 1986. 156